Application of Responsive Lamellar Membranes of Layered Materials for Microdroplet Handling, Sensing, and Energy Harvesting

A dissertation submitted to the
Indian Institute of Technology Guwahati as
partial fulfilment of the Degree of

DOCTOR of PHILOSOPHY

Submitted by

Arindom Bikash Neog

Roll No: 176122027

Department of Chemistry
Indian Institute of Technology Guwahati
Guwahati-781039 Assam, India
March 2024

Dedicated to the

unwavering pillars of my

journey – my Parents

INDIAN INSTITUTE OF TECHNOLOGY

GUWAHATI

Department of Chemistry

STATEMENT

I hereby declare that the matter embodied in this thesis entitled "***Application of Responsive Lamellar Membranes of Layered Materials for Microdroplet Handling, Sensing, and Energy Harvesting***" is the results of the investigations carried out by me at the Department of Chemistry, Indian Institute of Technology Guwahati, Assam, India under the guidance of Dr. Kalyan Raidongia.

In keeping with the general practice in reporting scientific observations, due acknowledgement has been made whenever the work described is based on the findings of other investigators.

Date: August, 2024 **Arindom Bikash Neog**

IIT Guwahati

INDIAN INSTITUTE OF TECHNOLOGY

GUWAHATI

Department of Chemistry

CERTIFICATE

This is to certify that the matter embodied in this thesis entitled **"*Application of Responsive Lamellar Membranes of Layered Materials for Microdroplet Handling, Sensing, and Energy Harvesting*"** has been carried out by **Mr. Arindom Bikash Neog** at the Department of Chemistry, Indian Institute of Technology Guwahati, Assam, India. It has not been submitted elsewhere for the award of any degree or diploma.

Date: August, 2024
IIT Guwahati

Dr. Kalyan Raidongia
(Thesis Supervisor)
Department of Chemistry
Indian Institute of Technology Guwahati
Guwahati-781039
Assam, India

PREFACE

The present thesis with the title “Application of Responsive Lamellar Membranes of Layered Materials for Microdroplet Handling, Sensing, and Energy Harvesting” is divided into six chapters. Chapter 1 delves into the significance of microdroplet handling, sensing, and energy harvesting across diverse domains. Additionally, it articulates the various pathways for generating 2D materials through the exfoliation of layered materials, the reconstruction of these materials, and the assembly of the resulting nanosheets into lamellar membranes. The chapter also outlines the manifold applications of these lamellar membranes.

In Chapter 2, a sophisticated hydrophobic bilayer membrane of reduced graphene oxide (r-GO) and agar (r-GO/agar) is discussed. This breakthrough allows for precise manipulation of microliter-range liquids. The membrane's U-shaped electrical actuator manages microdroplet weight by adjusting parameters such as surface tension, contact angle, and applied voltage. The wettability of the reduced graphene oxide in the membrane can be controlled by adjusting the surface roughness through the incorporation of gold nanoparticles. The rapid liquid mixing enables fast chemical reactions on a microliter scale. Additionally, the membrane is poised to simplify routine chemical analyses.

In Chapter 3, the potential of reconstructed layered materials based responsive membranes for on-site detection of chemical contaminants in liquid phases is explored. A bilayer membrane made of reduced graphene oxide (r-GO) and agar (r-GO/agar) shows significant responsiveness to solvent vapors in the air. The study suggests that the alteration in the shape of the r-GO/agar membrane is attributed to disparate changes in the mechanical attributes of its constituent components. Additionally, rectangular strips of the bilayer membrane exhibit shape morphing properties when immersed in liquid environments. The study finds that the bending angle and response time of the r-GO/agar strips are notably sensitive to minute quantities of impurities

within the solvent system, indicating a potential for leveraging this sensitivity for the detection of contaminants in liquid phases.

In Chapter 4, a bilayer actuator was developed using multiwalled carbon nanotubes (CNT) or oxidized multiwalled carbon nanotubes (o-CNT) combined with exfoliated two-dimensional (2D) vanadium pentoxide (VO) flakes to precisely manipulate reactive substances. These bilayer membranes exhibit light-controlled shape morphing and exceptional Joule heating effect, achieving high bending speeds under light and electrical stimulation. They can pick up and release reactive chemicals, support significant loads, transport microdroplets of hazardous chemicals, and sense the nature of materials they handle. The actuators could maintain shape-morphing characteristics after exposure to various liquids.

In Chapter 5, a new type of permselective nanofluidic membrane was created by coating a standard nylon membrane with two-dimensional functionalised nanosheets of vanadium pentoxide (V_2O_5). Tests showed that this coating improved the membrane's ability to allow certain ions to pass through. It was also found that using contrasting materials for the electrodes in energy-harvesting devices significantly increased their electrical output. Electrodes made from modified V_2O_5 and polyaniline (PANI) produced a high electrical potential from quiescent water, without needing a concentration gradient. When a pair of V_2O_5 and PANI electrodes in combination with permselective nanofluidic membrane were used, the overall energy produced increased by three times compared to traditional Ag/AgCl electrodes, when using a 10-fold concentration gradient.

The chapter 6 consist of overall conclusion of the work done during my PhD tenure and the future perspectives of the work.

.

ACKNOWLEDGEMENTS

With immense gratitude and a deep sense of appreciation I take this opportunity to thank all those who have supported and accompanied me throughout my PhD journey.

First and foremost, I wish to express my deepest and most sincere gratitude to my esteemed supervisor, **Dr. Kalyan Raidongia**. Words fall short of conveying my appreciation for the opportunity to work under his expert supervision. This thesis would not have been possible without his boundless support, insightful guidance, and invaluable suggestions. His tireless efforts, profound wisdom, and unwavering belief in my potential have motivated and inspired me throughout my PhD life. I consider myself incredibly fortunate to have had the privilege of working under such a remarkable mentor.

I am profoundly thankful to my doctoral committee members, **Prof. Biplab Mondal**, **Dr. Uttam Manna** and **Dr. Dipankar Srimani**, for their unwavering support and constructive input. Their valuable advice and insightful suggestions have greatly contributed to improving my thesis. Their constant encouragement and willingness to share their knowledge have shaped my research journey.

My heartfelt thanks also extend to all the faculty members of the Department of Chemistry at IIT Guwahati, whose encouragement and support have been invaluable. I am equally grateful to the department's technical staff for their indispensable assistance. The Central Instrument Facility (CIF) and the Department of Chemistry at IIT Guwahati have provided me access to essential resources, which I deeply appreciate. I am also thankful to IIT Guwahati for the financial support through the Scholarship, which has allowed me to pursue my research without financial constraints.

I wish to extend my deepest thanks to all the members of Dergaon Kamal Dowerah College, Dergaon. A special thanks are owed to the faculty and staff of the Department of Chemistry at

Dergaon Kamal Dowerah College, whose unwavering support has been crucial during my PhD journey. I am also profoundly grateful to all my teachers, beginning with my time at Don Bosco School, Dergaon, followed by Dergaon Kamal Dowerah College, and finally, Tezpur University, where I pursued my master's degree. Their teachings have laid the foundation for my academic pursuits, and I am forever indebted to them.

I owe a special gratitude to my senior, Dr. Raj Kumar Gogoi, whose consistent support, encouragement, and guidance have been a guiding light throughout my PhD journey. My heartfelt thanks also go out to Dr. Kundan Saha, Dr. Jumi Deka, Dr. Tukhar Jyoti Konch, Mr. Madhujya Buragohain, Ms. Trisha Dutta, Dr. Priyamjeet Deka, Mr. Raktim Gogoi, Ms. Barsha Rani Bora, Ms. Bipasha Saikia, Ms. Kiran Mayawad, Ms. Sonali Roy, Mr. Deepak Jyoti Deuri, Mr. Priyanku Garg, Mr. Amit Kumar Rajak, Mr. Bikash Kumar Das, Ms. Nabamallika Nath, Mr. Mrityunjoy Dey, and Ms. Parijat Pratim Das from Dr. Kalyan Raidongia's research group (Nanofluidic Lab). Your camaraderie, support, and encouragement have been a source of strength and motivation throughout this journey.

I am deeply grateful to my friends Silpeesikha Pathak, Sukanya Das, Partha Pratim Churi, Roktopol Hazarika, and Niranjan Ligira, to name a few among many. Their unwavering support and encouragement have been invaluable throughout my PhD journey. I would also like to thank my seniors Dr. Kangkan Talukdar and Dr. Monikha Chetia for the contant motivation in my journey. I would like to express my gratitude to my relatives and well-wishers for their unwavering support. I deeply appreciate their constant presence throughout this journey.

I am profoundly grateful to my beloved family. I would like to express my heartfelt thanks to my father (Deuta) **Darpan Kumar Neog**, my mother (Maa) **Aradhana Neog**, and my sister (Bhonti) **Prostuti Neog** for their limitless love, unwavering support, and constant encouragement. Their sacrifices and enduring struggles have contributed significantly to easing

my life's journey. I am incredibly fortunate to have a loving and supportive family who have stood by me through every challenge and celebrated every achievement. This accomplishment is as much theirs as it is mine.

To everyone who has played a part in this journey no matter how big or small, I offer my deepest and most sincere thanks. Your endless support, encouragement, and belief in me have been the pillars of this achievement.

Finally, I humbly acknowledge the divine guidance and blessings bestowed upon me by the Almighty throughout my PhD journey. With heartfelt gratitude, I submit myself to Him, sincerely thankful for His blessings that have enabled me to complete this thesis.

Arindom Bikash Neog

Synopsis

Chapter 1. Introduction

The discovery of graphene in 2004 opened up a world of possibilities triggering a wave of research and creativity in the expanding field of two-dimensional (2D) materials. Its outstanding electrical and thermal conductivities, mechanical robustness, optical transparency, and barrier characteristics established graphene as a material with enormous potential.[1–3] Its superiority over carbon nanotubes and fullerene sparked interest in studying atomically thin sheets of other layered materials such as boron nitride (BN), graphene oxide (GO),vanadium pentoxide (V_2O_5), molybdenum disulphide (MoS_2), tungsten disulphide (WS_2), and clays. Indeed, these graphene-like sheets demonstrated similar excellent capabilities, encouraging additional scientific research and innovation in the field of two-dimensional materials.[4–6]

2D materials are emerging to be a versatile building block for creating innovative materials for applications such as energy harvesting, energy storage, sensing and molecular/ionic separations.[7,8] These materials possess astonishing properties like high surface area, mechanical flexibility, and exceptional electrical conductivities and optical properties, making them potential candidates for responsive materials.[9,10] Another interesting quality of exfoliated 2D materials is that they can be easily reassembled or reconstructed in to freestanding lamellar membranes.[11,12] The reconstructed 2D materials respond dynamically to a variety of stimuli, like light, temperature, chemicals, and mechanical force.[13,14] Moreover, exfoliated 2D materials can be surface functionalised to imbue them with exotic properties for unique applications like light-responsiveness for optoelectronics and photodetection, thermoresponsiveness for thermal management and drug delivery, chemical-responsiveness for sensing and environmental monitoring, and mechanical-responsiveness for biomechanical sensors and wearable electronics.[15,16] Various 2D materials also possess enormous potential of

application in sensing technologies due to their unique characteristics and customizable responsiveness. Transition metal dichalcogenides (TMDs), such as MoS_2 and WSe_2, have semiconducting characteristics that can be altered by environmental variables, allowing for the construction of sensitive photodetectors and chemical sensors.[17] Furthermore, 2D materials like h-BN has excellent thermal stability and insulating characteristics, making it appropriate for temperature and strain monitoring.[18]

Apart from sensing applications, reconstructed 2D materials also possess large potential of application in energy harvesting processes such as reverse electrodialysis (RED), triboelectric nanogenerator (TENG), contrasting interfacial activity, and moisture-enabled nanogenerators (MEG).[19] RED generates electricity from the alteration in salt concentration between two solutions flowing through ion-selective membranes, which causes ions to move, creating an electric current. Energy harvesting employing interfacial activity of 2D materials takes advantage of their unique surface features to turn external inputs into electrical energy. The idea behind MEG is that water molecules are taken up from the atmosphere by surface-active materials, which then dissociate into mobile ions. Electricity is produced by the concentration gradient or evaporation-driven diffusion of these mobile ions in a charged matrix. The above discussion highlights the versatility of 2D materials in harvesting energy from several sources, paving the path for self-powered devices.[20]

Chapter 2. Electrical actuation of hydrophobic bilayer membranes of reduced graphene oxide and agar for inducing chemical reactions in microdroplets

Advancements in materials and techniques for manipulating fluids at nano- and microliter scales offer a valuable platform for studying interfacial interactions and controlling processes like convection, diffusion and chemical reactions with greater precision. These systems hold enormous potential for miniaturised analytical tools and high-throughput chemical micro-

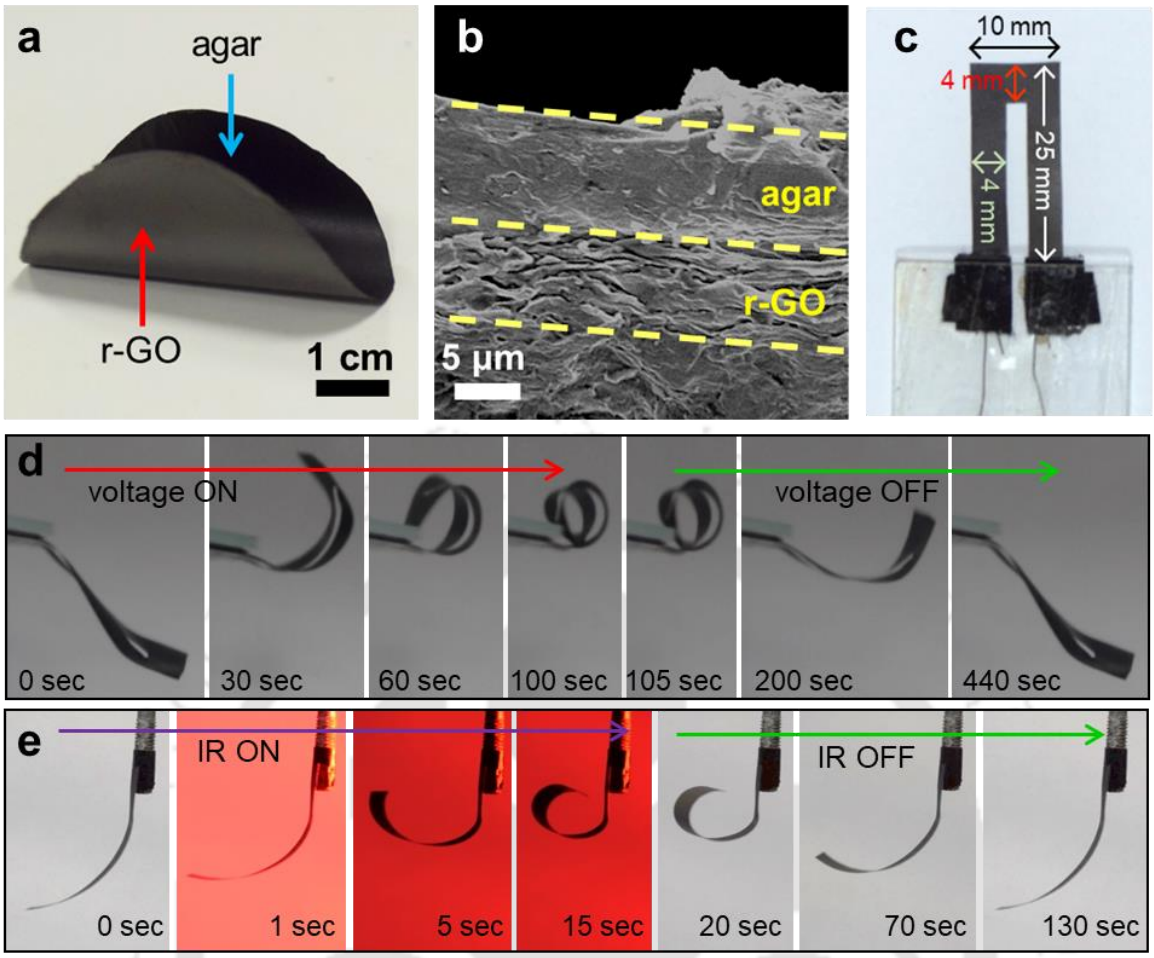

Figure 1: *Responsiveness of r-GO/agar bilayer membrane: (a) Digital photos of r-GO/agar bilayer membrane. (b) Cross-sectional FESEM image of the r-GO/agar bilayer membrane. (c) Photo showing a U-shaped strip of an r-GO/agar bilayer membrane. (d) Snapshots showing bending and recovery of the U-shaped stripe upon application of a potential of 26 V for 100 s. (e) Photos showing bending (for 15 s) and recovery movements of a bilayer strip upon exposing to IR light of intensity 5500 lux.*

reactors, enabling cheaper, faster, and more efficient performance in areas such as high-throughput synthesis, biochemical screening, and enzymatic reactions. This chapter shows how reduced graphene oxide (r-GO) and agar-based bilayer membranes can be utilised to fabricate electrically programmable smart arms that can handle liquids in the microliter length scale. This is the first effort to use actuators for managing microdroplets, despite the fact that several bilayer membranes made by stacking r-GO with various polymers and nanomaterials showed comparable electrical actuation characteristics. The present methodology offers several

benefits, including the ability to manage liquids at the single droplet scale, the potential to attain high precision via electronic control systems, the reduction of cross-contamination, the ease of scaling into numerous parallel components, and the suitability for the creation of autonomous or self-triggered smart reactors or analytical systems. Systems that can remotely handle liquids in single microdroplets are crucial for both basic research and technological applications. In this work, the creation of a hydrophobic bilayer membrane was demonstrated that has an accuracy of $\pm 5 \times 10^{-8}$ L for picking up and dropping liquids in the microliter regime when powered by electrical potential and infrared (IR) light. Variables such as the liquid's surface tension, the solid surface's contact angle, and the applied voltage regulate the weights of the microdroplets that are taken up by the U-shaped electrical actuator of the reduced graphene oxide (r-GO)/agar bilayer membrane. The wettability of the reduced graphene oxide fraction of the r-GO/agar bilayer membrane is controlled by adjusting the surface roughness by sandwiching varying concentrations of gold nanoparticles (AuNP). The sudden shattering of the droplets created a rapid mixing of liquids, which resulted in extremely quick chemical reactions on a microliter time scale. Chemical tests such as acid-base titration can also be easily and efficiently carried out with the r-GO/agar-based electrical arm.

Chapter 3. Application of reduced graphene oxide-based actuators for real-time chemical sensing of liquid and vapour phase contaminants

Innovative detection systems for trace liquid analysis are vital for various industrial applications, including safeguarding chemical laboratories, pharmaceutical production, environmental monitoring of water bodies, and optimizing emulsion-based systems. Accurate detection of aqueous impurities in organic solvents ensures safety and quality control, while monitoring organic contaminants in water is essential for environmental and food-related industries. In this study, real-time detection of pollutants dissolved in a liquid medium was accomplished, which is crucial for many technical and industrial activities. Reconstructed

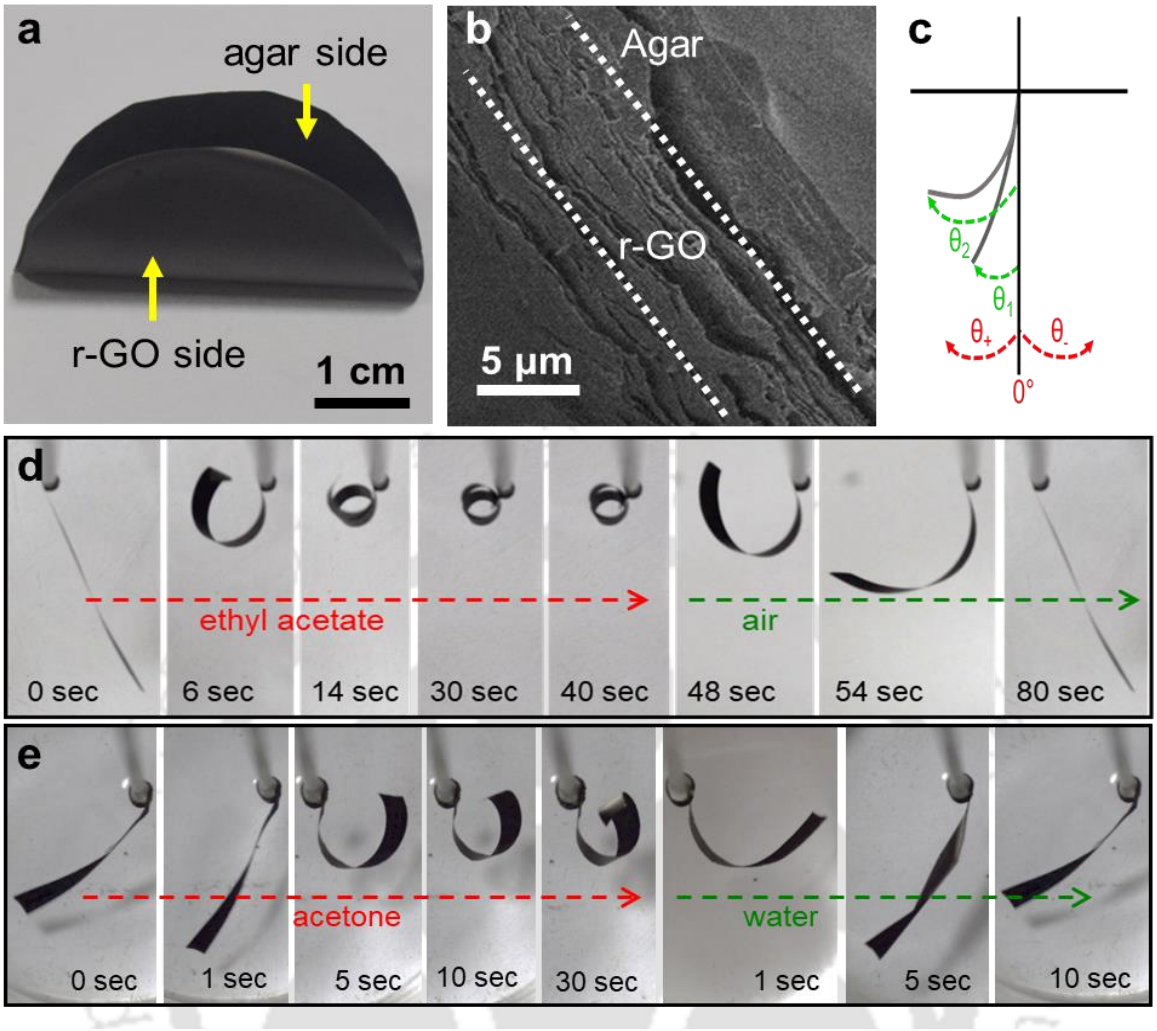

Figure 2: *Responsiveness of r-GO/agar bilayer membrane: (a) Digital photo of r-GO/agar bilayer membrane. (b) Cross-sectional FESEM image of the r-GO/agar bilayer membrane. (c) Schematic design of bending angle measurements. (d) Snapshots showing bending and recovery movements of a bilayer strip on exposing to ethyl acetate vapours. (e) Snapshots showing bending of the bilayer strip in acetone and its corresponding recovery in water.*

layered material-based responsive membranes were successfully used to detect chemical pollutants in liquids. A bilayer membrane formed by consecutive vacuum filtration of reduced graphene oxide and agar (r-GO/agar) showed extraordinary reactivity to the presence of solvent vapours in the surrounding atmosphere. The shape-morphing capability of the r-GO/agar membrane arises from unequal changes in the mechanical properties of its individual components. Remarkably, rectangular strips of this bilayer membrane also exhibit shape-transforming properties when submerged in a liquid medium. The speed at which these strips

of r-GO/agar membrane bend into a coil-like shape depends on the chemical nature of the molecules present in the liquid. However, the original shape of the strip readily reverts after immersion in water or air drying. Furthermore, the bending angle and response time of these strips are highly sensitive to trace impurities within the solvent system. This sensitivity can be exploited for detecting contaminants in the liquid phase, such as minute quantities of water molecules in acetone or various alcohol molecules in toluene.

Chapter 4. Biomimetic remote handling and sensing devices of multiwalled carbon nanotubes and vanadium pentoxide

Amidst increasing demands for chemical and biochemical products, there's a parallel rise in the industrial-scale use of toxic and explosive substances, posing persistent risks to technicians and workers. Addressing these concerns, there's a growing need for remote handling systems to mitigate direct exposure risks and enable safe manipulation of hazardous materials in controlled environments, particularly in settings where direct human access is limited due to various hazards. In this chapter, the development of bilayer actuators was presented comprising multiwalled carbon nanotubes (CNT)/oxidized multiwalled carbon nanotubes (o-CNT) and exfoliated two-dimensional vanadium pentoxide (VO) flakes, enabling precise manipulation of reactive substances via remote controls like light and electricity. Leveraging the differential photothermal activity of the carbon nanotubes-reconstructed VO, CNT-VO bilayer membranes were engineered with light-responsive shape-morphing properties (bending speed up to 45° s^{-1} under 15 klux light intensity). Similarly, by exploiting the unmatched Joule heating effect of o-CNT and VO membranes (o-CNT-VO), electrical voltage-driven actuation (bending speed up to 64.5° s^{-1} with a 12 V applied voltage) was achieved. These bilayer membranes exhibit remarkable capabilities such as picking up and dropping off reactive chemicals like potassium permanganate ($KMnO_4$) and sodium (Na) metal (up to ten times their total weight) using CNT-VO, and transporting microdroplets (25 µL) of toxic chemicals like sulfuric acid (H_2SO_4) and

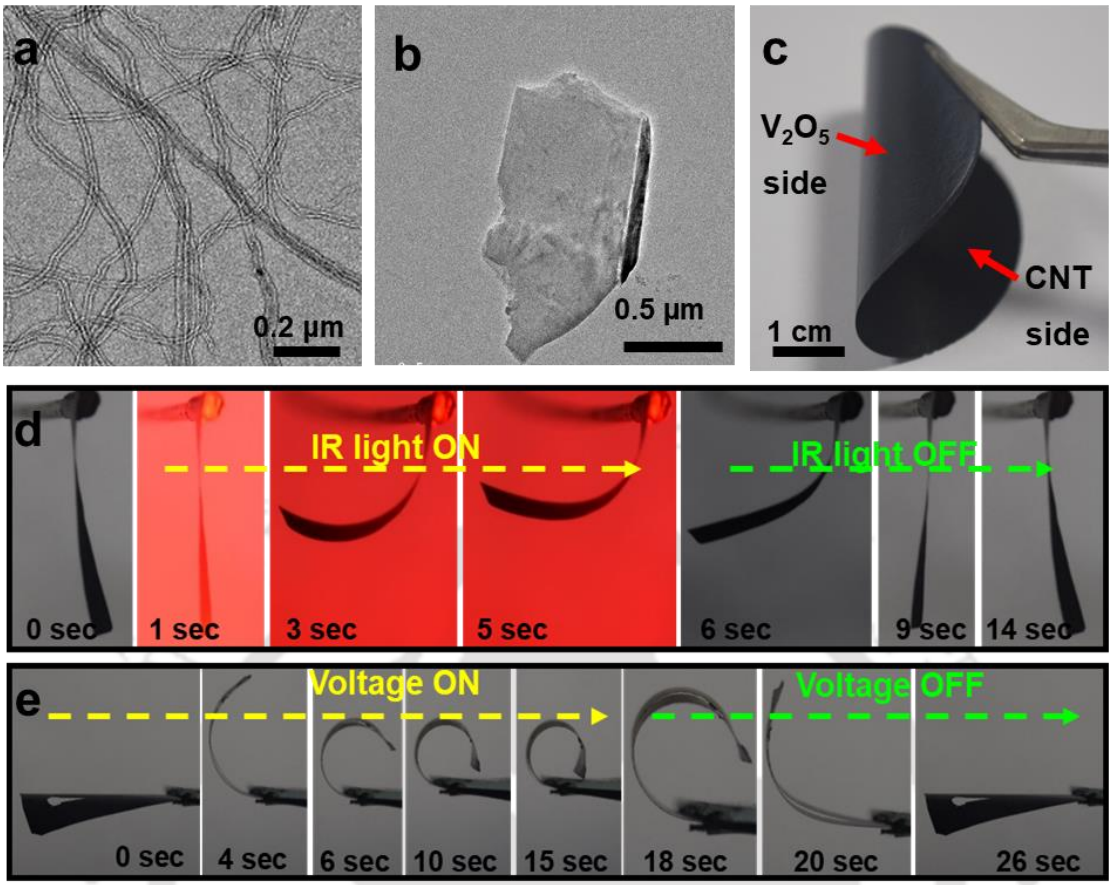

Figure 3: *FETEM images of (a) CNT and (b) V_2O_5 nanosheets. (c) Digital photo of CNT-VO bilayer membrane. (d) Photos showing bending (for 5 s) and recovery movements of a bilayer strip upon exposure to IR light of intensity 15 klux. (e) Snapshots showing bending and recovery of the U-shaped strip upon application of a potential of 12 V for 15 s.*

sodium hydroxide (NaOH) with o-CNT-VO. The reason behind these lies in their voltage responsiveness and rose petal like effect. Similar to human fingers, CNT-VO- based actuators demonstrate the ability to sense the nature of objects/materials they handle. Moreover, owing to the robustness of their components, the shape-morphing characteristics of CNT-VO strips remain unaffected even after exposure to acidic, basic, and organic liquids.

Chapter 5. Boosting of concentration gradient-driven energy output by employing electrodes possessing contrasting interfacial activity

Driven by the enormous theoretical potential, concentration gradient is actively pursued as a potential sustainable energy resource. Massive research activities are focused on developing

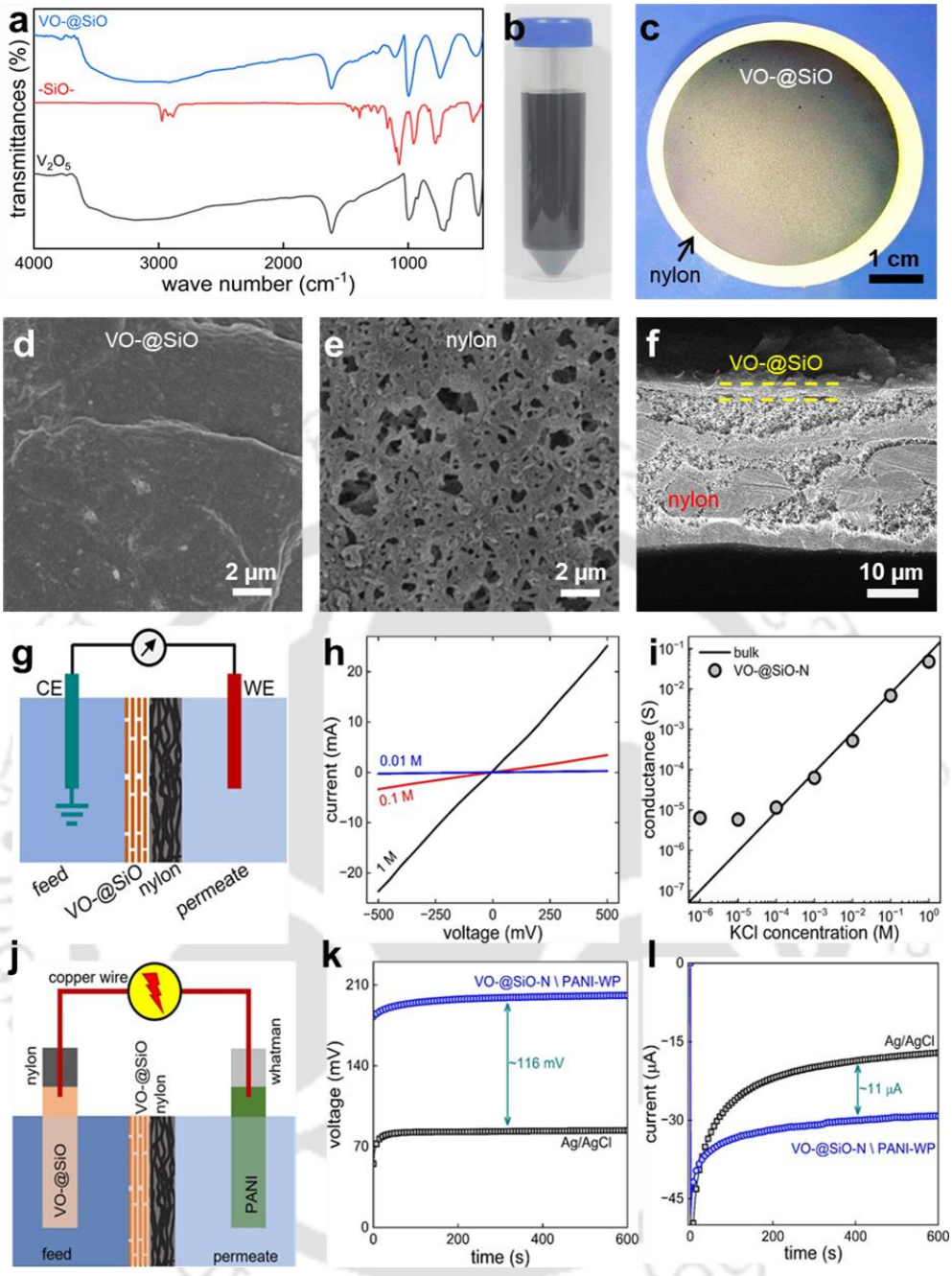

Figure 4: *(a) Comparison of IR spectra of V_2O_5 (black curve), bis[3-(triethoxysilyl) propyl]tetrasulfide (-SiO-, red curve) and VO-@SiO nanosheets (blue curve). Photo of (b) aqueous dispersion (1mg/mL) of VO-@SiO nanosheets and (c) VO-@SiO-N membrane. FESEM images showing the (d) VO-@SiO side, (e) nylon side and (f) cross-section of VO-@SiO-N membrane. (g) Schematic representation of the experimental set-up used to investigate the ion-transport characteristics. (h) Current versus voltage (IV) curves were measured through the VO-@SiO-N with 1, 0.1 and 0.01 M KCl as electrolyte. (i) KCl concentration dependence conductance. (j) Schematic diagram showing the energy generation setup to generate electricity. Comparison of (k) voltage and (l) current generated by VO-@SiO-N membranes (as ion selective membrane) under a gradient of 10 fold (C_{feed} = 1 M and $C_{permeate}$ = 0.1M KCl) using Ag/AgCl electrodes pair and VO-@SiO-N\PANI-WP electrodes pairs.*

vital components of concentration gradient-driven energy harvesting devices like perm-selective membranes and electrode systems. This chapter presents the development of a novel permselective nanofluidic membrane which was achieved through the coating of a commercial nylon membrane with two-dimensional nanosheets of vanadium pentoxide functionalised with –SiO– (VO-@SiO). The membrane potential (E_m) values obtained by deducting redox contributions of the Ag/AgCl electrode suggest that coating of ~14 μg.mm^{-2} VO-@SiO improves the transport number of non-ion selective nylon membranes from ~0.5 to ~0.8 (for K^+ ion). It was further demonstrated that the output potential of concentration gradient-driven energy harvesting devices' is significantly enhanced when materials with contrasting interfacial activities are employed as electrodes. Electrodes prepared from functionalized V_2O_5 and polyaniline (PANI) can generate electrical potential up to 150 mV through complementary charge transfer activities from quiescent water without any concentration gradient. By using a pair of V_2O_5 and PANI, the overall power of the concentration gradient-driven energy generator was improved by 300 % (with 10-fold concentration gradient), as compared to that of Ag/AgCl electrodes. As the functionalized V_2O_5 is negatively charged and PANI is positively charged, these materials create charge separation and break the electrical neutrality and thereby generates electrical energy. These scientific advancements collectively underscore the potential of this novel electrode system, as well as the promising prospects of blue energy harvesting through salinity gradients, offering valuable insights into sustainable energy generation from aquatic resources.

Chapter 6. Conclusions and future perspective

In summary, the exfoliation of layered materials like graphite and vanadium pentoxide into atomically thin layers was successfully achieved, which were then re-stacked to form freestanding lamellar membranes. Multi-responsive bilayer membranes made up of these materials combined with polymers such as agar and 1D material like MWCNT not only detect

changes in their environment but also exhibit distinct alterations in their physical properties. The precisely structured reconstructed lamellar membranes, combined with their plentiful sources and straightforward synthesis methods, provide an ideal platform for the creation of numerous smart materials through deliberate design. These systems hold promise for various application such as harvesting energy from waste solvent vapours and fluctuations in diurnal temperature and humidity; chemical sensors for electronics with minimal complexity and the development of biocompatible or transplantable smart devices. **Chapter 1** describes a general overview of layered materials, their exfoliation, and applications in various fields. **Chapter 2** demonstrates a new technique for remote handling of microdroplets by applying an electrical potential and/or IR light. The r-GO/agar-based bilayer actuators can pick up and drop off microdroplets with an ultra-high accuracy. The accuracy of the bilayer membranes could be further enhanced by manipulating its surface with nano and micro features to attain the rose petal like effect. **Chapter 3** demonstrates the possibility of applying reconstructed layered material-based responsive membranes (r-GO/agar) for detecting contaminants dissolved in liquid media. The shape of the bilayer strip prepared by re-stacking exfoliated layered materials is determined by the balance between the mechanical properties of the individual components. **Chapter 4** reveals that responsive bilayer membrane of CNT and VO could be exploited to develop remote handling systems for operating toxic/ explosive substances. The CNT-VO and o-CNT-VO based remote handling systems could not only be made to grasp and release substances but also sense the materials it is transporting just like human fingers. Unlike the previous three chapters, **chapter 5** demonstrates a novel electrode system of functionalized V_2O_5 and polyaniline which can generate electrical potential from quiescent water (without any concentration gradients) through complementary charge transfer activities. By using this potential generating electrode, the overall power of the concentration gradient driven energy generator could be improved by up to 300 %, as compared to that of Ag/AgCl electrodes.

Membranes based on two-dimensional layered materials have a bright future ahead of them, with great potential in a number of industries. Owing to their remarkable mechanical strength, permeability, and selectivity, these membranes have the potential to completely transform a number of industries, including gas separation, microdroplet handling, energy harvesting, energy storage, sensing, and water purification. Their adjustable qualities promote the development of sustainable practices by providing customized answers to industrial and environmental problems. Future applications will probably be made possible by ongoing research and development, which will improve the effectiveness and performance of both established and developing technology. Finally, in **chapter 6,** the conclusions were summarised from all the chapters and the future outlook of the membranes based on two-dimensional layered materials were discussed.

References

1 A. K. Geim, *Science*, 2009, **324**, 1530-1534.

2 K. S. Novoselov, A. K. Geim, S. V. Morozov, D. Jiang, Y. Zhang, S. V. Dubonos, I. V. Grigorieva and A. A. Firsov, *Science*, 2004, **306**, 666-669.

3 P. R. Wallace, *Phys. Rev.*, 1947, **71**, 622-634.

4 P. Ares and K. S. Novoselov, *Nano Mater. Sci.*, 2022, **4**, 3-9.

5 A. Gupta, T. Sakthivel and S. Seal, *Prog. Mater. Sci.*, 2015, **73**, 44-126.

6 R. Mas-Ballesté, C. Gómez-Navarro, J. Gómez-Herrero and F. Zamora, *Nanoscale*, 2011, **3**, 20-30.

7 N. R. Glavin, R. Rao, V. Varshney, E. Bianco, A. Apte, A. Roy, E. Ringe and P. M. Ajayan, *Adv. Mater.*, 2020, **32**, 1904302.

8 V. Shanmugam, R. A. Mensah, K. Babu, S. Gawusu, A. Chanda, Y. Tu, R. E. Neisiany, M. Försth, G. Sas, O. Das, V. Shanmugam, R. A. Mensah, M. Försth, G. Sas, O. Das, K. Babu, S. Gawusu, Y. Tu and R. E. Neisiany, *Part. Part. Syst. Charact.*, 2022, **39**, 2200031.

9 D. Akinwande, C. J. Brennan, J. S. Bunch, P. Egberts, J. R. Felts, H. Gao, R. Huang, J. S. Kim, T. Li, Y. Li, K. M. Liechti, N. Lu, H. S. Park, E. J. Reed, P. Wang, B. I. Yakobson, T. Zhang, Y. W. Zhang, Y. Zhou and Y. Zhu, *Extreme Mech. Lett.*, 2017, **13**, 42-77.

10 S. Das, M. Kim, J. W. Lee and W. Choi, *Crit. Rev. Solid State Mater. Sci.*, 2014, **39**, 231-252.

11 K. Saha, J. Deka, R. K. Gogoi, K. K. R. Datta and K. Raidongia, *ACS Appl. Nano. Mater.*, 2022, **5**, 15972-15999.

12 L. Prozorovska and P. R. Kidambi, *Adv. Mater.*, 2018, **30**, 1801179.

13 L. Ding, Y. Anying Wei, Y. Wang, H. Chen, J. Caro, H. Wang,] L Ding, Y. W. Ei, Y. Wang, H. Chen, H. H. W. Ang and J. C. Aro, *Angew. Chem. Int. Ed.*, 2017, **56**, 1825-1829.

14 R. K. Gogoi and K. Raidongia, *Adv. Mater.*, 2017, **29**, 1701164.

15 X. Cai, Y. Luo, B. Liu and H. M. Cheng, *Chem. Soc. Rev.*, 2018, **47**, 6224-6266.

16 K. Khan, A. K. Tareen, M. Aslam, R. Wang, Y. Zhang, A. Mahmood, Z. Ouyang, H. Zhang and Z. Guo, *J Mater. Chem. C*, 2020, **8**, 387-440.

17 W. Choi, N. Choudhary, G. H. Han, J. Park, D. Akinwande and Y. H. Lee, *Mater. Today*, 2017, **20**, 116-130.

18 J. Wang, F. Ma, W. Liang and M. Sun, *Mater. Today Phys.*, 2017, **2**, 6-34.

19 Y. Liu, J. Ping, Y. Ying, Y. Liu, J. Ping and Y. Ying, *Adv. Funct. Mater.*, 2021, **31**, 2009994.

20 Y. Fu, X. Guo, Y. Wang, X. Wang and J. Xue, *Nano Energy*, 2019, **57**, 783-790.

Contents

Chapter 1

Overview of microdroplet handling, sensing, energy harvesting, and the reconstruction of layered materials

1. Introduction

Technological developments followed by scientific inventions have enormously contributed to improving the quality and safety of human life. Over the last 100 years, exponential development has been observed in transportation, medical, and large-scale production. However, the curious human mind continues to explore new properties and phenomena in innovative materials and devices. This curiosity-driven scientific exploration continues to create technological marvels beyond the level of imagination. For example, Artificial Intelligence (AI) based systems have revolutionised the healthcare business by enabling the early detection of diseases through predictive analytics and advanced imaging techniques.[1,2] AI-driven autonomous vehicles have enhanced both road safety and efficiency.[3,4] Similarly, with microfluidic devices, chemical reactions and analysis could be carried out in the micro or nano-litre lengthscales, significantly minimising the cost and environmental impacts. With just a few blood drops, lab-on-a-chip technologies have been established for point-of-care diagnostics, enabling the speedy and exact identification of diseases, including cancer and infectious diseases.[5,6] Advanced nanomaterials are also being integrated into these microfluidic devices to enhance their performance and sensitivity. For example, gold nanoparticles are utilised in microfluidic devices' biosensors to recognise biomolecules at extremely low concentrations, aiding the early identification of sickness.[7,8] Likewise, smart devices are being engineered to perform jobs in challenging environments like exposure to radioactive rays, contamination with infectious diseases, extremely high and low temperatures, etc. One such example is using carbon nanotubes in radiation-resistant electronics and sensors, which are critical for tracking radiation levels in nuclear power plants and space missions. Compared to traditional materials, these carbon nanotube-based devices offer better durability and sensitivity, providing accurate monitoring even under intense radiation exposure.[9–12].

Graphene-based supercapacitors are transforming battery technology for electric vehicles and portable gadgets by providing high energy density and quick charging in the energy storage space.[13,14] In aerospace applications, graphene-based thermal management systems shelter delicate equipment from the high heat created upon re-entry into Earth's atmosphere.[15,16] Additionally, TiO_2 nanoparticles are utilised in antimicrobial coatings and self-cleaning surfaces, which are crucial in locations where infectious disorders are common. These surfaces are suitable for utilisation in high-risk situations like hospitals and laboratories since they can break down organic contaminants and kill bacteria when exposed to light.[17,18] Here in this thesis, we explore exfoliated 2D nanomaterials for creating devices capable of performing chemical reactions/ analysis in microdroplets, smart materials capable of shape morphing and chemical sensing, and harvesting electricity from concentration gradients.

Microdroplet handling techniques have revolutionised the manipulation of minute liquid volumes, affording precise control over experiments and diagnostics, particularly in lab-on-a-chip systems. Advancements in sensing technology have enabled the accurate detection of a wide array of biological and environmental signals, offering real-time insights critical for personalised healthcare and efficient monitoring. Simultaneously, energy harvesting technologies have addressed the need for sustainable power sources in these compact systems, effectively converting ambient energy into usable power and enabling autonomous operation without traditional batteries. Collectively, these technologies signify a trajectory of scientific discovery that tackles urgent global concerns and facilitates the development of effective, environmentally friendly systems that elevate energy sustainability, healthcare, and environmental monitoring. To further support a more effective and sustainable future, it is imperative that microdroplet handling, sensing, and energy harvesting technologies are comprehensively integrated and advanced. The upcoming section provides a detailed discussion of the three techniques.

1.1 Microdroplet handling

Microdroplet handling's history is intrinsically tied to the evolution of microfluidics, which originated in the mid of the 20th century. The demand for accurate control and analysis of small samples led to improvements in biology and chemistry, which led to the manipulation of small fluid volumes on a microscale. The techniques and procedures used to handle and control minute liquid volumes, which typically range from nanoliters (10^{-9} litres) to microliters (10^{-6} litres), are called microdroplet handling.[19–22] High precision, efficiency, and the execution of sophisticated micro-scale tests and operations are made possible by this precise manipulation, which is crucial for various scientific, medical, and industrial applications. Microdroplet handling finds extensive uses in drug screening, liquid transportation, bioassays, inkjet printing, and laboratory procedures that need exact volumes of minute droplets.[23–26] The scientific and industrial communities have been working hard to generate smaller droplets in recent years. As part of these efforts, smaller nozzle sizes and additional driving mechanisms like heat ejection, processes directed by the electric field, and pyroelectrodynamic-driven techniques have been used. The semiconductor industry's microfabrication techniques had a tremendous impact on developing microfluidic devices. The initial microfluidic devices were developed due to an investigation into the possibilities of microchannels for fluid manipulation during the 1970s and 1980s. The invention of the microdroplet generator by Stephen Quake et al. in the early 2000s heralded a revolutionary development in the control of microdroplets.[27] The "Quake valve," a microvalve system designed by Quake et al., substantially increased the capacity to make and regulate droplets inside microfluidic devices by allowing for precise control of fluid flow in microchannels. This invention made high-throughput analysis easier and opened the door to various uses in drug development, diagnostics, and biochemical assays. Interdisciplinary partnerships incorporating concepts from electrical engineering, materials science, and fluid mechanics to boost device performance and flexibility have fueled

developments in droplet microfluidics. A prominent field of microfluidics is droplet microfluidic technology, which principally manipulates droplets by separating continuous fluids into discrete droplets via the interaction of surface tension and shear force.[28–30] Compared to continuous flow systems, this technology provides various benefits, such as reduced droplet volumes, lesser reaction times, greater size controllability, and lower costs. With excellent control accuracy over droplet size and reactant reaction times, the droplets' micro-nano scale speeds up mixing and reaction rates. High reaction fidelity is guaranteed by separating droplets from outside impurities. These days, droplet microfluidic technology is frequently applied to improve chemistry and biology analytical techniques such as enzyme assays, high-throughput screening, protein crystallisation, and cell encapsulation.[31,32] Microdroplet handling is a major aspect of lab-on-a-chip technology, delivering unprecedented precision and efficiency for delicate biological research and industrial processes. The next section explores microdroplet handling techniques' principles and significant uses, including electrowetting, acoustic manipulation, magnetic handling, and microfluidic-based methods.

1.1.1 Microdroplet handling techniques

Microfluidics: A commonly used method in microdroplet manipulation is the microfluidic T-junction, where two fluids that do not mix come together at a junction to create droplets.[33–35] Monodisperse droplets can be formed by accurately regulating the flow velocity and viscosity of the fluids. The T-junction design exploits the geometric properties of the microchannel, resulting in the destabilisation of the dispersed phase. This is caused by the momentum shifts caused by the shear force of the continuous phase, ultimately leading to the creation of droplets. Thorsen et al. were the first to document the application of T-shaped microchannels in producing water-in-oil droplets.[36–38] They examined the forces contributing to droplet formation and observed how the droplets were distributed throughout various channels. The researchers discovered that the size of the droplets was affected by the shear and Laplace forces

exerted by the continuous phase. Additional research conducted by Shi et al. and Wehking et al. explored the impact of flow parameters on the creation of droplets in T-junctions.[39–45] These studies revealed the capacity to manipulate droplets' size and frequency. The flow-focusing device is a commonly employed technology in which a central stream of scattered phase fluid is constricted by two lateral streams of continuous phase fluid, creating droplets. This technique offers exceptional accuracy and mastery in regulating droplet size and consistency. Zeng et al. demonstrated the implementation of a closed-loop feedback control mechanism in a flow-focusing device, resulting in improved droplet formation stability and uniformity.[46–48]

Electrowetting: One versatile way for controlling microdroplets in microfluidic systems is electrowetting. Using this technology, a voltage is provided between a droplet and an electrode that is positioned underneath a microfluidic chip's substrate. The application changes the wetting behaviour of the liquid, resulting in surface tension gradients surrounding the droplet. This technology, named Electrowetting-on-Dielectric (EWOD), eliminates the need for mechanical moving elements and offers exact control over droplet movements, such as dispensing, conveying, splitting, and merging. Examples from the literature include the invention of digital microfluidic devices for chemical and biological functions, like the study of proteins and DNA. Furthermore, improvements in super wetting systems have enhanced control over droplet manipulation and surface wettability, with substantial repercussions for various industrial and technical applications.[49–51]

Acoustic manipulation: In microfluidic systems, acoustic manipulation influences microdroplets by producing pressure fields via sound waves. This approach, called acoustofluidics, generates surface acoustic waves (SAW) or bulk acoustic waves (BAW) using piezoelectric transducers. Precise control over droplet motions, such as sorting, directing, and trapping, is made feasible by these waves. The discovery of acoustic valves, using concentrated acoustic fields to regulate droplet movement within microfluidic channels, provides a low-

damage, non-contact technology ideal for biochemical study. Additionally, stable, distinct droplets that can be divided for different laboratory processes have been created using BAW devices to manipulate droplets, illustrating the potential of acoustic manipulation in developing effective, non-contact systems for intricate assays and industrial applications.[52–54]

Magnetic handling: Another method for manipulating microdroplets using magnetic fields in microfluidic devices is magnetofluidics or magnetic handling. By adding magnetic particles to droplets, this approach offers exact control over their behaviour and movement. The use of magnetic droplets in microfluidic devices for droplet creation, manipulation, and detection is one example from the literature. For example, droplet micro-magnetofluidic platforms have been utilised to construct magnetic Janus particles, making droplet merging and mixing conceivable. Moreover, magnetic nanoparticles have been created and changed by utilising continuous magnetic droplets, underlining their potential in biochemical testing and detecting procedures. Microdroplet handling has altered various scientific areas by accurately controlling minuscule liquid volumes. This technology is vital in chemical synthesis, materials production, biological testing, and other cutting-edge applications.[55–59]

1.1.2 Applications of microdroplet handling

Biological Assays: Microdroplet manipulation is often used in biological research to create isolated compartments for single-cell or single-molecule analysis. Precise biochemical reactions and high-throughput screening depend on this isolation. Droplet microfluidics, for example, has been applied to PCR-based research, allowing the amplification of DNA within individual droplets and enhancing the assay's sensitivity and specificity. Furthermore, microdroplets enable precise monitoring of reaction dynamics and crystal formation by offering a controlled environment for experiments on protein crystallisation and enzyme kinetics.[19,50,60–62]

Chemical Synthesis: Microdroplet handling has several benefits in chemical synthesis, including rapid mixing and accurate control over reaction conditions, especially for multistep chemical reactions. Novel functional materials and structures can now be manufactured owing to the advent of controlled droplet microfluidic systems, which can carry out sophisticated reaction protocols. Controlling reactions at liquid-liquid interfaces in bulk systems is challenging, but these systems can be managed effectively with the right approach.[19,26,63,64]

Materials Synthesis: Handling microdroplets is critical in synthesising materials, particularly when generating nanoparticles and nanostructures. With droplet microfluidics, functional components can be enclosed, and polymeric particles can be produced, enabling exact command over the composition and particle sizes. Magnetic nanoparticles important for applications like drug administration and magnetic resonance imaging (MRI) contrast agents, have been efficaciously manufactured using this technology.[23,26,65,66]

Emerging Applications: Microdroplet handling revolutionises fields like environmental monitoring and metabolic engineering, going beyond established applications. Microdroplet technologies in metabolic engineering offer fast assessment and optimisation of metabolic pathways and microbial strains by screening biomolecule production. Microdroplets are used in environmental monitoring as a sensitive and quick approach to examining the environment by identifying pollutants and pathogens in water samples.[24,26,28,31,49,67]

1.1.3 Significant findings in microdroplet handling

Several studies have highlighted significant progress in microdroplet manipulation, unveiling innovative methodologies and findings. Notably, an influential study delineated the efficacy of active and passive strategies in the controlled generation of microdroplets and investigated droplet formation within E-shaped microchannels.[68] Furthermore, an analysis of the dynamics of microdroplets resulting from drop impacts on superhydrophobic surfaces elucidated the critical impact velocities requisite for optimal droplet generation.[69] Moreover, research

focusing on active control mechanisms for microdroplets has underscored the potential of electrowetting-based systems in efficiently managing droplets for diverse applications.[70] Additionally, investigations into the evaporation properties of asymmetric microdroplets have demonstrated heightened local evaporation rates associated with droplet geometry, presenting insights for potential applications in next-generation solutions for electronics cooling.[71] Furthermore, the integration of electrowetting-on-dielectric technology in digital microfluidic systems has exhibited promising outcomes in facilitating dependable droplet manipulation for high-throughput analyses.[72] Studies on surface acoustic wave manipulation of microdroplets have revealed the utility of ultrasonic waves in enhancing assay performance by promoting droplet mobility and improving mixing efficiency, thereby expediting biological reactions.[73,74] Additionally, the encapsulation of cells within microdroplets has been explored, revealing its potential in independently studying cellular responses, providing valuable insights into drug responses and single-cell level cellular behaviour.[75] Investigations into droplet manipulation using temperature gradients have showcased the applicability of thermocapillary effects in directing and fusing droplets, thus potentially streamlining fluidic circuits and enhancing integration density in microfluidic devices.[76,77] In comparison to conventional bulk methods, accelerated synthesis rates have been achieved through the use of ionisation sources, such as paper spray and electrospray ionisation, which have made it easier to generate charged microdroplets and enable quick chemical reactions and high-throughput screening in pharmaceutical settings.[78] The utilisation of surface structures modelled after natural processes, including the hierarchical micropillars on the stigma of rose pistils, has further revealed breakthroughs in droplet manipulation. These designs allow accurate microdroplet transport and fusion via superhydrophobic surfaces with hydrophilic microtips.[79] Furthermore, a new digital optofluidics method has surfaced that uses LED gating to manage the fusion and transport of organic droplets the size of microliters for enhanced chemical synthesis.[80]

The aforementioned discoveries underscore the potential of microdroplet manipulation within various scientific and industrial realms. These findings further attest to the ongoing refinement of microdroplet manipulation strategies, thus presenting novel prospects for biological investigation and material fabrication.

1.1.4 Barriers to microdroplet handling

Challenges associated with microdroplet handling in microfluidics include environmental regulation, material compatibility, seamless integration of multiple functionalities, and achieving replicable results. The sensitivity of droplet generation to minute experimental variations underscores the criticality of ensuring consistency. Material compatibility issues arise due to potential interactions between diverse materials, jeopardising the functionality and stability of droplets. It is challenging to incorporate numerous activities into a single microfluidic device, and doing so typically relies on exact control over the generation, manipulation, and analysis of droplets. In addition, stable droplet behaviour depends on maintaining environmental control, including humidity and temperature.[81,82]

Newer advances have rectified some of these difficulties. The integration and miniaturisation of sophisticated processes on a single chip was made possible by lab-on-a-chip technology, enhancing functionality and decreasing sample volumes. Digital microfluidics gives tight control and adaptability by manipulating droplets using electric fields. The introduction of 3D printing has drastically transformed how devices are created, enabling speedy prototyping and personalization of microfluidic devices. The handling and manipulation of microdroplets have been further refined by automation and robotics, which has lowered human error and increased throughput.[26,28,31,81,83,84]

Microdroplet handling is a versatile and precise tool used in various scientific disciplines. Advancements in microfluidic technology have led to its increasing applications in chemical synthesis, material synthesis, biological testing, and other relevant fields. Recent studies

highlight the revolutionary potential of this technique in both fundamental research and practical applications. However, there is still untapped potential in the microdroplet handling technique that has yet to be fully realized.

1.2 Sensing

A sensor may be an apparatus that observes environmental changes and transmits this data to other electrical devices, usually a computer processor. It translates tangible occurrences into quantifiable digital signals so they may be read, observed, or handled further. Owing to their ability to capture and transform a range of physical qualities, such as heat, mass, pressure, temperature, and speed, into electrical impulses, sensors are vital components of modern technology. A computer analyses these electrical impulses to produce outputs that match specified measurements. These outputs are subsequently transmitted to the appropriate devices. A system may use several sensors with varied capacities to fulfil expanding operational needs, depending on how intricate its functionality is. Sensors considerably improve human existence in various circumstances through increased observation and reporting of the environment. Electrical sensors from stimuli produce electrical signals, and computers analyse these signals to produce relevant information to end users. One of the most complex technical breakthroughs is the medical sensor, which connects with smartphones and the Internet of Things (IoT) to track biological molecules and identify certain drugs. These sensors are indispensable for measuring changes in temperature and performing preventative steps. The evolution of sensor technology has reached a level where the absence of sensor data may impair important activities across numerous industries.[85–87]

There are numerous classes of sensors. One technique separates sensors into passive and active groups. Passive sensors, like metal detectors and thermal sensors, emit electric signals independently without needing an external power source, but active sensors, like radar and GPS, do. Detection techniques, such as electrical, biological, chemical, and radioactive

procedures, form the basis of another classification. Additionally, conversion phenomena are utilized to categorize sensors into analog and digital categories. Digital sensors generate discrete values (0s and 1s), whereas analog sensors provide a range of outputs. Some of the sensors that find use in everyday life are level sensors, temperature sensors, proximity sensors, pressure sensors, water quality sensors, gas sensors, IR sensors, smoke sensors, chemical sensors, image sensors, motion sensing devices, accelerometer sensors, gyroscope sensors, humidity sensors, optical sensors, and healthcare sensors.[85,88] Figure A shows the working of a sensor.

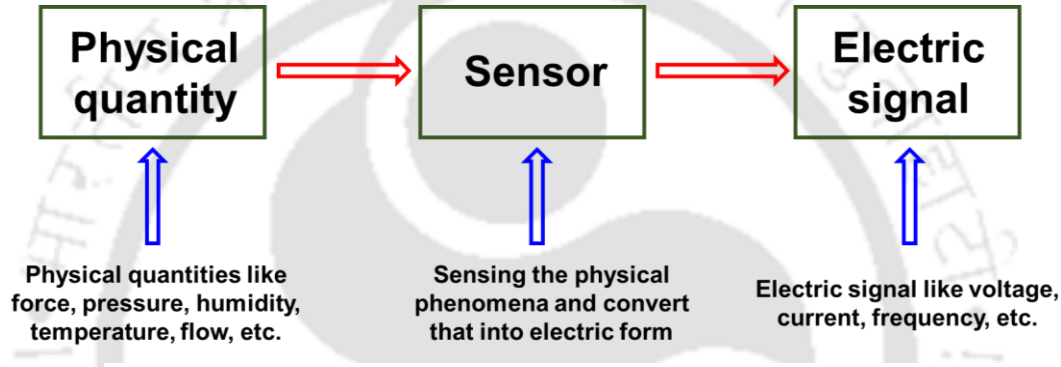

Figure A: *Illustration view on the working of a sensor.*

1.2.1 Principles of operation

The operation of a sensor is primarily dictated by the phenomenon it observes and the underlying physical principle it harnesses. A robust grasp of these concepts is indispensable for developing advanced sensing systems and optimising their practical utility.

Piezoelectric effect: The capacity of some materials to produce an electric charge in response to applied mechanical stress is known as the piezoelectric effect. Piezoelectric sensors, often used to monitor force, acceleration, and pressure, are based on this notion. A piezoelectric substance, like quartz, develops an electric charge directly proportional to the force exerted when it is mechanically deformed. After that, this charge can be quantified and related to the required physical quantity.[89,90]

Photoconductivity: The photoconductive effect, when a material's electrical conductivity alters in reaction to incident light, is the basis for photoconductive sensor operation. A photoconductive material's conductivity rises when photons impact it because they excite electrons to travel from the valence band to the conduction band. These sensors are typically found in imaging and light detection systems like CCD cameras and photodiodes.[91,92]

Capacitive sensing: When an object moves or is present, capacitance changes and is detected by capacitance sensors. Two conductive plates split by a dielectric material comprise a simple capacitive sensor. An object affects the electric field and capacitance when it moves or approaches between the plates. This variance can be quantified and exploited to derive the object's position, closeness, or other features. Displacement measuring tools, proximity sensors, and touchscreens all use capacitive sensing.[93–95]

Resistive sensing: Resistive sensors identify differences in electrical resistance brought on by various variables, including strain, temperature, and chemical composition. The resistance of a metal element in a resistive temperature detector (RTD) fluctuates with temperature in a predictable manner. Similarly, strain gauges change resistance to show deformation when stretched or squeezed. Gas sensors also use the resistive idea, where a sensing element's resistance varies in response to the concentration of a gas.[96–98]

The features and attributes of sensors, such as their sensitivity, precision, accuracy, resolution, range, linearity, reaction time, stability, and repeatability, define their functioning and establish whether or not they are suited for a certain application.

1.2.2 Sensing applications

The versatility and accuracy of sensing technologies have allowed them to be widely used in various industries, driving efficiency and innovation in various applications.

Industrial automation: Sensors promote safety, quality assurance, and production efficiency. Sensors for flow, pressure, and temperature are crucial for keeping an eye on and monitoring

industrial processes to guarantee appropriate operating conditions. Automated manufacturing is made feasible by proximity sensors and machine vision systems that determine the presence and orientation of objects on assembly lines. Furthermore, predictive maintenance uses vibration and sound sensors to track the status of the machinery to foresee and stop failures, which minimises maintenance costs and downtime.[99,100]

Environmental monitoring: A range of sensors monitor and assess environmental parameters, supplying crucial information for managing natural resources and solving environmental problems. Air quality sensors help control pollution and protect public health by measuring contaminants such as gases and particulate matter. Water quality sensors guarantee pure drinking water and resilient aquatic environments by identifying pollutants in rivers, lakes, and seas. Climate monitoring stations with temperature, humidity, and wind speed sensors help in climate change research and weather forecasting, supplying crucial information for disaster preparedness and policy decisions.[101]

Healthcare and medical devices: Sensors are crucial for monitoring, therapeutic, and diagnostic applications in healthcare and medical devices. Biosensors are instruments that identify biological molecules, making it possible to diagnose disorders like diabetes and infectious diseases promptly and precisely. Wearable sensors enable people to manage chronic illnesses and protect general health by monitoring vital signs, including blood pressure, heart rate, and blood oxygen levels. Extensive inner views of the body are made possible by modern imaging sensors used in CT and MRI scanners, which help with precise diagnosis and treatment planning. Therapeutic equipment with sensors, such as insulin pumps and pacemakers, guarantees accurate therapy delivery and improves patient results.[102,103]

Consumer electronics: Improvements in functionality and user experience are driven by sensors. Smartphones with accelerometers and gyroscopes may perform gesture detection, screen rotation, and augmented reality functions. While proximity sensors detect user presence

to preserve battery life, ambient light sensors adjust screen brightness for the optimal viewing experience. Mobile photography is being pushed to new heights by using image sensors in smartphones and tablet cameras to take high-resolution photographs and videos. Hands-free operation is made possible by voice recognition systems powered by microphones and acoustic sensors, which increases the accessibility and user-friendliness of gadgets.[87,104–106]

Automotive and transportation: Sensors enhance autos' user experience, efficiency, and safety. Engine characteristics are monitored by in-car sensors, which guarantee top performance and fuel economy. Road safety is considerably boosted by advanced driver-assistance systems (ADAS), which use radar, lidar, and video sensors to recognise hazards, maintain lane position, and automated emergency braking. By notifying drivers of low tyre pressure, tyre pressure monitoring systems (TPMS) maintain safe driving conditions. Public transportation sensors monitor vehicles' location and occupancy, allowing for the modification of routes and schedules to maximise service delivery.[107–109]

IoT and smart homes: Sensors build responsive, intelligent living spaces. Himidity and temperature sensors control heating, ventilation, and air conditioning (HVAC) systems to provide energy-efficient climate control. Motion sensors control lighting systems and detect intruders to increase security. Sensor-equipped smart appliances keep track of usage trends, enabling smartphone remote control and energy savings. Seniors can live more freely owing to IoT-enabled sensors in home health monitoring systems that measure critical indicators and warn caretakers. Sensors enable the IoT to connect gadgets, converting households into automated, effective, and flexible settings.[110,111]

1.2.3 Significant findings in sensing

The realm of chemical analysis has experienced notable progressions in sensing technologies, particularly within the domains of chemicals and biosensors. In-depth investigations into electrochemical glucose sensors have underscored their significance in diabetes management,

emphasizing the pivotal role of sensitivity and selectivity in ensuring dependable glucose monitoring.[112] Furthermore, scrutinising metal oxide nanostructures has revealed their advantageous characteristics, such as enhanced electrical properties and augmented surface area, amplifying their utility in diverse chemical sensing applications.[113,114] The emergence of adaptable and wearable chemical sensors has elicited considerable interest owing to their capacity for real-time monitoring of biochemical markers and environmental toxins, thus playing a crucial role in health management.[115] Moreover, integrating nanomaterials into food safety surveillance has facilitated the creation of sensors capable of identifying hazardous chemicals, thereby assuring food safety and protecting public health.[116] Significant breakthroughs have highlighted the importance of gas sensor technology in detecting perilous substances and augmenting environmental safety. This is particularly pertinent in identifying volatile organic compounds (VOCs) and ecologically hazardous substances, wherein the innovation of metal-organic frameworks (MOFs) for gas sensing devices has gained substantial momentum.[117] Simultaneously, the implementation of printed electrical gas sensors has enhanced accessibility and deployment across various scenarios, providing a cost-effective, lightweight, and potentially disposable alternative to traditional gas sensors.[118] Additionally, extensive research into tin oxide gas sensors underscores their efficacy in surveilling hazardous gases for stationary alarm systems, notwithstanding the extant challenges associated with sensitivity and specificity that necessitate attention.[119] However, gas sensor sensitivity and specificity challenges warrant further resolution. Collectively, these advancements underscore the ongoing innovation in sensing technologies and their pertinence across diverse chemical domains.

1.2.4 Challenges in sensing

Sensing technologies have made significant advancements, although they still have limitations that may diminish their utility. To minimize sensor drift, corrosion, and deterioration caused

by harsh temperatures, humidity, corrosive atmospheres, and ambient pollution, it is necessary to implement robust protective measures and use durable materials. Noise and interference, such as electromagnetic interference (EMI) caused by power lines and electrical devices, can conceal true signals. To maintain data accuracy, it is essential to employ adequate measures such as shielding, filtering, and signal processing. Power consumption is a significant issue, especially in IoT, portable, and remote applications. In these cases, the limited battery life requires energy harvesting, low-power electronics, and efficient power management to ensure long-term operation. Miniaturization and integration are essential for incorporating sensors into diverse devices. Nevertheless, this task has challenges maintaining longevity, distance coverage, and responsiveness, often requiring complex production techniques and meticulous planning to prevent signal overlap and disruption. Moreover, economic factors can hinder widespread adoption, particularly in developing countries or when implementing large-scale projects. These aspects include sensing mechanism complexity, material choice, manufacturing techniques, and maintenance requirements. To ensure the accurate, reliable, and cost-effective performance of sensors in various fields such as consumer electronics, industrial automation, healthcare, and environmental monitoring, it is crucial to tackle these challenges by employing innovative design, materials science, and engineering solutions.[85,120–123]

Soon, sensors will be more precise and intelligent, improving their effectiveness and decision-making capabilities. Enhanced sensing technology and process automation will lead to the development of more powerful and interconnected sensing equipment, increasing their use in a networked society. This advancement will benefit various applications, including food safety, biohazard detection, environmental monitoring, health tracking, industrial and aerospace uses. The demand for current intelligent sensors will be driven by digitisation's positive effects on production lead times, quality, and costs. Continual improvements in sensor networks are being made across industries, while AI technology has led to the creation of new, more innovative

sensor-based devices with autonomous behaviour and interaction. While significant, the advancement of sensing technology remains in an early developmental stage. There are plentiful opportunities for further exploration to refine sensors for widespread integration into daily life.

1.3 Energy harvesting

The depletion of fossil fuel reserves and the escalating environmental apprehensions have instigated the progress of energy harvesting, an innovative technology designed to capture and convert ambient energy from numerous sources into practical electrical power. Originating in the early 2000s in reply to the escalating demand for autonomous energy sources, particularly for wireless devices in remote areas, this technology encompasses various methodologies. These include thermal energy harvesting, leveraging thermoelectric generators to harness temperature differences; mechanical energy capture, reliant on vibration energy harvesting employing piezoelectric materials or electromagnetic induction; and solar energy harvesting, using photovoltaic cells to transform sunlight into electricity. Furthermore, triboelectric nanogenerators exploit charge separation resulting from material friction, while hydrokinetic energy harvesting harnesses the kinetic energy of flowing water. Each of these technologies offers distinct advantages and finds applications in areas such as smart sensor networks and the Internet of Things, serving as indispensable tools for energy extraction from the environment. Anticipated modifications in energy consumption can be attributed to advancements in materials science and engineering, poised to augment the versatility and efficiency of energy harvesting technologies, thereby fostering a more resilient and sustainable energy landscape.[124–126] Some frequently utilised energy harvesting technologies are presented below.

1.3.1 Energy harvesting techniques and applications

Solar energy harvesting: Photovoltaic (PV) cells are pivotal constituents in harnessing solar energy, affecting the direct conversion of sunlight into electricity through the photovoltaic

effect. The process commences with the incidence of photons from sunlight upon the surface of a semiconductor material, typically silicon. Engagement with these photons energises electrons within the semiconductor, liberating them from atomic bonds and forming electron-hole pairs. An internal electric field within the solar cell guides the charge carriers, prompting the movement of electrons toward the negative side and holes toward the positive side, thereby engendering direct current (DC) electricity. One approach to heightening the efficacy of photovoltaic cells involves utilising multi-junction cells, integrating diverse semiconductor materials to capture varied light wavelengths and optimise solar energy absorption. Recent advancements in solar technology encompass the adoption of organic solar cells, comprising organic materials as the active layer for light absorption, with the capability for printing on flexible substrates, thereby conferring lightweight and flexible solar panel production. Furthermore, research in light-trapping structures, such as textured surfaces, is directed at augmenting light absorption and enabling more efficient energy conversion. Accordingly, solar energy harvesting remains in a state of perpetual progression, endeavouring to broaden its application across diverse domains, ranging from expansive solar farms to residential rooftops.[127–129]

Vibrational energy harvesting: Vibrational energy harvesting involves the transformation of mechanical vibrations into electrical energy and is widely applicable in industrial, transportation, and wearable technology sectors. This technique encompasses three primary methods: piezoelectric, electromagnetic, and electrostatic. Piezoelectric energy harvesting employs specialised polymers or materials, for example quartz, which generate electric charges when exposed to mechanical stress or vibrations. These materials can effectively store energy, making this method particularly advantageous for small-scale applications with modest power requirements. Conversely, electromagnetic energy harvesting bank on the relative motion of an inductor coil and a magnet, following Faraday's law of electromagnetic induction. This

method is commonly favoured in larger applications, offering substantial energy output depending on vibration frequency and amplitude. Electrostatic energy harvesting involves the alteration of capacitance due to mechanical motion, influencing the distance between conductive plates to produce an electric current. It is frequently utilised in MEMS devices with compact dimensions and low power consumption. The versatility of vibration energy harvesting techniques allows for their integration across a broad spectrum of applications, enhancing the energy sustainability of devices, especially those utilised in remote monitoring systems.[130–132]

Thermal energy harvesting: Thermal energy harvesting, also known as thermoelectric production, involves the utilisation of thermoelectric generators (TEGs) to capture waste heat and convert it into useful electrical energy. This process is rooted in the Seebeck effect, which induces an electromotive force when two contradictory conducting materials experience a temperature differential. Within a TEG, one side is subject to heating while the opposite side remains at a lower temperature through a heat sink or external influences. Consequently, an electric current is generated as the charge carriers within the material migrate from the heated side to the cooler side due to the resulting temperature gradient. TEGs prove particularly beneficial when huge quantities of waste heat are generated, notably in automotive applications, industrial processes, and residential appliances. To enhance the efficiency of thermal energy harvesting, attention is directed towards developing thermoelectric materials with high thermoelectric efficiency, quantified by the figure of merit (ZT). Moreover, ongoing research explores alternative materials, including skutterudites, bismuth telluride, and organic nanocomposites, to optimise performance under diverse temperature gradients. Through the continued research and deployment of TEGs, converting wasted heat into usable electrical energy presents a tangible avenue to advance energy efficiency and diminish reliance on fossil fuels.[133–136]

Wind energy harvesting: The procedure of converting wind energy into electrical energy entails the utilisation of wind turbines or comparable technology. Key to this technological operation is the application of aerodynamic blades, which capture wind flow to set a generator-connected rotor in motion. The powertrain translates rotor motion into electrical energy, and the rotor assembly is the principal component of wind energy systems. The aerodynamic design of the blades enables their rotation by exploiting pressure differentials engendered by wind impact. Subsequently, the drivetrain harnesses this rotational motion to furnish mechanical energy to a generator, which effectuates its conversion into electrical energy. The resulting electricity may be utilised on-site or integrated into the grid to supply power to commercial or residential structures. Advancements in wind energy technology have facilitated the development of more efficient turbine designs, such as vertical-axis wind turbines (VAWT), capable of generating electricity in urban environments with spatial constraints and adept at capturing wind from varied directions. Concurrently, research endeavours seek to optimise materials, energy-storage mechanisms, and turbine blade length, targeting challenges associated with the unpredictability of wind speed. Given the sustainability and scalability of wind energy harvesting, it increasingly assumes a pivotal role in achieving global renewable energy objectives.[137–140]

Hydrokinetic energy harvesting: Electrical power can be generated from the movement of water by utilising hydrokinetic energy harvesting. This approach incorporates various turbine designs that function like wind turbines, whereby the motion of water induces rotational movement in the blades. Hydrokinetic devices can be strategically positioned in rivers, tidal streams, or ocean currents to capture the kinetic energy of water movement generated by tides, waves, and the natural flow of rivers. The rotational motion of water turns blades affixed to a rotor, thus driving a generator to produce energy. Noteworthy innovations include undersea turbines, designed to harness energy with minimal surface infrastructure, and ducted turbines,

enclosed for enhanced efficiency. Hydrokinetic energy harvesting is a sustainable energy source due to its adaptability, allowing deployment in areas with consistent water flow. Furthermore, recent advancements underscore efforts to minimise the environmental impact of these devices on aquatic habitats while optimising energy extraction capabilities. The burgeoning field of hydrokinetic technology holds significant potential to advance renewable energy capacities through integration into existing marine infrastructure.[141–143]

Electromagnetic energy harvesting: Electromagnetic energy harvesting allows energy extraction from various objects' dynamic electromagnetic fields, including equipment and power lines. Inductive coupling, which employs localised electromagnetic fields for energy transfer between coils, constitutes a fundamental stage in energy harvesting. Applying Faraday's law of induction enables voltage generation through alterations in an external electromagnetic field or the relative movement between the coils. This technology is particularly advantageous for wireless powering applications, as it enables the absorption of environmental energy without necessitating direct connections to power sources. The compact size of electromagnetic harvesting devices makes them appropriate for remote sensors and small-scale equipment implementation. Moreover, resonant inductive coupling significantly advances energy harvesting systems, enhancing energy transfer efficiency over short distances.[144–146]

Triboelectric nanogenerators (TENG): Triboelectric nanogenerators harness the triboelectric effect, which involves separating specific materials and subsequent electrical charging. This technology converts mechanical energy from motion into electrical energy by leveraging materials with differing electronegativities. The fundamental mechanism relies on the interaction of distinct materials, resulting in one material acquiring a positive charge and the other a negative charge. By utilising electrodes within a circuit to capture the electric potential stemming from this charge separation, TENGs generate an electrical current. Their

capacity to power small devices or sensors, especially in settings characterised by prevalent mechanical motion, such as smart fabrics and wearable electronics, has sparked considerable interest. Ongoing research aims to elevate the energy conversion efficiency of TENGs, optimise the materials used in their fabrication, and adapt their designs for practical deployment. TENGs hold substantial promise for advancing the field of energy harvesting due to their ability to generate electricity from routine activities like walking and vibration.[147–149]

1.3.2 Significant findings in energy harvesting

The latest advancements in energy collection devices highlight the crucial role of diverse chemical concepts and materials in improving sustainability and efficiency. Piezoelectric materials, known for their efficient conversion of mechanical vibrations into electrical energy, have been a focal point of energy harvesting research. Notable developments in the structural design of piezoelectric nanogenerators have resulted in increased energy output and mechanical durability.[150,151] Additionally, nanomaterials such as MXenes, characterised by higher mechanical and electrical conductivity, are being explored as prospective candidates for energy storage and harvesting applications.[152,153] Surface plasmon resonance has significantly enhanced light absorption and energy conversion rates, leading to more effective photocatalytic processes. Plasmonic nanocatalysis has been successfully integrated into solar energy conversion, yielding significant improvements.[154] Hybrid systems that integrate photonic and piezoelectric components have demonstrated the capacity to enhance energy harvesting synergistically, underscoring the interdisciplinary nature of contemporary research endeavours focused on optimising energy conversion technologies.[155,156] The pervasive appeal of sustainable energy has led to a surge in the popularity of energy harvesting from water sources. From an electrochemical perspective, energy harvesting technologies leverage various phenomena, including electrokinetics in evaporation, piezoelectric effects in stagnant water, and streaming currents in moving water. Streaming potentials, generated by flowing water, can

produce electricity as charged ions migrate along a conductive surface.[157] In evaporation-driven energy harvesting, liquid-solid triboelectric nanogenerators (LS-TENGs) harness electrokinetic principles to produce electricity during the evaporation process through ion migration and electrostatic interactions.[158] Moreover, piezoelectric materials play a crucial role in collecting energy from stationary water by converting mechanical stress from water motions into electrical energy, thereby highlighting the intrinsic relationship between chemical reactions and mechanical properties.[159] Perovskite solar cells have significantly revolutionised the field of solar energy applications, achieving power conversion efficiencies of 25% due to their exceptional light absorption and charge transport capabilities, attributable to their chemical stability and tunability. Furthermore, exploring nanostructured materials, such as titanium dioxide (TiO_2), for photocatalytic water splitting has led to the efficient harnessing solar energy for hydrogen production, offering a clean and sustainable fuel source.[160,161] Metal-organic frameworks (MOFs) have been investigated for their potential integration into solar energy systems. These studies have revealed that MOFs exhibit promise in efficiently capturing sunlight and facilitating charge carrier transport. As a consequence, they have shown an ability to boost the production of solar fuels.[162,163] The blooming of advanced photocatalysts, including graphitic carbon nitride (g-C_3N_4) for water splitting, has played a pivotal role in the efficient collection and transformation of solar energy into chemical fuels, effectively addressing the world's energy challenges.[164,165] Additionally, integrating metal halide perovskite materials into solar cells has yielded remarkable power conversion efficiencies, surpassing those of traditional silicon-based cells, owing to their distinctive electrical properties and enhanced light absorption capacities.[166,167]

1.3.3 Challenges of energy harvesting

Numerous constraints prohibit energy harvesting techniques from being extensively used and from being as successful as feasible. One of the key issues is the unpredictable and intermittent

nature of ambient energy sources, such as wind and solar power, which makes it more difficult to create systems that can reliably supply power. Because of this unpredictability, energy harvesting systems grow increasingly complex and expensive as advanced energy storage solutions are necessary to guarantee a regular supply.[168,169] Furthermore, a lot of energy harvesting techniques have poor power conversion efficiency, which means that to enhance energy capture and storage, breakthroughs in technology and materials are needed.[170] Furthermore, major engineering issues are associated with integration and downsizing when scaling these technologies for practical applications, particularly in the micro and nanoscale realms.[168] Certain methods may inadvertently result in resource depletion or management problems over time. Considering the sustainability and environmental impact of the materials used in energy harvesting devices is crucial.[171] In the realm of chemical engineering, energy harvesting systems present notable challenges, particularly in the realms of material selection and efficiency optimisation. A significant impediment lies in the quest for highly efficient materials that adeptly convert ambient energy sources, such as solar and kinetic energy, into viable electrical energy. Although perovskite solar cells have exhibited encouraging efficiency, concerns persist regarding their stability and propensity for environmental degradation, which can compromise their long-term reliability and performance.[172,173] Furthermore, the wide array of available energy sources often necessitates specialised chemical techniques to enhance energy conversion efficiency, giving rise to material synthesis and design complexities. Additionally, there exists a demand for innovative chemical mechanisms to facilitate seamless transitions between energy forms while upholding optimal functionality, thus enabling the seamless integration of energy harvesting devices with contemporaneous technologies. Resolving these challenges is a prerequisite for advancing energy harvesting technologies and validating their practicable deployment in real-world scenarios.

The significance of microdroplet handling, sensing, and energy harvesting technologies cannot be overstated, as they are pivotal for advancing diverse industries. Precise manipulation of fluids through microdroplet handling is essential for industrial and therapeutic applications, enhancing efficiency in chemical manufacturing and drug delivery tasks. Despite considerable progress in this domain, substantial scope exists for further research and innovation.

Using cutting-edge materials in sensing technologies has facilitated highly accurate and sensitive detection methodologies. These sensors are indispensable for environmental monitoring and point-of-care diagnostics, with ample room for ongoing development and research. Innovative materials have the capacity to markedly enhance sensing capabilities, particularly in relation to sensitivity and specificity across diverse applications.

Energy harvesting technologies represent another critical area with significant potential for development. Pursuing ingenious methods to harvest and harness energy from microenvironments remains imperative as the demand for efficient and sustainable energy sources continues to escalate. Incorporating layered materials holds promise for substantially enhancing energy harvesting devices, paving the way for imaginative approaches to power various devices, particularly in the rapidly expanding field of wearable technology.

This thesis scrutinises the potential and breakthroughs attainable by applying layered materials in the relatively unexplored microdroplet handling, sensing, and energy harvesting disciplines. The objective of the research is to make a valuable contribution to the growing repository of knowledge and to catalyse future innovations.

1.4 Exfoliation and reconstruction of layered materials into lamellar membranes

Ancient civilisations were the first to recognise layered materials, such as mica and graphite, naturally found in rock formations and minerals. This early fascination laid the foundation for scientific exploration that has spanned thousands of years, leading to the advanced discipline

of materials science today. A significant turning point in this journey occurred in the 19th century when Benjamin Collins Brodie identified the layered structure of graphite. This discovery provided a new understanding of the atomic-level composition of layered materials. The knowledge of graphite structure and similar materials was further advanced through single-crystal X-ray diffraction.[174,175]

Layered materials have distinct layers of intralayer/covalently linked atomic planes, separated by weak interlayer forces like van der Waals interactions. This weak connection separates individual layers into atomically thin 2D nanosheets through top-down exfoliation. Another method of creating 2D nanosheets involves bottom-up synthesis, where individual atoms or molecules are combined to form 2D structures with specific features. These technologies have expanded the range of 2D materials, developing numerous exfoliation procedures and synthesis methods.[176]

In the 1970s, scientists confirmed the layered structure of hydrotalcite, also known as layered double hydroxide (LDH), using X-ray diffraction studies, which was a significant achievement. This discovery sparked much interest in understanding these materials' layered structures more deeply, leading to the development of techniques for extracting single-layer, two-dimensional (2D) nanosheets from these structures. These efforts aimed to uncover unique characteristics present in materials in their pure two-dimensional state, such as exceptional electrical, mechanical, and thermal properties.[177,178]

In 2004, Andre Geim and Konstantin Novoselov made a significant breakthrough by successfully exfoliating graphene using a simple scotch tape method.[179,180] This achievement provided experimental evidence for many theoretical studies and showcased the remarkable properties of graphene, such as its exceptional electrical and thermal conductivity, mechanical strength, and optical transparency. The successful exfoliation of graphene marked the start of a new era in material science. This breakthrough led to the exploration of other inorganic

materials such as boron nitride (BN),[181] MXene,[182] molybdenum sulfide (MoS_2),[183] tungsten sulfide (WS_2),[184] clays[185] and more. Various methods, including mechanical cleavage, sonication, ion intercalation, chemical vapour deposition, and hydrothermal synthesis, have been utilised to produce these nanosheets, employing both top-down and bottom-up approaches.[186,187] The unique structure-dependent properties of these 2D nanosheets, different from their bulk counterparts, have created numerous possibilities in catalysis,[188] sensing,[189] energy storage and conversion,[188,190] electronic devices,[191] and biomedicine.[192] Reconstructed 2D materials have a great deal of potential for use in energy harvesting processes like triboelectric nanogenerators (TENG),[193] contrasting interfacial activity,[194] reverse electrodialysis (RED),[195,196] and moisture-enabled nanogenerators (MEG),[197] in addition to sensing applications.[198–200] When two solutions pass over ion-selective membranes with varying salt concentrations, ions migrate and produce an electric current, which is how RED produces energy. Utilising the distinct surface characteristics of two-dimensional materials, energy harvesting using their interfacial activity converts external inputs into electrical energy. MEG work on the principle that surface-active materials absorb water molecules from the atmosphere and split them into mobile ions. These mobile ions diffuse in a charged matrix due to evaporation or concentration gradients, which generate electricity. The above discussion highlights the versatility of 2D materials in harvesting energy from several sources, paving the path for self-powered devices.

The remarkable properties of individual 2D nanosheets are challenging to maintain when assembled into larger structures. The reassembly process often loses its unique nanoscale features due to strong inter-sheet attractions, such as van der Waals forces and π-π stacking.[176] However, new assembly techniques like vacuum,[185,201] pressure-assisted filtration,[202] and wet-spinning[203] are being developed to create larger structures that retain the exceptional properties of 2D nanosheets. Constructing large-scale structures from 2D nanosheets preserves and

enhances specific characteristics, resulting in new functions. For example, graphene sheets produced vertically on metal substrates exhibit unique responses to current frequency and restructured graphene oxide (GO) membranes display high tensile strength and selective permeability.[204–206] These advancements have prompted the study of layered membranes made from other 2D materials like BN, MXene, and MoS_2, demonstrating distinct features not present in their bulk or individual forms.

Continued study and development in layered materials hold vast potential for various advanced technological applications. The path from ancient observations to modern scientific advances demonstrates the enduring fascination and ongoing endeavour to understand and utilise the unique properties of layered materials. Isolating 2D nanosheets from bulk materials is important to enhance their characteristics. Consequently, the exfoliation and synthesis of layered materials are gaining significance in the research community. In the following section, the commonly used exfoliating techniques for preparing atomically thin 2D nanosheets are discussed, along with specific examples

1.4.1 Exfoliation techniques

Exfoliation techniques like ball milling, electrochemical intercalation, and micromechanical cleavage can create few-layer or even monolayer two-dimensional materials that are hundreds of micrometers wide and, for some methods, in large numbers. In contrast, shear flow and ultrasonication exfoliation methods typically result in larger volumes and a continuous process that produces laterally smaller 2D material sheets. Selecting the appropriate procedure for a particular application, material, or final quality is crucial because these various exfoliation techniques offer significant differences in processing time, yield, and material quality. Figure 1.1 displays a schematic overview of exfoliation techniques.

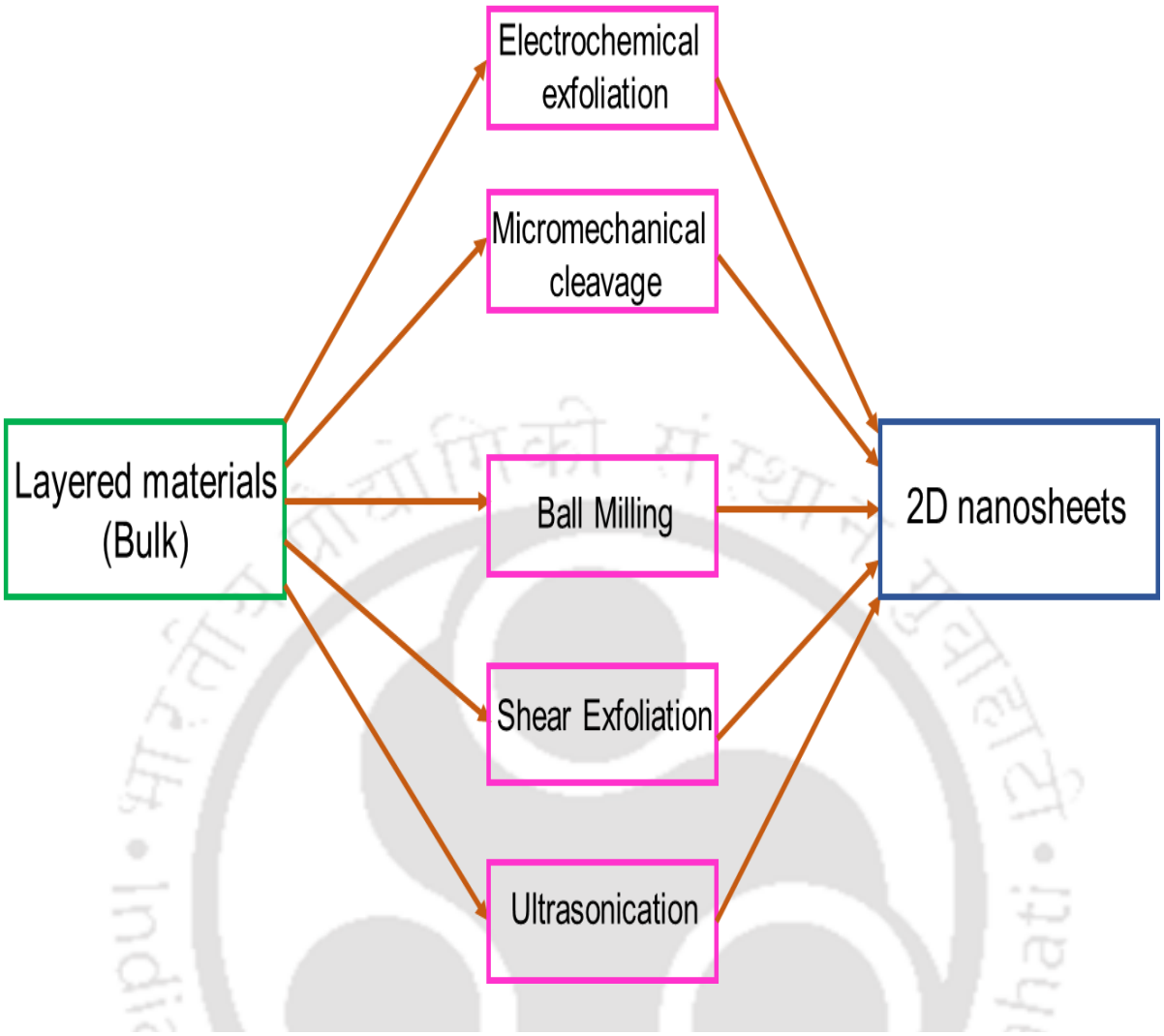

Figure 1.1: *The five most popular methods for exfoliation. The most popular methods for exfoliating 2D materials are micromechanical cleavage, ball milling, ultrasonication, shear exfoliation, and electrochemical exfoliation. These methods use a mix of chemical and mechanical forces to separate layers of 2D materials.*

Micromechanical cleavage: Initially, removing thin layers of atoms from bulk crystals was accomplished through the "Scotch tape" technique, also known as micromechanical cleavage.[186] This technique involves placing a graphite flake onto a strip of tape, folding it over itself, and then repeatedly peeling it off. As each layer is peeled off, the graphite flakes become thinner and thinner. Then, the tape is pushed onto a surface, leaving layers of different thicknesses, as shown in Figure 1.2.[186,207] Novoselov et al. pioneered this technique of isolating

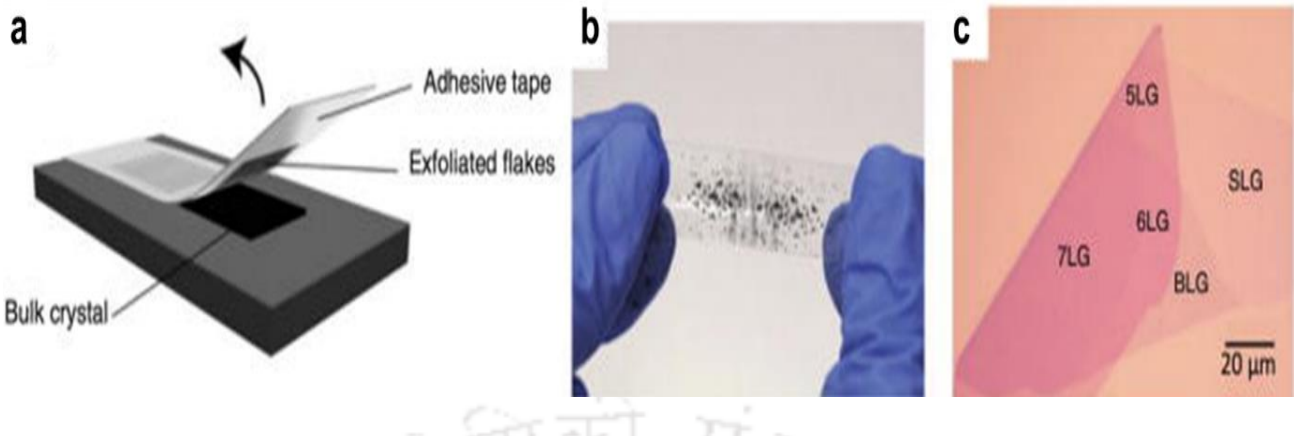

Figure 1.2: *Micromechanical cleavage techniques using scotch tape. (a) A diagram illustrating the micromechanical cleavage method for exfoliating 2D material. (b) Partially exfoliated graphene on scotch tape. (c) An optical microscope image shows exfoliated single-layer, bilayer, and multilayer graphene flakes. (Images copied from (a)-(c) Appl. Phys. Rev., 2022, **9**, 1238–1244.)*

a single layer of 2D material called micromechanical cleavage, which involves mechanical exfoliation. Researchers conducted an experiment where they brushed a freshly prepared graphite surface against another surface, resulting in the deposition of various flakes. The flakes were analysed using transmission electron microscopy (TEM) and atomic force microscopy (AFM), which revealed the presence of monolayers. Micromechanical cleavage is an uncomplicated and inexpensive method of exfoliation that offers numerous benefits. This technique enables the creation of high-quality, single-crystalline mono- and few-layer nanosheets, particularly boron nitride. It also allows for precise shaping through the combination of etching procedures and manipulation of etching time and other relevant parameters while providing robust control over conductance modulation. Notably, the electron transport properties of the samples remain intact following micromechanical extraction from the bulk, ensuring that the essential attributes of the 2D materials are preserved. However, micromechanical cleavage has some downsides, such as limited to small-scale fabrication and the lack of technology for large-scale continuous monolayers. It is also not a simple technique for boron nitride nanosheets (BNNS), and controlling the flake lateral size and thickness is

challenging. Additionally, adhesive remnants may be left behind, potentially contaminating the samples. Exfoliation efficiency strongly depends on the interfacial adhesion between the substrate and the 2D materials, making the process less uniform and difficult to optimise.[208,209]

Ball milling: The traditional method for isolating 2D materials is adhesive tape-based micromechanical exfoliation. However, ball milling has emerged as a mechanical exfoliation technology that is suitable for large-scale production.[186] Researchers have successfully adapted ball milling, historically used to create alloys from metallic powders, to exfoliate layered 2D materials in bulk. By using shear, rolling, and impact forces exerted by the balls in the milling

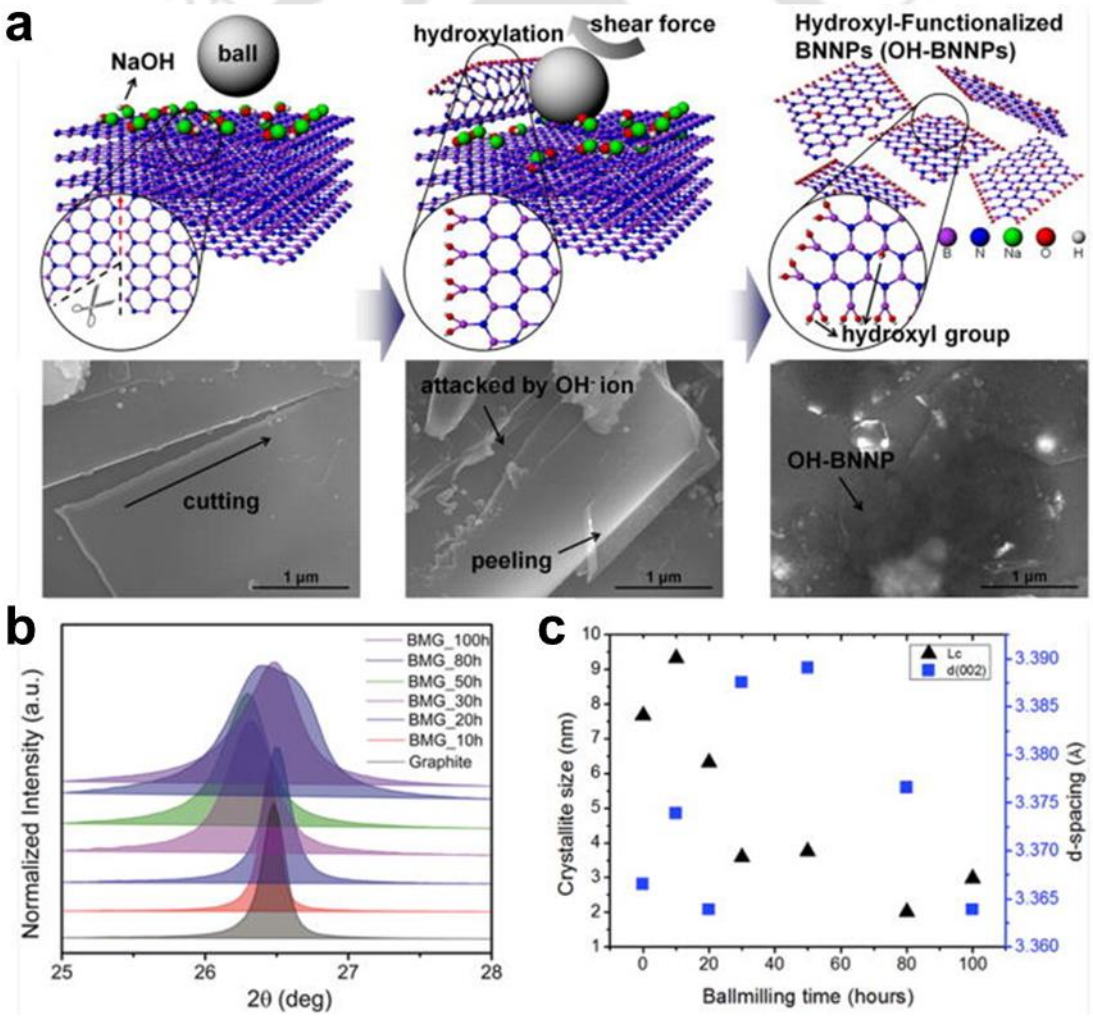

Figure 1.3: *Ball milling exfoliation mechanisms of 2D materials. (a) Schematic representation of the hBN exfoliation mechanism with accompanying SEM pictures. (b) XRD and (c) change in interplanar spacing with ball-milled graphene milling time. (Images copied from (a) Nano Lett., 2015,* ***15****, 1238–1244 and (b)-(c) Sci. Rep., 2018,* ***8****, 1–6.)*

process, they are able to overcome van der Waals bonding and separate the 2D layers. For instance, Lee et al. utilised ball milling to exfoliate hexagonal boron nitride (hBN) in the presence of sodium hydroxide (NaOH), resulting in minimal structural damage and a high yield of flakes up to 1.5 μm in width (Figure 1.3a).[210] However, the aggressive nature of ball milling can cause flaws and lower yields in multilayer materials due to shear and impact pressures (Figure 1.3b,c).[211] Despite these limitations, ball milling offers a scalable method for producing layered materials at a far higher rate than alternative synthesis methods. Ball milling has several notable benefits for exfoliating 2D materials. It can efficiently produce high-quality boron nitride (BN) nanosheets with a high yield and is highly scalable. The process can produce thermostable, highly concentrated hBN suspensions up to 90 mg/ml with an outstanding yield of about 98%. Effective dispersion in water and other solvents is achieved by using BN nanosheets covalently grafted with hydroxyl groups, accomplished using methods such as β-cyclodextrin-assisted ball milling. The low-energy milling process preserves high crystallinity and chemical purity because the nanosheets are torn rather than vertically impacted. The use of milling agents reduces contamination and ball impacts, further improving dispersibility and yield. This groundbreaking method can efficiently generate nanosheets from a wide range of layered materials. Ball milling has several drawbacks, such as the challenge of achieving a high yield of monolayers. Strong collisions and vertical impacts in high-energy ball milling can potentially fracture particles and impair crystallinity. Additionally, the pure state of 2D nanosheets may be impacted by lingering chemical species. To maximize efficiency and output yield, careful adjustment of several parameters is required, including milling speed, ball-to-powder ratio, ball size, and milling agents.[212,213]

Ultrasonication: Micro-mechanical cleavage and ball milling are used to separate layers to generate exfoliation physically. However, many materials can be more gently treated and exfoliated using ultrasonication. During ultrasonication, a solution containing dispersed bulk

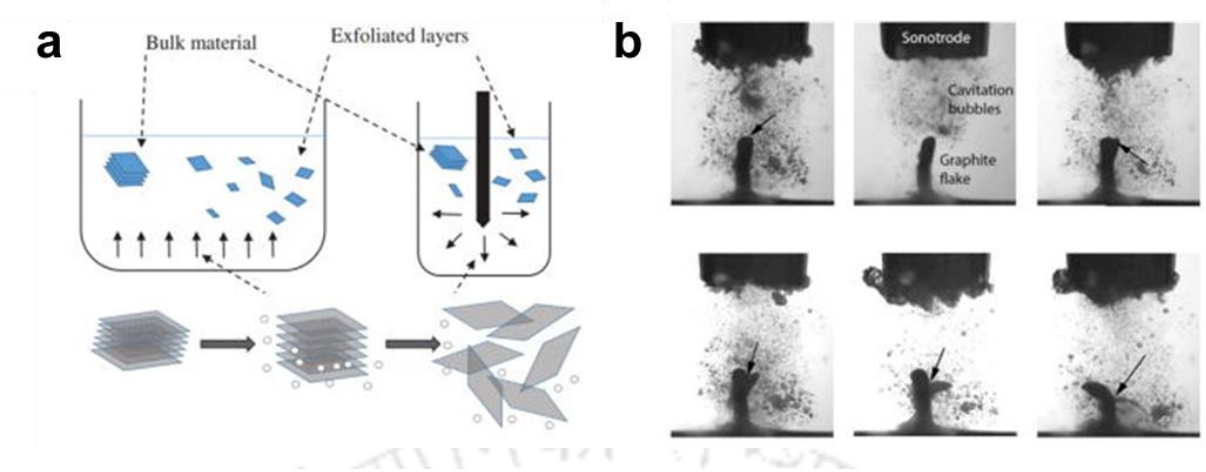

Figure 1.4: *Liquid sonication exfoliation mechanisms of 2D materials. (a) A schematic of liquid sonication shows how bulk material is divided into 2D nanosheets by ultrasonication,(b) high-speed sequence of frames illustrating the ultrasonication exfoliation of a graphene flake. (Images copied from (a) Nanophotonics, 2020, **9**, 2169–2189 and (b) Carbon, 2020, **168**, 737–747.)*

materials is exposed to ultrasonic waves generated by a transducer. These waves generate multiple unstable cavitation bubbles which, upon collapsing inward, produce high temperatures, pressures, and high-velocity liquid jets in the local environment. This mechanism provides a strong hydrodynamic shear force to overcome the weaker van der Waals interactions between layers, effectively exfoliating very small 2D layers from the bulk material. The exfoliated 2D materials typically have lateral diameters of only a few micrometres and thicknesses of a few layers yields of roughly 1 wt. % are usual, but can be raised to 7–12 wt. % with subsequent processing. Figure 1.4a shows a schematic[214], and Figure 1.3b presents a high-speed image sequence of the ultrasonic exfoliation of a graphene flake.[215] Ultrasonication provides several significant advantages, such as versatility and scalability, making it appropriate for large-scale production. It is a low-cost process that permits exfoliated boron nitride nanosheets (BNNS) to be readily dispersed in different organic solvents. The method produces high-quality graphene flakes with few defects, allowing them to be deposited in various conditions and on different substrates, offering more flexibility compared to other methods. Ultrasonication, a straightforward procedure that may be conveniently performed

using common laboratory equipment, remains unaffected by exposure to air or water. Graphene dispersions generated through this process remain stable for a period exceeding six months, with observed yields as high as 72.5%. However, ultrasonication also has limitations. More research is required to control the flakes' thickness and lateral size distribution, as the current sheets is relatively low, and achieving effective exfoliation requires prolonged sonication treatments. Additionally, there is a risk of chemical residues from organic solvents remaining on the flakes, and the lateral flake size may be inconsistent. The energy needed for exfoliation technique yields an uncontrolled number of layers. The production of single-layer graphene is balanced by the interaction between the solvent and graphene for solvents with similar surface energies. Nonetheless, solvents may degrade with prolonged or high-intensity sonication. Moreover, the electrical characteristics of the films may be hindered by residual surfactants.[186,216,217]

Shear exfoliation: High shear mixing is a scalable alternative technique for exfoliating 2D materials in a solution. This approach acts by dispersing nanoparticle clusters in a solution by the viscous forces produced when the solution flows rapidly through a narrow channel, separating the agglomerates. The cohesive forces between the particles result in the solvent imposing large shear forces on the two-dimensional particles. When the solvent weakens the van der Waals forces and mixes with shear forces, it causes the van der Waals bonds to break, resulting to the creation of thinner sheets of 2D materials. Furthermore, the solvent's shear pressures increase the amount to which molecules are inserted between the 2D layers. This process of intercalation results in a further decrease in the strength of van der Waals forces in such a way that is mutually beneficial. As a consequence, this procedure creates 2D sheets with few flaws because the forces needed for exfoliation are significantly weaker compared to

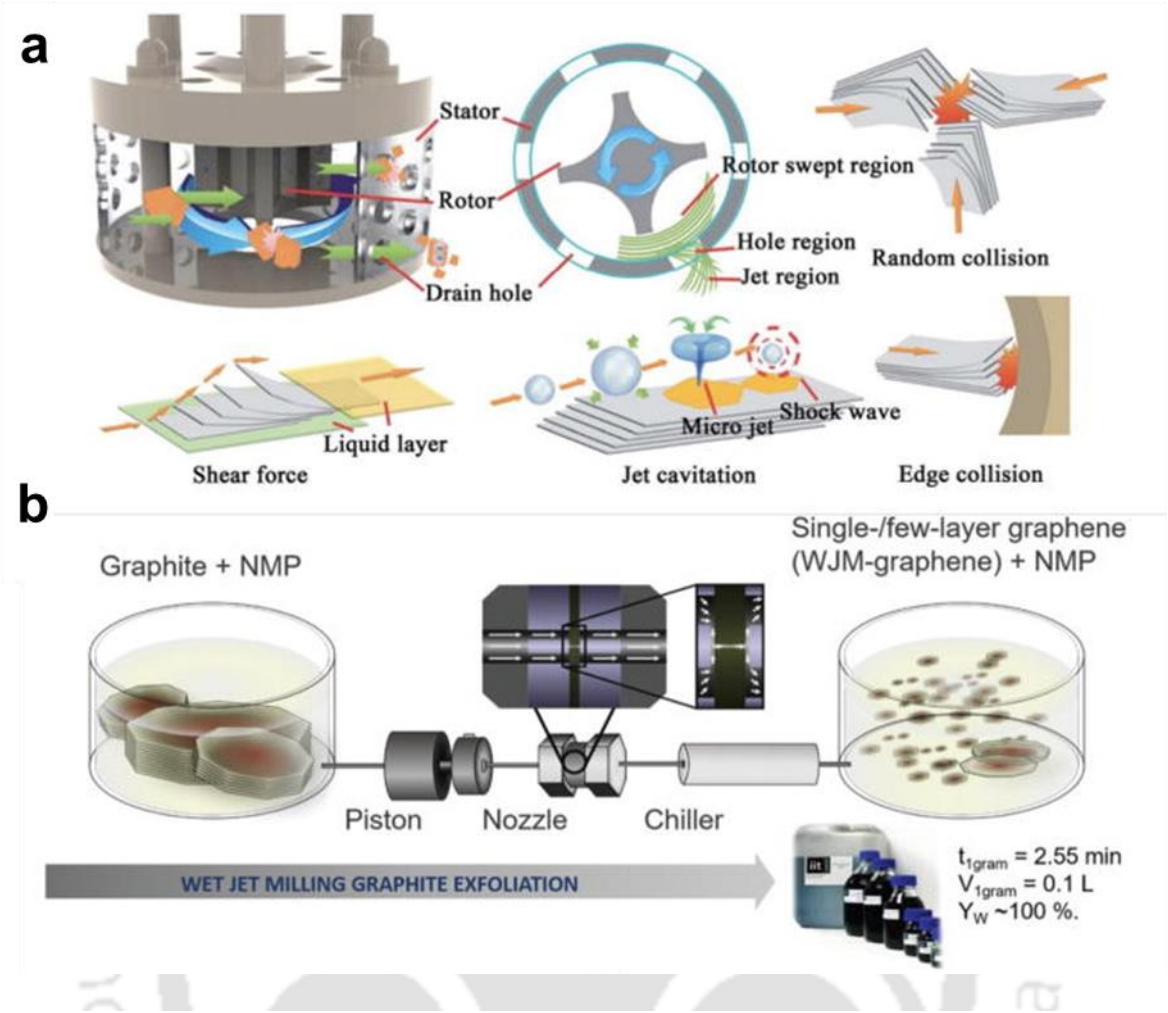

Figure 1.5: *Shear exfoliation mechanisms of 2D materials. (a) Schematic of a high shear mixer and mechanisms permitting exfoliation of layer materials in shear mixture. (b) Schematic of the compressible flow exfoliation process. (Images copied from (a) Adv. Mater., 2018, **30**, 1800200 and (b) Adv. Funct. Mater., 2019, **29**, 1807659.)*

alternative approaches. Nevertheless, it is necessary to maintain a careful equilibrium between these pressures to ensure successful exfoliation while avoiding any injury to the exfoliated 2D sheets.

Liu et al. exploited a high-shear mixer to separate graphene nanosheets with a remarkably low number of flaws.[218] Their shear mixer consists of a high-speed rotor and a stator, as depicted in Figure 1.5a. Another contemporary approach for exfoliating layered materials applying shear force is the compressible flow exfoliation (CFE) procedure developed by Rizvi et al.[219] This approach employs a high-pressure compressible gas instead of a liquid to obtain yields as high

as 10%. Wet jet milling is another scalable and continuous solution-based shear exfoliation technology reported recently for generating few-layer 2D materials (Figure 1.5b).[220] Shear exfoliation offers various advantages, including being a mature, scalable, and generally accessible technology. It creates exfoliated flakes that can be unoxidised and free of basal-plane flaws, resulting in high-quality graphene at a higher yield than sonication procedures. This approach supports a higher range of production quantities, from hundreds of millilitres to hundreds of litres and beyond, with concentration decaying only slightly as volume grows, leading to a production rate that scales with volume. Additionally, shear exfoliation requires a tunable "soft energy" source, unlike ball milling and high shear sonication, and its maximal production rate is substantially higher than that of traditional sonication-based procedures. Moreover, it does not require specialised surfactants to stabilise the exfoliated graphene. Shear exfoliation has various disadvantages, such as having a minimum shear rate to be applied. It requires several assistance mechanisms as Taylor–Couette flow, turbulence-assisted methods, vortex fluidic exfoliation, and temperature help, which add complexity to the process. This approach is not optimal for obtaining vast volumes of monolayers, and the exfoliated nanosheets are rather small in lateral size compared to those produced by mechanical cleavage. Additionally, surfactants are typically utilised to maintain the dispersion of 2D materials in solution, which might leave residues on the 2D sheets. Organic solvents like NMP and DMF are sometimes utilised in the exfoliation process, and these solvents are difficult to wash off, potentially leaving organic residues on the 2D sheets.[186,221–223]

Electrochemical exfoliation: Electrochemical exfoliation is a scalable process capable of creating vast numbers of 2D nanosheets in a liquid solution (electrolyte) using an electrical current, achieved either through cathodic reduction or anodic oxidation. The electrical current introduces ions into the electrolyte, which are attracted to the bulk 2D material and intercalate between its layers. This intercalation weakens the van der Waals bonds, thereby separating the

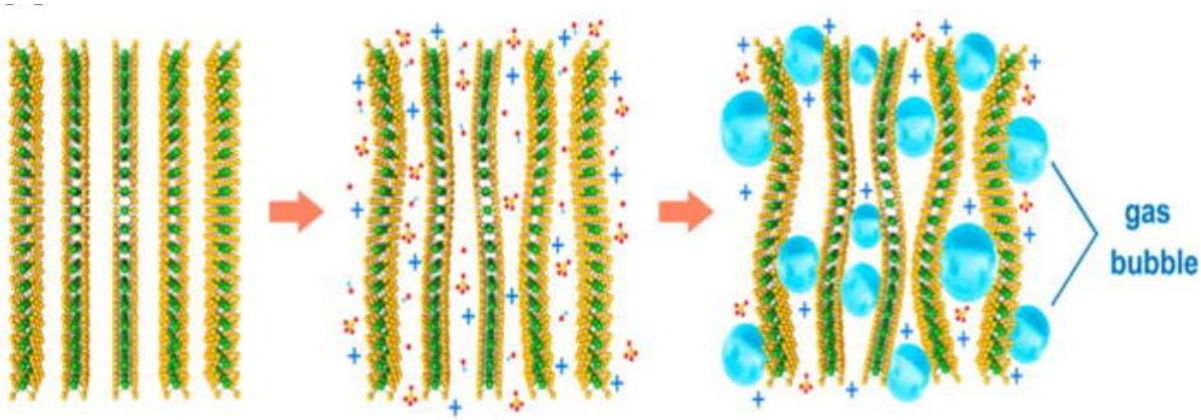

Figure 1.6: *Schematic illustration of ion intercalation and exfoliation of 2D sheets in the electrochemical method. (Image copied from ACS Nano, 2014,* ***8****, 6902–6910.)*

layers by a one-step, rate-controlled exfoliation process.[224] Electrochemical exfoliation technologies are generally straightforward to develop, build, and operate under ambient conditions. In 2014, Liu et al. first demonstrated a mechanism for the anodic exfoliation of MoS_2 in an aqueous Na_2SO_4 solution.[225] The charge of the ion is not stated, but it intercalates into the MoS_2 layers when a positive voltage is supplied to the bulk MoS_2 electrodes, as shown in Figure 1.6. As a result of the oxidation of radicals and anions, O_2 and/or SO_2 gas is created, which greatly increases the interlayer distance of MoS_2, allowing the separation of MoS_2 flakes from the bulk crystals. However, owing to the electro-oxidation process occurring on the surface of the electrode made of bulk material, the products are quickly oxidised, affecting the quality and degree of exfoliated MoS_2. Electrochemical exfoliation has various advantages, including the capability to mass-produce 2D materials and create graphene of acceptable quality. This approach results in graphene with excellent conductivity, with a sheet resistance of roughly 210 Ω/sq, and enables for the high-efficiency, large-scale synthesis of graphene with low defect content (ID/IG sub 0.1). It preserves the intrinsic structure of both graphene and MoS_2, and functions as a single-stage approach without requiring ultrasonication or subsequent processing when employing a solvent-based methodology. The technique is highly efficient when combined with shear exfoliation, and it can lead to possible composite design at a large

scale when partnered with electrochemical functionalisation. Additionally, it permits the rapid growth of high-yield black phosphorus through cathodic intercalation and breakdown of solvated cations. Electrochemical exfoliation in organic solutions makes the procedure eco-friendly and provides a modest and scalable approach for exfoliating transitional metal dichalcogenides. The challenges associated with electrochemical exfoliation encompass the intricacy of the exfoliation procedure and the necessity for additional sonication when employing highly ordered pyrolytic graphite (HOPG) for graphene exfoliation, leading to dispersion. Additional processes, such as organic radical aid, are necessary to control defect formation. There is a vast variety of thickness in the exfoliated layered materials, and the oxidation during the exfoliation process can destroy the nanosheets. The procedure may entail the use of ionic electrolytes, high boiling point organic solvents, and other chemicals, which can abandon residues on the exfoliated nanosheets. Cationic diameter is an essential element for successful electrochemical exfoliation, and structural defects such as scrolling, wrinkling, and fracture are observed in the resultant nanosheets.[186,226–229]

Chemical exfoliation: One well-known chemical exfoliation method is ion intercalation, in which appropriate ions are intercalated to reduce the van der Waals collaboration between layers.[230–233] Alkali metal intercalation into the spacious layers of transition metal dichalcogenides (TMDs) is a particularly good option owing to their moderately wide interlayer distances and weak interlayer interactions (Figure 1.7) Using n-butyl lithium (in hexane) as the intercalating agent, Joensen et al. pioneered this method in 1986 to separate single-layer MoS_2.[234] Lithium ion insertion causes a change in the MoS_2 local crystal structure, transforming the 2H phase into the metallic 1T phase, which has advantageous optical and electrical characteristics for cutting-edge applications. Nevertheless, there are a number of

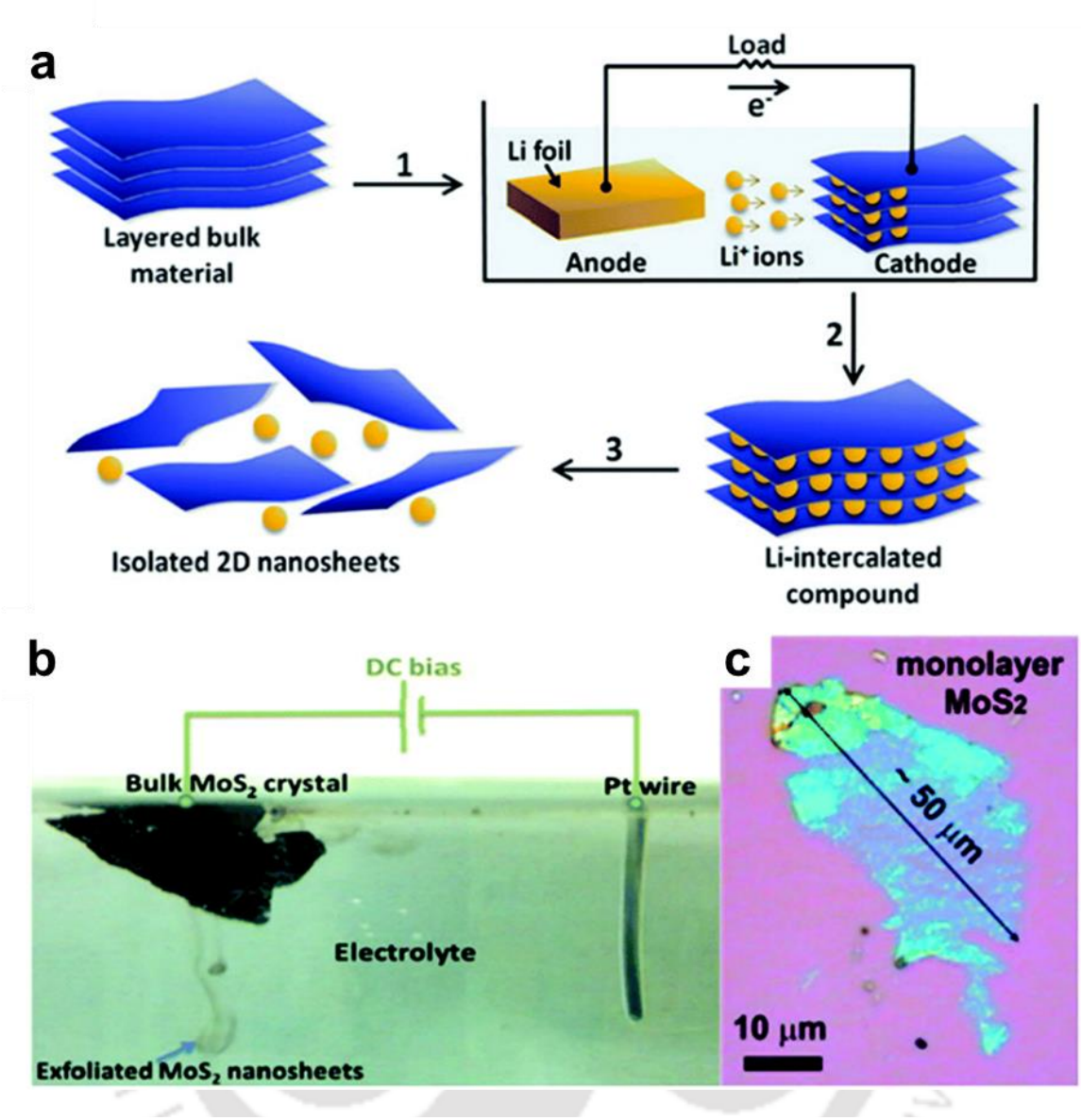

Figure 1.7: *(a) Schematic illustrating the electrochemical lithiation process used to exfoliate stacked bulk crystals to create 2D nanosheets. (b) Bulk MoS_2 electrochemical exfoliation experimental setup. (c) A monolayer MoS_2 nanosheet image captured with an optical microscope using an electrochemical exfoliation method. (Images copied from Nanoscale, 2015, **7**, 19358–19376.)*

drawbacks to the ion intercalation process, such as lengthy reaction times-often several days and the necessity for high operating temperatures. In addition, partial lithium insertion produces a decreased yield of single-layer sheets, whereas disproportionate lithiation can result in over-lithiation and MoS_2 breakdown or Li_2S precipitation. Huang et al. devised a different method based on an electrochemical procedure to get over these restrictions and produce a high

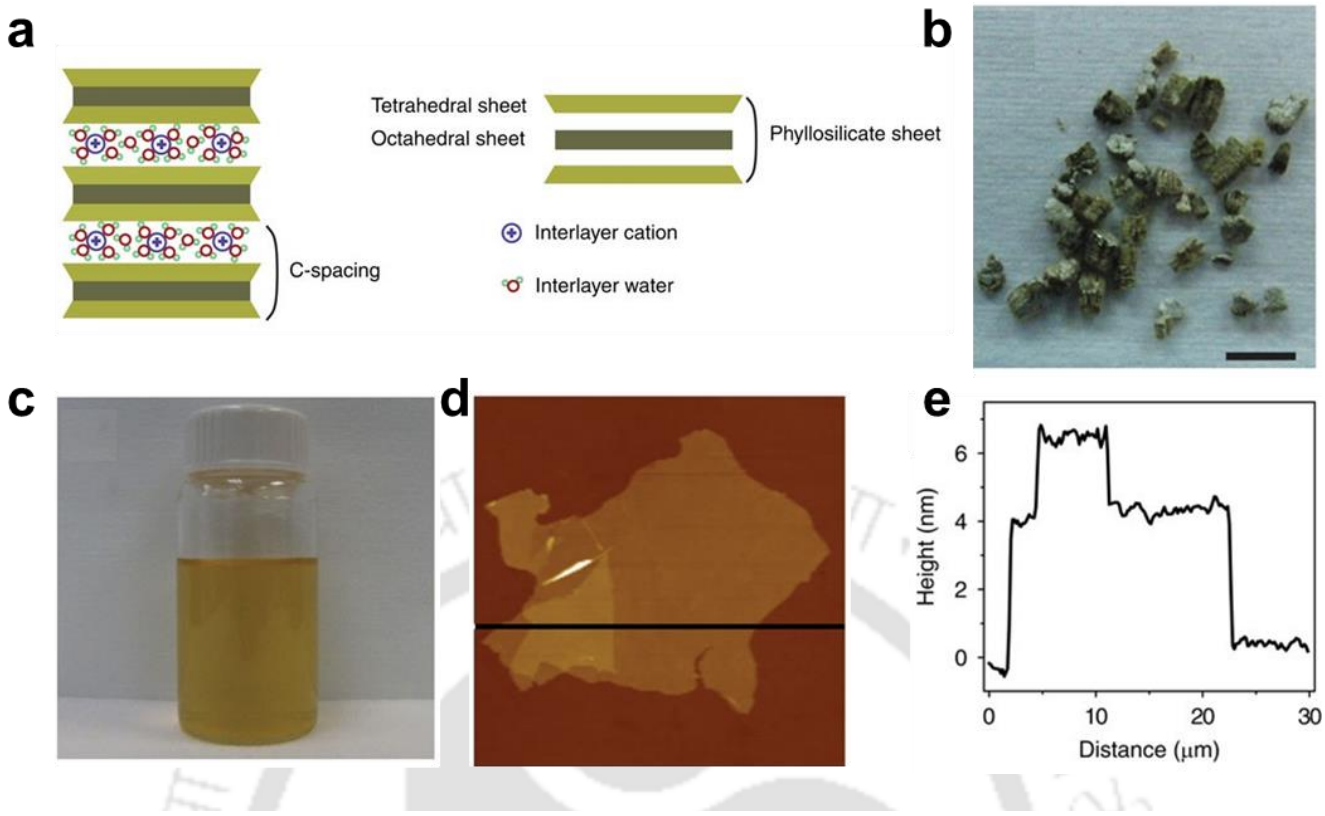

Figure 1.8: *(a) Layer structure model of vermiculite. (b) Thermally expanded vermiculite crystals (scale bar, 5 mm), which can be exfoliated by ion exchange. (c) A single to few-layer dispersion in water. They are few-layer stacks with lateral dimensions in the tens of microns, as seen by the (d) atomic force microscopy (AFM) image and (e) corresponding AFM height profile of exfoliated flakes. (Images copied from Nat. Commun., 2015,* ***6****, 1–7.)*

yield of single-layer 2D materials with controllable lithium insertion extent.[235] This technique uses graphene and bulk layered materials (such MoS_2, WS_2, TaS_2, TiS_2, ZrS_2, and graphene) as the material for cathode and an anode made of lithium foil in an electrochemical test cell. A galvanostatic discharge procedure is used to implant lithium under control, and it is then exfoliated in ethanol or water. The same group also looked at how discharge currents and cut-off voltages affected the manufacture of high-quality inorganic nanosheets, for example, $NbSe_2$, BN, WSe_2, Sb_2Se_3, and Bi_2Te_3.[236]

The ion-exchange method is a comparable liquid exfoliation approach that involves exchanging smaller intercalated ions for bigger ones (as shown in Figure 1.8). Greater ion intercalation widens the interlayer gap, which reduces the strength of the interactions between neighbouring

layers. Then, using mechanical shaking or sonication, layered materials with weak interlayer attractions can be exfoliated into 2D nanostructures.[237]

1.4.2 Advantages of lamellar membranes

Facile and scalable fabrication: Lamellar membranes reconstructed via vacuum filtration offer facile and scalable fabrication, rendering them highly appropriate for various applications. These membranes can be produced in a cost-effective manner, with the fabrication process easily scalable to meet various demands, from small-scale laboratory research to large-scale industrial production. The thickness of these membranes can be adjusted from a few nanometers to tens of micrometers by simply tuning the concentration and volume of the nanosheet dispersion used in the filtration process, providing flexibility for different applications. The lateral dimensions of the membrane are primarily constrained by the filtration apparatus, allowing for customisation based on specific requirements. Additionally, the large aspect ratio of the 2D nanosheets provides a substantial area for interactions with adjacent nanosheets, facilitating the creation of well-defined lamellar structures. This characteristic enhances the mechanical strength and stability of the membranes, making them reliable and efficient for long-term use.[237–239]

Enhanced separation efficiency and high selectivity: By efficiently filtering out impurities and particles, lamellar membranes' distinctive layered structure offers remarkable separation efficiency. Because of this structure, the pore diameters inside the layers may be precisely controlled and can be designed to either selectively permit or block particular molecules or ions. Because of their great selectivity, which guarantees that only desired chemicals pass through while impurities are effectively removed, these membranes are flawless for applications where strict purity standards are necessary, such gas separation and water purification.[240–242]

Increased durability and mechanical strength: The layered construction of lamellar membranes gives them an inherent mechanical strength. The membrane's resilience is increased by this structure, which keeps it intact even under physical forces and strains. Lamellar membranes have a longer operational lifespan and are more resilient, even in harsh situations. Because of their greater endurance, they require less maintenance and replacement, which lowers their cost when used in commercial and industrial settings.[243,244]

Decreased fouling and high flux: One of the lamellar membranes' key benefits is their capacity to lessen fouling, a frequent problem in filtration procedures. The layered construction minimizes obstructions and maintains constant performance by creating various paths for fluid flow that prevent particles from accumulating on the membrane surface. High flux rates are also likely with this design, making it possible to treat huge volumes of fluid quickly. For high-demand applications, efficient and continuous operation is ensured by combining low fouling and high flux.[245,246]

Thermal stability and versatile applications: Lamellar membranes have a extensive range of applications owing to their high versatility. Among other industries, they are frequently employed in gas separation, medical filtration, and water purification. Their capacity to withstand high temperatures is a result of their thermal stability, which broadens their applications. Lamellar membranes are reliable for industrial and technological applications due to their temperature stability.[198,237,247]

Chemical resistance and controlled pore size: Another important benefit of lamellar membranes is their resistance to chemical degradation. Their durability and functionality in processes involving aggressive substances can be ensured by their ability to manufacture materials that can tolerate hostile chemical conditions. During construction, the pore diameters inside the layers can be carefully regulated, enabling the membrane's filtering capabilities to be fine-tuned to match specific requirements. Lamellar membranes' capacity to offer

customised solutions for intricate filtration problems is made possible by their combination of chemical resistance and pore sizes that can be adjusted, which increases their efficacy and versatility in certain applications.[248,249]

Modifiable channel width and diffusion length: A vast array of homogeneous and well-defined nanochannels is formed between neighbouring nanosheets by the layer-by-layer deposition of nanosheets. The membrane can be tailored for the separation of desired-sized and-shaped molecules or ions from bulk solutions by adjusting this interlayer gap by the insertion of particular molecules or other nanoscale materials. The lengths of these nanochannels can also be controlled by varying the membrane thickness and the lateral dimensions of the 2D flakes. In situations where great selectivity is required, it is advantageous to increase the thickness and sheet size; in contrast, these parameters should be lowered for high flux. Furthermore, other chemical and physical techniques can be used to alter the lateral size of the nanosheets, offering additional ways to modify the length of the nanochannels. This tunability provides a great deal of flexibility by allowing membranes to be designed specifically for specialised separation tasks. This increases the membranes' utility in a variety of disciplines, including gas separation, water purification, and biomedical applications.[237,250–252]

1.4.3 Applications of lamellar membranes

Nanofluidics: Water is an important molecule for all known living forms, and its passage through properly designed micro/nano capillaries is fundamental to several biological processes. Consequently, knowing the behaviour of water under nanoscale confinement is vital for furthering the development of new integrated engineering systems. This discipline, known as nanofluidics, focuses on the dynamics of liquid flow within structures limited to the nanoscale size. In contrast to bulk systems, nanofluidic transport is greatly impacted by the surface charge characteristics of channel walls, resulting in unique transport phenomena. For example, within charged nanochannels, the conductivity of ionic species is controlled by the

surface charge, particularly in low electrolyte concentration settings and in sufficiently narrow channels. Here, transport processes are governed by size exclusion or molecular recognition effects, which determine the behavior of transporting species.[252–255]

The transport of ions within nanofluidic channels is substantially influenced by the creation of an electric double layer (EDL) at the interface between the channel walls and the electrolyte. The EDL can be described by the Debye layer thickness (λ) and the differential in number densities of counter-ions and co-ions within this area. The charge density gradient, which comes from the perm-selectivity of the nanochannels, provides a unique ion transport dynamic that dramatically differs from that observed in bulk electrolyte solutions. In such conditions, the ionic conductance within nanochannels becomes largely governed by surface charge rather than the overall ion concentrations in the reservoir. Consequently, ionic conductivity in nanochannels is many orders of magnitude higher than in bulk solutions, particularly at low electrolyte concentrations. This particular conductivity characteristic has led to significant interest in refining the shape and surface chemistry of manufactured nanofluidic channels to regulate molecular and ionic transport processes. Research in this area advances the understanding of fundamental nanofluidic transport principles and supports a range of applications, including biomedical analysis, DNA sequencing, ultrafiltration, seawater desalination, and nanofluidic energy conversion.[256–258]

Raidongia et al. were the earliest to demonstrate that a 2D lamellar graphene oxide membrane (GOM) is an exemplary candidate for nanofluidic ion transport.[255] They investigated surface-charge-governed ionic transport through self-assembled GOM in the horizontal (in-plane) direction. Their findings revealed that the conductivity of various electrolytes at low concentrations in the GOM was significantly higher compared to that in bulk electrolyte solutions, as illustrated in Figure 1.9.

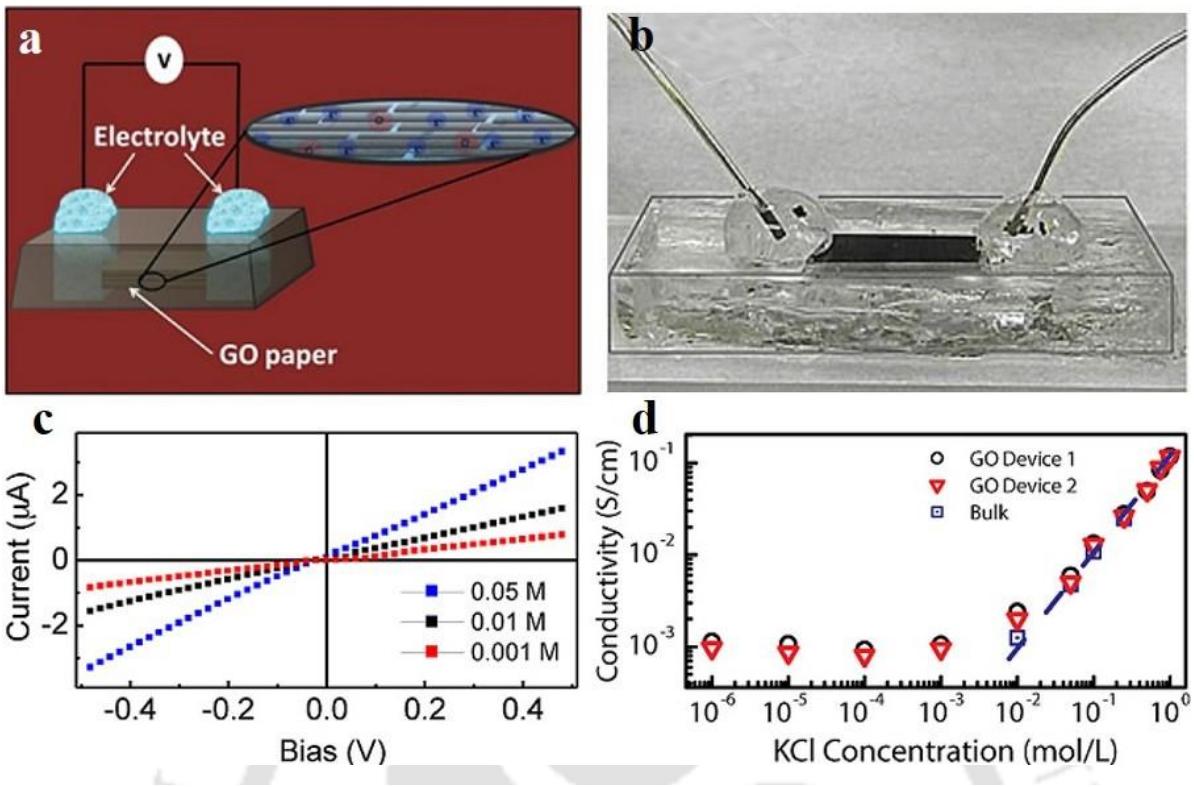

Figure 1.9: *In-plane water diffusion through lamellar GOM: (a) Schematic depiction and (b) picture of the nanofluidic device of GO membrane. (c) I-V curves recorded at different KCl electrolyte concentrations and (d) plot of ionic conductivity vs KCl electrolyte concentration through the nanofluidic channels of GO. (Image copied from J. Am. Chem. Soc., 2012,* ***134****, 16528-16531.)*

Self-assembled clay-based 2D nanofluidic channels with surface charged-governed proton conductivity were reported by Shao et al.[237] They have employed 2D proton channels made by stacking sheets of vermiculite that has been exfoliated again Figure 1.10). These 2D channels' proton conductivity is stable throughout orders of magnitude variations in reservoir concentration and is greater than that of acid solution at concentrations up to 0.1 M. It was discovered that proton transport happens via a Grotthuss mechanism, with a mobility of 1.2 × 10-3 cm^2 V^{-1} s^{-1} and an activation energy of 0.19 eV, respectively. It was shown that even after annealing at 500 °C in air, vermiculite nanochannels exhibited remarkable thermal stability while retaining their proton conduction functions.

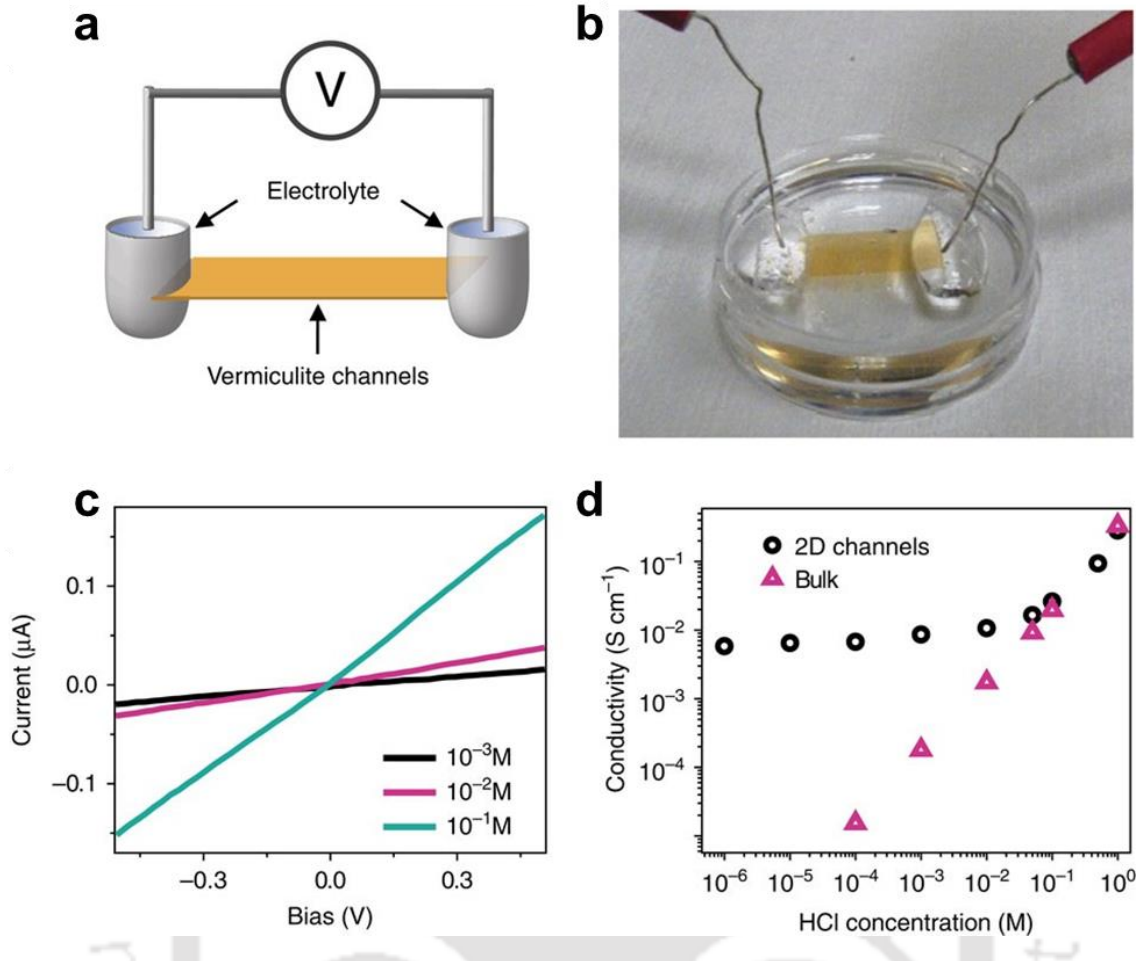

Figure 1.10: *Proton transport across vermiculite channels controlled by surface charge. (a) The vermiculite nanofluidic device schematic depiction; (b) a picture of the device. (c) Illustrative I–V curves via the two-dimensional channels. (d) The relationship between ionic conductivity and electrolyte concentration. The defining feature of surface charge-governed transport is the departure from bulk solution at low proton concentration. (Images copied from Nat. Commun., 2015, **6**, 1–7.)*

Geim and co-workers reported an ultra-thin graphene oxide membrane (GOM) that is super-permeable toward water and water vapour but impermeable to all gases and liquids despite only being a few atoms thick.[259] Water moves vertically via the GOM's 2D nano-capillaries (as can be seen in Figure 1.11b). These two-dimensional layered materials can be used in membrane separation and filtration processes owing to this vertical water transit method. Many 2D layered materials, such as hexagonal boron nitride (hBN), clay minerals, transition metal dichalcogenide (TMDC), transition metal oxides (TMO), MXene, etc., have been revealed to

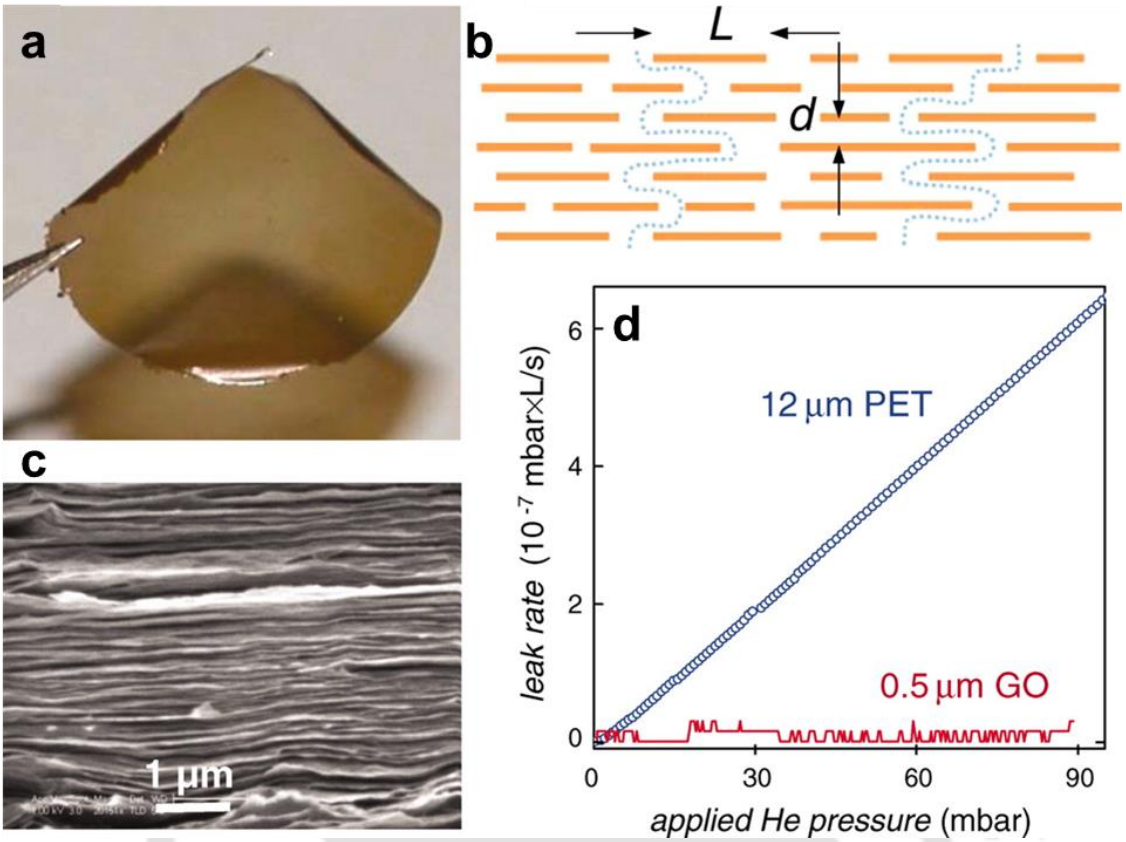

Figure 1.11: *Cross-plane water diffusion via lamellar GOM: (a) Digital picture of a GO membrane. (b) Cross-sectional FESEM image reveals the arrangement of individual sheets in the reassembled GO membrane. (c) Schematic design of the 2D capillaries in GO membrane demonstrating the cross-plane water permeability through the defeats. (d) Helium permeability through GO membrane and a reference polyethylene terephthalate (PET) film. (Image copied from Science, 2012,* ***335****, 442–444.)*

be useful building blocks to create nanochannels, drawing inspiration from the groundbreaking work of Huang et al. and Geim et al.[253,254,260]

Gogoi et al. created a flexible, freestanding membrane constructed of vanadium pentoxide (V_2O_5) that exhibits ionic transport characteristics dependent on its shape.[261] They showed that rectangularly cut V_2O_5 membranes yield linear current-voltage (I-V) curves, but triangular V_2O_5 membranes display nonlinear, diode-like I-V curves within the surface-charge-governed region. The rectification ratio of the 2D asymmetric V_2O_5 membranes can be accurately regulated by modifying the triangle's base-to-tip ratio. Furthermore, the triangular shape of the

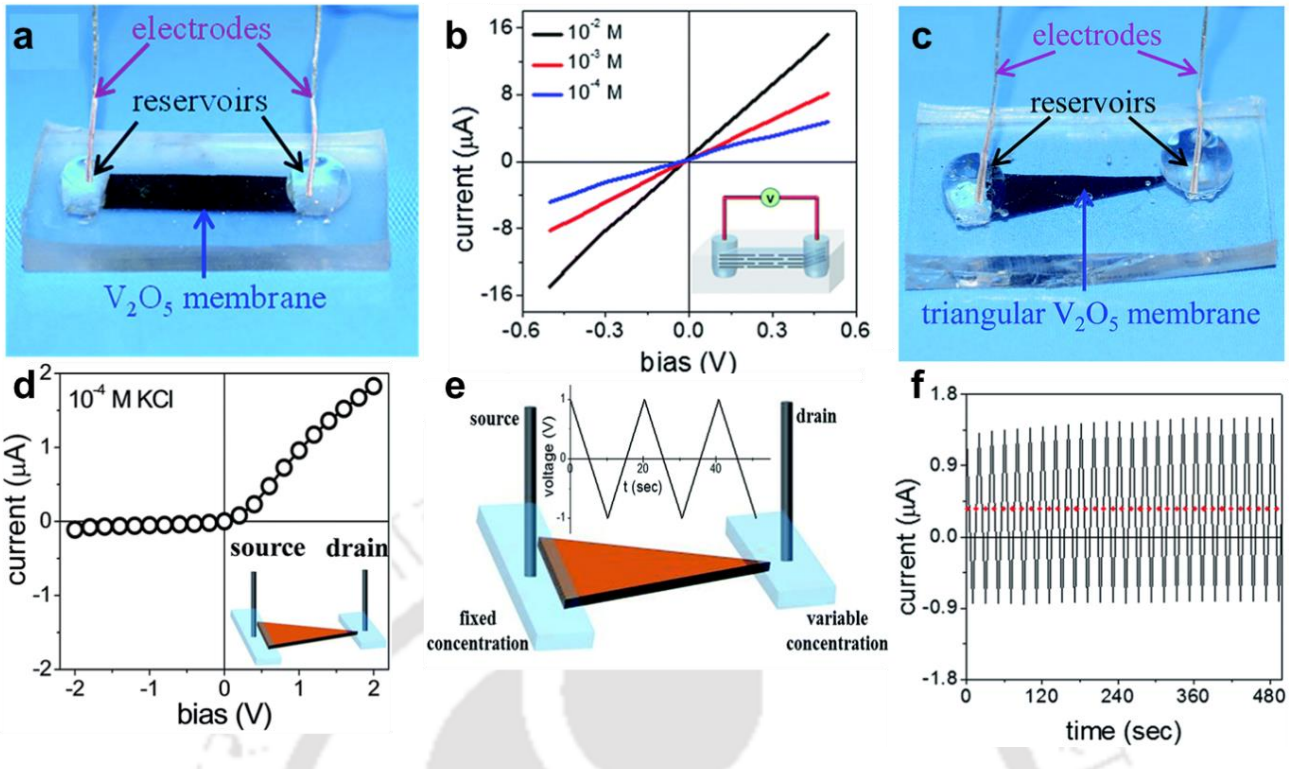

Figure 1.12: *Reconstructed V_2O_5 ionic conduits as a two-dimensional cation pump: (a) A digital image of a rectangular nanofluidic conduit made of V_2O_5. I-V curves captured via the rectangular V_2O_5 membrane are displayed in (b). (c) Digital image of a nanofluidic conduit based on a triangle V_2O_5 membrane. (d) IV curves obtained at 10^{-4} M KCl electrolyte concentration via the triangular V_2O_5 conduit. (e) The triangular nanofluidic ion pump is represented schematically and functions in a fluctuating electric field with a mean value of zero. (f) A plot of current through a V_2O_5 triangle strip recorded under a varying electric field with a mean value of zero (between +1 V and -1 V) displays as a function of time. (Images copied from J. Mater. Chem. , 2019, **7**, 10552–10560.)*

V_2O_5 membrane can work as an ion rectifier and can also act as an ion pump, promoting the uphill transport of ionic species against a concentration gradient when subjected to a fluctuating external potential with a mean value of zero (Figure 1.12).

Molecular separation and water purification: Lamellar membranes provide a viable solution to the worldwide water crisis by facilitating crucial processes like molecular separation and water purification.[240,262–265] Because of their layered structure, lamellar membranes efficiently divide molecules according to their sizes and chemical composition. The recreated lamellar membranes have tunable physicochemical properties and well-defined uniform nanopores, which make them an excellent material for water purification and size-selective molecule

separation. Through the network of interconnecting nanochannels, ions and molecules move through these membranes in a zigzag pattern. By adjusting its thickness, the membrane's flux may be controlled. These nanochannels are appropriate for size-based ion separations because their heights are often similar to the hydration radii of the ions. These membranes make use of nanostructured materials, including layered double hydroxides or graphene oxide, which reject impurities and provide extremely selective routes for water molecules. Lamellar membranes work well in water filtration because of their great selectivity and permeability. They effectively eliminate a variety of contaminants, such as organic compounds, heavy metals, and microorganisms, guaranteeing clean and safe drinking water. These membranes are superior to conventional ones because of their fine control over surface chemistry and pore size. Lamellar membranes are also ecologically benign and energy-efficient. Their durability prolongs their operational lifespan, reducing waste, and their capacity to function at low pressures minimises energy use. Lamellar membranes have the potential to transform molecular separation and water purification processes, advancing global sustainable water management as research into them advances. The creation of 2D membranes, like graphene oxide, g-C_3N_4, and MXene, can greatly aid molecular sieving operations. These newly developed inorganic 2D materials have the potential to produce improved membranes with better solvent permeability, molecular selectivity, and long-term stability than conventional polymer-based membranes. Because of their ability to effectively retain target molecules through small interlayer spacing, GO analogues have been the subject of substantial research in molecular sieving among these 2D materials. On the other hand, GO membrane solvent transfer is comparatively slow. Improving water permeability has been the main focus of current research; however, increasing the interlayer spacing in GO membranes can also enhance the solvent flux rate. Nair et al. conducted liquid phase diffusion studies and observed that thick GO membranes have a sharp cutoff size of nano-channels at around 0.9 nm.[266] Species with a hydrated radius bigger than

roughly 0.45 nm were filtered out, while smaller species such as K^+, Mg^{2+}, and AsO_4^{3-} ions permeated at nearly the same rate, indicating minimal dependency on ion charge (Figure 1.13a). These early results revealed that the nano-channels between GO flakes have tremendous promise for highly selective water penetration. This revelation has stimulated substantial study into the usage of GO membranes with a lamellar structure for water filtration. Membranes compatible with polymer filters and exhibit remarkable resilience in aquatic conditions were created by Mengmeng et al. using layered MoS_2 platelets.[267] These lamellar MoS_2 membranes are gas-tight and allow unhindered water vapour penetration, just as graphene oxide membranes. The bulk-to-2D dimensional transition energy penalty is probably why the lamellar MoS_2 membrane also demonstrated diffusion selectivity for aqueous ions and molecular sieving capabilities for organic vapour.

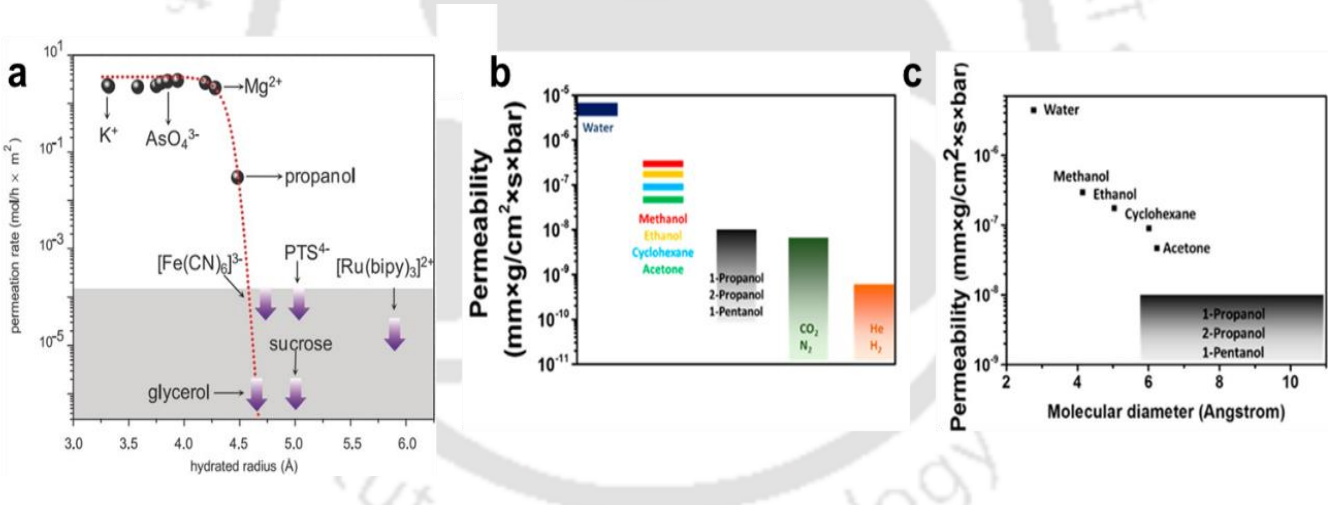

Figure 1.13: *(a) Size selective permeability of ions and molecules across lamellar GO membrane. (b) Permeability of various gases and vapors through the layered MoS2 membrane (with gradient ramps indicating the predicted permeability). (c) Dependence of the permeability on the molecule size. (Images copied from (a) Science (1979), 2014,* ***343****, 752–754 and (b)-(c) Nano Lett., 2017,* ***17****, 2342–2348.)*

Energy conversion and harvesting: 2D lamellar membranes show a lot of potential for energy harvesting methods that are safe for the environment.[268–271] For instance, streaming potential has been harvested by taking advantage of the electrokinetic transport of ions across the

lamellar membrane nanochannels. At the interface between liquid and solid surfaces, an electrical double layer (EDL) forms when an electrolyte and a solid surface come into contact. Selective transit of counterions through the nanochannels occurs when the EDL of two opposing sides overlaps, repelling co-ions and attracting counterions. Consequently, as Quincke et al. (1859) discovered, the pressure-driven liquid flow through a porous plug or nanochannels produces a streaming current along the flow direction.[272,273] A corresponding streaming potential, which increases with growing flow velocity and falls with increasing electrolyte concentration, accompanied the streaming current. Since then, a plethora of nanofluidic systems have been employed for electrical energy harvesting from the pressure-driven liquid flow. The potential of lamellar graphene hydrogel membranes (GHM), clay, and boron nitride membranes in energy harvesting applications has been demonstrated by their use as 2D nanofluidic generators that translate hydraulic motion into streaming ionic current.

Aligned multi-walled carbon nanotube sheets were used to fabricate a flexible fluidic nanogenerator (FFNG).[274] An EDL forms at the interface between the fluid and the carbon surface due to the carbon nanotubes' negative zeta potential. The deposited cations create a stern layer, and electrons are taken from the CNT to balance the net charge of the Stern layer. When 0.6 M NaCl solution was passed over the FFNG, a voltage of about 121 mV was obtained; this voltage was then augmented to 151 mV by applying a larger NaCl solution (4 M). A greater potential was produced by lengthening the contact between the FFNG and the solution because of the increased imbalanced charge at the front half (Figure 1.14).

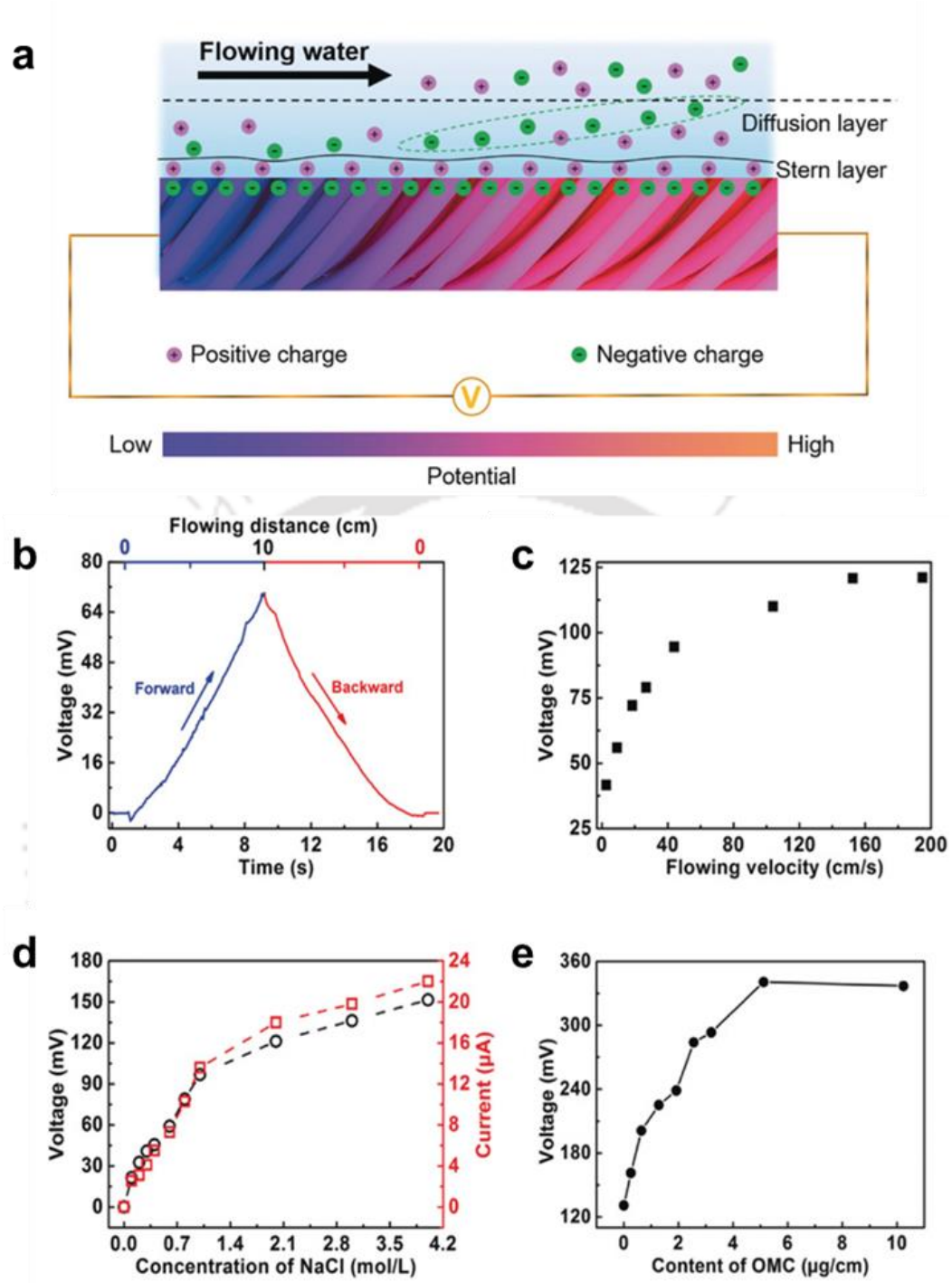

Figure 1.14: *(a) A schematic representation of the system that demonstrates how potential is generated as liquid flows through the FFNG. (b) The output voltage of a saturated NaCl solution in a reciprocating flow at 1.2 cm s−1.(c) Voltage output in relation to flow (A 0.6 M NaCl solution is permitted to circulate.) (d) The relationship between output voltage and current and NaCl concentration.(f) The voltage produced by repeatedly immersing FFNG integrated with ordered mesoporous carbon (OMC) into a NaCl solution. (Images copied from Angew. Chem. Int. Ed., 2017,* ***56****, 12940–12945.)*

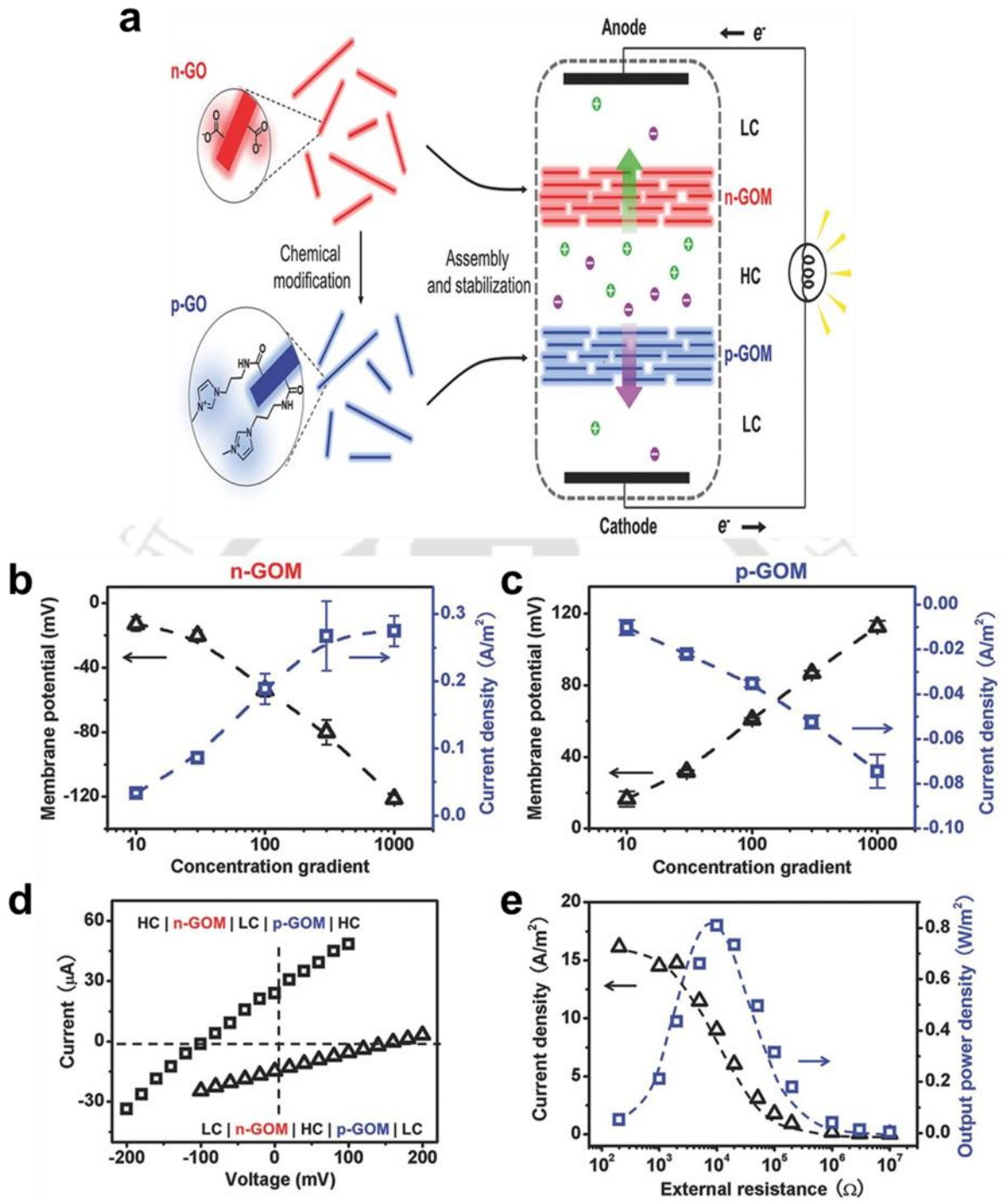

Figure 1.15: *(a) A schematic representation of the ion transport mechanism and the experimental setup. When selectively diffusing counter ionic species are present, the transmembrane potential and measured current density are produced (b) for negatively charged GOM and (c) for positively charged GOM. (d) The single-unit nanofluidic reverse electrodialysis device's current-voltage responses. (e) A pair of complementary charge-selective GOMs were combined to obtain the desired power density. (Images copied from Adv. Funct. Mater., 2017,* ***27****, 1603623.)*

Another electrokinetic phenomenon that is used to extract electrical energy is reverse electrodialysis. This procedure involved the fabrication of devices with several electrolyte solution chambers, each separated by semipermeable membranes that regulate the electrolyte concentration of the solutions. Ions with certain charges are spontaneously driven over the perm-selective membrane by the gradient of the chemical potential that forms at the interface between the two liquids, producing a net flux of selective ions. Membranes that possess superior nanofluidic ionic conductivity and ion-selectivity are the most promising options for producing osmotic power. Ji et al. have created a 2D nanofluidic reverse electrodialysis device using a cascading pair of oppositely charged graphene oxide nanochannels.[275] The intrinsic GO surface charge was changed from negative to positive by preassembly alteration. It was shown that both GOM pairs could produce high-performance osmotic energy conversion when used as RED units. High trans-membrane potential difference and diffusion flow are the results of significant charge separation caused by complementing ionic diffusion in tandem alternating GOM pairs. This GOM pair can achieve an output power density of almost 0.77 Wm^{-2}, which is approximately 54% greater than that of commercial ion-exchange membranes (Figure 1.15). Kundan et al. fabricated a device that harnesses energy by evaporation, using extremely thin two-dimensional nanofluidic channels in a reconstructed V_2O_5 membrane.[276] This device has an energy density of up to 40 mWm^{-2}. Systematic studies were done to examine the impact of internal device parameters, such as channel diameters, membrane thickness, and electrode separation, as well as external environmental conditions, such as atmospheric temperature and relative humidity, on energy efficiency. Remarkably, any physical harm inflicted against the V_2O_5 apparatus could be rectified by the straightforward act of applying a small amount of water. The evaporation-induced nanogenerators could be joined together to combine the voltage and current generated by each individual device (Figure 1.16).

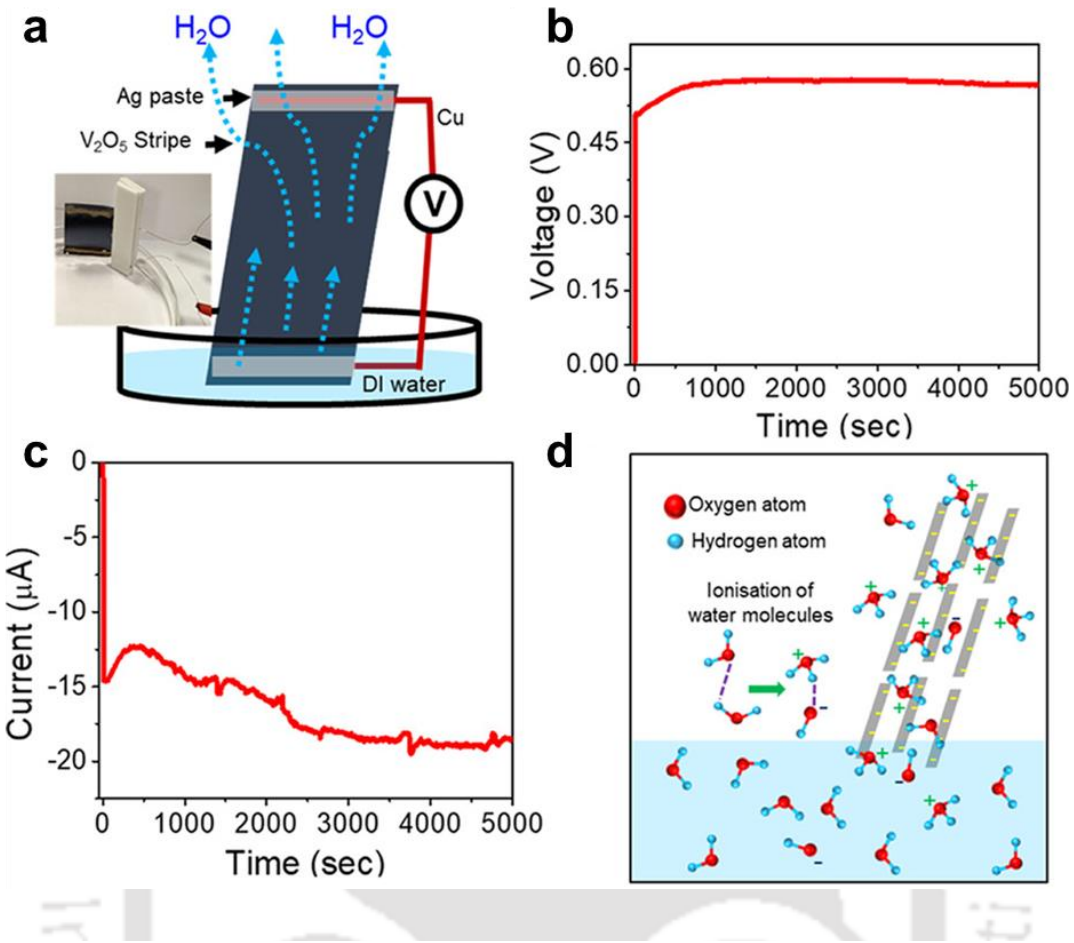

Figure 1.16: *(a) Diagrammatic representation of the experimental setup where the active material's lower end was submerged directly in DI water during the evaporation-induced energy-harvesting process. Evaporation-driven (b) voltage and (c) current produced by use of a 20 mm × 10 mm × 0.035 mm V2O5 strip. The studies are conducted at 25 °C and 65% relative humidity. (d) Schematic representation of the electrokinetic streaming potential production mechanism caused by evaporation. (Images copied from ACS Appl. Energy Mater., 2021,* ***4****, 8410–8420.)*

For hundreds of years, water the medium of life has also functioned as a reliable energy source. Nevertheless, most water-based energy harvesting methods rely on either quick evaporation of molecules or rapid flow. He et al. have devised a carbon:water system that produces electricity from quiescent water by the use of two electrodes that are polarized differently: pure CNT (PCNT) and oxygen modulated CNT (OCNT).[277] The difference in the charge transfer interaction between the water molecules and the electrodes was identified as the cause of the electric current flow. One device produced an output current of up to 6.7 μA and an open-

circuit voltage of 0.28 V in deionized water. Notably, the water source had no effect on the device's functionality. Similar voltage (and current) values were produced by water from other sources, such as rivers, tap water, and reclaimed water, indicating the device's broad applicability in various settings (Figure 1.17).

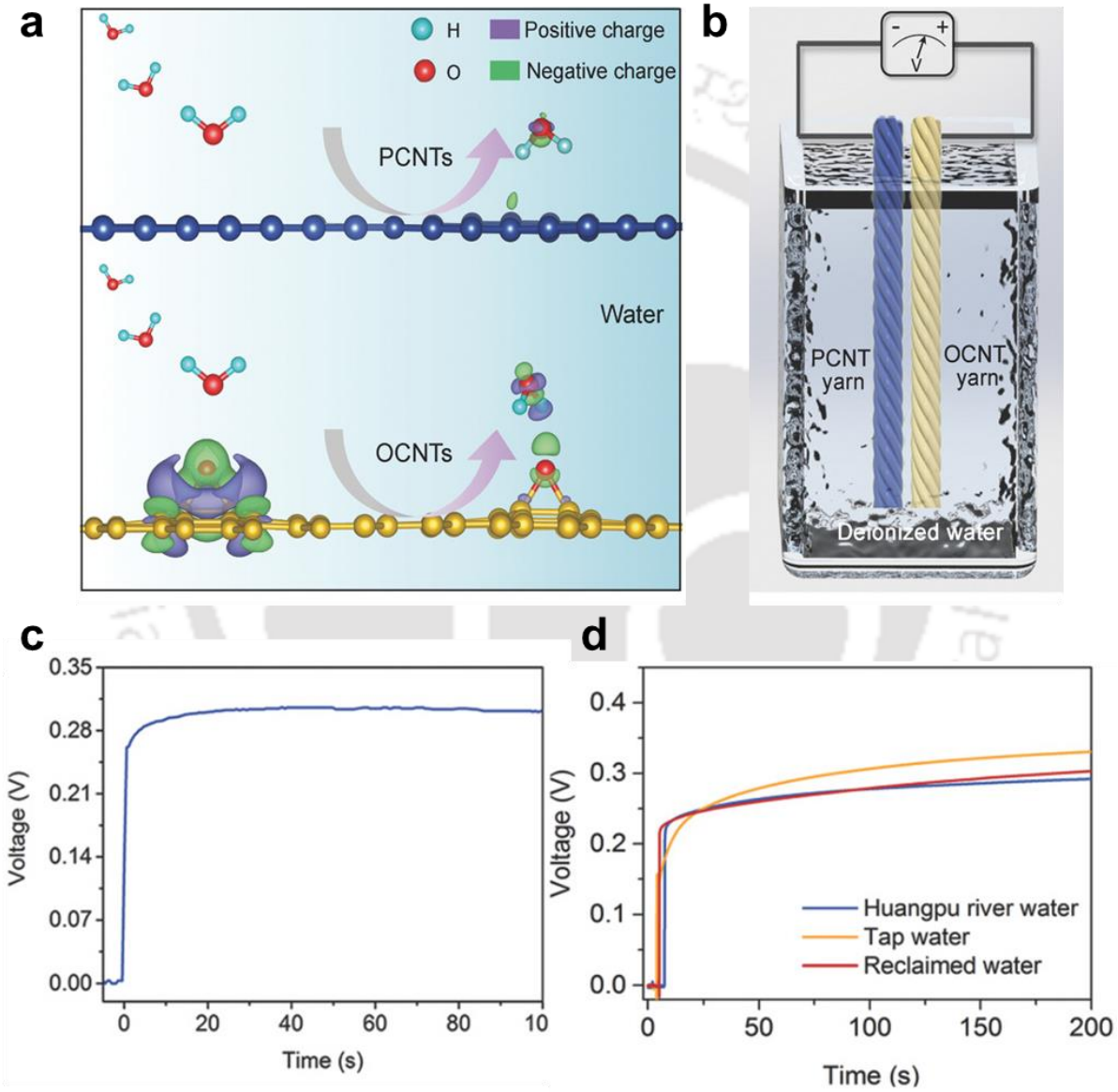

Figure 1.17: *(a) A DFT calculation showing the variation in charge density at the water-PCNT and OCNT contact. (b) A schematic illustration showing the water-carbon device setup for the experiment. (c) The device's output voltage as a function of time after submerging it in deionized water. (d) The carbon:water device's open-circuit voltage in water from various sources. (Images copied from Adv.Mater., 2018,* ***30****, 1707635.)*

Deka et al. extracted energy from calm water resources by taking advantage of the complementing charge transfer activities of reduced graphene oxide (r-GO) flakes doped with boron (B-r-GO) and nitrogen (N-r-GO).[194] The B-r-GO/N-r-GO devices, which generate open-circuit voltages of up to 570 mV when submerged in water, were created by coating individual B-r-GO and N-r-GO samples on cellulose membranes after they were made by heating graphene oxide sheets with boric acid and urea. To facilitate the creation of wearable energy devices, the B-r-GO/N-r-GO samples are also coated on non-specific materials such as denim clothes (Figure 1.18).

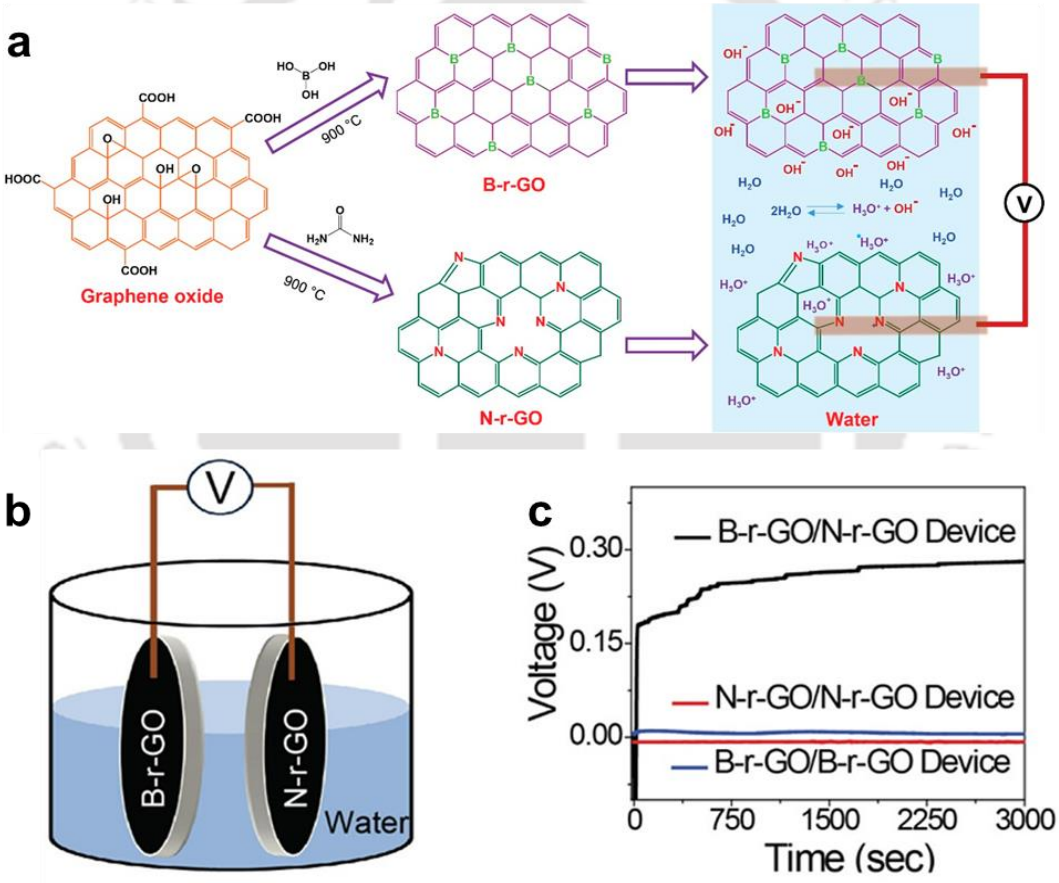

Figure 1.18: *(a) A schematic illustration of the synthesis process and the contrasting interfacial activities of N-r-GO and B-r-GO flakes in water. (b) A schematic of the experimental setup used for energy harvesting from quiescent water. (c) The open-circuit voltage generated when immersing a N-r-GO/N-r-GO device (red curve), a B-r-GO/B-r-GO device (blue curve) and B-r-GO/N-r-GO device (black curve) in still water. (Images copied from ACS Appl. Nano. Mater. 2019, **2**, 7997-8004.)*

Energy storage: Lamellar membranes made mostly of 2D nanomaterials are very advantageous for energy storage applications. These membranes have outstanding mechanical stability and ionic conductivity, which are necessary for effective energy storage devices. 2D nanomaterials, including graphene, Mxene and transition metal dichalcogenides, have a special layered structure that enables fast ion transport and large surface area, improving the efficiency of batteries and supercapacitors. Their resilience and adaptability also enhance the durability and dependability of the equipment. In general, 2D nanomaterial lamellar membranes have a great deal of promise for improving energy storage devices' efficiency, capacity, and robustness.[278,279]

Vildan et al. have effectively produced MXene aerogels featuring highly ordered lamellar structures using unidirectional freeze-casting of aqueous solutions of $Ti_3C_2T_x$ without additives.[280] Pressing or calendering procedures were then used to transform these aerogels into usable supercapacitor electrode sheets (Figure 1.19). The final properties can be precisely tuned owing to the significant control this processing approach offers over densities (ranging over two orders of magnitude), lamellar spacing (which provides electrolyte-accessible sites), and film thickness. With a density of 13 mg cm^{-3}, the produced MXene aerogel reaches capacitances of 380 F g^{-1} at 2 mV s^{-1} and 75 F g^{-1} at 50 mV s^{-1}. The MXene aerogel has a

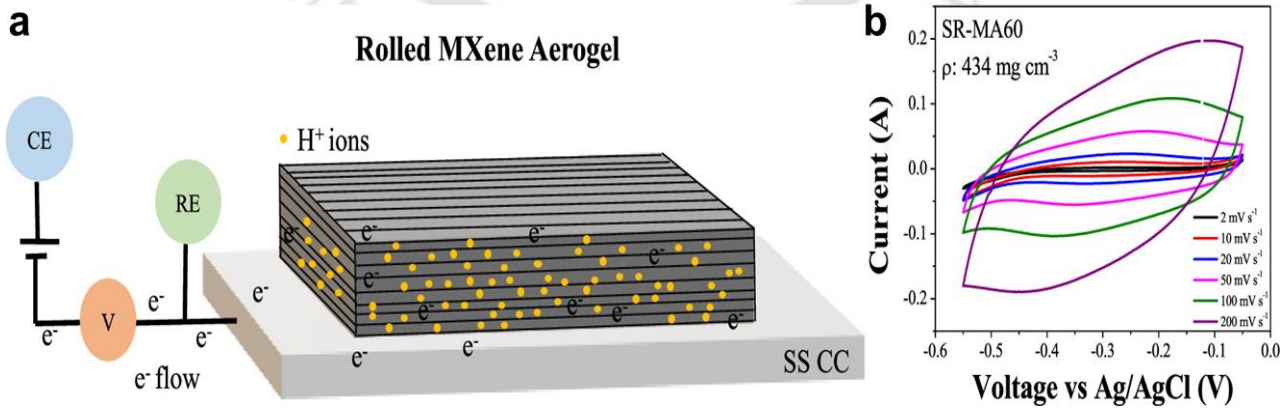

Figure 1.19: *(a) Schematic of the supercapacitor assembly. (b) Electrochemical performance of as-prepared $Ti_3C_2T_x$ aerogels (MA). (Images copied from ACS Appl. Energy Mater., 2020, **3**, 411–422.)*

better rate capability of 309 F g^{-1} at 50 mV s^{-1} when it is calendered into a porous film with a thickness of 60 μm and a density of 434 mg cm^{-3}. Moreover, the volumetric capacitance of the rolled electrodes was 104 times higher as compared to that of the MXene aerogel in its as-prepared state.

Nanoreactor: A fresh approach to regulate the kinetics and result of chemical reactions was made possible by the small gaps that existed between the 2D nanosheets of the lamellar membranes. Actually, the best platform for examining the true impact of nano-confinement in chemical reactions is the 2D nanoreactor. Because 2D materials are easily stacked into membranes and re-exfoliated into 2D sheets, the reactions' outcomes can be easily compared under comparable chemical environments with and without confinement. Saha et al. showed off the potential for researching catalytic reaction kinetics in the small interlayer gaps seen in lamellar membranes.[281] Palladium and gold nanoparticles integrated into restacked vermiculite membranes were utilized as nano-reactors for the catalytic reduction of nitro-arene compounds. These membranes demonstrated a notable increase in the catalytic reaction efficiencies and a decrease in the amount of reducing agent needed for the reaction (Figure 1.20).

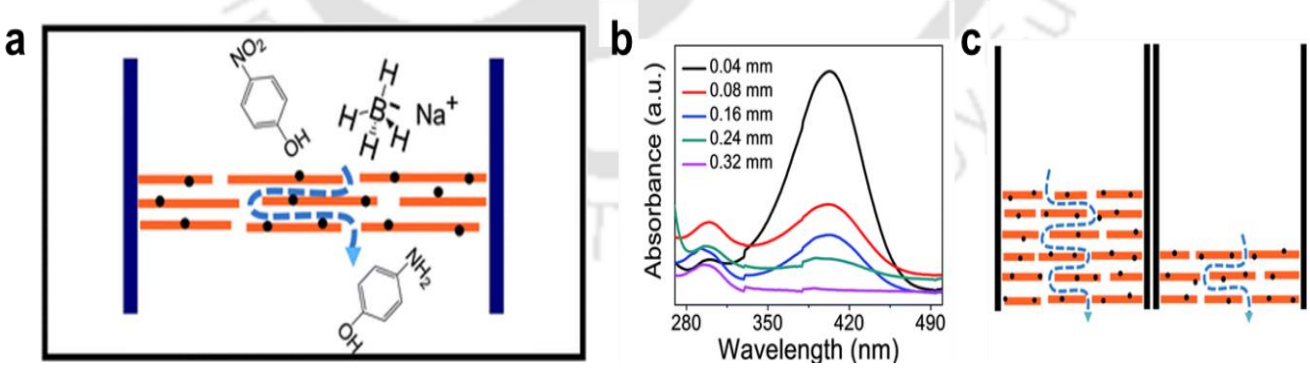

Figure 1.20: *(a) Schematic illustration of a nano-reactor with Pd nanoparticles integrated within a lamellar vermiculite membrane.The UV-Vis spectra in (b) demonstrate the reduction of 4-NP to 4-AP within the catalytic nanochannels of Pd-VM membranes with varying thicknesses. (c) A schematic depiction of the relationship between membrane thickness and catalytic channel length.(Images copied from J. Mater. Chem. A, 2018, **6**, 22931–22939.)*

Smart materials: Bilayer membranes are produced by depositing 2D nanosheets over the membranes of other nanomaterials, such as carbon nanotubes, owing to the ease with which reconstructed lamellar membranes can be made. These bilayer membranes' distinct qualities allow them to interact with their surroundings in a non-parallel way, making them potentially

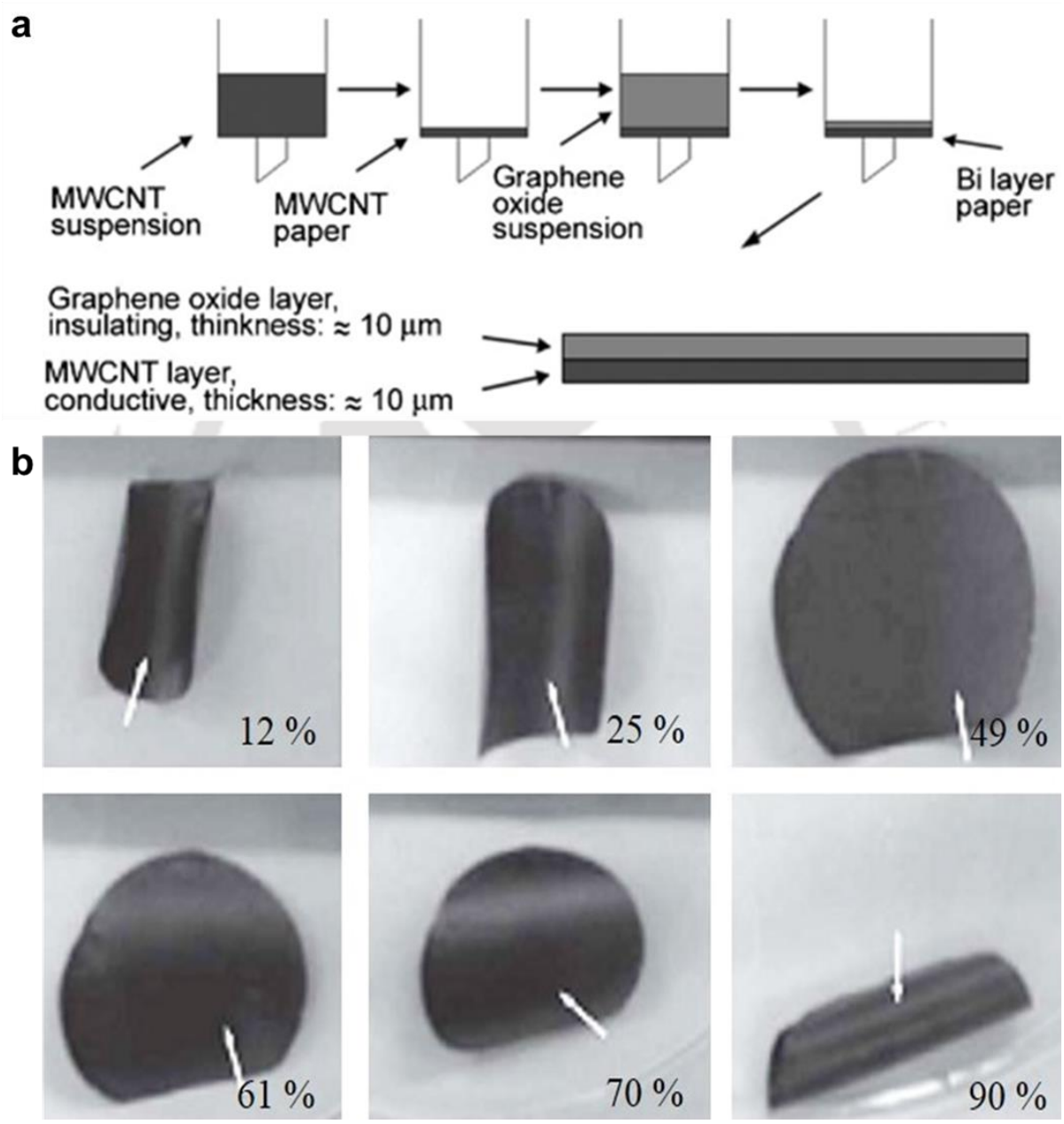

Figure 1.21: *(a) A schematic representation of the fabrication process of the bilayer actuator using graphene oxide and multi-walled carbon nanotubes. (b) An electronic image of a bilayer film. (c) The bilayer membrane's shape-changing caused by moisture. The graphene oxide layer's surface is shown by a white arrow. (Image copied from Small, 2010,* ***6****, 210–212.)*

useful as smart materials. These materials are intelligent enough to sense changes in their surrounding conditions, such as light, temperature, humidity, pH, gasses, and voltage, and they may respond to these changes by modifying certain physical characteristics, such as size, shape, color, and current.[185,198,200,201,282,283] Park et al. fabricated a hydration-induced actuating bilayer membrane based on GO and multi-walled carbon nanotubes (MWCNTs) by sequentially filtering each material's water-based dispersion.[284] Schematic of the fabrication process is shown in Figure 1.21a. This bilayer membrane changes shape in a predetermined order in response to variations in humidity. It curves toward the GO side at low RH (12%), opens up as RH increases, and becomes flat at RH 55% to 60%. As the humidity is increased

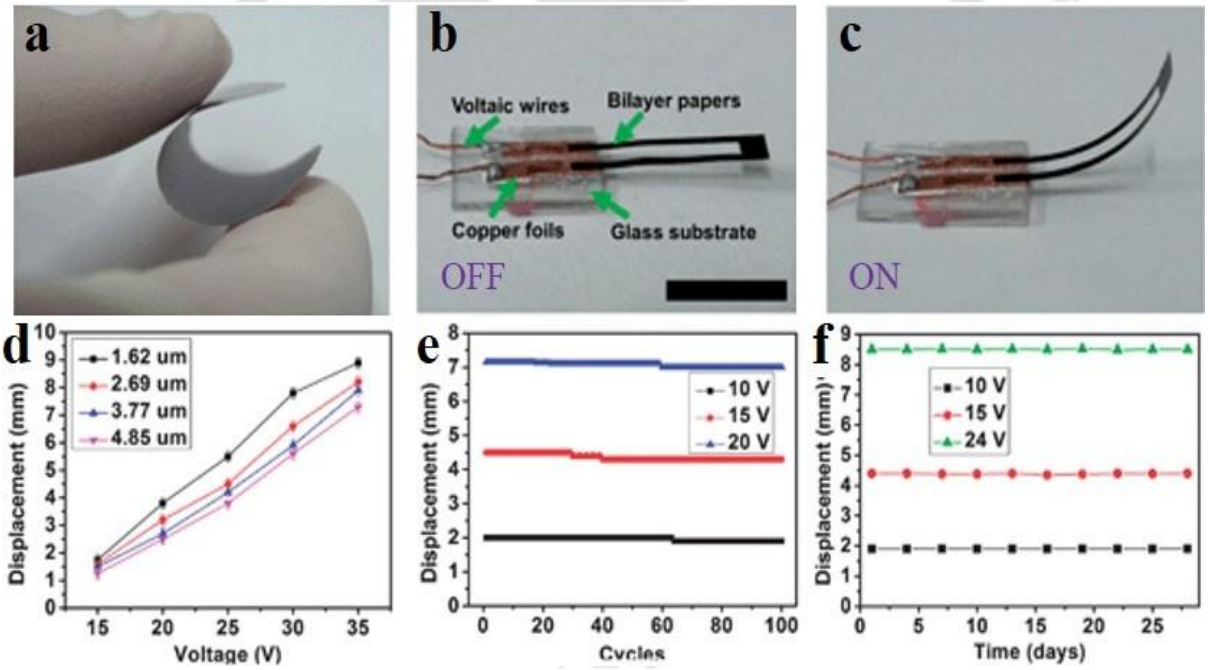

Figure 1.22: *(a) Digital image of a bilayer membrane made by vacuum filtering graphene dispersion and then graphene oxide dispersion in turn. Digital image showing the bilayer actuator when it is connected to a voltage source in (b) the off and (c) the on states. The actuator bent toward the GO side when voltage was applied, or in the ON mode, and it remained in that position when the voltage was removed. (d) Evaluation of bilayer membranes with different GO thicknesses in terms of bending (displacement) versus applied voltage. The actuators' displacement stability as a function of (e) number of cycles repeated and (f) number of days. (Images copied from Nanoscale, 2013,* ***5****, 9123–9128.)*

further, the paper begins to curl in the way of the MWCNT, reaching its full curl at RH 85% (Figure 1.21b).

An electrothermal bilayer actuator based on graphene and graphene oxide (GO) has been created by Bi et al.[285] Graphene and graphene oxide (GO) have different thermal expansion properties, while having comparable layered structures and Young's modulus values. When current flows through the electrically conducting graphene layers, heat is produced that is sufficient to heat the bilayer actuator's insulating GO layers. The bilayer actuator on current treatment is activated as a resu lt of this rise in local temperature (Figure 1.22).

One of the rising field of research is the photomechanical effect, where light energy is direct turned into mechanical energy. Zhang et. al. has demonstrated a photo actuator by accumulating single-walled carbon nanotubes (SWNTs) on the suraface of a polymeric filter paper (polycarbonate, PC membrane), which transforms light to mechanic energy and may be utilized as oscillators and motors.[286] The quick response of the PC/SWNTs is ascribed to the

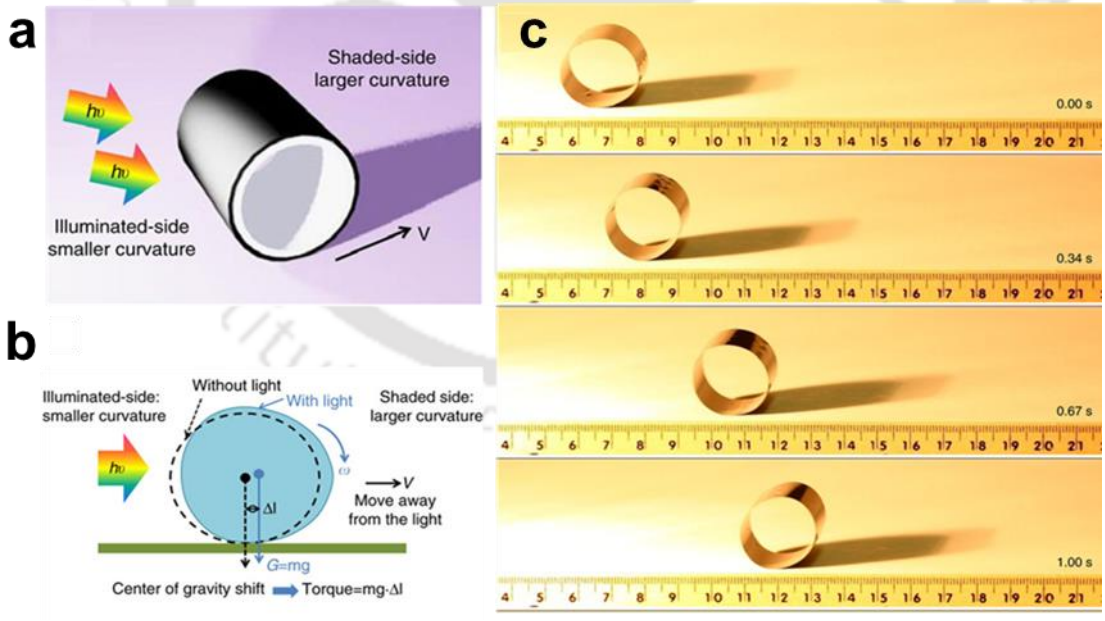

Figure 1.23: *A fast forward-moving motor driven by light. (a) Schematic depicting the functioning scheme of the motor under light. (b) Schematic depicting the displacement in the center of gravity of the motor due to the directional light exposure. The resulting torque moves the motor away from the light source. (c) Optical picture series as a function of time displaying a forward-moving motor operated by a halogen lamp. (Images copied from Nat. Commun. 2014, **5**, 1-8).*

low heat capacity, strong thermal conductivity and the outstanding near-infrared light absorption of the SWNT thin layer. Non-uniform illumination on the motor (made by connecting PC/SWNT film together into a cylinder) from an angled light source causes the curvature to decrease on the light-facing side, i.e., the area that gets more illumination has the propensity to be flattened, seen in Figure 1.23. This produces a change to the center of mass of the motor, consequently resulting in a torque that pulls the motor away from the light source.

A flexible bilayer actuator with a high temperature was created by Wang et al. using thermally stable materials like boron nitrite (BN) and carbon nanotubes (CNT).[287] This bilayer actuator can function up to 2000 K in an inert atmosphere with a response time of 100 ms. It is made by sequentially filtering CNT and BN dispersions (Figure 1.24). It is stable after 10,000 cycles with very little deviation. When selective Joule heating (current application) is applied to these thermally stable materials with varying thermal-expansion coefficients, the thin-film actuator

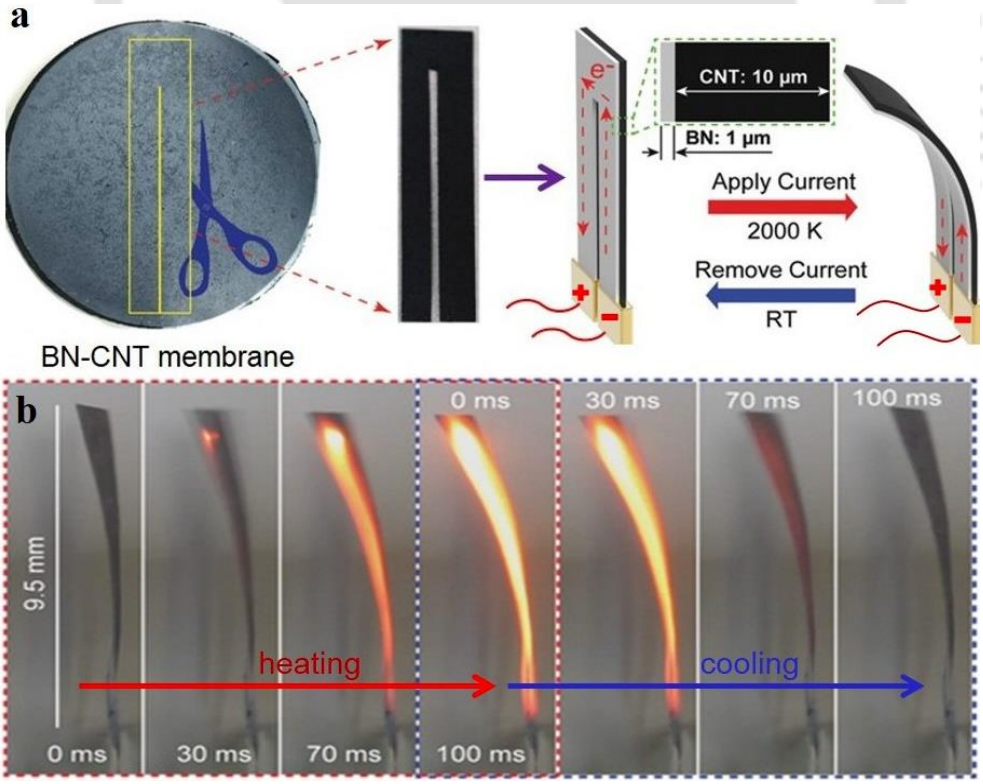

Figure 1.24: *High temperature carbon nanotube-boron nitrite (CNT-BN) bilayer actuator: (a) A schematic depicting the CNT-BN bilayer actuator. (b) Screenshots demonstrating how the actuator responded to the heating and cooling procedures. (Images coped from Adv. Mater., 2016,* ***28****, 8618–8624.)*

reversibly moves toward the BN side. A significant effective differential in thermal expansion occurs in the bilayers as a consequence of the selective heating triggered by the electrically conducting CNT and the insulating BN. Furthermore, the CNT layer does not heat up BN nanosheet films, which has low thermal conductivity. This further widens the thermal expansion gap between the CNT and BN layers, allowing the actuator to react to heat faster.

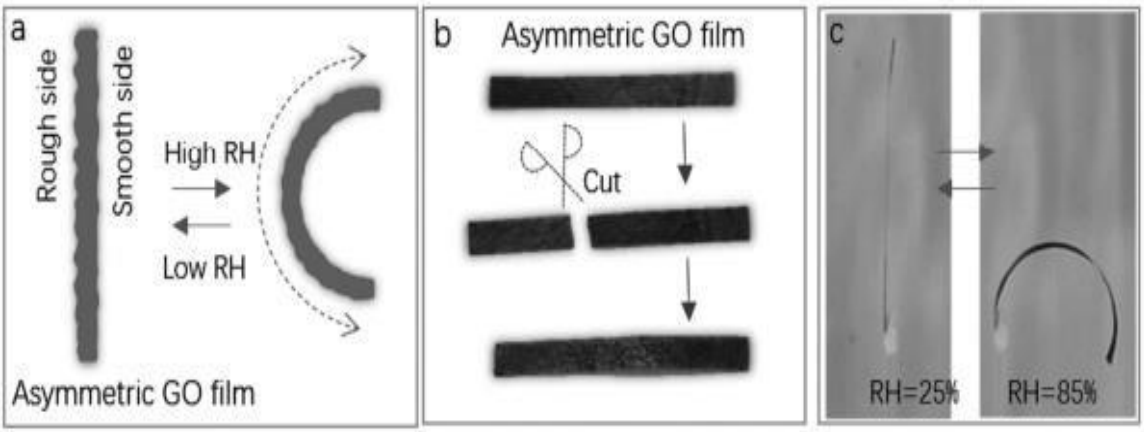

***Figure 1.25**: (a) GO film schematic with uneven surface roughness. (b) Before and after photos of the a-GO film during the healing process. (c) A picture showing how the healed a-GO film reacted to the change in humidity. (Images copied from Adv. Funct. Mater., 2017, **27**, 1703096.)*

Because of the rising temperature, the actuation (measured in displacement) increases as the applied current increases.

Huhu et al. have shown that functional graphene oxide (GO) structures may mend themselves when exposed to moisture.[288] By merely misting a tiny quantity of water into the fissures of fractured GO structures, such as 3D foams, 2D films, and 1D fibers, they were able to initiate the healing process (Figure 1.25). These GO structures can retain their unique functionality while regaining their remarkable mechanical properties. After breaking and healing, the capacity to revert to its previous shape in response to external stimuli, such as twisting and bending, can be regained.

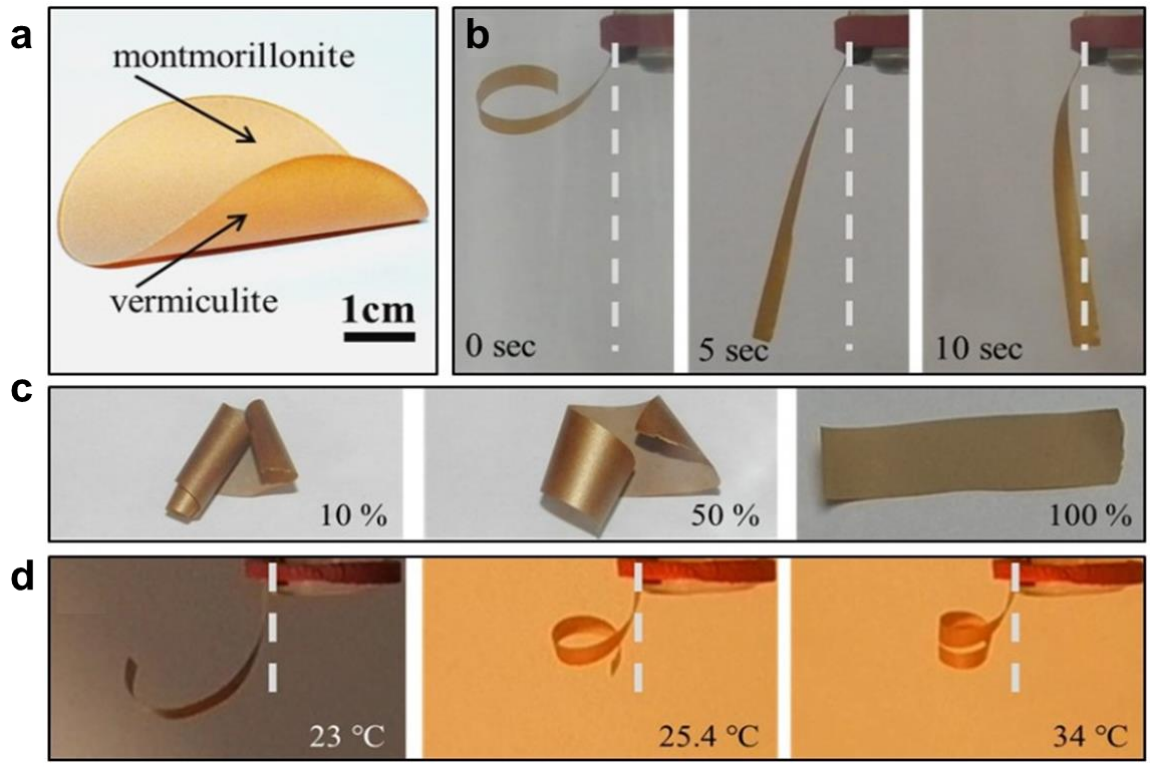

Figure 1.26: *(a) Digital photo of a CCBM. Snapshots showing the shape transformation of CCBM strips induced by (b) methanol vapours, (c) humidity and (d) temperature. (Images copied from Adv. Mater., 2017,* ***29****, 1701164.)*

By rearranging layers of naturally occurring clay minerals, Gogoi et al. demonstrated the creation of a highly sensitive multiresponsive clay-clay bilayer membrane (CCBM).[198] It was discovered that the CCBM morphed in a particular way in response to minuscule changes in the environment, such as temperature, humidity, and the presence of solvents. Additionally, the CCBM showed remarkable resilience; it was unaffected by exposure to corrosive chemical vapours, heating to 500 °C, cooling in liquid N_2, or any other extreme condition. The primary mechanism behind the CCBM's shape modification was ascribed to the components' uneven reactions to outside stimuli (Figure 1.26).

Han et al. used UV light to unilaterally reduce the lamellar GO membrane in order to create a moisture-responsive smart material.[289] As the surrounding relative humidity (RH%) rises, the bilayer GO-rGO bilayer membrane changes shape towards the rGO side (Figure 1.27a). It was

discovered that the degree of GO membrane decrease affected how much the membrane bent. Furthermore, artificial tendrils that curl into helical structures at high atmospheric humidity

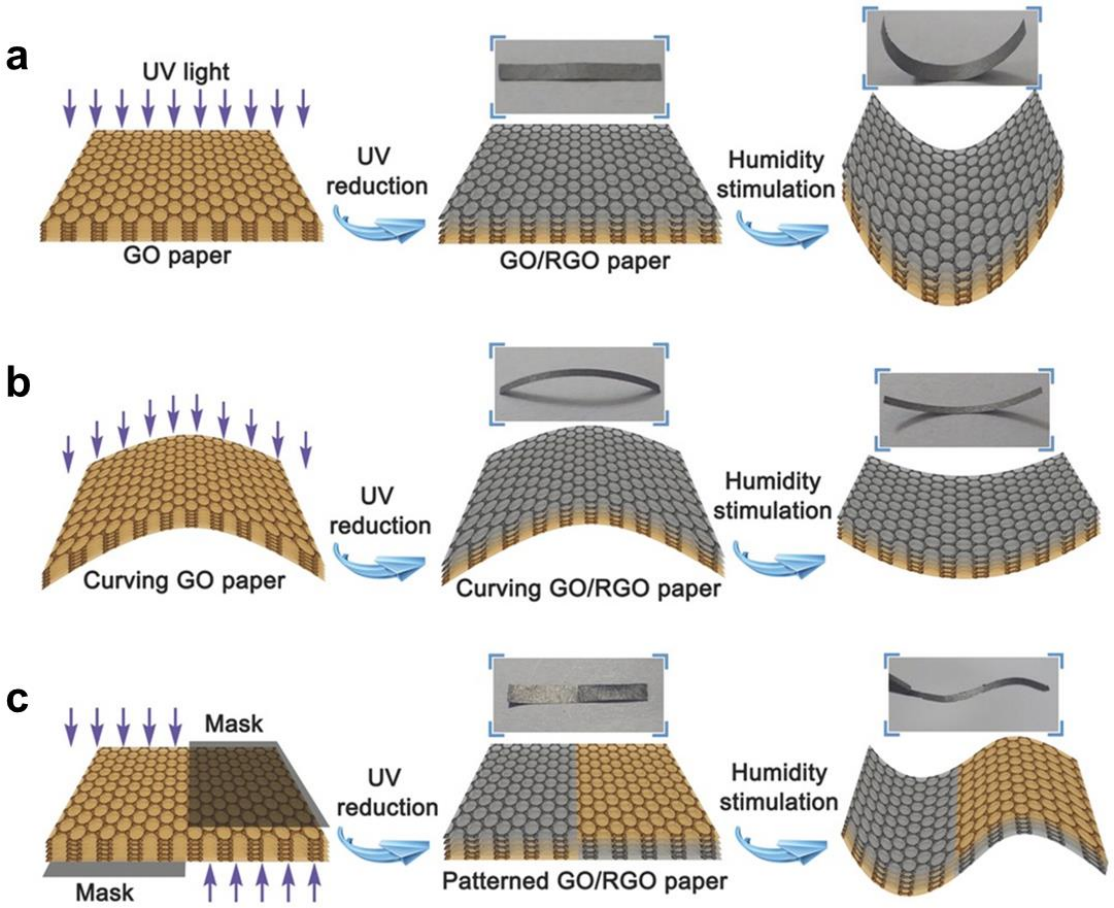

Figure 1.27: *Diagrammatic representation of the GO/RGO bilayer actuator design principle, showing the a) flat, b) curved, and c) patterned GO/RGO papers, as well as their predictable responses to humidity in the surrounding air. Digital images of GO/RGO bilayer ribbons in both wet and dry environments are included as insets. (Images copied from Adv. Funct. Mater., 2015,* ***25****, 4548–4557.)*

levels are created through programmed reduction of the GO membrane (shown in Figure 1.27c).

The majority of smart materials created by reassembling layered materials only show responsiveness in an atmosphere of air, not in a liquid. Asymmetrically modified graphene film-based actuators[290] and graphene oxide/vermiculite bilayer membranes[200] are exceptional examples (Figure 1.28). Surface-modified graphene film strips exhibit a reversible swing motion when scanned using a cyclic voltammogram (CV) in an electrolyte containing 1 M

$NaClO_4$.[290] Strips taken from a PPy/graphene bilayer film were similarly shown to have analogous actuation capabilities.[291] Within a solvent media with opposing polarity, the bilayer

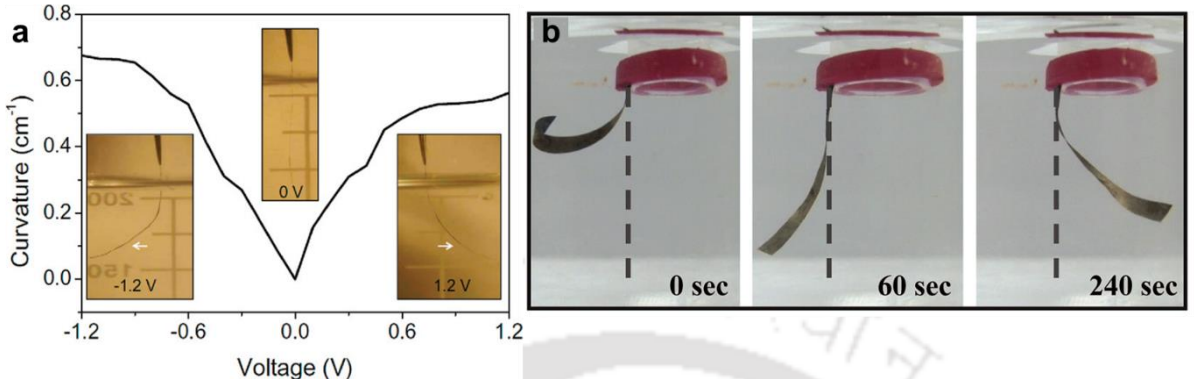

Figure 1.28: *(a) A plot of an asymmetric rGO strip's curvature change versus applied voltage. (b) Snapshots of the bending movements of a bilayer stripe of vermiculite/graphene in methanol. (Images copied from (a) ACS Nano, 2010, **4**, 6050–6054 and (b) J. Mater. Chem. A, 2017, **5**, 3523–3533.)*

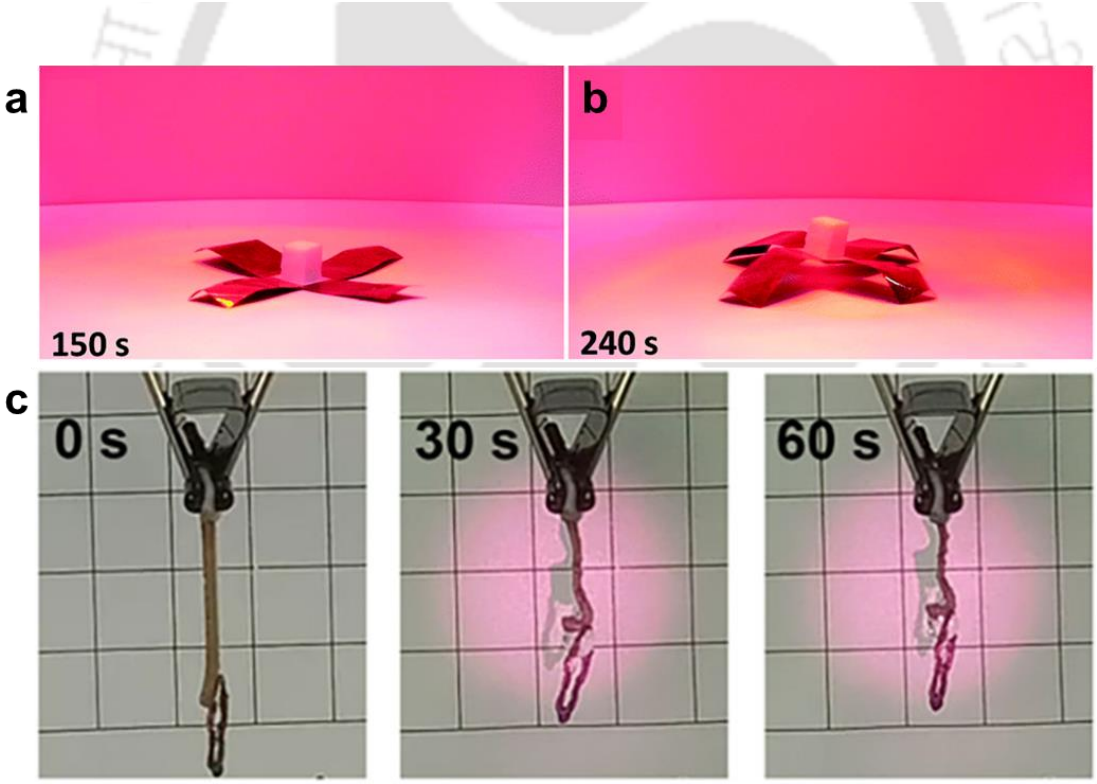

Figure 1.29: *(a) The optical photograph depicts the GO/BOPP intelligent robot reacting to near-infrared light. (b) Optical photograph depicting the weightlifting function of the intelligent robot in response to near-infrared light. (c) The actuation movement of the NIR-driven gradient PNIPAm/GO hydrogel under load after 60 seconds of irradiation. (Images copied from (a) Nanoscale, 2017, **9**, 9825–9833 and (b) ACS Appl. Mater. Interfaces, 2018, **10**, 7688–7692.)*

membranes composed of vermiculite and graphene oxide also demonstrated a reversible bending behavior.[200]

A lot of research has been done to develop new strategies for the accurate control of materials using remote stimuli like heat, light, solvent vapor, or electricity. Materials that respond to stimulation seem like the best options for creating remote handling devices. The amount of research on materials that respond to stimuli has increased dramatically in recent years. For example, a GO fiber moisture-triggered actuator has the ability to move through small openings like a "hook."[292] Furthermore, GO/BOPP[293] and PNIPAm/GO[294] hydrogel-based intelligent robots are capable of lifting and moving loads several times higher as compared to their own body weight (Figure 1.29). Other actuation systems that have lately been created are likewise able to repeatedly grab, release, and move items. Scholars are currently investigating new approaches and utilizing various energy types, including light, heat, and electricity, to enable the remote manipulation of materials.

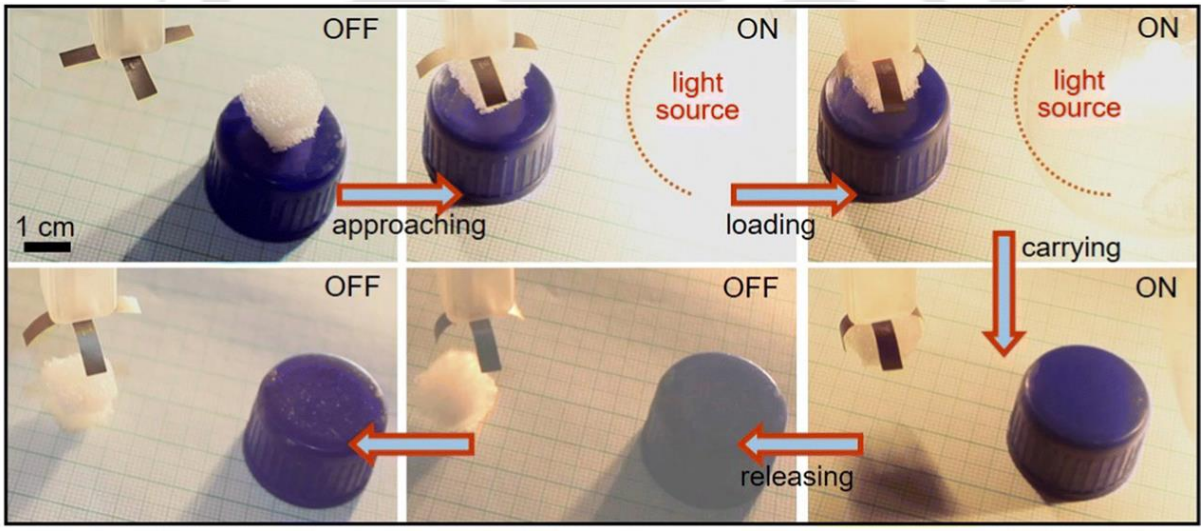

Figure 1.30: *Photos showing the white light (1000 W, 50000 lux.) induced translocation of an object by the V_2O_5-vermiculite bilayer actuator. (Images copied from Mater. Adv., 2023,* ***4****, 3619–3627.) (Images copied from Adv. Funct. Mater., 2015,* ***25****, 4548–4557.)*

Saikia et al. reported a material that responds to light and vapor made by sequentially assembling exfoliated 2D sheets of V_2O_5 and vermiculite.[201] When exposed to light, this bilayer

membrane made of vermiculite and V_2O_5 displayed amazing shape-morphing abilities. This bilayer membrane's ability to flex in response to light makes it useful for translocating objects from one place to another as shown in the snapshots in Figure 1.30.

1.5 Conclusion

In summary, atomically thin 2D nanosheet research has made great strides in the last decade. Because of their nano-dimensions, these nanosheets show distinctive features that open up new possibilities for the development of novel self-assemblies. Reconstructed lamellar membranes from 2D nanosheets exhibit unique properties like size-selective ionic and molecular transportation, ionic current rectification, and environmental responsiveness, which are not present in their bulk or isolated forms. These special qualities makes the lamellar membranes of layered materials as attractive candidate for a wide range of applications.

Even with all of the work that has gone into developing and understanding these membranes, thorough studies by scholars from a variety of fields are necessary to fully realize their potential in real-world applications. Subsequent investigations should prioritize enhancing the stability and scalability of these membranes, refining their operational characteristics for specific uses, and exploring their integration into complex systems. Interdisciplinary collaboration is crucial for addressing the complexities of synthesizing, characterizing, and utilizing these advanced materials. Advances in computational modelling and experimental methods combined with creative approaches to nanofabrication will be crucial in revealing new features and uses for 2D nanosheet-based membranes. By utilising the complementary properties of several 2D materials and investigating hybrid systems, we can create groundwork for revolutionary developments in fields like microdroplet handling, sensing, energy harvesting, environmental remediation, biomedical devices, and smart materials. Consequently, 2D nanosheet-based membrane research and development can drive new technologies and applications as well as revolutionize a variety of sectors.

1.6 References

1 F. Jiang, Y. Jiang, H. Zhi, Y. Dong, H. Li, S. Ma, Y. Wang, Q. Dong, H. Shen and Y. Wang, *Stroke. Vasc. Neurol.*, 2017, **2**, 230–243.

2 E. J. Topol, *Nat. Med.*, 2019, **25**, 44–56.

3 S. E. Shladover, *J. Intell. Transp. Syst.*, 2018, **22**, 190–200.

4 G. Bathla, K. Bhadane, R. K. Singh, R. Kumar, R. Aluvalu, R. Krishnamurthi, A. Kumar, R. N. Thakur and S. Basheer, *Mob. Inf. Sys.*, 2022, **2022**, 7632892.

5 P. Yager, T. Edwards, E. Fu, K. Helton, K. Nelson, M. R. Tam and B. H. Weigl, *Nature*, 2006, **442**, 412–418.

6 R. B. Fair, A. Khlystov, T. D. Tailor, V. Ivanov, R. D. Evans, V. Srinivasan, V. K. Pamula, M. G. Pollack, P. B. Griffin and J. Zhou, *IEEE Des. Test Comput.*, 2007, **24**, 10–24.

7 L. A. Dykman and N. G. Khlebtsov, *Acta Naturae*, 2011, **3**, 34.

8 N. L. Rosi and C. A. Mirkin, *Chem. Rev.*, 2005, **105**, 1547–1562.

9 G. Suman, M. Pulikkathara and R. Wilkins, *IEEE Trans. Nanotechnol.*, 2021, **20**, 517–524.

10 M. Zhu, H. Xiao, G. Yan, P. Sun, J. Jiang, Z. Cui, J. Zhao, Z. Zhang and L. M. Peng, *Nat. Electron.*, 2020, **3**, 622–629.

11 S. Verma, B. Sarma, K. Chaturvedi, D. Malvi and A. K. Srivastava, *Compos. Interfaces*, 2023, **30**, 223–251.

12 E. Bekyarova, I. Kalinina, M. E. Itkis, L. Beer, N. Cabrera and R. C. Haddon, *J. Am. Chem. Soc.*, 2007, **129**, 10700–10706.

13 M. F. El-Kady, Y. Shao and R. B. Kaner, *Nat. Rev. Mater.*, 2016, **1**, 1–14.

14 M. D. Stoller, S. Park, Z. Yanwu, J. An and R. S. Ruoff, *Nano Lett.*, 2008, **8**, 3498–3502.

15 P. Goli, S. Legedza, A. Dhar, R. Salgado, J. Renteria and A. A. Balandin, *J. Power Sources*, 2014, **248**, 37–43.

16 A. A. Balandin, *Nat. Mater.*, 2011, **10**, 569–581.

17 J. Schneider, M. Matsuoka, M. Takeuchi, J. Zhang, Y. Horiuchi, M. Anpo and D. W. Bahnemann, *Chem. Rev.*, 2014, **114**, 9919–9986.

18 A. Fujishima, T. N. Rao and D. A. Tryk, *J. Photochem. Photobiol. C: Photochem. Rev.*, 2000, **1**, 1–21.

19 A. B. Theberge, F. Courtois, Y. Schaerli, M. Fischlechner, C. Abell, F. Hollfelder and W. T. S. Huck, *Angew. Chem. Int. Ed.*, 2010, **49**, 5846–5868.

20 D. H. Yoon, J. Ito, T. Sekiguchi and S. Shoji, *Micromachines*, 2013, **4**, 197–205.

21 G. M. Whitesides, *Nature*, 2006, **442**, 368–373.

22 N. Horiuchi, *Nat. Photonics*, 2024, **18**, 111–111.

23 Z. Chen, S. Kheiri, E. W. K. Young and E. Kumacheva, *Langmuir*, 2022, **38**, 6233–6248.

24 S. Fasciano and S. Wang, *SLAS Technol.*, 2024, **29**, 100090.

25 A. G. Niculescu, C. Chircov, A. C. Bîrcă and A. M. Grumezescu, *Int. J. Mol. Sci.*, 2021, **22**, 2011.

26 A. Huebner, S. Sharma, M. Srisa-Art, F. Hollfelder, J. B. Edel and A. J. DeMello, *Lab Chip*, 2008, **8**, 1244–1254.

27 T. M. Squires and S. R. Quake, *Rev. Mod. Phys.*, 2005, **77**, 977–1026.

28 Y. Ding, P. D. Howes and A. J. Demello, *Anal. Chem.*, 2020, **92**, 132–149.

29 E. Brouzes, M. Medkova, N. Savenelli, D. Marran, M. Twardowski, J. B. Hutchison, J. M. Rothberg, D. R. Link, N. Perrimon and M. L. Samuels, *Proc. Natl. Acad. Sci. U.S.A.*, 2009, **106**, 14195–14200.

30 C. Jiu-Sheng and J. Jia-Huan, *Chin. J. Anal. Chem.*, 2012, **40**, 1293–1300.

31 J. S. Barea, J. Lee and D. K. Kang, *Micromachines*, 2019, **10**, 412.

32 M. Zagnoni and J. M. Cooper, *Methods Cell. Biol.*, 2011, **102**, 23–48.

33 Z. Liu, J. Zhao, Y. Pang and X. Wang, *Microfluid. Nanofluid.*, 2018, **22**, 1–9.

34 S. M. S. Murshed, S. H. Tan, N. T. Nguyen, T. N. Wong and L. Yobas, *Microfluid. Nanofluid.*, 2009, **6**, 253–259.

35 R. Ma, Q. Zhang, T. Fu, C. Zhu, K. Wang, Y. Ma and G. Luo, *J. Ind. Eng. Chem.*, 2018, **65**, 272–279.

36 T. Thorsen, R. W. Roberts, F. H. Arnold and S. R. Quake, *Phys. Rev. Lett.*, 2001, **86**, 4163.

37 J. Husny and J. J. Cooper-White, *J. Nonnewton Fluid Mech.*, 2006, **137**, 121–136.

38 Y. Zhang, X. Chen and W. Han, *Chem. Eng. Technol.*, 2021, **44**, 1241–1250.

39 Y. Chen and Z. Deng, *J. Fluid Mech.*, 2017, **819**, 401–434.

40 K. Sripadaraja, M. N. Satyanarayan and G. Umesh, *ISSS J. Micro Smart Sys.*, 2021, **10**, 103–117.

41 R. Singh, S. S. Bahga and A. Gupta, *J. Fluid Mech.*, 2020, **905**, A29.

42 J. Yin and S. Kuhn, *Chem. Eng. Sci.*, 2022, **261**, 117874.

43 Y. Pang, Q. Zhou, X. Wang, Y. Lei, Y. Ren, M. Li, J. Wang and Z. Liu, *AIChE J.*, 2020, **66**, e16290.

44 J. D. Wehking, M. Gabany, L. Chew and R. Kumar, *Microfluid. Nanofluid.*, 2014, **16**, 441–453.

45 L. Peng, M. Yang, S. S. Guo, W. Liu and X. Z. Zhao, *Biomed. Microdevices*, 2011, **13**, 559–564.

46 W. Zeng, S. Li and Z. Wang, *Sens. Actuators A: Phys.*, 2015, **233**, 542-547.

47 D. Huang, K. Wang, Y. Wang, H. Sun, X. Liang and T. Meng, *J. Frankl. Inst.*, 2020, **357**, 5302–5316.

48 Y. Luo, Z. Zheng, X. Zheng, Y. Li, Z. Che, J. Fang, L. Xi, N. T. Nguyen and C. Song, *Sens. Actuators B: Chem.*, 2022, **365**, 131936.

49 P. Teng, D. Tian, H. Fu and S. Wang, *Mater. Chem. Front.*, 2020, **4**, 140-154.

50 N. Vergauwe, D. Witters, F. Ceyssens, S. Vermeir, B. Verbruggen, R. Puers and J. Lammertyn, *J. Micromech. Microeng.*, 2011, **21**, 054026.

51 F. Malloggi, H. Gu, A. G. Banpurkar, S. A. Vanapalli and F. Mugele, *Eur. Phys. J. E*, 2008, **26**, 91–96.

52 X. Ding, P. Li, S. C. S. Lin, Z. S. Stratton, N. Nama, F. Guo, D. Slotcavage, X. Mao, J. Shi, F. Costanzo and T. J. Huang, *Lab Chip*, 2013, **13**, 3626–3649.

53 K. Kolesnik, M. Xu, P. V. S. Lee , V. Rajagopal and D. J. Collins, *Lab Chip*, 2021, **21**, 2837-2856.

54 P. Zhang, H. Bachman, A. Ozcelik and T. J. Huang, *Ann. Rev. Anal. Chem.*, 2020, **13**, 17–43.

55 Y. Zhang, A. Zhou, S. Chen, G. Z. Lum and X. Zhang, *Biomicrofluidics*, 2022, **16**, 11301.

56 E. Al-Hetlani and M. O. Amin, *Microchimica Acta.*, 2019, **186**, 1–37.

57 A. N. Surendran, R. Zhou and Y. Lin, *J. Med. Devices*, 2021, **15**, 024001

58 M. A. Bijarchi, A. Favakeh, E. Sedighi and M. B. Shafii, *Sens. Actuators A: Phys.*, 2020, **301**, 111753.

59 G. P. Zhu, Q. Y. Wang, Z. K. Ma, S. H. Wu and Y. P. Guo, *Biosensors*, 2022, **12**, 156.

60 X. L. Guo, Y. Wei, Q. Lou, Y. Zhu and Q. Fang, *Anal. Chem.*, 2018, **90**, 5810–5817.

61 P. Garstecki, S. T. S. Kaminski, P. Garstecki and T. S. Kaminski, *Chem. Soc. Rev.*, 2017, **46**, 6210–6226.

62 S. Mashaghi, A. Abbaspourrad, D. A. Weitz and A. M. van Oijen, *TrAC Trends Anal. Chem.*, 2016, **82**, 118–125.

63 T. S. Kaminski and P. Garstecki, *Chem. Soc. Rev.*, 2017, **46**, 6210-6226.

64 K.-H. Huang, N. M. Morato, Y. Feng and R. G. Cooks, *Angew. Chem.*, 2023, **135**, e202300956.

65 K. I. Ohno, K. Tachikawa and A. Manz, *Electrophoresis*, 2008, **29**, 4443–4453.

66 T. S. Kaminski, O. Scheler and P. Garstecki, *Lab Chip*, 2016, **16**, 2168–2187.

67 L. Shang, Y. Cheng and Y. Zhao, *Chem. Rev.*, 2017, **117**, 7964–8040.

68 L. Chatterjee and S. Chatterjee, *bioRxiv*, 2022, **11**, 518020.

69 M. S. Reza, Y. S. Ko, B. E. Jeon, P. Sen and C. Lee, *Phys. Fluids*, 2024, **36**, 052013.

70 N. A. Md Yunus, N. F. Ismail, I. Abdul Halin, N. Sulaiman and M. N. Mohtar, *Results Phys.*, 2018, **11**, 847–852.

71 L.Shan, J. Li, B. Ma, X. Jiang, B.Dogruoz and D. Agonafer, *Exp. Therm. Fluid Sci.*, 2019, **109**, 109889.

72 W. Wang, Q. Cai, S. Xu and X. Chen, *Biosensors*, 2024, **14**, 44.

73 A. L. Zhang, *Ferroelectrics*, 2022, **589**, 218–227.

74 Y. Huang, P. K. Das and V. R. Bhethanabotla, *Sens. Actuators Rep.*, 2021, **3**, 100041.

75 L. Howell, V. Anagnostidis and F. Gielen, *Adv. Mater. Technol.*, 2022, **7**, 2101053.

76 Y. Alhendal, A. Turan and A. Kalendar, *Acta Astronautica*, 2016, **126**, 265-274.

77 W. Mao, A. Oron and A. Alexeev, *Phys. Fluids*, 2013, 25, 072101.

78 L. M. Mayr and D. Bojanic, *Curr. Opin. Pharmacol.*, 2009, **9**, 580-588.

79 L. Wang, Y. Tan, K. Gan, L. Liu, X. Chen, M. Tang, B. Hu and W. Wu, *Langmuir*, 2021, **37**, 4129–4136.

80 A. Venancio-Marques and D. Baigl, *Langmuir*, 2014, **30**, 4207–4212.

81 N. T. Nguyen, M. Hejazian, C. H. Ooi and N. Kashaninejad, *Micromachines*, 2017, **8**, 186.

82 C. G. Yang, Z. R. Xu and J. H. Wang, *TrAC Trends Anal. Chem.*, 2010, **29**, 141-157.

83 U. Lehmann, S. Hadjidj, V. K. Parashar, C. Vandevyver, A. Rida and M. A. M. Gijs, *Sens. Actuators B: Chem.*, 2006, **117**, 457-463.

84 Z. Dong and Q. Fang, *TrAC Trends Anal. Chem.*, 2020, **124**, 115812.

85 M. Javaid, A. Haleem, S. Rab, R. Pratap Singh and R. Suman, *Sens. Int.*, 2021, **2**, 100121.

86 S. Zhang, M. H. Ang, W. Xiao and C. K. Tham, *Sensors*, 2009, **9**, 1499–1517.

87 M. Stikic, D. Larlus, S. Ebert and B. Schiele, *IEEE Trans. Pattern Anal. Mach. Intell.*, 2011, **33**, 2521–2537.

88 M. Javaid, A. Haleem, R. P. Singh, S. Rab and R. Suman, *Sens. Int.*, 2021, **2**, 100110.

89 J. F. Tressler, S. Alkoy and R. E. Newnham, *J. Electroceram.*, 1998, **2**, 257–272.

90 C. Y. K. Chee, L. Tong and G. P. Steven, *J. Intell. Mater. Syst. Struct.*, 1998, **9**, 3–19.

91 V. V. Petrov, V. V. Sysoev, I. O. Ignatieva, I. A. Gulyaeva, M. G. Volkova, A. P. Ivanishcheva, S. A. Khubezhov, Y. N. Varzarev and E. M. Bayan, *Sensors*, 2023, **23**, 5617.

92 S. Hullavarad, N. Hullavarad, D. Look and B. Claflin, *Nanoscale Res. Lett.*, 2009, **4**, 1421–1427.

93 A. J. Cheng, L. Wu, Z. Sha, W. Chang, D. Chu, C. H. Wang and S. Peng, *Adv. Mater. Technol.*, 2023, **8**, 2201959.

94 R. Puers, *Sens. Actuators A: Phys.*, 1993, **37–38**, 93–105.

95 Z. Ma, Y. Zhang, K. Zhang, H. Deng and Q. Fu, *Nano Mater. Sci.*, 2023, **5**, 265–277.

96 Y. Zhu, Y. Liu, Y. Sun, Y. Zhang and G. Ding, *IEEE Sens. J.*, 2022, **22**, 15635–15649.

97 C. C. Wang, S. A. Akbar and M. J. Madou, *J. Electroceram.*, 1998, **2**, 273–282.

98 G. Saggio, F. Riillo, L. Sbernini and L. R. Quitadamo, *Smart Mater. Struct.*, 2015, **25**, 013001.

99 B. Babayigit and M. Abubaker, *IEEE Syst. J.*, 2024, **18**, 120–133.

100 T. Reininger, F. Welker and M. Zeppelin, *Sens. Actuators A: Phys.*, 2006, **129**, 270-274.

101 W. Bourgeois, A. C. Romain, J. Nicolas and R. M. Stuetz, *J. Environ. Monit.*, 2003, **5**, 852–860.

102 L. Wang, Z. Lou, K. Jiang and G. Shen, *Adv. Intell. Sys.*, 2019, **1**, 1900040.

103 A. Darwish and A. E. Hassanien, *Sensors*, 2011, **11**, 5561–5595.

104 Y. G. Park, S. Lee and J. U. Park, *Sensors*, 2019, **19**, 4353.

105 R. B. Mishra, N. Atab, A. M. Hussain and M. M. Hussain, *Adv. Mater. Technol.*, 2021, **6**, 2002023.

106 C. K. Wu, C. T. Cheng, Y. Uwate, G. Chen, S. Mumtaz and K. F. Tsang, *IEEE Trans. Consum. Electron.*, 2023, **69**, 937–948.

107 J. Guerrero-Ibáñez, S. Zeadally and J. Contreras-Castillo, *Sensors*, 2018, **18**, 1212.

108 P. Mohankumar, J. Ajayan, R. Yasodharan, P. Devendran and R. Sambasivam, *Measurement*, 2019, **140**, 305–322.

109 H. Askari, A. Khajepour, M. B. Khamesee and Z. L. Wang, *Nano Energy*, 2019, **66**, 104103.

110 R. Krishnamurthi, A. Kumar, D. Gopinathan, A. Nayyar and B. Qureshi, *Sensors*, 2020, **20**, 6076.

111 D. Ding, R. A. Cooper, P. F. Pasquina and L. Fici-Pasquina, *Maturitas*, 2011, **69**, 131–136.

112 A. Heller and B. Feldman, *Chem. Rev.*, 2008, **108**, 2482–2505.

113 M. Nadporozhskaya, N. Kovsh, R. Paolesse and L. Lvova, *Chemosensors*, 2022, **10**, 35.

114 P. Kassal, M. D. Steinberg and I. M. Steinberg, *Sens. Actuators B: Chem.*, 2018, **266**, 228–245.

115 H. Zhao, R. Su, L. Teng, Q. Tian, F. Han, H. Li, Z. Cao, R. Xie, G. Li, X. Liu and Z. Liu, *Nanoscale*, 2022, **14**, 1653.

116 I. Ivanišević, S. Milardović and P. Kassal, *Food Technol. Biotechnol.*, 2021, **59**, 216-237.

117 S. M. Majhi, A. Ali, P. Rai, Y. E. Greish, A. Alzamly, S. G. Surya, N. Qamhieh and S. T. Mahmoud, *Nanoscale Adv.*, 2022, **4**, 697–732.

118 G. Barandun, L. Gonzalez-Macia, H. S. Lee, C. Dincer and F. Güder, *ACS Sens.*, 2022, **7**, 2804–2822.

119 J. Watson, *Sens. Actuators*, 1984, **5**, 29–42.

120 R. Hoekstra, P. Blondeau and F. J. Andrade, *Anal. Bioanal. Chem.*, 2018, **410**, 4077-4089.

121 D. Puccinelli and M. Haenggi, *IEEE Circ. Syst. Mag.*, 2005, **5**, 19–29.

122 X. Sheng, J. Tang, X. Xiao and G. Xue, *IEEE Sens. J.*, 2013, **13**, 3733–3741.

123 B. F. Spencer, M. E. Ruiz-Sandoval and N. Kurata, *Struct. Control Health Monit.*, 2004, **11**, 349–368.

124 H. Ryu, H.-J. Yoon, S.-W. Kim, H. Ryu, H.-J. Yoon and S.-W. Kim, *Adv. Mater.*, 2019, **31**, 1802898.

125 H. B. Radousky and H. Liang, *Nanotechnol.*, 2012, **23**, 502001.

126 A. Harb, *Renew. Energy*, 2011, **36**, 2641–2654.

127 D. Lau, N. Song, C. Hall, Y. Jiang, S. Lim, I. Perez-Wurfl, Z. Ouyang and A. Lennon, *Mater. Today Energy*, 2019, **13**, 22–44.

128 D. Hao, L. Qi, A. M. Tairab, A. Ahmed, A. Azam, D. Luo, Y. Pan, Z. Zhang and J. Yan, *Renew. Energy*, 2022, **188**, 678–697.

129 Z. Abdin, M. A. Alim, R. Saidur, M. R. Islam, W. Rashmi, S. Mekhilef and A. Wadi, *Renew. Sustain. Energy Rev.*, 2013, **26**, 837–852.

130 A. Muscat, S. Bhattacharya and Y. Zhu, *Sensors*, 2022, **22**, 5555.

131 R. L. Harne and K. W. Wang, *Smart Mater. Struct.*, 2013, **22**, 023001.

132 C. Wei and X. Jing, *Renew. Sustain. Energy Rev.*, 2017, **74**, 1–18.

133 G. Hu, X. Ning, M. Hussain, U. Sajjad, M. Sultan, H. M. Ali, T. R. Shah and H. Ahmad, *Sustain. Energy Techol. Assessments*, 2021, **48**, 101651.

134 A. Usman, F. Xiong, W. Aftab, M. Qin, R. Zou, A. Usman, F. Xiong, W. Aftab, M. Qin and R. Zou, *Adv. Mater.*, 2022, **34**, 2202457.

135 R. A. Kishore and S. Priya, *Mater.*, 2018, **11**, 1433.

136 J. Paul, A. K. Pandey, Y. N. Mishra, Z. Said, Y. K. Mishra, Z. Ma, J. Jacob, K. Kadirgama, M. Samykano and V. V. Tyagi, *Renew. Sustain. Energy Rev.*, 2022, **161**, 112321.

137 S. M. H. D. Perera, G. Putrus, M. Conlon, M. Narayana and K. Sunderland, *Energies*, 2022, **15**, 9299.

138 A. Ali, S. Ali, H. Shaukat, E. Khalid, L. Behram, H. Rani, W. A. Altabey, S. A. Kouritem and M. Noori, *Results Eng.*, 2024, **21**, 101777.

139 L. Zhao and Y. Yang, *Shock Vib.*, 2017, **2017**, 3585972.

140 A. Truitt and S. N. Mahmoodi, *Int. J. Precis. Eng. Manuf.*, 2013, **14**, 1667–1675.

141 M. S. Güney and K. Kaygusuz, *Renew. Sustain. Energy Rev.*, 2010, **14**, 2996–3004.

142 N. D. Laws and B. P. Epps, *Renew. Sustain. Energy Rev.*, 2016, **57**, 1245–1259.

143 W. I. Ibrahim, M. R. Mohamed, R. M. T. R. Ismail, P. K. Leung, W. W. Xing and A. A. Shah, *Energy Rep.*, 2021, **7**, 2021–2042.

144 Y. H. Zhang, A. Lee and C. H. Lee, *Sens. Actuators A: Phys.*, 2024, **370**, 115207.

145 M. R. Sarker, M. H. M. Saad, J. L. Olazagoitia and J. Vinolas, *Electronics*, 2021, **10**, 1108.

146 P. Carneiro, M. P. Soares dos Santos, A. Rodrigues, J. A. F. Ferreira, J. A. O. Simões, A. T. Marques and A. L. Kholkin, *Appl. Energy*, 2020, **260**, 114191.

147 Z. Lin Wang and Z. L. Wang, *Adv. Energy Mater.*, 2020, **10**, 2000137.

148 C. Wu, A. C. Wang, W. Ding, H. Guo and Z. L. Wang, *Adv. Energy. Mater.*, 2019, **9**, 1802906.

149 T. Cheng, J. Shao and Z. L. Wang, *Nat. Rev. Methods Primers*, 2023, **3**, 1–13.

150 J. Briscoe and S. Dunn, *Nano Energy*, 2015, **14**, 15–29.

151 V. E. Ogbonna, A. P. I. Popoola and O. M. Popoola, *Front. Energy Res.*, 2022, **10**, 1051081.

152 D. P. Pabba, M. Satthiyaraju, A. Ramasdoss, P. Sakthivel, N. Chidhambaram, S. Dhanabalan, C. V. Abarzúa, M. J. Morel, R. Udayabhaskar, R. V. Mangalaraja, R. Aepuru, S. K. Kamaraj, P. K. Murugesan and A. Thirumurugan, *Micromachines*, 2023, **14**, 1273.

153 Q. T. H. Ta, D. Thakur and J. S. Noh, *Chemosensors*, 2023, **11**, 477.

154 M. Dhiman, *J. Mater. Chem. A*, 2020, **8**, 10074–10095.

155 X. B. Fan, S. Yu, B. Hou and J. M. Kim, *Isr. J. Chem.*, 2019, **59**, 762–773.

156 X. Liu, L. He, R. Liu, D. Hu, L. Zhang and G. Cheng, *Rev. Sci. Instrumen.*, 2023, **94**, 031501.

157 D. Xu, M. Yan and Y. Xie, *Electrophoresis*, 2024, **45**, 244–265.

158 J. Chi, C. Liu, L. Che, D. Li, K. Fan, Q. Li, W. Yang, L. Dong, G. Wang and Z. L. Wang, *Adv. Sci.*, 2022, **9**, 2201586.

159 A. Naqvi, A. Ali, W. A. Altabey and S. A. Kouritem, *Energies*, 2022, **15**, 7424.

160 В. Харківського Національного Університету, S. M. Kovalenko, V. V Ivanov, F.-A. Miannay, A. Idrissi and O. N. Kalugin, *Kharkov Univ. Bull. Chem. Ser.*, 2020, **34**, 6–56.

161 G. Liu, K. Du, S. Haussener and K. Wang, *ChemSusChem*, 2016, **9**, 2878–2904.

162 J. C. Tan and B. Civalleri, *CrystEngComm*, 2014, **17**, 197–198.

163 A. Millet, P. T. Cesana, K. Sedillo, M. J. Bird, G. S. Schlau-Cohen, A. G. Doyle, D. W. C. MacMillan and G. D. Scholes, *Acc. Chem. Res.*, 2022, **55**, 1423–1434.

164 Y. Yang, W. Niu, L. Dang, Y. Mao, J. Wu and K. Xu, *Front. Chem.*, 2022, **10**, 955065.

165 X. Tao, Y. Zhao, S. Wang, C. Li and R. Li, *Chem. Soc. Rev.*, 2022, **51**, 3561–3608.

166 K. Zhang, M. Ma, P. Li, D. H. Wang and J. H. Park, *Adv. Energy Mater.*, 2016, **6**, 1600602.

167 H. Huang, B. Weng, H. Zhang, F. Lai, J. Long, J. Hofkens, R. E. Douthwaite, J. A. Steele and M. B. J. Roeffaers, *J. Phys. Chem. Lett.*, 2022, **13**, 25–41.

168 T. Becker, M. E. Kiziroglou, M. Duffy, B. Zaghari and E. M. Yeatman, *IEEE Power Electron. Mag.*, 2023, **10**, 57–64.

169 K. Calautit, D. S. N. M. Nasir and B. R. Hughes, *Renew. Sustain. Energy Rev.*, 2021, **147**, 111230.

170 Y. Bai, H. Jantunen and J. Juuti, *Adv. Mater.*, 2018, **30**, 1707271.

171 K. G. Lemessy, K. Manohar, A. Adeyanju, A. Campus, K. Robert Kent, A. Ba and amani Ba, *J. Sci. Res. Rep.*, 2020, **26**, 107–116.

172 M. I. H. Ansari, A. Qurashi and M. K. Nazeeruddin, *J. Photochem. Photobiol. C Photochem. Rev.*, 2018, **35**, 1–24.

173 P. P. Boix, K. Nonomura, N. Mathews and S. G. Mhaisalkar, *Mater. Today*, 2014, **17**, 16–23.

174 D. D. L. Chung, *J. Mater. Sci.*, 2015, **51**, 554–568.

175 A. W. Hull, *Phys. Rev.*, 1917, 10, 661.

176 D. L. Duong, S. J. Yun and Y. H. Lee, *ACS Nano*, 2017, **11**, 11803–11830.

177 Q. Wang and D. Ohare, *Chem. Rev.*, 2012, **112**, 4124–4155.

178 S. Kannan, *Catal. Surv. Asia*, 2006, **10**, 117–137.

179 A. H. Castro Neto, F. Guinea, N. M. R. Peres, K. S. Novoselov and A. K. Geim, *Rev. Mod. Phys.*, 2009, **81**, 109–162.

180 K. S. Novoselov, A. K. Geim, S. V. Morozov, D. Jiang, Y. Zhang, S. V. Dubonos, I. V. Grigorieva and A. A. Firsov, *Science*, 2004, **306**, 666–669.

181 X. F. Jiang, Q. Weng, X. Bin Wang, X. Li, J. Zhang, D. Golberg and Y. Bando, *J. Mater. Sci. Technol.*, 2015, **31**, 589–598.

182 J. C. Lei, X. Zhang and Z. Zhou, *Front. Phys.*, 2015, **10**, 276–286.

183 X. Li and H. Zhu, *J. Materiomics*, 2015, **1**, 33–44.

184 M. Donarelli and L. Ottaviano, *Sensors*, 2018, **18**, 3638.

185 K. Saha, J. Deka, R. K. Gogoi, K. K. R. Datta and K. Raidongia, *ACS Appl. Nano Mater.*, 2022, **5**, 15972–15999.

186 M. A. Islam, P. Serles, B. Kumral, P. G. Demingos, T. Qureshi, A. Meiyazhagan, A. B. Puthirath, M. S. Bin Abdullah, S. R. Faysal, P. M. Ajayan, D. Panesar, C. V. Singh and T. Filleter, *Appl. Phys. Rev.*, 2022, **9**, 041301.

187 V. Shanmugam, R. A. Mensah, K. Babu, S. Gawusu, A. Chanda, Y. Tu, R. E. Neisiany, M. Försth, G. Sas, O. Das, V. Shanmugam, R. A. Mensah, M. Försth, G. Sas, O. Das, K. Babu, S. Gawusu, Y. Tu and R. E. Neisiany, *Part. Syst. Charact.*, 2022, **39**, 2200031.

188 L. Tang, X. Meng, D. Deng, X. L. Bao Tang, X. Meng, D. Deng, X. Bao and L. Tang, *Adv. Mater.*, 2019, **31**, 1901996.

189 M. V. Sulleiro, A. Dominguez-Alfaro, N. Alegret, A. Silvestri and I. J. Gómez, *Sens. Biosensing Res.*, 2022, **38**, 100540.

190 X. Zhang, L. Hou, A. Ciesielski, P. Samorì, X. Zhang, L. Hou, A. Ciesielski and P. Samori, *Adv. Energy Mater.*, 2016, **6**, 1600671.

191 B. M. Nichols, A. L. Mazzoni, M. L. Chin, P. B. Shah, S. Najmaei, R. A. Burke and M. Dubey, *Semiconduct. Semimet.*, 2016, **95**, 221–277.

192 A. Jayakumar, A. Surendranath and M. PV, *Int. J. Pharm.*, 2018, **551**, 309–321.

193 Y. ; Zhou, J.-H. ; Zhang, S. ; Li, H. ; Qiu, Y. ; Shi, L. Pan, W. Zhang, G. Cheng, Y. Zhou, J.-H. Zhang, S. Li, H. Qiu, Y. Shi and L. Pan, *Micromachines*, 2023, **14**, 1043.

194 J. Deka, K. Saha, S. Kumar, H. K. Srivastava and K. Raidongia, *ACS Appl. Nano Mater.*, 2019, **2**, 7997–8004.

195 K. Kwon, J. Han, B. H. Park, Y. Shin and D. Kim, *Desalination*, 2015, **362**, 1–10.

196 A. H. Avci, R. A. Tufa, E. Fontananova, G. Di Profio and E. Curcio, *Energy*, 2018, **165**, 512–521.

197 S. Pramanik, C. Sengupta, S. Sharma, S. Mondal, D. K. Goswami and T. Mondal, *ACS Appl. Electron. Mater.*, 2024.

198 R. Kumar Gogoi, K. Raidongia, R. K. Gogoi and K. Raidongia, *Adv. Mater.*, 2017, **29**, 1701164.

199 F. D. Jochum and P. Theato, *Chem. Soc. Rev.*, 2013, **42**, 7468–7483.

200 R. K. Gogoi, K. Saha, J. Deka, D. Brahma and K. Raidongia, *J. Mater. Chem. A*, 2017, **5**, 3523–3533.

201 P. P. Saikia, P. Garg, K. Mayawad, T. Paul, A. B. Neog, B. J. Sarmah, K. Raidongia and R. K. Gogoi, *Mater. Adv.*, 2023, **4**, 3619–3627.

202 S. Xia, M. Ni, T. Zhu, Y. Zhao and N. Li, *Desalination*, 2015, **371**, 78–87.

203 W. Eom, H. Shin, R. B. Ambade, S. H. Lee, K. H. Lee, D. J. Kang and T. H. Han, *Nat. Commun.*, 2020, **11**, 1–7.

204 K. H. Thebo, X. Qian, Q. Zhang, L. Chen, H. M. Cheng and W. Ren, *Nat. Commun.*, 2018, **9**, 1–8.

205 A. Vesel, R. Zaplotnik, G. Primc and M. Mozetič, *Mater.*, 2019, **12**, 2968.

206 K. Yu, P. Wang, G. Lu, K. H. Chen, Z. Bo and J. Chen, *J. Phys. Chem. Lett.*, 2011, **2**, 537–542.

207 H. Li, J. Wu, X. Huang, G. Lu, J. Yang, X. Lu, Q. Xiong and H. Zhang, *ACS Nano*, 2013, **7**, 10344.

208 X. Zhang, Y. Li, W. Mu, W. Bai, X. Sun, M. Zhao, Z. Zhang, F. Shan and Z. Yang, *2d Mater.*, 2021, **8**, 032002.

209 K. E. Whitener and P. E. Sheehan, *Diam. Relat. Mater.*, 2014, **46**, 25–34.

210 D. Lee, B. Lee, K. H. Park, H. J. Ryu, S. Jeon and S. H. Hong, *Nano Lett.*, 2015, **15**, 1238–1244.

211 Z. Mohanta, H. S. Atreya and C. Srivastava, *Sci. Rep.*, 2018, **8**, 1–6.

212 X. Fan, D. W. Chang, X. Chen, J. B. Baek and L. Dai, *Curr. Opin. Chem. Eng.*, 2016, **11**, 52–58.

213 D. Shi, M. Yang, B. Chang, Z. Ai, K. Zhang, Y. Shao, S. Wang, Y. Wu, X. D. Hao Shi, M. Z. Yang, B. Chang, Z. Z. Ai, K. Zhang, Y. L. Shao, S. Z. Wang, Y. Z. Wu and X. P. Hao, *Small*, 2020, **16**, 1906734.

214 B. Fu, J. Sun, G. Wang, C. Shang, Y. Ma, J. Ma, L. Xu and V. Scardaci, *Nanophoton.*, 2020, **9**, 2169–2189.

215 A. V. Tyurnina, I. Tzanakis, J. Morton, J. Mi, K. Porfyrakis, B. M. Maciejewska, N. Grobert and D. G. Eskin, *Carbon*, 2020, **168**, 737–747.

216 S. Mazzotta, S. Lettieri, G. Ferraro, M. Bartoli, M. Etzi, C. F. Pirri and S. Bocchini, *Processes*, 2024, **12**, 759.

217 M. Malaki, A. Maleki and R. S. Varma, *J. Mater. Chem. A*, 2019, **7**, 10843–10857.

218 L. Liu, Z. Shen, M. Yi, X. Zhang and S. Ma, *RSC Adv.*, 2014, **4**, 36464–36470.

219 R. Rizvi, E. P. Nguyen, M. D. Kowal, W. H. Mak, S. Rasel, M. Akibul Islam, A. Abdelaal, A. S. Joshi, S. Zekriardehani, M. R. Coleman and R. B. Kaner, *Adv. Mater.*, 2018, **30**, 1800200.

220 S. Bellani, E. Petroni, A. Esau Del Rio Castillo, N. Curreli, B. Martín-García, R. Oropesa-Nuñez, M. Prato, F. Bonaccorso, S. Bellani, E. Petroni, A. E. Del Rio Castillo, N. Curreli, B. Martín-García, F. Bonaccorso Graphene Labs, R. Oropesa-Nuñez, F. Bonaccorso BeDimensional SpA and M. Prato, *Adv. Funct. Mater.*, 2019, **29**, 1807659.

221 S. Biccai, S. Barwich, D. Boland, A. Harvey, D. Hanlon, N. McEvoy and J. N. Coleman, *2d Mater.*, 2018, **6**, 015008.

222 W. Zheng and L. Y. S. Lee, *Matter*, 2022, **5**, 515–545.

223 J. Y. Chung, Y. Yuan, T. P. Mishra, C. Joseph, P. Canepa, P. Ranjan, E. H. S. Sadki, S. Gradečak and S. Garaj, *Nat. Commun.*, 2024, **15**, 1-9.

224 Y. Fang, X. Li, J. Li, C. Yao, H. Y. Hoh, X. Hai, J. Lu and C. Su, *J. Mater. Chem*, 2019, **7**, 25691–25711.

225 N. Liu, P. Kim, J. H. Kim, J. H. Ye, S. Kim and C. J. Lee, *ACS Nano*, 2014, **8**, 6902–6910.

226 Y. Fang, X. Li, J. Li, C. Yao, H. Y. Hoh, X. Hai, J. Lu and C. Su, *J. Mater. Chem. A*, 2019, **7**, 25691–25711.

227 S. Yang, P. Zhang, A. S. Nia, X. Feng, S. Yang, P. Zhang, A. S. Nia and X. Feng, *Adv. Mater.*, 2020, **32**, 1907857.

228 X. Lu, M. Cai, X. Wu, Y. Zhang, S. Li, S. Liao and X. Lu, *Small*, 2023, **19**, 2206702.

229 M. Zhao, C. Casiraghi and K. Parvez, *Chem. Soc. Rev.*, 2024, **53**, 3036–3064.

230 Y. Huang, J. Guo, Y. Kang, Y. Ai and C. M. Li, *Nanoscale*, 2015, **7**, 19358–19376.

231 M. S. Stark, K. L. Kuntz, S. J. Martens and S. C. Warren, *Adv. Mater.*, 2019, **31**, 1808213.

232 Z. Li, D. Li, H. Wang, P. Chen, L. Pi, X. Zhou and T. Zhai, *Small Methods*, 2021, **5**, 2100567.

233 Y. Wu, D. Li, C. L. Wu, H. Y. Hwang and Y. Cui, *Nat. Rev. Mater.*, 2022, **8**, 41–53.

234 P. Joensen, R. F. Frindt and S. R. Morrison, *Mater. Res. Bull.*, 1986, **21**, 457–461.

235 X. Huang, Z. Zeng and H. Zhang, *Chem. Soc. Rev.*, 2013, **42**, 1934–1946.

236 Z. Zeng, T. Sun, J. Zhu, X. Huang, Z. Yin, G. Lu, Z. Fan, Q. Yan, H. H. Hng and H. Zhang, *Angew. Chem. Int. Ed.*, 2012, **51**, 9052–9056.

237 J. J. Shao, K. Raidongia, A. R. Koltonow and J. Huang, *Nat. Commun.*, 2015, **6**, 1–7.

238 D. A. Dikin, S. Stankovich, E. J. Zimney, R. D. Piner, G. H. B. Dommett, G. Evmenenko, S. T. Nguyen and R. S. Ruoff, *Nature*, 2007, **448**, 457–460.

239 H. A. Becerril, J. Mao, Z. Liu, R. M. Stoltenberg, Z. Bao and Y. Chen, *ACS Nano*, 2008, **2**, 463–470.

240 M. Fathizadeh, W. L. Xu, F. Zhou, Y. Yoon, M. Yu, M. Fathizadeh, W. L. Xu, F. Zhou, M. Yu and Y. Yoon, *Adv. Mater. Interfaces*, 2017, **4**, 1600918.

241 F. Moghadam and H. B. Park, *Curr. Opin. Chem. Eng.*, 2018, **20**, 28–38.

242 J. M. Luque-Alled, C. Moreno and P. Gorgojo, *Curr. Opin. Chem. Eng.*, 2023, **39**, 100901.

243 M. Thakur, N. Cai, M. Zhang, Y. Teng, A. Chernev, M. Tripathi, Y. Zhao, M. Macha, F. Elharouni, M. Lihter, L. Wen, A. Kis and A. Radenovic, *npj 2D Mater. Appl.*, 2023, **7**, 1–10.

244 X. Wang, Y. Sun and K. Liu, *2d Mater.*, 2019, **6**, 042001.

245 P. Deka, S. Roy, T. Jyoti Konch, B. Rani Bora, R. Gogoi, A. Bikash Neog, K. Sundararajan, S. Subbiah and K. Raidongia, *Chem. Eng. J.*, 2023, **469**, 143964.

246 R. Han, X. Ma, Y. Xie, D. Teng and S. Zhang, *RSC Adv.*, 2017, **7**, 56204–56210.

247 Y. Lin, Y. Bai, Y. Fang, Z. Chen, S. Yang, X. Zheng, S. Tang, Y. Liu, J. Zhao and J. Huang, *J. Phys. Chem. Lett.*, 2018, **9**, 654–658.

248 Y. Yang, K. U. Lao and R. A. Distasio, *Phys. Rev. Lett.*, 2019, **122**, 026001.

249 Y. H. Gu, X. Yan, Y. Chen, X. J. Guo and W. Z. Lang, *2d Mater.*, 2020, **7**, 045016.

250 S. Qin, D. Liu, G. Wang, D. Portehault, C. J. Garvey, Y. Gogotsi, W. Lei and Y. Chen, *J. Am. Chem. Soc.*, 2017, **139**, 6314–6320.

251 J. Lao, R. Lv, J. Gao, A. Wang, J. Wu and J. Luo, *ACS Nano*, 2018, **12**, 12464–12471.

252 R. K. Gogoi, A. B. Neog, T. J. Konch, N. Sarmah and K. Raidongia, *J. Mater. Chem. A*, 2019, **7**, 10552–10560.

253 Y. Xu, *Adv. Mater.*, 2018, **30**, 1702419.

254 L. Bocquet, *Nat. Mater.*, 2020, **19**, 254–256.

255 K. Raidongia and J. Huang, *J. Am. Chem. Soc.*, 2012, **134**, 16528–16531.

256 T. J. Konch, T. Dutta, M. Buragohain and K. Raidongia, *ACS Omega*, 2021, **6**, 20379–20387.

257 T. J. Konch, T. Dutta, A. B. Neog, R. Gogoi and K. Raidongia, *J. Phys. Chem. C*, 2021, **125**, 17939–17949.

258 T. J. Konch, R. K. Gogoi, A. Gogoi, K. Saha, J. Deka, K. A. Reddy and K. Raidongia, *Mater. Chem. Front.*, 2018, **2**, 1647–1654.

259 R. R. Nair, H. A. Wu, P. N. Jayaram, I. V. Grigorieva and A. K. Geim, *Science*, 2012, **335**, 442–444.

260 M. Macha, S. Marion, V. V. R. Nandigana and A. Radenovic, *Nat. Rev. Mater. 2019 4:9*, 2019, **4**, 588–605.

261 R. K. Gogoi, A. B. Neog, T. J. Konch, N. Sarmah and K. Raidongia, *J. Mater. Chem. A*, 2019, **7**, 10552–10560.

262 K. Sears, L. Dumée, J. Schütz, M. She, C. Huynh, S. Hawkins, M. Duke and S. Gray, *Mater.*, 2010, **3**, 127–149.

263 X. Tang, B. Guo, S. Zhang, X. Tan and H. Zheng, *J. Environ. Chem. Eng.*, 2023, **11**, 109450.

264 R. Das, P. Solís-Fernández, D. Breite, A. Prager, A. Lotnyk, A. Schulze and H. Ago, *Chem. Eng. J.*, 2021, **420**, 127721.

265 M. B. Asif, S. Iftekhar, T. Maqbool, B. K. Pramanik, S. Tabraiz, M. Sillanpää and Z. Zhang, *Chem. Eng. J.*, 2022, **432**, 134335.

266 R. K. Joshi, P. Carbone, F. C. Wang, V. G. Kravets, Y. Su, I. V. Grigorieva, H. A. Wu, A. K. Geim and R. R. Nair, *Science*, 2014, **343**, 752–754.

267 M. Deng, K. Kwac, M. Li, Y. Jung and H. G. Park, *Nano Lett.*, 2017, **17**, 2342–2348.

268 S. Hong, J. K. El-Demellawi, Y. Lei, Z. Liu, F. Al Marzooqi, H. A. Arafat and H. N. Alshareef, *ACS Nano*, 2022, **16**, 792–800.

269 M. K. Shahzad, F. H. Memon, F. Soomro, M. Iqbal, A. Ibrar, A. A. Memon, J. H. Lim, K. H. Choi and K. H. Thebo, *J. Environ. Chem. Eng.*, 2023, **11**, 109329.

270 L. Cao, H. Wu, C. Fan, Z. Zhang, B. Shi, P. Yang, M. Qiu, N. A. Khan and Z. Jiang, *J. Mater. Chem. A*, 2021, **9**, 14576–14581.

271 J. Wang, L. Wang, N. Shao, M. He, P. Shang, Z. Cui, S. Liu, N. Jiang, X. Wang and L. Wang, *Chem. Eng. J.*, 2023, **452**, 139531.

272 S. A. Amba, G. V. Ohilingar and C. M. Beeson, *J. Can. Pet. Technol.*, 1964, **3**, 8–14.

273 S. Wall, *Curr. Opin. Colloid Interface Sci.*, 2010, **15**, 119–124.

274 Y. Xu, P. Chen, J. Zhang, S. Xie, F. Wan, J. Deng, X. Cheng, Y. Hu, M. Liao, B. Wang, X. Sun and H. Peng, *Angew. Chem.. Int. Ed.*, 2017, **56**, 12940–12945.

275 J. Ji, Q. Kang, Y. Zhou, Y. Feng, X. Chen, J. Yuan, W. Guo, Y. Wei and L. Jiang, *Adv. Funct. Mater.*, 2017, **27**, 1603623.

276 K. Saha, J. Deka and K. Raidongia, *ACS Appl. Energy Mater.*, 2021, **4**, 8410–8420.

277 S. He, Y. Zhang, L. Qiu, L. Zhang, Y. Xie, J. Pan, P. Chen, B. Wang, X. Xu, Y. Hu, C. Thang Dinh, P. De Luna, M. Norouzi Banis, Z. Wang, T.-K. Sham, X. Gong, B. Zhang, H. Peng, E. H. Sargent, S. He, L. Qiu, L. Zhang, J. Pan, P. Chen, B. Wang, X. Xu, Y. Hu, B. Zhang, H. Peng, Y. Zhang, Y. Xie, X. Gong, C. T. Dinh, E. H. Sargent, P. De Luna, M. N. Banis, Z. Wang and T. Sham, *Adv. Mater.*, 2018, **30**, 1707635.

278 F. H. Memon, F. Rehman, J. Lee, F. Soomro, M. Iqbal, S. M. Khan, A. Ali, K. H. Thebo and K. H. Choi, *Sep. Purif. Rev.*, 2023, **52**, 43–57.

279 L. Dai, K. Huang, Y. Xia and Z. Xu, *Green Energy Environ.*, 2021, **6**, 193–211.

280 V. Bayram, M. Ghidiu, J. J. Byun, S. D. Rawson, P. Yang, S. A. McDonald, M. Lindley, S. Fairclough, S. J. Haigh, P. J. Withers, M. W. Barsoum, I. A. Kinloch and S. Barg, *ACS Appl. Energy Mater.*, 2020, **3**, 411–422.

281 K. Saha, J. Deka, S. Hens, S. Saikia and K. Raidongia, *J. Mater. Chem. A*, 2018, **6**, 22931–22939.

282 R. K. Gogoi and K. Raidongia, *J. Mater. Chem. A*, 2018, **6**, 21990–21998.

283 R. K. Gogoi, A. B. Neog, N. Sarmah and K. Raidongia, *J. Mater. Chem. A*, 2019, **7**, 21157–21167.

284 S. Park, J. An, J. Won Suk, R. S. Ruoff, S. Park, J. An, J. W. Suk and R. S. Ruoff, *Small*, 2010, **6**, 210–212.

285 H. Bi, K. Yin, X. Xie, Y. Zhou, S. Wan, F. Banhart and L. Sun, *Nanoscale*, 2013, **5**, 9123–9128.

286 X. Zhang, Z. Yu, C. Wang, D. Zarrouk, J. W. T. Seo, J. C. Cheng, A. D. Buchan, K. Takei, Y. Zhao, J. W. Ager, J. Zhang, M. Hettick, M. C. Hersam, A. P. Pisano, R. S. Fearing and A. Javey, *Nat. Commun.*, 2014, **5**, 1–8.

287 C. Wang, Y. Wang, Y. Yao, W. Luo, J. Wan, J. Dai, E. Hitz, K. Fu, L. Hu, C. Wang, Y. Wang, Y. Yao, W. Luo, J. Wan, J. Dai, E. Hitz, K. Fu and L. Hu, *Adv. Mater.*, 2016, **28**, 8618–8624.

288 H. Cheng, Y. Huang, Q. Cheng, G. Shi, L. Jiang, L. Qu, H. Cheng, Y. Huang, Q. Cheng, L. Qu, G. Q. Shi and L. Jiang, *Adv. Funct. Mater.*, 2017, **27**, 1703096.

289 D. D. Han, Y. L. Zhang, Y. Liu, Y. Q. Liu, H. B. Jiang, B. Han, X. Y. Fu, H. Ding, H. L. Xu and H. B. Sun, *Adv. Funct. Mater.*, 2015, **25**, 4548–4557.

290 X. Xie, L. Qu, C. Zhou, Y. Li, J. Zhu, H. Bai, G. Shi and L. Dai, *ACS Nano*, 2010, **4**, 6050–6054.

291 J. Liu, Z. Wang, X. Xie, H. Cheng, Y. Zhao and L. Qu, *J. Mater. Chem.*, 2012, **22**, 4015–4020.

292 H. Cheng, J. Liu, Y. Zhao, C. Hu, Z. Zhang, N. Chen, L. Jiang, L. Qu, H. Cheng, J. Liu, Y. Zhao, C. Hu, Z. Zhang, N. Chen and L. Qu, *Angew. Chem. Int. Ed.*, 2013, **52**, 10482–10486.

293 L. Chen, M. Weng, P. Zhou, L. Zhang, Z. Huang and W. Zhang, *Nanoscale*, 2017, **9**, 9825–9833.

294 Y. Yang, Y. Tan, X. Wang, W. An, S. Xu, W. Liao and Y. Wang, *ACS Appl. Mater. Interfaces*, 2018, **10**, 7688–7692.

Chapter 2

Electrical actuation of hydrophobic bilayer membranes of reduced graphene oxide and agar for inducing chemical reactions in microdroplets

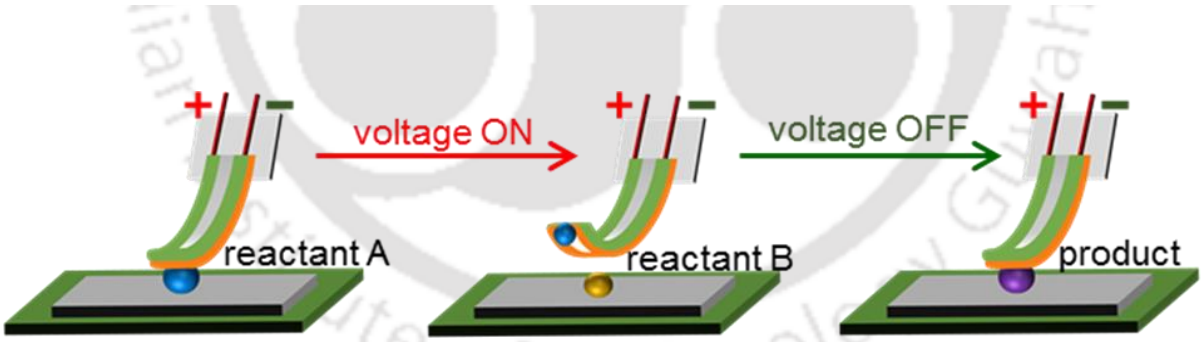

ACS Appl. Nano Mater., 2020, **3**, 6629-6635.

Summary

Systems capable of remotely handling liquids in individual microdroplets are crucial for technological applications and fundamental research. In this chapter, we demonstrate the creation of a hydrophobic bilayer membrane that can be controlled using electrical potential and infrared (IR) light to pick up and release liquids in the microliter range, with an accuracy of $\pm 5 \times 10^{-8}$ Liters. The weight of the microdroplet handled by the U-shaped electrical actuator of the r-GO/agar bilayer membrane is managed by adjusting parameters such as the liquid's surface tension, the contact angle of the solid surface, and the applied voltage. The wettability of the reduced graphene oxide (r-GO) component of the r-GO/agar bilayer membrane is controlled by modifying the surface roughness through the incorporation of varying amounts of gold nanoparticles (AuNP). Rapid mixing of liquids due to the abrupt breakup of droplets results in ultrafast chemical reactions on the microliter scale. The r-GO/agar-based electrical arm can also facilitate routine chemical analyses, such as acid-base titration, in a quick, simple, and chemical-efficient manner.

2.1 Introduction

The development of novel materials and techniques for precise manipulation of fluids at the nano and microliter scale represents a crucial area of research with significant implications.[1] These systems serve as a valuable platform for investigating fundamental interfacial interactions, allowing for enhanced control over processes such as diffusion, convection, mixing, and chemical reactions. Operating at nano or microliter dimensions enables the optimized management of interfacial phenomena.[2–9] Moreover, these systems exhibit vast potential in chemical and biological fields, offering opportunities for miniaturized analytical setups[10,11] and high-throughput chemical microreactors.[12] Implementing miniaturized liquid handling systems can revolutionize various domains, including high-throughput synthesis,[13,14] biochemical screening,[15] protein crystallization,[16,17] and enzymatic reactions,[18–20] by enabling cost-effective, rapid, and efficient performance of chemical processes and analyses.

Numerous endeavours have been undertaken to explore the diverse array of applications afforded by systems capable of manipulating liquids at the nano- or microliter scale.[1,21–23] Primarily, the focus has been on developing droplet-based microfluidic systems,[24–27] which have emerged as a leading approach in this domain. These systems have been utilized for creating miniature yet highly efficient biochemical and chemical screening platforms with high throughput, as evidenced by prior studies.[15,18,28] To enhance these applications, various precise manipulation techniques have been suggested, including minuscule pumping mechanisms,[29] utilization of intense light exposure,[30] and harnessing centrifugal force[31] for controlling liquid droplets within microfluidic channels.[32] Despite these advancements, practical hurdles such as cross-contaminations,[9] blockages,[33] and the necessity for accurate liquid pumping systems[34] impede the practical implementation of these systems. Furthermore, microfluidic systems confront limitations in handling liquids at the individual microdroplet level.[19,35] In response to these challenges, alternative approaches like water-oil emulsions[36,37] and liquid marbles[38,39]

have been proposed as potential solutions. While these strategies are effective in managing liquids at the single droplet level, they are limited by significant drawbacks, including a high propensity for cross-contamination,[9] operational challenges,[40] and the necessity for strictly non-miscible liquid systems,[41,42] which collectively diminish their accuracy and practical utility. Innovative methods have been proposed for the on-demand capture and release of micro- and nanoliter-sized droplets in both air and fluid environments. Notable examples include the use of mechanical devices with switchable adhesion properties and smart surfaces exhibiting contrasting 'petal' and 'lotus' effects.[43,44]

2.2 Scope of the present investigation

Unconventional methods for manipulating fluids at nano and microliter scales is crucial for understanding interfacial interactions and enhancing applications in chemical and biological sciences. Current microfluidic technologies face challenges like cross-contamination and blockages, limiting their effectiveness.[9,33,40–42] The goal is to develop innovative solutions that overcome these issues, enabling precise, efficient, and scalable liquid handling systems, with significant implications. In this chapter, we present the fabrication of electrically controllable smart arms designed to handle liquids at the microliter scale, utilizing reduced graphene oxide (r-GO) and agar-based bilayer membranes. Although several bilayer membranes composed of r-GO and various polymers in addition to nanomaterials have shown similar electrical actuation behaviours,[45–51] this research represents the first effort to utilize such actuators for microdroplet manipulation. The proposed approach offers significant advantages, including (a) the capability to manage liquids at single droplet scales, (b) the potential for achieving high precision via electronic control systems, (c) the reduction of cross-contamination, (d) scalability to accommodate a large number of parallel units and (e) suitability for the development of self-operating or self-triggering smart reactors or analytical systems.

Reduced Graphene Oxide (r-GO)

The chemical reduction of graphene oxide (GO), which largely eliminates oxygen-containing functional groups such hydroxyl, alkoxy, carbonyl, and carboxylic acid, yields reduced graphene oxide.[52,53] By bridging the gap between the insulating qualities of GO and the highly conductive nature of pristine graphene, this reduction process aids in the restoration of part of the electrical conductivity lost in GO. Because r-GO retains some of its residual functional groups, it disperses well in a variety of solvents and integrates more easily into a wider range of materials. Furthermore, r-GO's characteristics can be precisely tuned because of these functional groups, giving precision control over its electrical performance, solubility, and chemical reactivity. Because of its adaptability, r-GO can be used in a wide range of fields, including electronics, where its increased conductivity can be advantageous for creating flexible conductive films. Because of its large surface area and conductive network, which enhance charge storage and transfer, r-GO is utilized in energy storage devices including supercapacitors and batteries. Moreover, r-GO is a desirable option for drug delivery systems, biosensors, and biomedical devices due to its biocompatibility and functionalizability.[54–56]

Agar

Agar is a gelatinous material that is made from the cell walls of some red algae, mostly from the genera Gracilaria and Gelidium. It is a complex polysaccharide made up of agaropectin and agarose chemically. Because of its linear structure of repeating agarobiose units, agarose gives gelling qualities; on the other hand, agaropectin's more branching, heterogeneous makeup adds viscosity. Made primarily of 3,6-anhydro-L-galactose (AHGal) and D-galactose units linked alternatively by α-(1→3) and β-(1→4) glycosidic linkages, agar is a linear polysaccharide.[57] The capacity of agar to form gels at comparatively low concentrations and maintain stability throughout a broad temperature range–melting at around 85°C and solidifying at approximately 32–40°C makes it unusual. Because of this characteristic, it is perfect for a wide range of uses.

In microbiology, for example, it can be used as a solid growth medium for culturing bacteria and fungi. Agar is also utilized in the food business to stabilize gel and thicken goods like ice cream, jellies, and desserts. It is also used as a carrier for drug delivery and in gel electrophoresis.[58–60]

Lotus and Petal effect

Superhydrophobic surfaces have attracted significant attention due to their numerous practical applications, including self-cleaning, anti-fouling, anti-reflection, oil-water separation membranes, micro-droplet transportation and drag reduction in microfluidics.[61–69] Superhydrophobicity refers to surfaces with a water contact angle exceeding 150°, which is caused by low surface energy and high surface roughness. This property is present in a variety of naturally occurring biological surfaces, such as lotus leaves, duck feathers, water strider legs, rose petals, and gecko feet. Water droplets on surfaces can be classified into two categories based on their behaviour. The first category includes sticky superhydrophobic surfaces that have a high contact angle hysteresis. These surfaces cause water droplets to adhere to them even when the surface is inverted, as shown by the petal effect. The second category includes slippery superhydrophobic surfaces that have a low contact angle hysteresis. These surfaces allow water droplets to easily roll off and possess self-cleaning properties similar to the lotus effect. Slippery and sticky superhydrophobic biological surfaces are made of hierarchical microstructures and nanostructures i.e. dual-structured surfaces. In order to discriminate between the wetting behaviours of rose petals, which reveal strong adhesion, and lotus leaves, which exhibit low adhesion, dynamic contact angle measurements on these dual-structured surfaces have been comprehensively investigated. The presence of a large contact angle on the hierarchically structured surfaces of lotus leaves and rose petals suggests that the water droplets are in the Cassie state because they are lying on top of the micro/nanostructures with air pockets trapped underneath. In contrast, the water droplet completely wets the rough surface in the

Wenzel condition, making full contact with the solid. Due to the larger microstructures present on the surface of rose petals, water droplets are able to penetrate the microscale grooves but not the nanoscale structures. As a result, rose petals exhibit a greater adhesive characteristic compared to lotus leaves. These bigger microstructures are dubbed the Cassie impregnating wetting state, and they induce the noticeable CA hysteresis in addition to aiding in contact line pinning.[70–72]. The Wenzel, as well as the Cassie-Baxter states, are shown in Figure A.

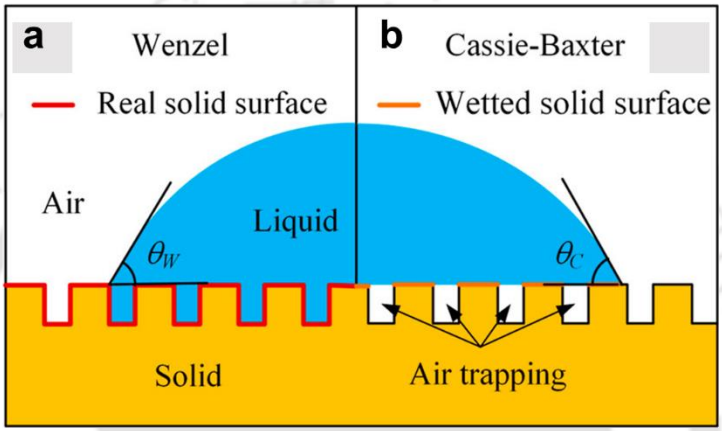

Figure A: *(a) Wenzel wetting state. (b) Cassie–Baxter wetting states.*

The Wenzel model describes homogeneous wetting using the following equation[73,74]

$$\cos\theta_w = r\cos\theta_y$$

where θ_w and θ_y represent the Wenzel contact angle and the Young contact angle, respectively, and 'r' is the roughness ratio. This ratio is defined as the ratio of the true area of a surface to its projected area.

The Cassie model describes heterogeneous wetting using the following equation

$$\cos\theta_c = rf\cos\theta_y + f - 1$$

where θ_c and θ_y are the Cassie contact angle and the Young contact angle, respectively. 'r' is the ratio of the actual area to the projected area of the solid surface, which is wetted by the liquid, and 'f' is the area fraction of the projected wet area.

2.3 Experimental section

Materials: Graphite powder and hydrogen peroxide (H_2O_2) were purchased from Sigma-Aldrich. Potassium permanganate ($KMnO_4$), sulfuric acid(H_2SO_4), hydrochloric acid (HCl), acetone, *N*,*N*-dimethylformamide (DMF), $HAuCl_4$ solution and trisodium citrate were purchased from Merck.

Preparation of graphene oxide and reduced graphene oxide:

Graphene oxide (GO) was synthesized following a modified Hummers' method.[75] Initially, 2 g of graphite powder was introduced into 50 mL of concentrated H_2SO_4, maintaining the temperature below 5 °C. Subsequently, 6 g of $KMnO_4$ was gradually incorporated into the reaction mixture under continuous stirring. Following the addition of $KMnO_4$, the mixture was stirred for an additional 2 hours at 35 °C. Thereafter, 100 mL of deionized water were gradually added, followed by 10 mL of H_2O_2 under constant stirring. The resultant yellow slurry was then subjected to successive washings with 10% HCl solution and acetone until the pH of the filtrate exceeded 5. For the preparation of reduced graphene oxide (r-GO), the synthesized GO was dispersed in DMF (0.5 mg/ml) and refluxed at 153 °C for 2 hours.[76]

Preparation of r-GO membrane:

A 40 ml dispersion of r-GO in DMF was subjected to vacuum filtration using a polytetrafluoroethylene (PTFE) membrane with a pore size of 5 µm. Following filtration, the resulting membrane was dried in an oven at 70 °C for a duration of 2 hours. Upon completion of the drying process, the freestanding r-GO membrane was carefully peeled off from the PTFE substrate.

Preparation of agar membrane:

Agar was combined with cold deionized (DI) water at a concentration of 1 mg/ml and heated to 100 °C until complete dissolution occurred. The resulting clear solution was then poured into a petri dish and allowed to cool to room temperature. The gel-like substance formed was

subsequently dried in an oven at 70 °C until a semi-transparent agar membrane was obtained, which could then be peeled off.

Preparation of r-GO/agar bilayer membrane:

An r-GO membrane was initially formed by vacuum filtering 40 ml of a 0.5 mg/ml r-GO dispersion through a PTFE membrane. After air-drying the greyish-black r-GO membrane, 20 ml of an agar dispersion was filtered through it. The agar dispersion was prepared by mixing agar powder in DMF using a probe sonicator (Labman, Model: PRO-650) for 30 minutes with 1s on & 1s off pulses. The resulting r-GO/agar bilayer membrane was then dried in an oven at 70 °C for 2 hours before being peeled off from the PTFE membrane.

Preparation of gold nanoparticles (AuNp):

A 37.5 ml aqueous solution of gold chloride (0.254 mM) was heated to boiling under vigorous stirring in a conical flask. Subsequently, 4.5 ml of a trisodium citrate solution (34 mM, prepared in water) was rapidly injected into the $HAuCl_4$ solution, maintaining a molar ratio of 1.5:1 (trisodium citrate to $HAuCl_4$).[77] The reaction reached completion within 4 to 5 minutes, yielding gold nanoparticles with a size range of 20-30 nm.

Preparation of AuNp sandwiched r-GO/agar bilayer membrane:

Initially, 10 ml of r-GO dispersion (0.5 mg/ml in DMF) was vacuum filtered through a PTFE membrane and allowed to dry. Subsequently, a dispersion of AuNp (0.059 mg/ml, 6 ml for 0.354 mg and 10 ml for 0.59 mg) was passed through the pre-formed r-GO membrane. To encapsulate the AuNp, an additional 30 ml of r-GO dispersion (0.5 mg/ml in DMF) was filtered through the AuNp containing r-GO membrane. After the AuNp sandwiched r-GO membrane was dried, 20 ml of agar dispersion (1 mg/ml in DMF) was filtered through it, forming the final bilayer membrane.

2.4 Characterizations

Nanosheets of GO and r-GO were characterized by Atomic Force Microscope (AFM) (Make: Oxford; Model: Cypher). AuNp were characterized by Field Emission Transmission Electron Microscope (FETEM) (JEOL; Model: 2100F). The morphology and the cross-sections of the membranes were examined by Field Emission Scanning Electron Microscope (FESEM) (Make: Zeiss, Model: Sigma). r-GO and GO membranes were also characterized by Raman Spectroscopy (Make: Horiba Jobin Vyon, Model: LabRam HR). X-ray diffraction studies were carried out by employing a Bruker D-205505 Cu-Kα radiation (λ = 1.5406 Å). The shape transformations as well as droplet lifting of the bilayer membranes in presence of voltage and infrared light was filmed using a digital camera, Nikon D 5200. The photo-thermal images of the membranes were captured using a High-resolution Thermal Camera, Testo 872. All the electrical experiments were done using a source meter instrument (Keithley 2450). Contact angle measurements were performed on a Holmarc Goniometer instrument.

2.5 Results and discussion

2.5.1 Fabrication and characterization of the membranes

In the first step, bilayer membranes of r-GO/agar were prepared by vacuum filtering dispersions of agar (in DMF) through a reconstructed r-GO membrane. The r-GO membrane itself was fabricated by restacking r-GO flakes prepared by heating a DMF dispersion of GO (0.5 mg/ml) at 153 °C for 2 hours. Homogeneous dispersion of agar (a natural polysaccharide), in DMF (1 mg/ml) was prepared by probe sonicating (1s on & 1 s off pulse) the sample for 30 minutes. Thus prepared r-GO/agar membrane was heated in a hot-air oven for 2 hours at ~70 °C before peeling it off from the PTFE filtration membrane. Figure 2.1a displays an AFM image of the flakes as well as a digital snapshot of the starting GO dispersion (inset). The

average diameter and dispersibility of the flakes did not appear to be impacted by the reduction procedure as can be seen from the AFM image in Figure 2.1b. A freestanding r-GO membrane

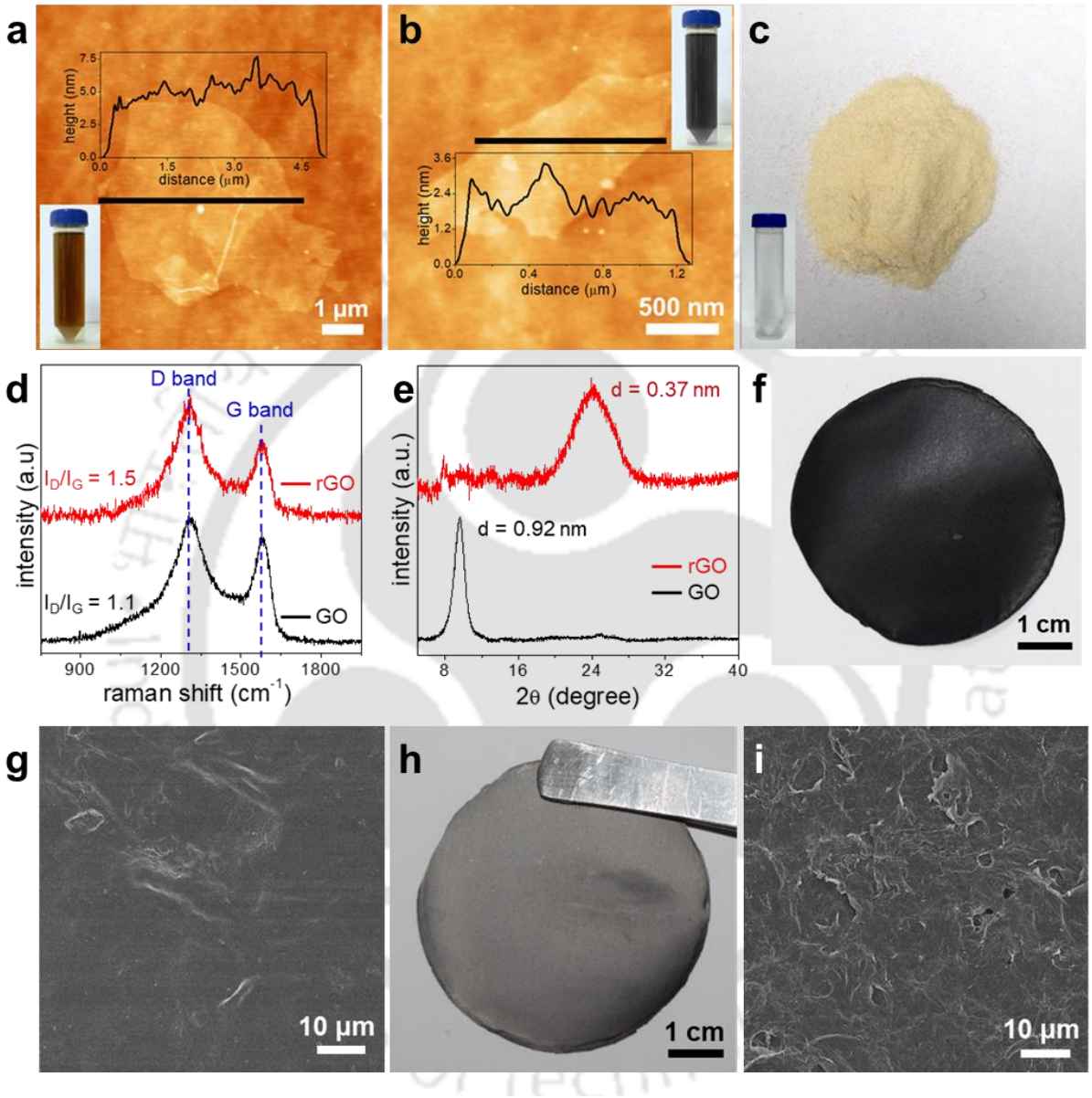

Figure 2.1: *AFM images (corresponding height profile of the nanosheets and respective dispersions in DMF in the insets) of (a) GO and (b) r-GO nanosheets. Photos showing (c) agar powder (its dispersion in DMF in the inset). Plots comparing the (d) Raman spectra and (e) XRD patterns of GO and r-GO membranes. Photos showing (f) agar side and (h) r-GO side of the r-GO/agar bilayer membrane. FESEM images showing the (g) agar and (i) r-GO sides of the bilayer membrane.*

was obtained by vacuum filtering the r-GO dispersion in DMF (inset of Figure 2.1b) via a hydrophilic PTFE membrane. The reconstructed membranes' Raman and XRD characterizations are shown in Figure 2.1d and 2.1e respectively. For the GO membrane, the D band peak was measured at 1310 cm^{-1} and the G band peak at 1580 cm^{-1}. The D band peak for the r-GO sample was determined to remain at 1310 cm^{-1}, whereas the G band peak was moved down to 1576 cm^{-1}.[78] For GO and r-GO, the I_D/I_G ratio was determined to be 1.1 and 1.5 respectively,[79] where I_D denotes the D band's intensity and I_G denotes the G band's intensity. Increasing defect concentrations during the reduction process from GO to r-GO are confirmed by the increase in the I_D/I_G value for r-GO.[80] The XRD investigations revealed that the GO

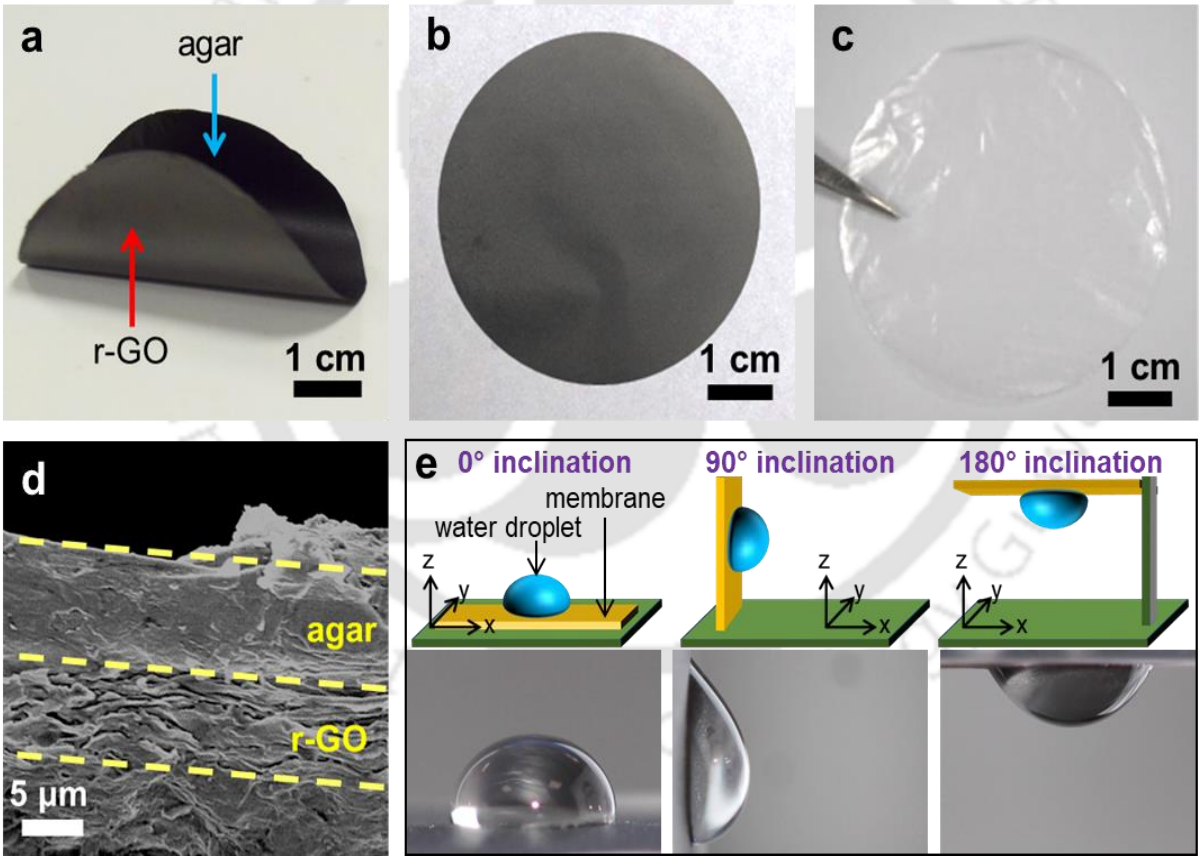

Figure 2.2: *Characterization of r-GO/agar bilayer membrane: Digital photos of (a) r-GO/agar bilayer, (b) individual r-GO membrane fabricated by the vacuum-assisted filtration method, and (c) individual agar membrane. (d) Cross-sectional FESEM image of the r-GO/agar bilayer membrane. (e) Schematic illustration (top row) and digital photos (bottom row) of water droplet on the r-GO surface of the bilayer membrane at 0, 90, and 180° inclinations.*

membrane exhibited a distinct diffraction peak at a 2θ value of 9.6°, which is equivalent to an interplanar spacing of 0.92 nm. The XRD pattern of the r-GO membrane showed a broad diffraction pattern with a peak corresponding to an interplanar spacing of 0.37 nm (at 2θ value of 24°).

In Figure 2.2a, a digital photo of a typical r-GO/agar bilayer membrane is compared with that of pure r-GO (Figure 2.2b) and agar (Figure 2.2c) membranes. The grayish-black colored r-GO side of the bilayer membrane can be easily distinguished from the shiny black colored agar side. Similarly, the two fractions of the r- GO/agar bilayer membrane can also be identified under a cross-sectional FESEM examination. A typical image distinguishing the lamellar r-GO fraction of the membrane from the smooth agar side is shown in Figure 2.2d. In Figure 2.1g and 2.1i, the FESEM image of the smooth outer surface of the agar side of the bilayer membrane is compared with that of the wavy r-GO side. The wavy r-GO side of the bilayer membrane with an AFM measured average roughness of 9.6 nm (Figure 2.3c), was found to be hydrophobic in nature, it displayed a water contact angle of 90° (Figure 2.3d). Interestingly, the hydrophobic r-GO side of the bilayer membrane possesses remarkable adhesiveness towards water droplets. Water droplets were pinned on to the hydrophobic surfaces even after

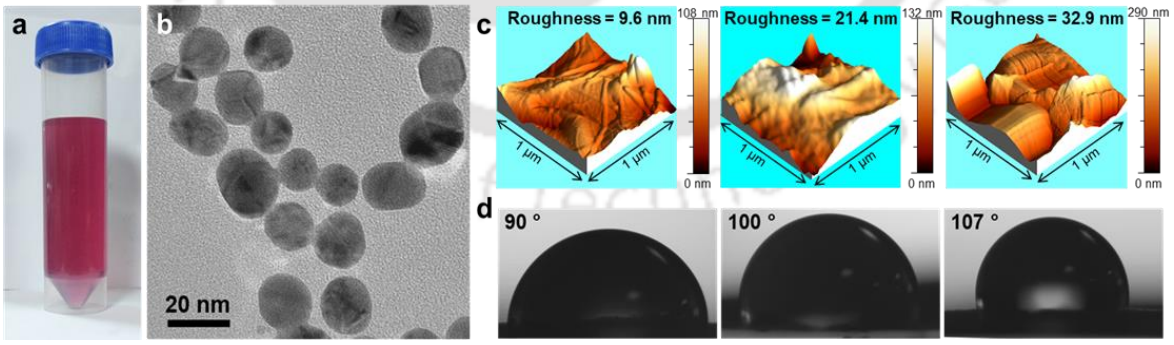

Figure 2.3: *(a) Aqueous dispersion of AuNp. (b) TEM image of AuNp. (c)The AFM measured average roughness of the r-GO side of an r-GO/agar bilayer membrane: pure r-GO side (roughness = 9.6 nm), r-GO side containing 0.354 mg (roughness = 21.4 nm) and 0.59 mg (roughness = 32.9 nm) AuNp. (d) Contact angle measurements on the r-GO side of an r-GO/agar bilayer membranes, pure r-GO side (90°) and r-GO side containing 0.354 mg (100°) and 0.59 mg (107°) AuNp. (Droplet size: 1.5 µL)*

turning it upside down. Figure 2.2e shows digital photos of a 20 µL water droplet hanged on to the r-GO surface at inclinations of 0°, 90° and 180°. The contact angle of the r-GO surface of the bilayer membrane was further increased by sandwiching ~ 20-30 nm sized AuNp between the r-GO flakes. A digital photo of an aqueous dispersion of AuNp along with FETEM characterization are shown in Figure 2.3a and 2.3b. With the increasing content of the AuNp from 0 to 0.354 and 0.59 mg (r-GO to AuNp ratios of 113:0, to 113:2 and 113:3.3 by weight) the AFM measured average roughness was found to be increased from 9.6 to 21.4 and 32.9 nm (Figure 2.3c), and simultaneously, the contact angle was found to be increased from 90° to 100° and 107°, respectively (Figure 2.3d).

2.5.2 Voltage- induced responsiveness of r-GO/agar bilayer membrane

In order to study the response of the r-GO/agar membrane towards electrical potential, a U-shaped strip was cut from the bilayer membrane, and copper wires were connected to both ends of the strip by using conducting carbon tape. A digital photo of the U-shaped device with detailed geometrical dimensions (thickness ~ 23 microns) is shown in Figure 2.4a. Through the copper wires, an electrical voltage was applied between the two terminals of the device with the help of a sourcemeter (Keithley 2450) instrument. As shown in the snapshots of Figure 2.4b, upon application of a potential difference (26 V) across the two arms, the U-shaped r-GO/agar device started curling towards the agar side with a bending speed of 9 $°s^{-1}$. The strip transformed back to its original shape as soon as the potential difference was released.

Interestingly, the bending angle and bending speed of the r-GO/agar device was found to be tunable by varying the magnitude as well as the time-duration of the applied voltage. As shown in the snapshots of Figure 2.5a, 2.5b, 2.5c, 2.5d, 2.5e and 2.4b, a systematic enhancement in the magnitude of the voltage (applied for 100 seconds) increased both bending speed (from 0.6 $°s^{-1}$ at 15 V to 9 $°s^{-1}$ at 26 V), as well as the extent of bending (from 126˚ at 15 V to 400˚ at 26 V), shown in Figure 2.4d and 2.4e. Similarly, Figure 2.4c shows that for a specific voltage, the

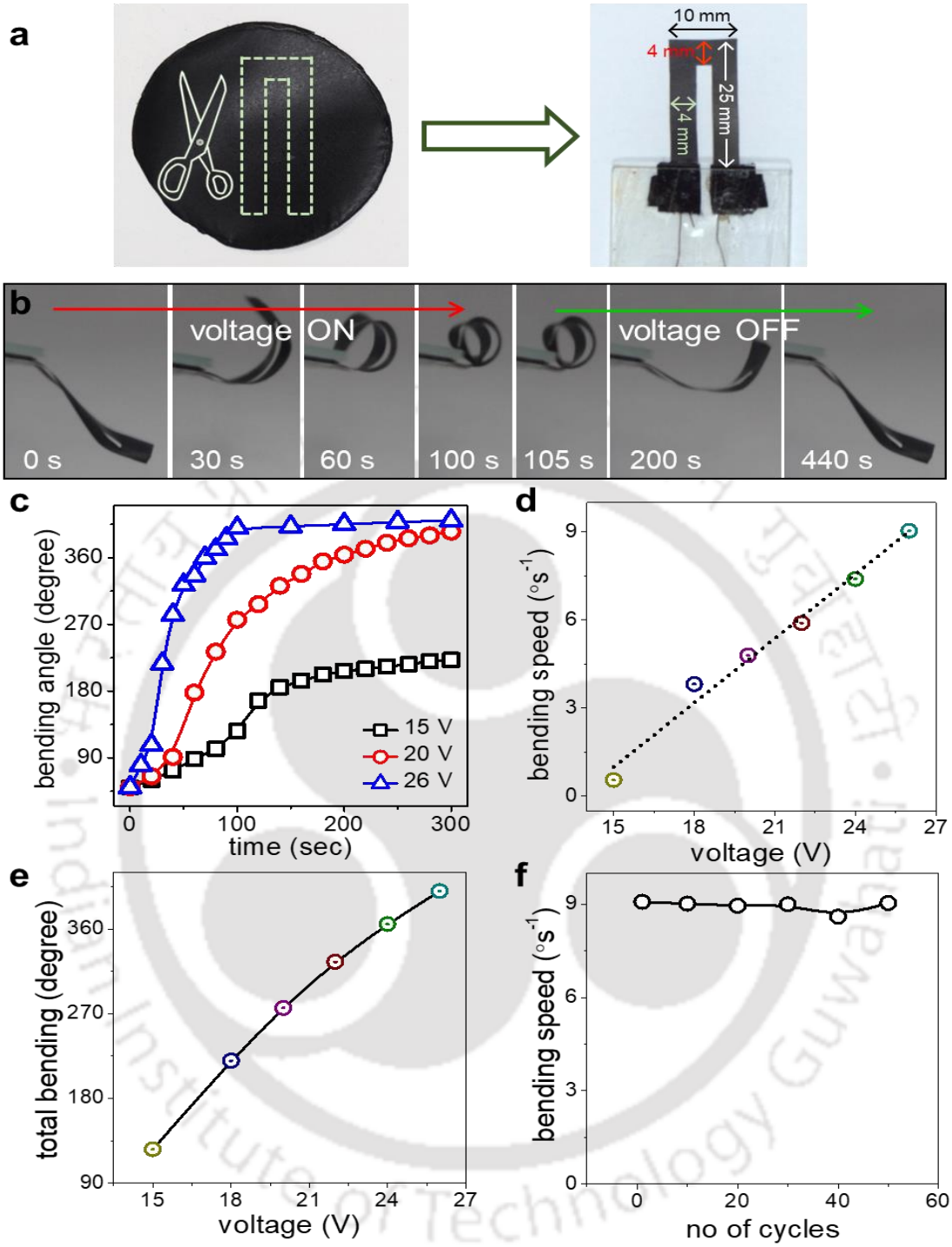

Figure 2.4: *(a) Photo showing the cutting of a U-shaped strip from an r-GO/agar bilayer membrane (thickness, 23 microns) and fabrication of the corresponding U-shaped actuator device. (b) snapshots showing bending and recovery of the U-shaped strip upon application of a potential of 26 V for 100 s. (c) Plot showing total bending achieved upon application of potentials of 15, 20, and 26 V for 300 s. Plots comparing (d) the bending speeds and (e) the total bending angle of a U-shaped r GO/agar bilayer device upon application of different voltages for 100 seconds. (f) Deviations in the voltage induced bending speeds (26 V) in the 1st, 10th, 20th, 30th, 40th and 50th cycle of a U-shaped strip of the r-GO/agar bilayer membrane.*

extent of bending increases with increasing time until it reaches saturation (snapshots are shown in Figure 2.6). The voltage induced bending of the r-GO/agar device was found to be

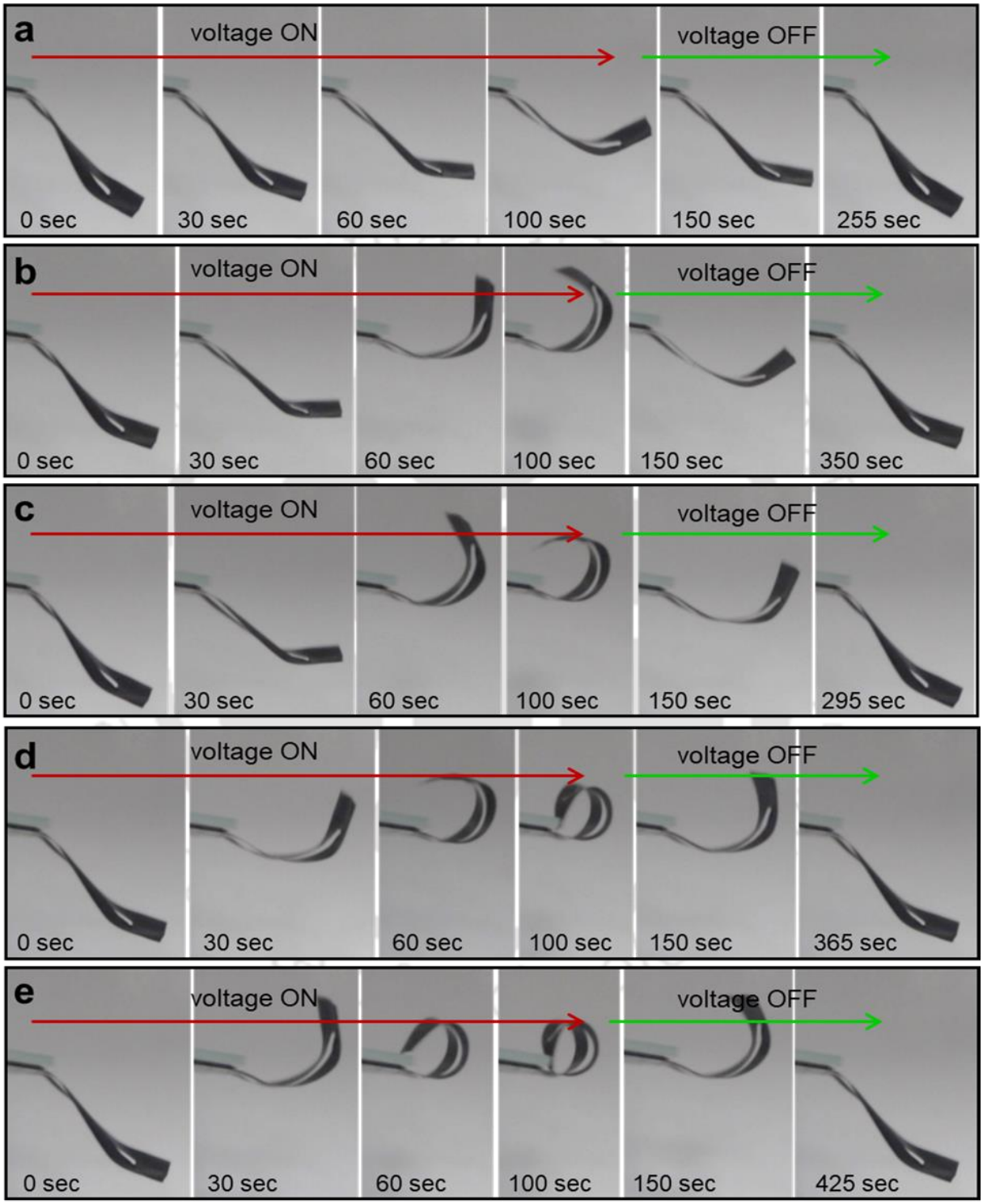

Figure 2.5: *Voltage induced responsiveness of r-GO/agar bilayer membrane: Snapshots showing the bending and recovery movements of a U-shaped bilayer strip of r-GO/agar bilayer membrane at applied voltages of (a) 15 V, (b) 18 V, (c) 20 V, (d) 22 V and (e) 24 V, respectively.*

highly reversible, and the deviations (± 0.18 $°s^{-1}$) in the voltage (26 V) induced bending speeds in the 1st, 10th, 20th, 30th, 40th and 50th cycle is shown in Figure 2.4f.

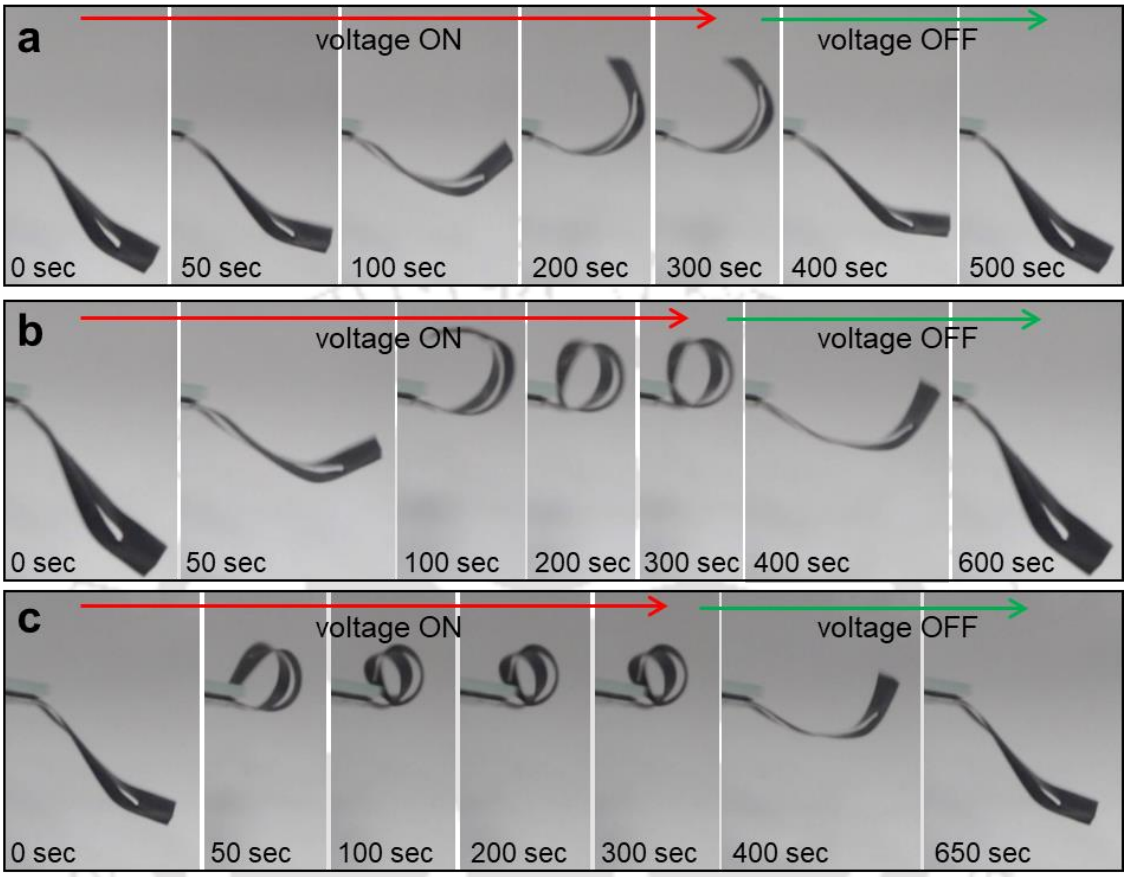

Figure 2.6: *Snapshots showing the bending movements of a U-shaped device made from r-GO/agar bilayer membrane upon application of potential difference of magnitude (a) 15 V, (b) 20 V and (c) 26 V for 300 seconds.*

The voltage induced bending of the r-GO/agar device is attributed to inhomogeneous joule heating of the two components. In order to confirm the same, temperatures of the U-shaped device made from individual r-GO and agar membranes were recorded by employing a thermal camera after applying a potential of 26 V for 30 seconds. As shown in Figure 2.7, the application of the potential increased the temperature of the U-shaped device of r-GO membrane from 22.7 °C to 27.6 °C, but no such changes in temperature were observed when the potential was applied to the U-shaped device of agar membrane. It is well-established in

the relevant literature that the shape of a bilayer membrane is determined by the equilibrium between the mechanical properties of two constituting layers.[81–84] The voltage induced thermal imbalance between the two layers of the r-GO/agar bilayer membrane also moves the mechanical equilibrium to a new position ensuring a transformation in the shape of the strip.

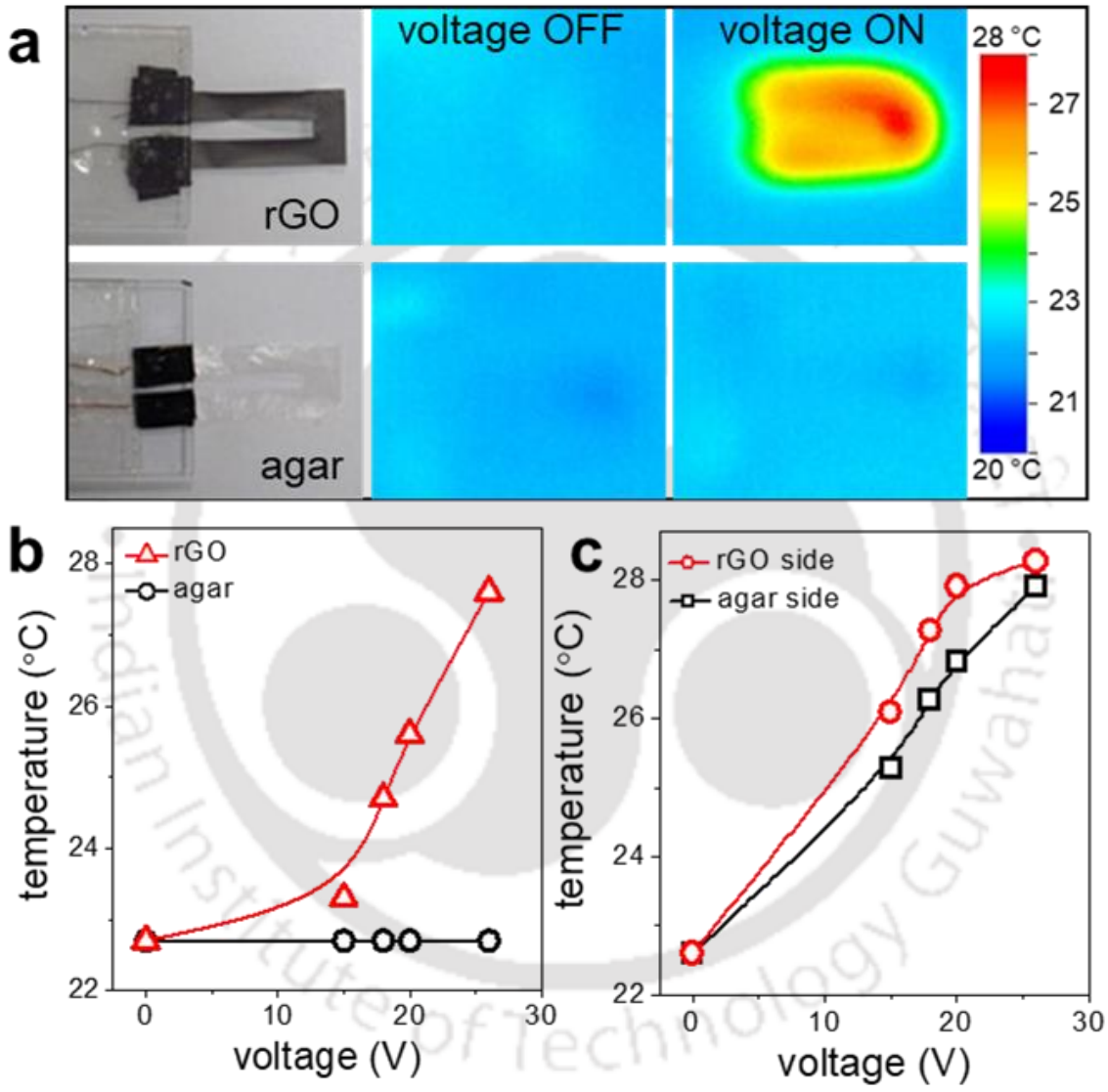

Figure 2.7: *Mechanism of voltage induced responsiveness: (a) Comparison of the photothermal images of the U-shaped device of pure r-GO and agar during OFF and ON (26 V for 30 s) states of the voltage (b) Plot showing the changes in temperature of the individual U-shaped devices of r-GO and agar when subjected to different applied voltages. (c) Comparison of the temperatures on both the sides of the U-shaped device of r-GO/agar bilayer membrane when subjected to different applied voltages.*

2.5.3 IR light induced responsiveness of r-GO/agar bilayer membrane

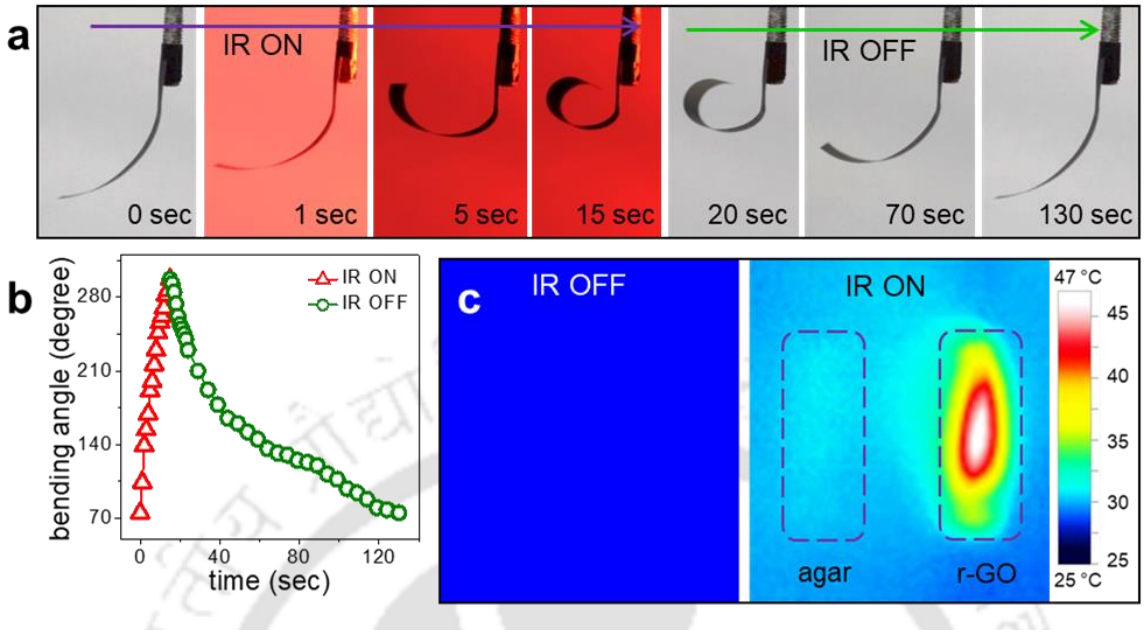

Figure 2.8: *Photos showing bending (for 15 s) and recovery movements of a bilayer strip upon exposure to IR light of intensity 5500 lux. (b) Plots showing bending angle vs time of an r-GO/agar bilayer strip upon exposure of IR light for 15 s. (c) Photothermal images showing the temperature change of the individual agar and r-GO strips upon application of IR light for 30 s.*

The shape of the r-GO/agar bilayer membrane was also found to be sensitive towards IR light. As shown in Figure 2.8a, a rectangular strip of dimensions 25 × 4 × 0.023 mm^3 was fixed to a steel rod and exposed to an IR light (5500 lux). Within 15 seconds of exposure to the IR light, the strip responded by bending towards the agar side (bending speed of 27 $°s^{-1}$), and recovered its original shape with a speed of 9 $°s^{-1}$ upon removal of the light source. In Figure 2.8a, the snapshots of the movement of the bilayer strip are shown in the presence and absence of the IR light. A plot of bending angle versus time is shown in Figure 2.8b. Similar to voltage induced bending movements, this light (IR) induced bending of the r-GO/agar strip is also attributed to the IR induced inhomogeneous heating on the opposite sides of the bilayer strip. As shown in Figure 2.8c, irradiation of IR light for 30 seconds increased the temperature of the agar

membrane by ~ 3 °C (27 to 30 °C). In contrast, irradiation of light (IR) for 30 seconds raised the temperature of r-GO membrane by 18 °C (27 to 45 °C).

2.5.4 Remote handling of microdroplets

The voltage and light sensitivity of the r-GO/agar bilayer strip was exploited to handle liquids in the microliter-sized droplets. Typically, a known amount of liquid (~ 0.025g) was dropped on to a hydrophobic surface (like taro leaf, contact angle 150°) placed on a highly sensitive weighing balance. The U-shaped r-GO/agar bilayer strip (details of the dimensions are in Figure 2.4a) was fixed on a movable stage in the vicinity of the weighing balance (shown in the Figure 2.9a). Upon application of the potential difference (20 V), the tip of the U-shaped strip moved upwards by bending towards the agar side. In this position, the stage was moved such a way that the tip of the U-shaped strip is located just above the bulk liquid droplet placed on the taro leaf. As the potential difference was released the bilayer strip regains its original position and the r-GO side of the bilayer strip touched the liquid droplet. When the potential difference was reapplied, the strip again moved in the upward direction lifting a tiny fraction of the droplet. The picked-up weight of the tiny droplet was calculated from the difference between the weights of the bulk liquid droplet before and after the electrical arm picked-up a tiny fraction of it. The picked-up micro droplet was then transferred to a hydrophilic surface by releasing the potential difference. However, it is important to note that the aqueous droplets cannot be transferred to hydrophobic substrates. As a typical example, Figure 2.9a shows picking up a tiny droplet of 10^{-2} M aqueous HCl solution weighing 5.2 ± 0.03 mg from a bulk droplet placed on a taro leaf. For better visualization, the droplet was transferred to a hydrophilic pH paper by regulating the applied voltage. The change in the color of the pH paper by the acidic droplet is clearly visible in Figure 2.9a. By monitoring the weight change of the pH paper before and after adding the tiny liquid droplet, the transferred weight of the droplet was measured.

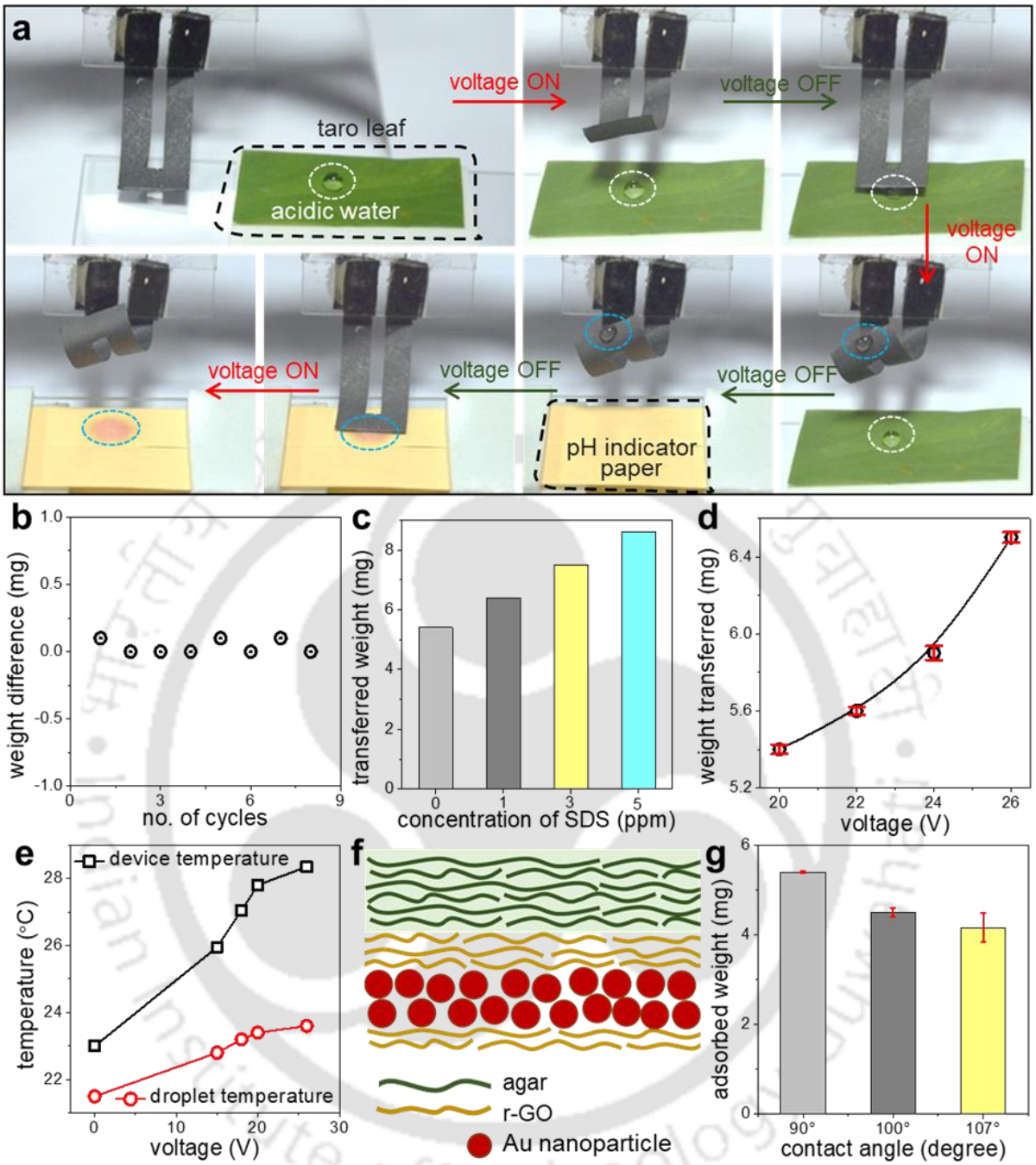

Figure 2.9: *(a) Snapshots of a U-shaped r-GO/agar device picking up a tiny droplet from a bulk droplet of 10^{-2} M aqueous solution of HCl, and its subsequent transfer to a pH indicator paper. (b) The plot of retention weight vs repetitive cycles of the r-GO surface, determined by subtracting the transferred weight from the picked-up weight. (c) The transferred weight of the water droplet containing 0, 1, 3, and 5 ppm SDS by applying a potential of 20 V. Plot of (d) transferred weight (DI water) and (e) surface temperature of r-GO/agar strip and water micro droplet as a function of applied voltage. (f) Schematic illustration of the tuning of membrane roughness by incorporating AuNp onto the r-GO side of the bilayer membrane. (g) Bar diagram showing picked-up weight of microdroplet by r-GO/agar strip with different wettability (contact angle), with an applied voltage of 20 V.*

In Figure 2.9b, the retention weight of the r-GO surface determined by subtracting transferred weight from picked-up weight is plotted for different repetitive cycles. One of the most pertinent issues of the open-air micro droplet transfer processes is the evaporation caused by large exposed surface area. The experimental data in Figure 2.9a and 2.9b shows that under our experimental condition (22 °C, RH = 75 %) the error associated with evaporation can be limited to less than 1% of the droplet weight.

The amount of liquid picked-up by the U-shaped r-GO/agar bilayer strip can be tuned by varying parameters like surface tension of the liquid, applied voltage, and contact angle of the r-GO surface. Under a constant applied voltage of 20 V, the picked-up weight of the droplet was found to be increasing with increasing concentration of the surfactants (SDS), shown in Figure 2.9c. Effects such as the decreasing surface tension and increasing affinity towards the r-GO surface is attributed for the systematic increment in the picked-up weight of the SDS containing water droplet by the r-GO/agar bilayer strip. Similarly, the picked-up weight of the water droplet was also studied as a function of the applied voltage. With increasing applied voltage from 20 V to 26 V the picked-up weight of the droplet was increased from 5.4 to 6.5 mg. Interestingly, the picked-up weight of the liquid sample can be increased with a precision of ± 0.03 mg by increasing applied voltage as can be seen in Figure 2.9d. Along with higher bending speed, the increased applied voltage also increases the surface temperature of the r-GO fraction of the bilayer membrane. The increased surface temperature is also induced to the droplets. Figure 2.9e shows that the temperature of the droplet measured by IR camera increases linearly with increasing surface temperature of the device caused by a successive enhancement to the applied voltage. The increasing temperature is known to decrease the surface tension of the liquids.[85] The faster bending movement and higher surface temperature of the strip with increasing applied voltage are accounted for the systematic increment in the picked-up weight values of the liquid sample. The picked-up weight of the liquid was also

found to be decreasing with increasing contact angle of the surface that touched the liquid droplet. Figure 2.9g shows the plot of the picked-up weights of the droplets as a function of contact angle of the solid surface. The contact angle itself was varied by sandwiching different amounts of AuNp (Schematic of the process is shown in Figure 2.9f) to r-GO side of the bilayer membrane under a constant applied voltage of 20 V. The r-GO/agar-based electrically controlled liquid handling system possesses large potential as a miniature chemical reactor or analytical systems. As a proof of the concept, the reaction between $MgSO_4.7H_2O$ and $BaCl_2.2H_2O$ was carried out by the electrical droplet lifting method. Typically, a 5 µL droplet of $MgSO_4$ in water (concentration 1M) was picked up by the r-GO/agar U-shaped bilayer strip from the surface of a taro leaf by applying a voltage of 20 V. The picked-up droplet was dropped on a 10 µL droplet of aqueous $BaCl_2$ (concentration 1M, placed on another taro leaf surface) just by releasing the applied voltage. Details of the electrically controlled chemical reactor are shown in Figure 2.10a. As can be seen from the snapshots in Figure 2.10a, as soon as the two droplets touched each other, the droplet of $MgSO_4$ broke down and completely mixed with that of $BaCl_2$. The completion of the reaction was indicated by the white precipitation formed in the mixed droplet (Figure 2.10b). The analysis of the high-resolution videos suggested that the reaction was completed within 40 seconds of contact. The rapid breaking and mixing of liquid droplets are accounted for this ultrafast chemical reaction in the microliter length-scale. Due to dramatic rise in the viscosity of liquids inside microfluidic channels such reaction takes a much longer time. In order to verify the advantage of droplet breaking, a similar reaction was also carried out on an open channel (1 mm width) made of taro leaf. As can be seen in Figure 2.10c, two 5 µL droplets of $MgSO_4$ and $BaCl_2$ were placed on the channel about 0.5 cm apart and slowly brought into the contact in the sideways. The entire process was monitored and recorded on a digital camera. As can be seen, the white colored products ($BaSO_4$) were first formed at the interfaces and slowly extended towards the opposite

ends of the droplets. The total time taken by droplets for the mixing and completing of the reaction was calculated to be ~ 312 seconds, snapshots are shown in the Figure 2.10c.

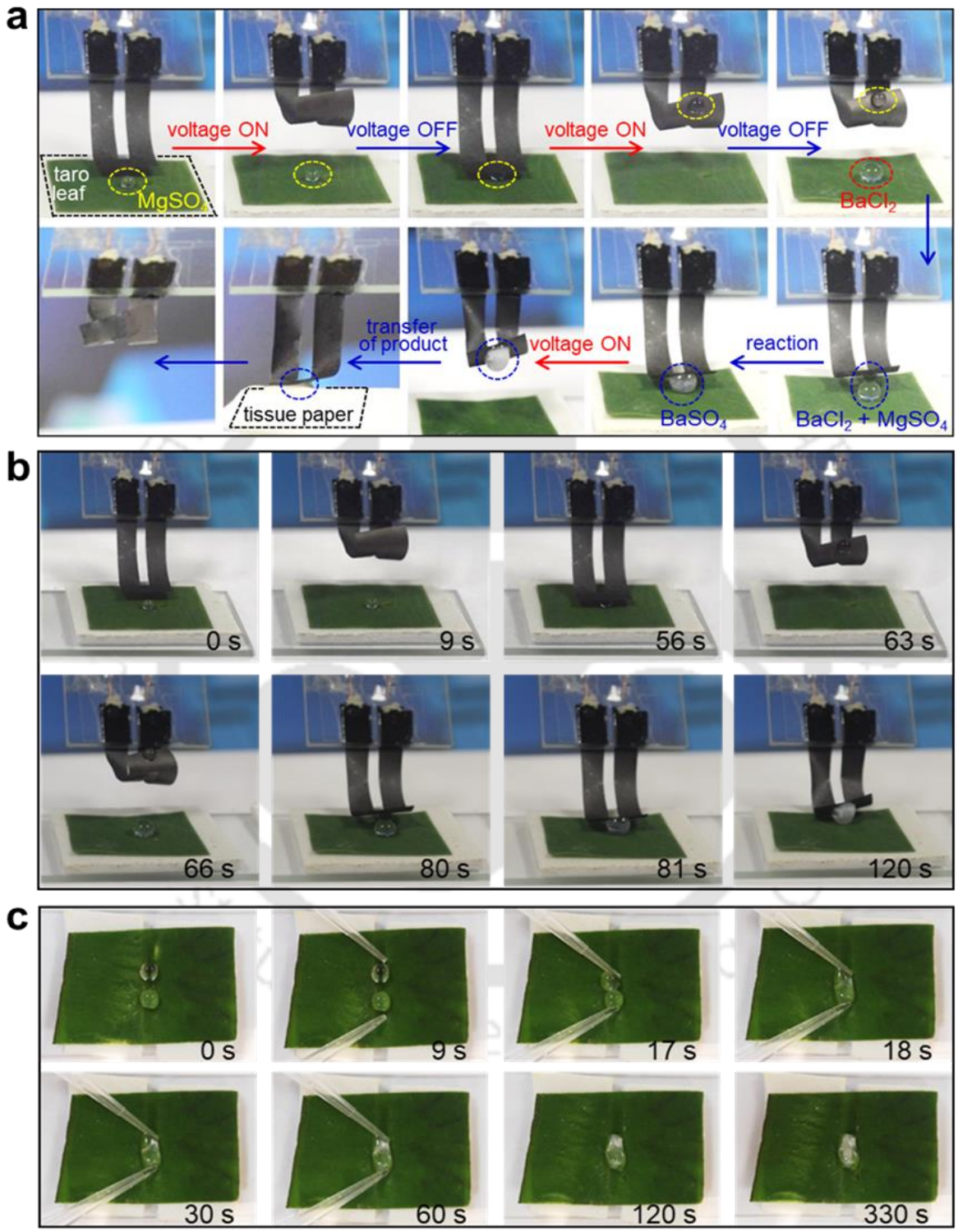

Figure 2.10: *(a) Small scale reaction between $MgSO_4$ and $BaCl_2$ carried out by a U-shaped device of r-GO/agar bilayer membrane. Comparing the reaction time between $MgSO_4$ and $BaCl_2$ (a) performed by the r-GO/agar-based U-shaped device with the one (b) performed on a 1 mm wide channel of hydrophobic taro leaf in sidewise contact mode.*

In contrast, the same reaction performed by the electrically controlled U-shaped device took just 40 seconds for the completion.

The electrically controllable responsive bilayer membrane based micro reactor can also be used to perform routine chemical analyses in a very chemical-efficient manner. For example, Figure 2.11 shows snapshots of an acid-base titration performed by a U-shaped device in the microliter level. Typically, a bulk droplet of 10^{-2} M NaOH was placed on top of a taro leaf surface. The U-shaped r-GO/agar bilayer strip (details of the dimensions are in Figure 2.4a) was employed to lift a tiny fraction (5.3 mg) of it leaving behind the bulk liquid sample. The picked-up micro droplet was then placed on top of a 5.3 mg 10^{-2} M HCl droplet (pre-mixed with phenolphthalein indicator) on a taro leaf surface by releasing the potential difference. As soon as the droplets

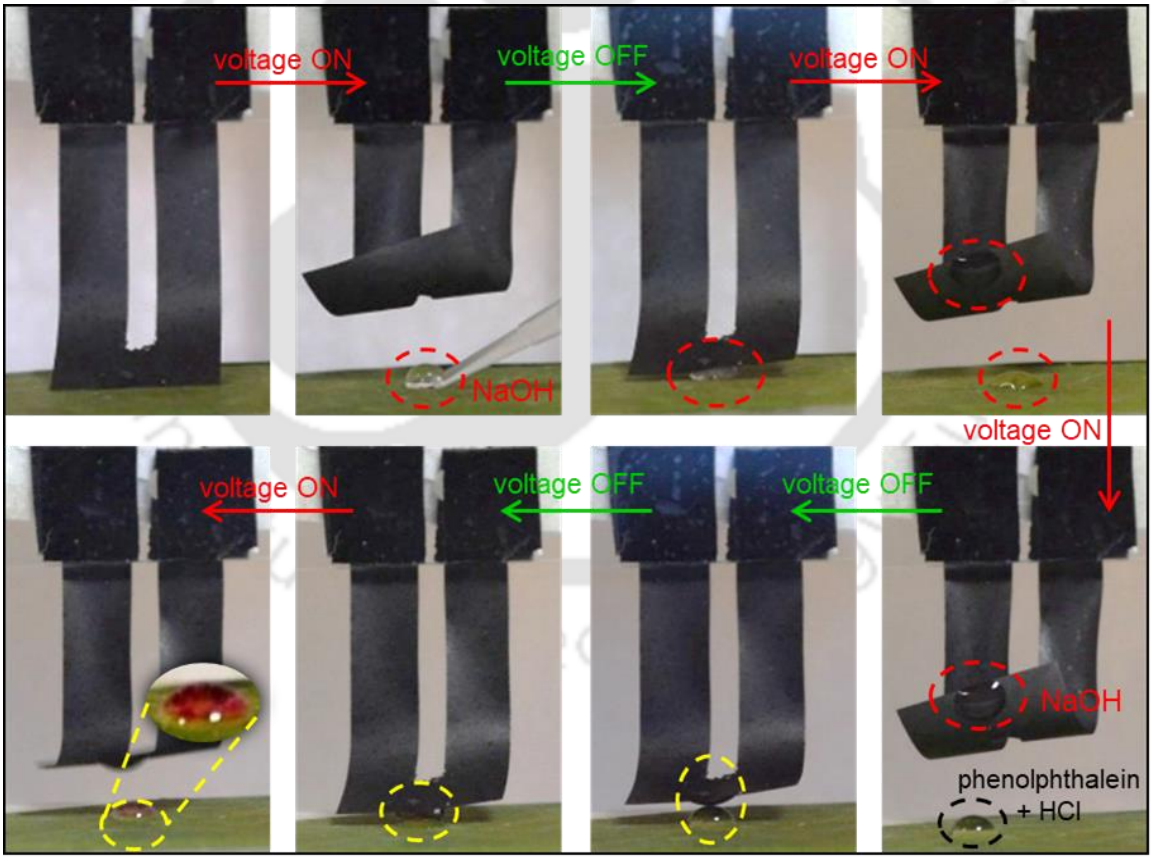

Figure 2.11: *Performance of acid−base titration in the microliter length scale. Snapshots showing titration between HCl and NaOH carried out by a U-shaped r-GO/agar device by taking phenolphthalein as the indicator. The appearance of pink colour denotes reaching end point.*

touched each other they broke down and mixed together to complete the reaction. The occurrence of the end-point of the titration was monitored from the appearance of pink color of the indicator, as shown in the snapshots of Figure 2.11. This experiment along with the one shown in Figure 2.9a suggest that the r-GO/agar-based cantilever is chemically inert to a wide range of pH values (pH = 2 to 12), making it suitable for a variety of chemical applications.

The liquid handling capability of the r-GO/agar bilayer strip was also studied by using IR light of intensity 5500 lux. Typically, a 10 µL droplet of water was placed on a hydrophobic taro leaf surface. A rectangular strip (dimensions 15 × 5 × 0.023 mm^3) of the r-GO/agar bilayer membrane was cut and fixed onto a steel rod in such a way that it can touch the water droplet. When the IR light was turned on, the strip bent in the upward direction. During that period a 10 µL water droplet was placed under it. As the IR light was turned off, the strip regained its original shape and touched the water droplet from the r-GO side of the strip. The water droplet got attached to the r-GO surface and moved-up along the bilayer strip when the IR source is turned on again. Now, the taro leaf surface was replaced by a hydrophilic tissue paper and the IR source was turned off. As soon as the water droplet touched the tissue paper it got detached

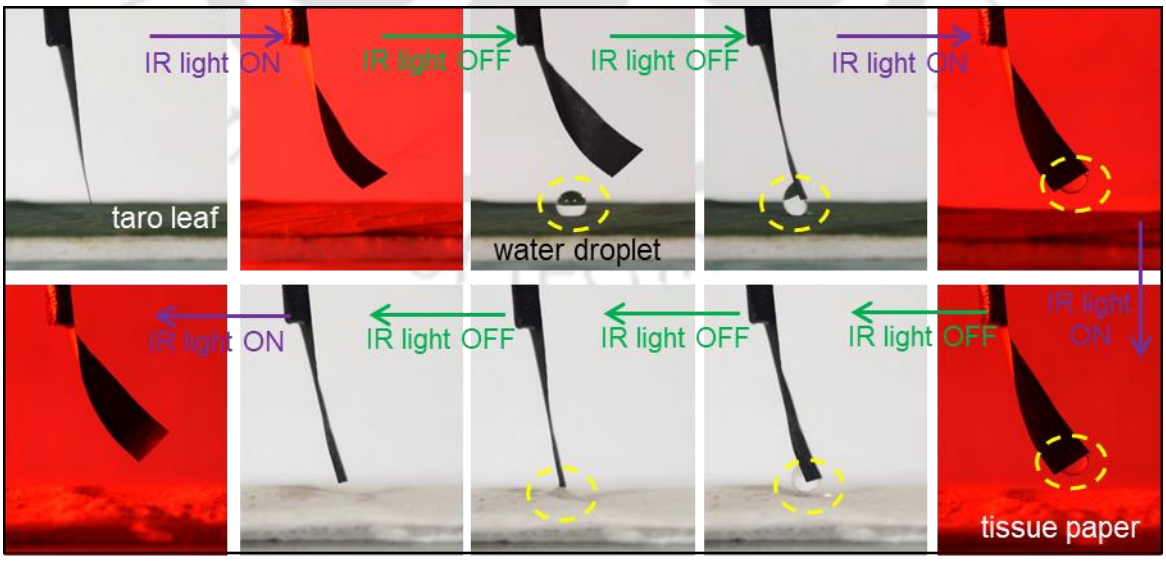

Figure 2.12: *IR-induced droplet lifting: snapshots showing a rectangular-shaped strip of r-GO/agar bilayer membrane picking up a10µL water droplet from a taro leaf surface and its corresponding transfer to a hydrophilic tissue paper.*

from the bilayer strip and the transfer was completed. (Snapshots of the entire process are shown in Figure 2.12).

2.6 Conclusions

This chapter presents a novel technique for the remote manipulation of microdroplets by utilizing electrical potential and IR light. The developed bilayer actuators, composed of reduced graphene oxide and agar, demonstrate the capability to pick up and release microdroplets with a precision of $\pm 5 \times 10^{-8}$ Liters. The accuracy of these bilayer membranes can be further improved by introducing nano and micro-scale surface features to achieve the rose petal like effect. Overall, these systems exhibit significant potential for the development of self-operating miniature chemical reactors and analytical devices. By integrating appropriate microscopy and spectrophotometry techniques, the electrically and light-responsive bilayer membranes can be further miniaturized to manipulate analytes at the nano or picogram scale. Considering the vast array of available two-dimensional nanomaterials and the numerous possibilities for surface modification, this method could pave the way for the creation of responsive materials with specialized wettability surfaces, enabling advanced studies and applications in reduced-dimensional chemistry.

2.7 References

1 Z. Dong, J. Ma and L. Jiang, *ACS Nano*, 2013, **7**, 10371–10379.

2 C. L. Hansen, E. Skordalakest, J. M. Berger and S. R. Quake, *Proc. Natl. Acad. Sci. U.S.A.*, 2002, **99**, 16531–16536.

3 T. S. Frost, V. Estrada, L. Jiang and Y. Zohar, *Microfluid. Nanofluid.*, 2019, **23**, 1–13.

4 S. J. Kim, F. Wang, M. A. Burns and K. Kurabayashi, *Anal. Chem.*, 2009, **81**, 4510–4516.

5 C. Y. Lee, C. L. Chang, Y. N. Wang and L. M. Fu, *Int. J. Mol. Sci.*, 2011, **12**, 3263–3287.

6 K. Ward and Z. H. Fan, *J. Micromech. Microeng.*, 2015, **25**, 094001.

7 A. J. DeMello, *Nature*, 2006, **442**, 394–402.

8 B. H. Weigl and P. Yager, *Science*, 1999, **283**, 346–347.

9 H. Song, D. L. Chen and R. F. Ismagilov, *Angew. Chem. Int. Ed.*, 2006, **45**, 7336–7356.

10 V. Srinivasan, V. K. Pamula and R. B. Fair, *Anal. Chim. Acta.*, 2004, **507**, 145–150.

11 A. Kecskemeti and A. Gaspar, *Anal. Chim. Acta.*, 2018, **1021**, 1–19.

12 W. Y. Lin, Y. Wang, S. Wang and H. R. Tseng, *Nano Today*, 2009, **4**, 470–481.

13 D. Liu, S. Cito, Y. Zhang, C.-F. Wang, T. M. Sikanen, H. A. Santos, D. Liu, S. Cito, Y. Zhang, C. Wang, T. M. Sikanen and H. A. Santos, *Adv. Mater.*, 2015, **27**, 2298–2304.

14 M. Thiele, A. Knauer, A. Csáki, D. Mallsch, T. Henkel, J. M. Köhler and W. Fritzsche, *Chem. Eng. Technol.*, 2015, **38**, 1131–1137.

15 Y. Liu and G. Li, *Sci. Rep.*, 2018, **8**, 1–9.

16 B. Zheng, L. S. Roach and R. F. Ismagilov, *J. Am. Chem. Soc.*, 2003, **125**, 11170–11171.

17 Y. Zhu, L. N. Zhu, R. Guo, H. J. Cui, S. Ye and Q. Fang, *Sci. Rep.*, 2014, **4**, 1–9.

18 W. D. Ristenpart, J. Wan and H. A. Stone, *Anal. Chem.*, 2008, **80**, 3270–3276.

19 S. Mashaghi, A. Abbaspourrad, D. A. Weitz and A. M. van Oijen, *TrAC Trends Anal. Chem.*, 2016, **82**, 118–125.

20 D. Simon, F. Obst, S. Haefner, T. Heroldt, M. Peiter, F. Simon, A. Richter, B. Voit and D. Appelhans, *React. Chem. Eng.*, 2018, **4**, 67–77.

21 A. B. Theberge, F. Courtois, Y. Schaerli, M. Fischlechner, C. Abell, F. Hollfelder and W. T. S. Huck, *Angew. Chem. Int. Ed.*, 2010, **49**, 5846–5868.

22 Q. Zhang, L. He, X. Zhang, D. Tian and L. Jiang, *ACS Nano*, 2020, **14**, 1436–1444.

23 Q. Meng, B. Xu, M. He, R. Bian, L. Meng, P. Wang, L. Jiang and H. Liu, *ACS Appl. Mater. Interfaces*, 2018, **10**, 26819–26824.

24 T. S. Kaminski, O. Scheler and P. Garstecki, *Lab Chip*, 2016, **16**, 2168–2187.

25 L. Shang, Y. Cheng and Y. Zhao, *Chem. Rev.*, 2017, **117**, 7964–8040.

26 A. Suea-Ngam, P. D. Howes, M. Srisa-Art and A. J. Demello, *Chem. Commun.*, 2019, **55**, 9895–9903.

27 Y. Ding, P. D. Howes and A. J. Demello, *Anal. Chem.*, 2020, **92**, 132–149.

28 K. I. Ohno, K. Tachikawa and A. Manz, *Electrophoresis*, 2008, **29**, 4443–4453.

29 G. M. Walker and D. J. Beebe, *Lab Chip*, 2002, **2**, 131–134.

30 J. A. Lv, Y. Liu, J. Wei, E. Chen, L. Qin and Y. Yu, *Nature 2016 537:7619*, 2016, **537**, 179–184.

31 D. A. Duford, D. D. Peng and E. D. Salin, *Anal. Chem.*, 2009, **81**, 4581–4584.

32 X. Lv, W. Wang and H. Yu, *Adv. Eng. Mater.*, 2019, **21**, 1900977.

33 L. Zhang, A. Parison and Y. He, *Adv. Powder Technol.*, 2017, **28**, 2886–2892.

34 R. Z. Gao, M. Hébert, J. Huissoon and C. L. Ren, *HardwareX*, 2020, **7**, e00096.

35 P. Garstecki, S. T. S. Kaminski, P. Garstecki and T. S. Kaminski, *Chem. Soc. Rev.*, 2017, **46**, 6210–6226.

36 Y. Ma, J. Thiele, L. Abdelmohsen, J. Xu and W. T. S. Huck, *Chem. Commun.*, 2013, **50**, 112–114.

37 P. Zhu, T. Kong, X. Tang and L. Wang, *Nat. Commun.*, 2017, **8**, 1–10.

38 G. McHale and M. I. Newton, *Soft Matter*, 2011, **7**, 5473–5481.

39 Z. Xin and T. Skrydstrup, *Angew. Chem. Int. Ed.*, 2019, **58**, 11952–11954.

40 L. Zhang, K. Chen, H. Zhang, B. Pang, C.-H. Choi, A. S. Mao, H. Liao, S. Utech, D. J. Mooney, H. Wang, D. A. Weitz, L. Zhang, K. Chen, H. Zhang, B. Pang, H. Wang, C. Choi, A. S. Mao, S. Utech, D. J. Mooney, D. A. Weitz and H. Liao, *Small*, 2018, **14**, 1702955.

41 F. Vinet, P. Chaton and Y. Fouillet, *Microelectron. Eng.*, 2002, **61–62**, 41–47.

42 P. A. Basilio, A. M. Torres Rojas, E. Corvera Poiré and L. F. Olguín, *Microfluid. Nanofluid.*, 2019, **23**, 1–11.

43 X. Tang, P. Zhu, Y. Tian, X. Zhou, T. Kong and L. Wang, *Nat. Commun.*, 2017, **8**, 1–10.

44 J. N. Wang, Y. Q. Liu, Y. L. Zhang, J. Feng and H. B. Sun, *NPG Asia Mater.*, 2018, **10**, e470–e470.

45 Y. Zhou, H. Bi, X. Xie and L. Sun, *8th Annual IEEE International Conference on Nano/Micro Engineered and Molecular Systems*, 2013, 911–914.

46 H. Bi, K. Yin, X. Xie, Y. Zhou, S. Wan, F. Banhart and L. Sun, *Nanoscale*, 2013, **5**, 9123–9128.

47 W. Sang, L. Zhao, R. Tang, Y. Wu, C. Zhu and J. Liu, *Macromol. Mater. Eng.*, 2017, **302**, 1700239.

48 T. Y. Zhang, Q. Wang, N. Q. Deng, H. M. Zhao, D. Y. Wang, Z. Yang, Y. Liu, Y. Yang and T. L. Ren, *Appl. Phys. Lett.*, 2017, **111**, 121901.

49 Q. Wang, Y. T. Li, T. Y. Zhang, D. Y. Wang, Y. Tian, J. C. Yan, H. Tian, Y. Yang, F. Yang and T. L. Ren, *Appl. Phys. Lett.*, 2018, **112**, 133902.

50 L. Chang, M. Huang, K. Qi, Z. Jing, L. Yang, P. Lu, Y. Hu and Y. Wu, *Macromol. Mater. Eng.*, 2019, **304**, 1800688.

51 B. Han, H.-B. Sun, L. Zhu, Y.-Y. Gao and Y.-L. Zhang, *Opt. Lett.*, 2019, **44**, 1363–1366.

52 D. R. Dreyer, S. Park, C. W. Bielawski and R. S. Ruoff, *Chem. Soc. Rev.*, 2009, **39**, 228–240.

53 S. Stankovich, D. A. Dikin, G. H. B. Dommett, K. M. Kohlhaas, E. J. Zimney, E. A. Stach, R. D. Piner, S. B. T. Nguyen and R. S. Ruoff, *Nature*, 2006, **442**, 282–286.

54 G. Eda and M. Chhowalla, *Adv. Mater.*, 2010, **22**, 2392–2415.

55 S. Pei and H. M. Cheng, *Carbon*, 2012, **50**, 3210–3228.

56 J. Zhang, H. Yang, G. Shen, P. Cheng, J. Zhang and S. Guo, *Chem. Commun.*, 2010, **46**, 1112–1114.

57 X. Chen, X. Fu, L. Huang, J. Xu and X. Gao, *Carbohydr. Polym.*, 2021, **265**, 118076.

58 M. Lahaye and C. Rochas, *International Workshop on Gelidium*, 1991, 137–148.

59 Y. H. Pandya, M. Bakshi, A. Sharma and H. Pandya, *Pharm. Innov. J.*, 2022, **11**, 1151–1157.

60 D. W. Renn, *Ind. Eng. Chem. Pro. Res. Dev.*, 1984, **23**, 17–21.

61 C. M. Collins and M. Safiuddin, *Infrastruct.*, 2022, **7**, 46.

62 Y. Liu, J. Tang, R. Wang, H. Lu, L. Li, Y. Kong, K. Qi and J. H. Xin, *J. Mater. Chem.*, 2007, **17**, 1071–1078.

63 M. Zhang, S. Feng, L. Wang and Y. Zheng, *Biotribology*, 2016, **5**, 31–43.

64 Y. T. Cheng, D. E. Rodak, C. A. Wong and C. A. Hayden, *Nanotechnol.*, 2006, **17**, 1359.

65 A. Marmur, *Langmuir*, 2004, **20**, 3517–3519.

66 D. Ebert and B. Bhushan, *J. Colloid Interface Sci.*, 2012, **384**, 182–188.

67 S. Parra-Vicente, P. F. Ibáñez-Ibáñez, M. Cabrerizo-Vílchez, I. Sánchez-Almazo, M. Á. Rodríguez-Valverde and F. J. M. Ruiz-Cabello, *Colloids Surf. B Biointerfaces*, 2024, **236**, 113832.

68 B. Bhushan and M. Nosonovsky, *Philos. Trans. R. Soc. A*, 2010, **368**, 4713–4728.

69 L. Almonte, C. Pimentel, E. Rodríguez-Cañas, J. Abad, V. Fernández and J. Colchero, *Nano Select*, 2022, **3**, 977–989.

70 Q. Wan, X. Hu, T. Yu, P. Guo, J. Wang, H. Shi and S. Chen, *Langmuir*, 2024, **40**, 15196–15204.

71 K. Y. Yeh, K. H. Cho, Y. H. Yeh, A. Promraksa, C. H. Huang, C. C. Hsu and L. J. Chen, *Nanotechnol.*, 2014, **25**, 345303.

72 S. Bandyopadhyay, A. Shristi, V. Kumawat, A. Gope, A. Mukhopadhyay, S. Chakraborty and R. Mukherjee, *Langmuir*, 2023, **39**, 6051–6060.

73 K. Y. Yeh, L. J. Chen and J. Y. Chang, *Langmuir*, 2008, **24**, 245–251.

74 L. Feng, Y. Zhang, J. Xi, Y. Zhu, N. Wang, F. Xia and L. Jiang, *Langmuir*, 2008, **24**, 4114–4119.

75 F. Kim, J. Luo, R. Cruz-Silva, L. J. Cote, K. Sohn and J. Huang, *Adv. Funct. Mater.*, 2010, **20**, 2867–2873.

76 K. Ai, Y. Liu, L. Lu, X. Cheng and L. Huo, *J. Mater. Chem.*, 2011, **21**, 3365–3370.

77 J. Dong, P. L. Carpinone, G. Pyrgiotakis, P. Demokritou and B. M. Moudgil, *KONA Powder Part. J.*, 2020, **37**, 224–232.

78 G. T. S. How, A. Pandikumar, H. N. Ming and L. H. Ngee, *Sci. Rep.*, 2014, **4**, 1–8.

79 S. Fang, D. Huang, R. Lv, Y. Bai, Z. H. Huang, J. Gu and F. Kang, *RSC Adv.*, 2017, **7**, 25773–25779.

80 T. N. Lin, M. R. Inciong, S. R. M. S. Santiago, T. W. Yeh, W. Y. Yang, C. T. Yuan, J. L. Shen, H. C. Kuo and C. H. Chiu, *Sci. Rep.*, 2016, **6**, 1–9.

81 Q. Zhao, J. W. C. Dunlop, X. Qiu, F. Huang, Z. Zhang, J. Heyda, J. Dzubiella, M. Antonietti and J. Yuan, *Nat. Commun.*, 2014, **5**, 1–8.

82 R. K. Gogoi, K. Saha, J. Deka, D. Brahma and K. Raidongia, *J. Mater. Chem. A*, 2017, **5**, 3523–3533.

83 R. K. Gogoi and K. Raidongia, *Adv. Mater.*, 2017, **29**, 1701164.

84 R. K. Gogoi, A. B. Neog, N. Sarmah and K. Raidongia, *J. Mater. Chem. A*, 2019, **7**, 21157–21167.

85 S. J. Palmer, *Phys. Educ.*, 1976, **11**, 119.

Chapter 3

Application of reduced graphene oxide-based actuators for real-time chemical sensing of liquid and vapour phase contaminants

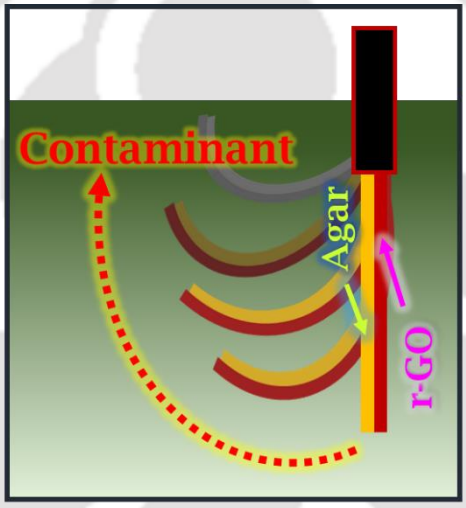

New J. Chem., 2021, **45**, 16883-16891.

Summary

The real-time detection of contaminants dissolved in liquid media is of paramount importance for various technological and industrial applications. This work explores the feasibility of utilizing reconstructed layered materials-based responsive membranes for *in-situ* detection of chemical contaminants in liquid phases. A bilayer membrane, created through sequential vacuum filtration of reduced graphene oxide (r-GO) and agar (r-GO/agar), exhibits significant responsiveness to the presence of solvent vapours in the surrounding atmosphere. The shape-morphing property of the r-GO/agar membrane is attributed to differential changes in the mechanical properties of its individual components. Rectangular strips of this bilayer membrane demonstrate shape-transforming properties within liquid media. Depending on the chemical nature of the molecules within the liquid medium, the r-GO/agar membrane strips bend at a specific rate to form a coil-like shape. The original shape of the strips is easily restored after immersion in water or drying in air. The bending angle and response time of the r-GO/agar strips are sensitive to trace amounts of impurities in the solvent system. This sensitivity can be harnessed for detecting contaminants in liquid phases, such as trace amounts of water molecules in acetone or various alcohol molecules in toluene.

3.1 Introduction

The development of novel systems capable of detecting trace amounts of one liquid within another is essential for technological and industrial operations.[1,2] For instance, identifying small amounts of water in organic solvents is crucial for ensuring safety in chemical laboratories and in the production of pharmaceuticals and other vital chemicals.[3,4] Similarly, detecting organic contaminants in water is vital for monitoring environmental water bodies, drinking water technologies, and the food industry.[5–8] Accurate measurement of water content in oil provides valuable insights into the dynamic behaviour of various emulsion-based systems.[1,9,10] Additionally, excessive water in lubricants can lead to abrasive wear and corrosion of machinery, underscoring the importance of monitoring aqueous contaminants in these substances.[2]

Given its practical importance, novel techniques are being developed for the easy, quick, and real-time detection of liquid molecules within the matrix of another liquid. Notable examples include photoluminescent (PL)-based sensors, NMR spectroscopy-based techniques, and titration-based methods. PL-based methods involve detecting changes in the luminescence properties of fluorophores when they come into contact with water molecules, using a fluorimeter instrument. Commonly used fluorophores for this purpose include quantum dots, fluorescent organic molecules, metal-organic hybrid materials, metal-organic frameworks, polymers, and ceramics.[8,11–16] Similarly, in ^{19}F NMR spectroscopy-based sensing, anhydrous fluoride reagents are used to detect trace amounts of water dissolved in organic solvents.[17] All these processes involve highly complicated and complex synthesis procedures as well as expensive instrumentation.[18] Additionally, the organic-water probes used in these methods are rarely recoverable, making them unsuitable for long-term use.[4]

Given their broad applicability across diverse fields such as sensing,[19] robotics,[20] drug delivery,[21] artificial muscles,[22] and space technology,[23] smart materials have been synthesized

from a variety of substances, including polymers,[24] alloys,[25] ceramics,[26] and nanomaterials.[27] Recently, innovative smart bilayer membranes have been developed by assembling exfoliated layers of two-dimensional materials.[28,29] Layered materials such as graphite, V_2O_5, MoS_2, and clays consist of 2D sheets stacked together through weak forces like van der Waals attractions or hydrogen bonding. These 2D sheets can be exfoliated into individual nanosheets and reassembled into macroscopic membranes, known as reconstructed layered materials. Smart materials fabricated from these reconstructed layered materials offer numerous advantages, including straightforward fabrication techniques, the potential for both pre- and post-assembly modifications, ease of scalability, high sensitivity, and robustness.[19,28–31] Notable examples of bilayer membrane-based smart materials include GO-r-GO,[32,33] GO/CNT,[34] vermiculite/GO,[29] vermiculite/montmorillonite,[28] and GO/PPy(polypyrrole)[35] bilayer membranes. These membranes exhibit highly reversible shape-morphing characteristics in response to multiple stimuli, such as organic solvent vapors, humidity, temperature, and light.[28,29] Most smart materials made from layered structures show responsiveness only in air, not in liquid media. However, there are notable exceptions. For example, actuators made from asymmetrically modified graphene films[36] and vermiculite/graphene oxide[29] bilayer membranes can function effectively in liquid environments, demonstrating their unique capabilities compared to other layered smart materials. Strips of surface-modified graphene film show reversible swing motion upon cyclic voltammetric (CV) scanning in 1M $NaClO_4$ electrolyte.[36] Similarly, strips from PPy/graphene[37] bilayer films and vermiculite/graphene oxide[29] bilayer membranes exhibit reversible bending behavior in solvents with contrasting polarity. Additionally, a few polymer-based materials have demonstrated responsiveness in liquid media, though their potential for detecting contaminants or impurities in such environments remains unexplored.[38–41]

3.2 Scope of the present investigation

Significant progress has been made in the field of smart actuators across a wide range of applications; however, their potential for detecting contaminants or impurities in liquid media remains largely unexplored. To the best of our knowledge, reconstructed bilayer membrane-based actuators have not yet been employed for the detection of trace amounts of liquid molecules dispersed in another liquid medium. In this work, we propose an alternative method for the real-time detection of trace chemicals in a liquid medium by monitoring the shape changes of smart material. We fabricated responsive bilayer membranes through sequential vacuum filtration of reduced graphene oxide (r-GO) and agar dispersions. U-shaped strips of the r-GO/agar bilayer membrane were utilized to induce chemical reactions in microdroplets using electrical potential and infrared light as remote triggers.[42] Additionally, various r-GO and GO-based composites have been explored for applications such as photoelectrochemical sensing of prostate-specific antigen and H_2S screening.[43–47] However, these applications typically require sophisticated instrumentation and are applicable to very specific systems. The bilayer strips of r-GO/agar demonstrated excellent responsiveness in liquid media, showing the capability to detect trace amounts of liquid contaminants within another liquid. Thus, the r-GO/agar membrane holds potential for applications in liquid medium sensing and the detection of chemical vapours under ambient atmospheric conditions.

3.3 Experimental section

Materials: Graphite powder and hydrogen peroxide (H_2O_2) were purchased from Sigma-Aldrich. Potassium permanganate ($KMnO_4$), sulfuric acid(H_2SO_4), hydrochloric acid (HCl), acetone and *N*,*N*-dimethylformamide (DMF) were purchased from Merck.

Preparation of graphene oxide and reduced graphene oxide:

Modified Hummers' method was followed for the synthesis of Graphene Oxide (GO). 2 g of graphite powder was added to 50 ml of concentrated H_2SO_4,[48] maintaining a temperature below

5 °C. Under constant stirring, 6 g of $KMnO_4$ was slowly added and stirred for additional 2 hours at 35 °C. This step was followed by slow addition of 100 ml of deionised (DI) water, after which 10 ml of H_2O_2 was added under constant stirring. The yellow slurry formed was first washed with 10 % HCl solution and later with acetone until the filtrate's pH value increased above 5. For the preparation of r-GO, GO obtained by the above method was dispersed (0.5 mg/ml) in DMF and refluxed at 153 °C for 2 hours.[49]

Preparation of r-GO membranes:

40 ml of the dispersion of r-GO in DMF was subjected to vacuum filtration through a polytetrafluoroethylene (PTFE) membrane of pore size 5 µm. This was followed by drying it at 70 °C for 2 hours. After air drying, reconstructed r-GO membranes could be peeled off easily from the PTFE membrane.

Preparation of agar membranes:

1 mg/ml mixture of agar in DI water was heated at 100 °C until we get a clear solution, which was then poured into a petri dish. The solution cooled down to room temperature and formed a gel-like substance which was then dried in an oven at 70 °C. A semi-transparent agar membrane could be peeled off easily from the petri dish.

Preparation of r-GO/agar bilayer membrane:

Firstly, 40 ml of r-GO (from 0.5 mg/ml GO dispersion) dispersion was vacuum filtered through a PTFE membrane resulting in a greyish-black membrane. After the r-GO membrane appeared to be dried, 20 ml of agar dispersion was filtered through it. Agar dispersion itself was prepared by mixing agar powder in DMF (1 mg/ml) under probe sonication (Labman, Model: PRO-650) for 30 minutes (1s on & 1s off pulse). Thus prepared bilayer membrane of r-GO/agar could be easily peeled off from the PTFE membrane by heating in a hot air oven at 70 °C for 2 hours.

3.4 Characterizations

Atomic Force Microscope (AFM) (Make: Oxford; Model: Cypher) was used for characterizing nanosheets of GO and r-GO. Morphology and cross-section of the membranes were examined by Field Emission Scanning Electron Microscope (FESEM) (Make: Zeiss, Model: Sigma). Membranes of r-GO and GO were characterized by Raman Spectroscopy (Make: Horiba Jobin Vyon, Model: LabRam HR). Bruker D-205505 Cu-Kα radiation (λ = 1.5406 Å) was employed for X-ray diffraction studies. The shape transformations of the bilayer membranes was filmed using a digital camera, Nikon D 5200. The stress-strain curves were recorded in a 5kN Electromechanical Universal Testing Machine (Make: Zwick Roell : Z005TN).

3.5 Results and Discussion

3.5.1 Characterizations of exfoliated nanosheets and membranes

Multi-responsive bilayer membrane of reduced graphene oxide and agar (r-GO/agar) was prepared by vacuum filtering dispersion of agar (in DMF) through a reconstructed r-GO membrane.[42] The r-GO fraction of the membrane was prepared through reduction of GO by heating its dispersion (0.5 mg/mL in DMF) at 153 °C for 2 hours. A digital photo of the starting GO dispersion (inset of Figure 3.1a) along with AFM image of the flakes are shown in the Figure 3.1a. The reduction process did not seem to affect the dispersibility as well as average dimension of the flakes, representative AFM image is shown in Figure 3.1b. Vacuum filtration of the r-GO dispersion in DMF (inset of Figure 3.1b) through a hydrophilic PTFE membrane yielded freestanding r-GO membrane. Homogeneous dispersion of agar was prepared by probe sonicating (1s on and 1s off pulse) the mixture (1 mg/mL in DMF) for 30 minutes. The prepared bilayer membrane of r-GO/agar could be peeled off from the PTFE membrane by heating in a hot air oven (70 °C for 2 hours). Digital images of r-GO/agar bilayer membrane along with

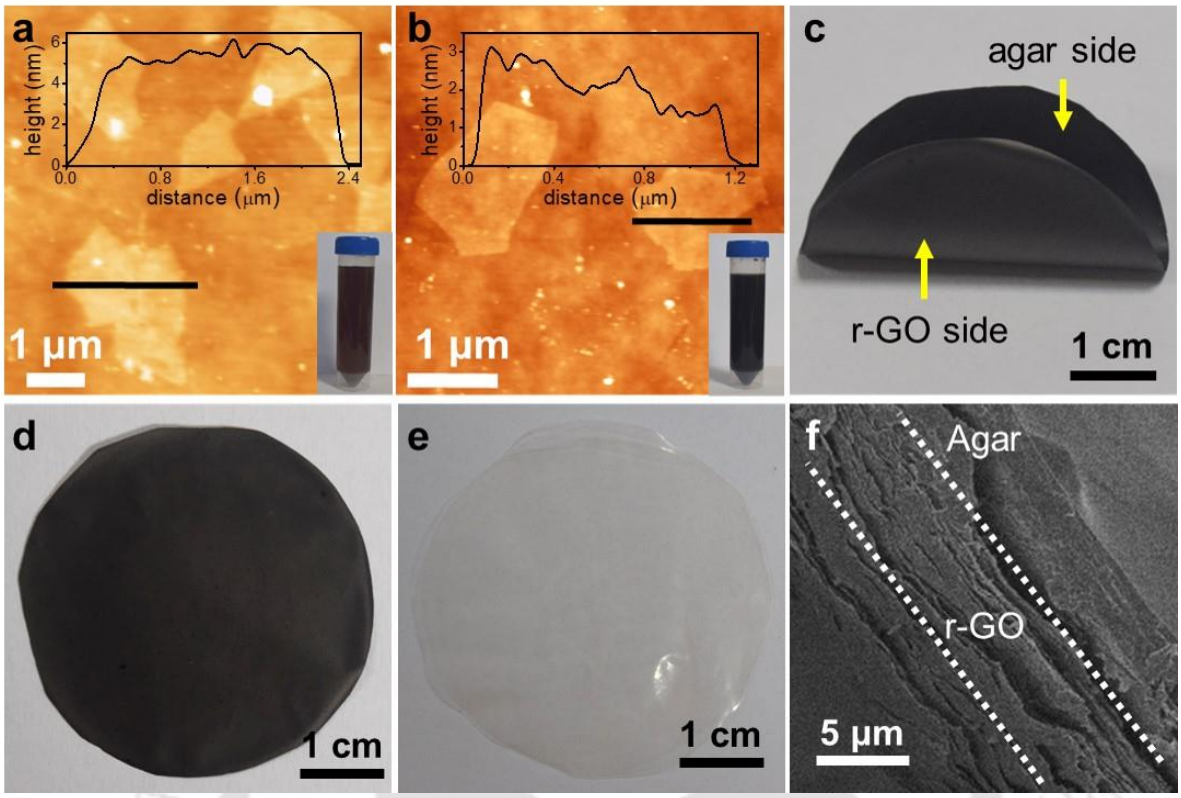

Figure 3.1: AFM images (along with the corresponding height profile of the nanosheets and respective dispersions in DMF in the insets) of (a) GO and (b) r-GO nanosheets. Digital photos of the (c) r-GO/agar bilayer, (d) individual r-GO membrane fabricated by the vacuum-assisted filtration method and (e) agar membrane. (f) Cross-sectional FESEM image of the r-GO/agar bilayer membrane

individual freestanding membranes of r-GO and agar are shown inFigure 3.1c, 3.1d and 3.1e respectively. Raman and XRD characterizations of the reconstructed membranes can be found in the Figure 3.2a and 3.2b respectively. The G band in the Raman spectra signifies in-plane vibrations of sp^2 bonded carbon atoms whereas the D band denotes out of plane vibrations attributed to the presence of structural defects. I_D/I_G is a measure of the defects present on the graphene structure. The peak of the D band for GO membrane was found at 1335 cm^{-1} and the peak of the G band at 1592 cm^{-1}. For the r-GO sample, the peak of D band was found to be at same position (1335 cm^{-1}) while that of G band was shifted downwards to 1587 cm^{-1}.[50] The I_D/I_G ratio was calculated for GO and r-GO to be 1.21 and 1.49 respectively,[51] where I_D is the

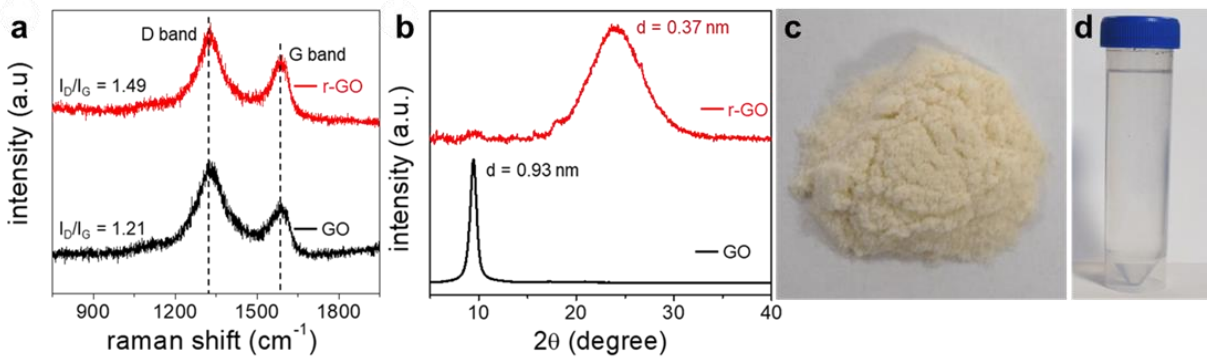

Figure 3.2: *(a) Raman spectra and (b) XRD patterns of GO and r-GO membranes. Digital photos of (c) agar powder and (d) agar dispersion in DMF*

intensity of the D band and I_G is the intensity of the G band. The increase in the I_D/I_G value for r-GO confirms increasing defect concentrations during the reduction process of GO to r-GO.[52] In case of XRD studies, the GO membrane showed a sharp diffraction peak at 2θ value of 9.4° corresponding to an interplanar spacing of 0.93 nm. A broad diffraction pattern with peak corresponding to an interplanar spacing of 0.37 nm (at 2θ value of 24°) appeared in the XRD pattern of the r-GO membrane.

While the r-GO side of the r-GO/agar bilayer membrane appears to be greyish-black, the agar-side looks shiny-black in colour. The lamellar r-GO fraction can be easily distinguished from

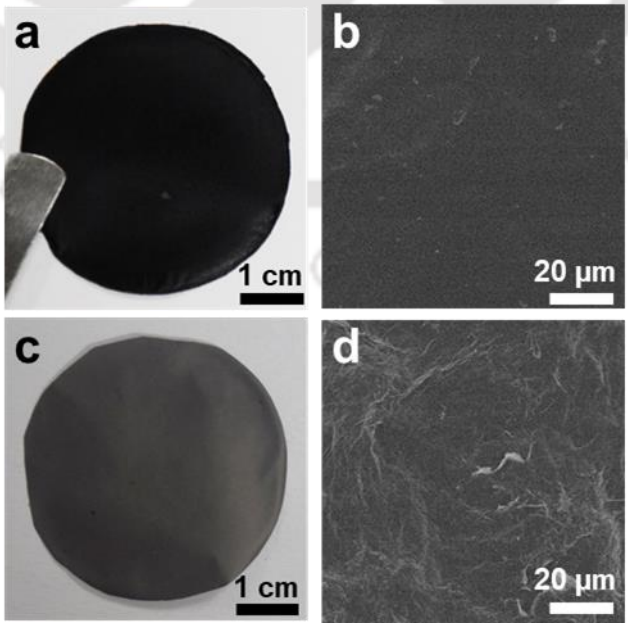

Figure 3.3: *Digital photos of (a) agar side and (c) r-GO side of the bilayer membrane. FESEM images of (b) agar and (d) r-GO sides of the r-GO/agar bilayer membrane.*

the smoother agar side in the cross-sectional FESEM image shown in Figure 3.1f. The FESEM images of the surface of agar and r-GO sides of the bilayer membrane are shown in Figure 3.3b and 3.3d respectively. The surface of agar side is characterized by a smooth morphology, while that of r-GO side can be recognized by the wave-like morphology.

3.5.2 Vapour-induced shape morphing characteristics of r-GO/agar bilayer strips

The shape of the r-GO/agar membrane was found to be responsive towards the presence of solvent vapour in its surrounding. In order to illustrate the responsiveness of r-GO/agar membrane, a rectangular strip (dimensions 25 × 4 × 0.023 mm^3) cut from the bilayer membrane was fixed to a rod and exposed to vapours generated from 10 mL of the respective solvents placed in a 250 mL beaker (at 23 °C). A fixed distance of 3 cm was maintained between the strip and the solvent throughout the experiments. Figure 3.4a and 3.4b shows the experimental

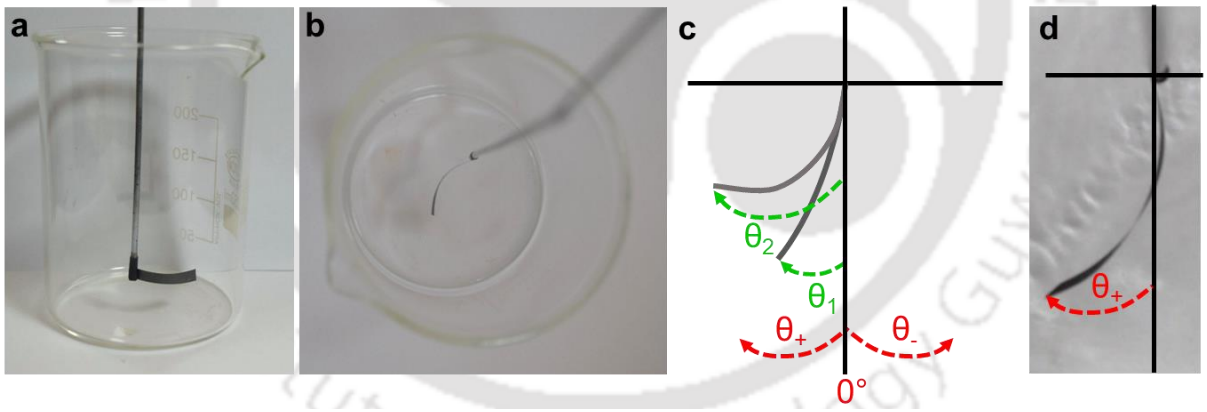

Figure 3.4: *Digital photos showing the experimental setup used for studying the vapour induced shape alteration behaviour of the r-GO/agar bilayer strip (a) side view and (b) top view. (c) Schematic diagram of the design employed for bending angle measurements, and (d) bending angle measured for the r-GO/agar bilayer strips in response to solvent vapours.*

set-up used for studying the solvent vapour induced responsiveness. Upon exposure of ethyl acetate vapours, the strip immediately recognized the changes in the surrounding and responded by bending towards the agar side. Once the strip was taken away from the vapours, it regained its original shape within 40 seconds of exposure to the open-air atmosphere. To

quantify the degree of bending an imaginary straight line was drawn along the axis of the rod, where the strip was fixed. A schematic illustration of the process is shown in Figure 3.4c and 3.4d. When the r-GO/agar strip was aligned with that imaginary axis, the bending angle was considered to be zero degree, when it moved towards left, the angle was counted in positive values. When the tip of the strip moved towards right, the angle was counted in negative values. Greater the extent of bending higher the values of the bending angle. Naturally, the r-GO/agar strip bent towards the agar side, which is in the direction of a positive angle. Upon exposure to vapours, it moved towards the agar side, which increases the bending angle in positive values. The changes in the bending angle in the presence of ethyl acetate vapours as a function of time is shown in the Figure 3.5, and from the slope of this curve, the bending speed of the strip was calculated to be 55 $°s^{-1}$. Upon removal of the ethyl acetate vapours, the strip regained its original configuration with a recovery speed of 77 $°s^{-1}$. Figure 3.6a shows the bending and recovery movements of the strip induced by ethyl acetate environment. This solvent-induced responsiveness study was also carried out in the presence of 2-propanol, acetone, tetrahydrofuran (THF), ethanol, chloroform, dichloromethane (DCM) and methanol vapours.

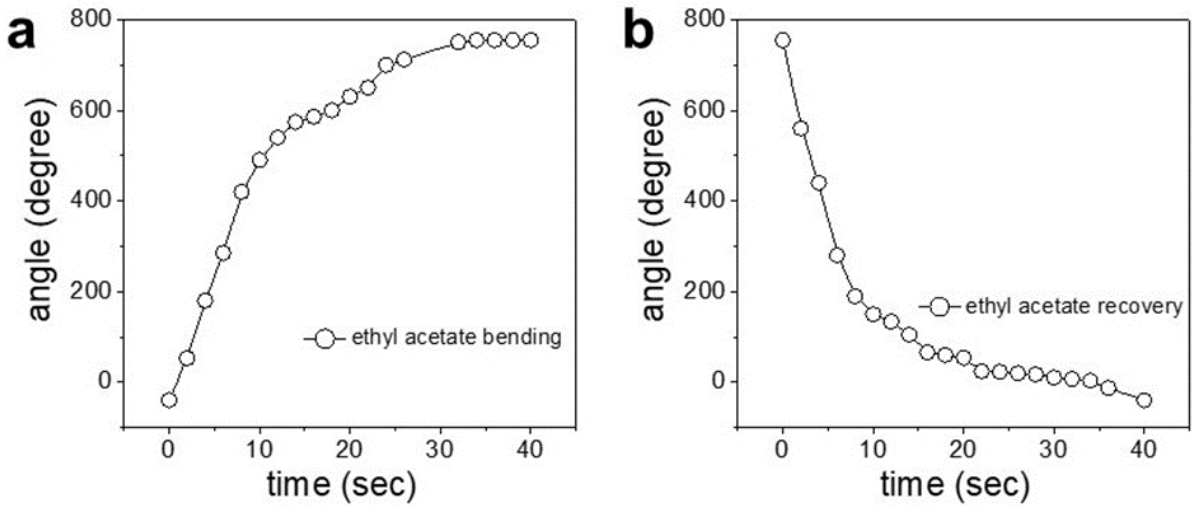

***Figure 3.5**: Plots showing the bending movements of the r-GO/agar bilayer strip (a) in ethyl acetate environment and (b) in open atmosphere*

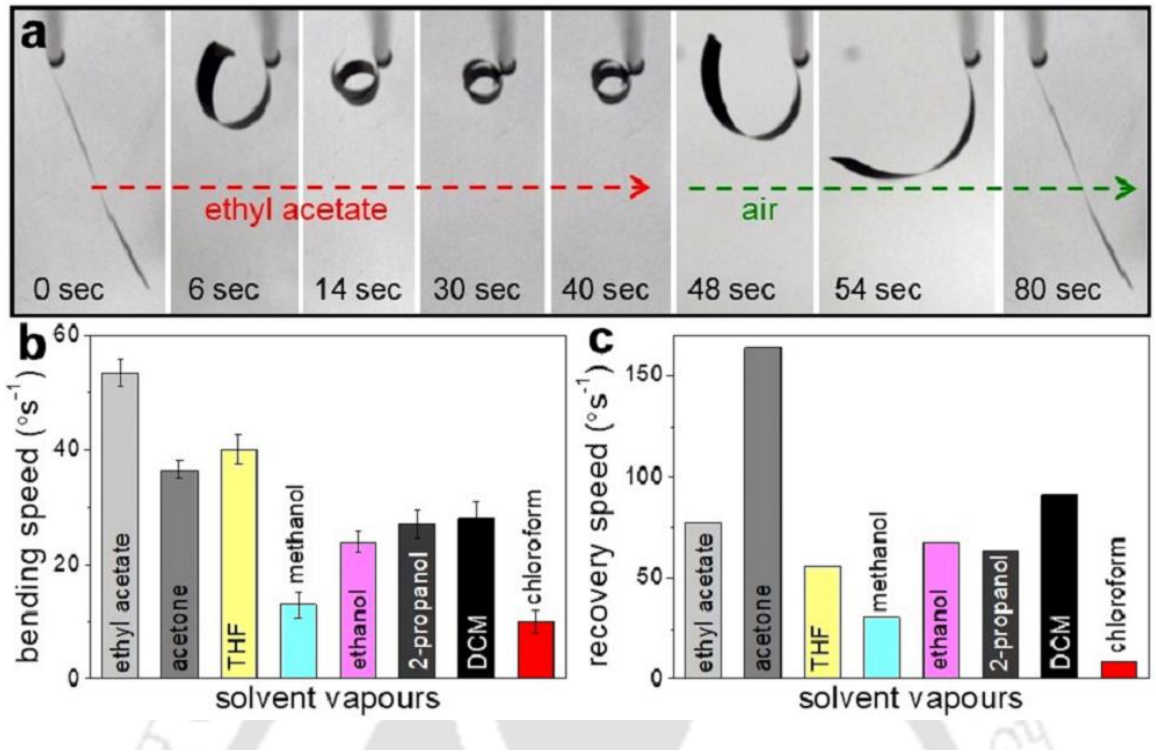

Figure 3.6: *(a) Snapshots showing bending and recovery movements of a bilayer strip upon exposer to ethyl acetate vapours. (b) Bar diagrams representing bending speeds of a bilayer strip upon exposer to different solvent vapours and (c) corresponding recovery speeds after removal of the solvent vapours.*

The strip responded to the vapours of all the solvents by bending towards the agar side with specific bending speeds. Snapshots of the bending and recovery movements of the strip in the presence of 2-propanol, acetone, THF, ethanol, chloroform, DCM and methanol vapours are shown in Figure 3.7a, 3.7b, 3.7c, 3.7d, 3.7e, 3.8a and 3.8b respectively. The bending and the recovery speeds of the bilayer strips in presence of different solvent vapours are compared in Figure 3.6b and 3.6c respectively. For each solvent vapour, the bending experiment was repeated for 50 cycles, and the variations in the bending speed between 1st, 25th and 50th cycles are denoted as error bars in Figure 3.6b.

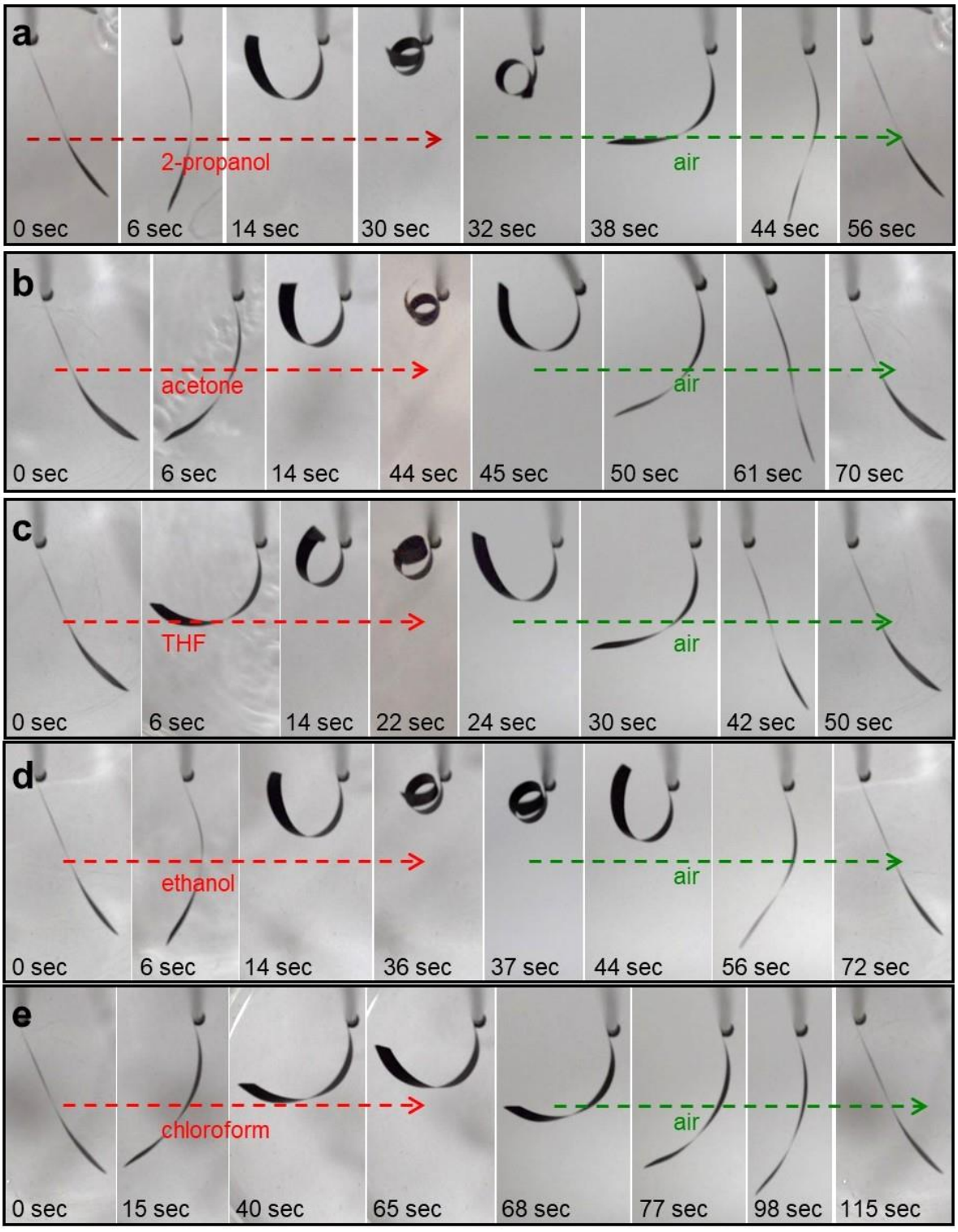

Figure 3.7: *Snapshots showing the bending and recovery movements of a bilayer strip of r-GO/agar bilayer strip in presence of (a) 2-propanol, (b) acetone, (c) THF, (d) ethanol and (e) chloroform vapours.*

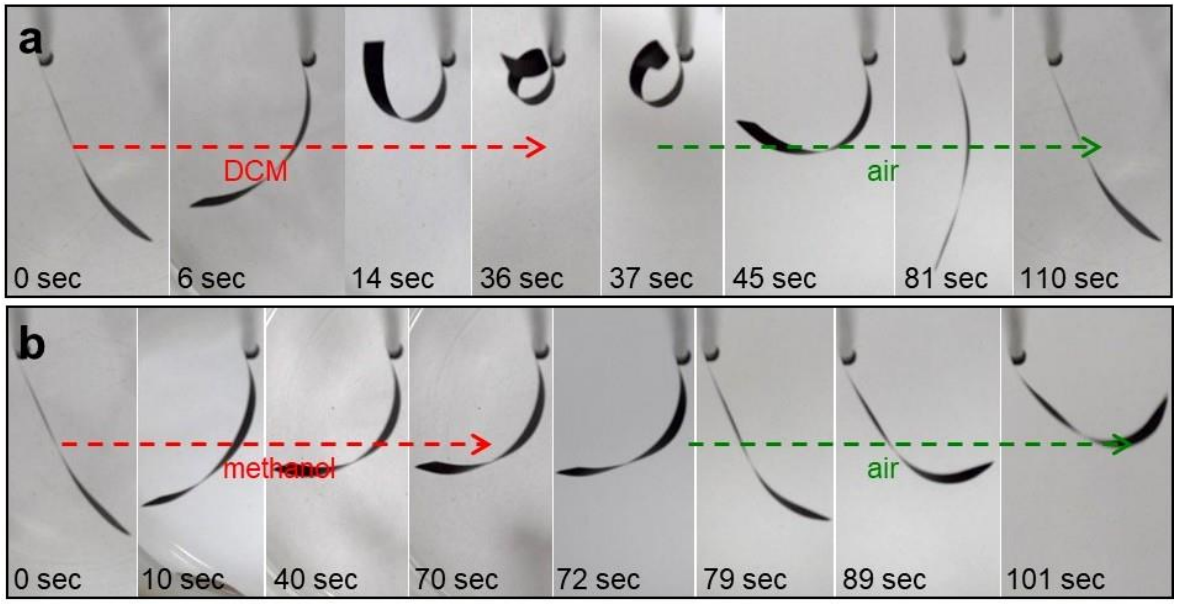

Figure 3.8: *Snapshots showing the bending and recovery movements of a bilayer strip of r GO/agar bilayer membrane in presence of (a) DCM and (b) methanol vapours*

The shape morphing properties of such bilayer systems are attributed to unequal alteration in the mechanical properties of the individual components. In order to study the variation in the mechanical properties of the individual component of the bilayer membrane, bending stiffness values were calculated by using the Lorentzen & Wettre two-point method[28,29] in different environmental conditions. At first, bending stiffness values of individual membranes were measured under air atmosphere, which was followed by repetition of the measurement after being exposed to a particular solvent vapour. Schematic illustration of the bending stiffness measurement process is shown in Figure 3.9a. Lorentzen & Wettre 2-point method was employed to calculate the bending stiffness of the individual strips. Known loads were used to apply a force at one end while keeping the other end of the strip fixed to a glass slide.

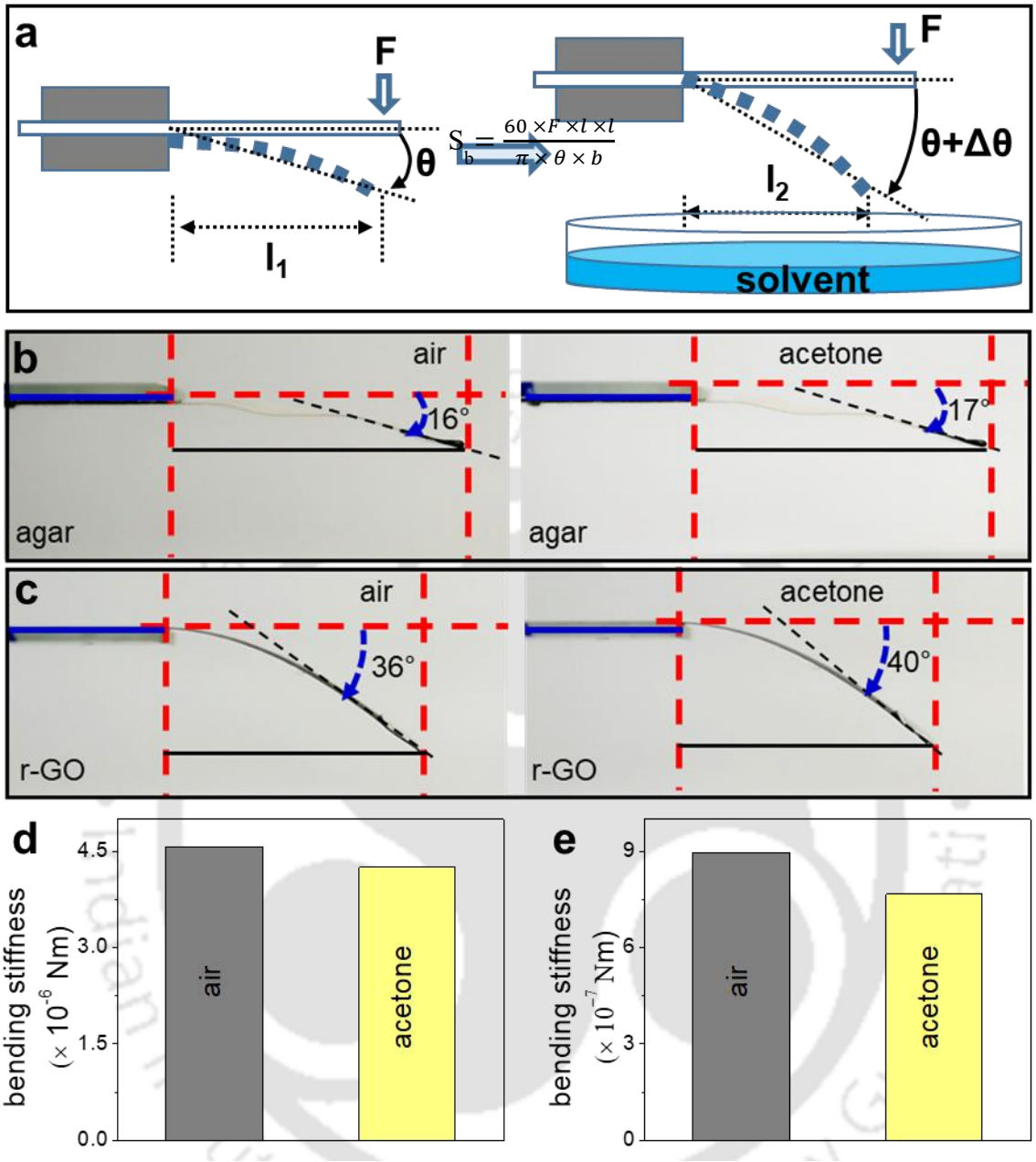

Figure 3.9: *(a) Schematic illustration of the bending stiffness measurements in the presence and absence of solvent vapours using the Lorentzen & Wettre two-point method. Snapshots of (b) agar and (c) r-GO strips with load applied on one end in open atmosphere and on exposing to vapours of acetone. Bar diagrams demonstrating the bending stiffness of (d) agar and (e) r-GO strips in absence and presence of acetone vapours.*

The weight and dimensions of the agar strip used for the experiment was 5.2 mg and 20 mm x 4 mm x 50 µm respectively. Likewise, r-GO strip was handled a load of 2.5 mg having dimensions 20 mm x 4 mm x 42 µm. Bending stiffness (S_b) was calculated using the following equation:

$$S_b = \frac{60 \times F \times l^2}{\pi \times \theta \times b}$$

Where, bending force (F) = weight × gravitational constant, l = distance between the fixed end and the load, θ = deflection, b = width of the strip. At first bending angle was calculated in open atmosphere after which strips were exposed to acetone vapours causing further bending. The changes in the bending stiffness values due to the presence of acetone was calculated and plotted in Figure 3.9d and 3.9e. The bar diagrams reveal that the r-GO strip displayed a greater decrease (14.4 %) in the stiffness values upon exposure to acetone in comparison to that of the agar strip (6.9 %). This uneven change in the stiffness values of the two components of the bilayer membrane upon exposure to solvent vapours is attributed to the bending performance. The irregular alteration in the bending stiffness values in the presence of solvent vapours is accredited to different intercalating nature of the solvent molecules. In order to understand the cause of uneven change in the mechanical properties, the rate of permeation of the solvent vapours through the individual membranes were measured by using a gravimetric method.

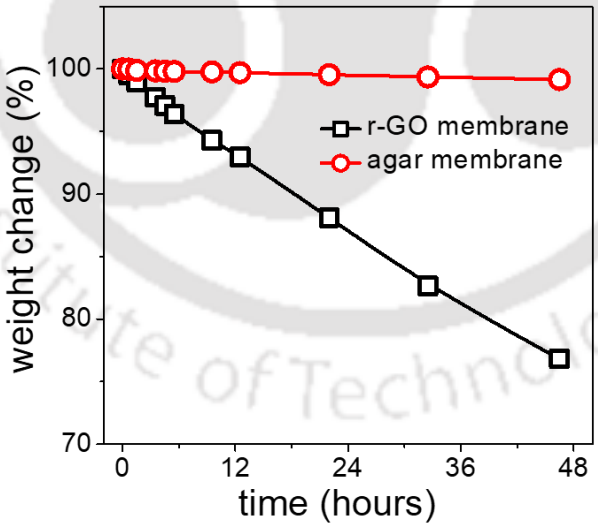

Figure 3.10: *Change in weight % of the vials as a result of evaporation of acetone through the individual membranes. Significant weight loss was found in case of the vial covered with r-GO membrane as compared to that covered with agar membrane.*

Typically, two glass vials were filled-up with acetone and sealed with r-GO and agar membranes by using freshly prepared polydimethylsiloxane (PDMS) elastomer as the glue.

Both the vials were kept in a closed chamber, and maintained a constant humidity of 20 %. The weights of the vials were taken at regular intervals of time to determine the rate of evaporation of acetone vapours through the individual membranes. As can be seen in the Figure 3.10, the decrease in weight was found to be higher in the case of the vial covered with r-GO membrane as compared to that of the agar membrane, suggesting that acetone can penetrate into the r-GO membrane and alter its properties to a extend greater than that of the agar membrane.

3.5.3 Solvent-induced shape transformation of r-GO/agar bilayer strips

The strips of r-GO/agar bilayer membrane also displayed a remarkable shape transforming property inside liquid medium. The responsiveness of the bilayer strip (of dimensions 25 × 4 × 0.023 mm^3) was studied by dipping it directly inside liquid medium. As shown in Figure 3.11a, as soon as the r-GO/agar strip was dipped into acetone, it bents towards the agar side

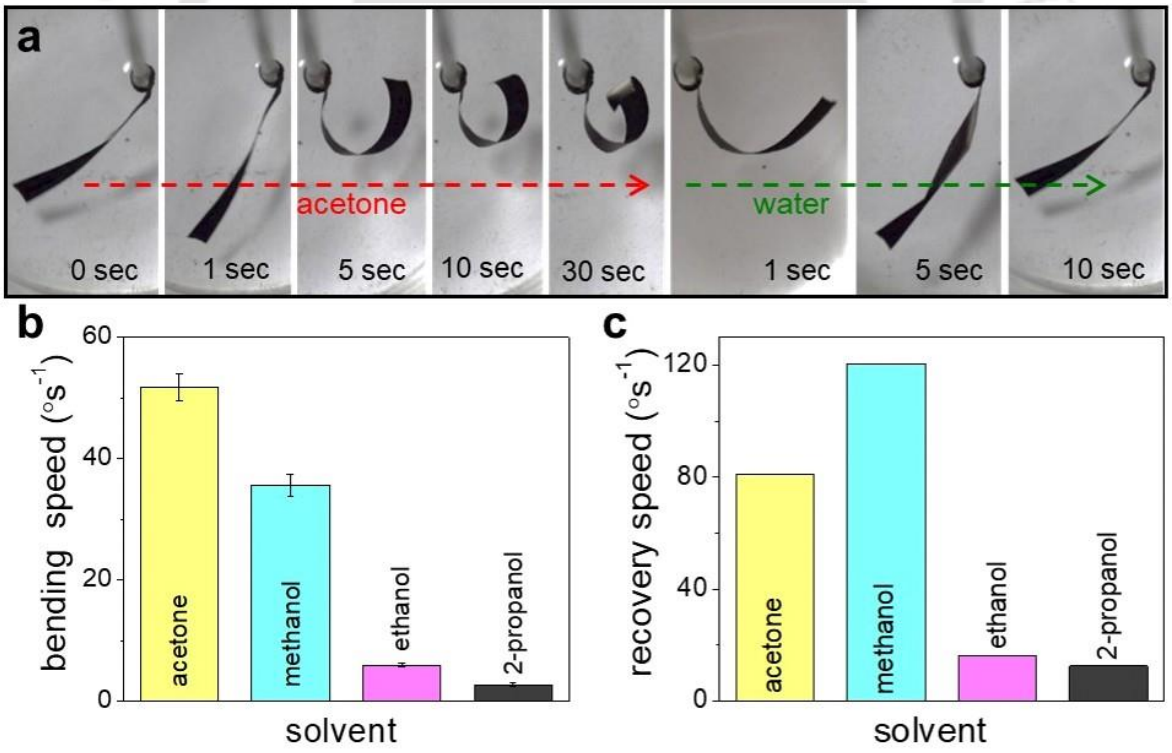

Figure 3.11: *(a) snapshots showing the bending and recovery movements of the bilayer strip upon exposure to ethyl acetate vapours. (b) Bar diagrams representing the bending speeds of the bilayer strip upon exposure to different solvent vapours and (c) the corresponding recovery speeds after the removal of the solvent vapours.*

forming a loop within ~ 30 seconds. The strip stayed in that loop shape, as long as it was submerged into liquid acetone. The bending speed of the strip inside liquid acetone was calculated to be 55º s^{-1}. When the r-GO/agar strip was pulled out of acetone medium and dipped in water, it recovered the original shape within 10 seconds, with a recovery speed of 81º s^{-1}. The snapshots of the bending movement of the bilayer strip inside the acetone-water system are shown in Figure 3.11a. Similar solvent-induced responsiveness of the bilayer membrane inside liquid medium was also investigated with methanol-water, ethanol-water and 2-propanol-water systems, and snapshots of the bending movements are shown in Figure 3.12a, 3.12b and 3.12c respectively. Similar to the acetone, the strip bent towards the agar side after immerging in liquid methanol, ethanol and 2-propanol, and recovered its original configuration after dipping in water. The bending and recovery speeds of the r-GO/agar strip, after immerging

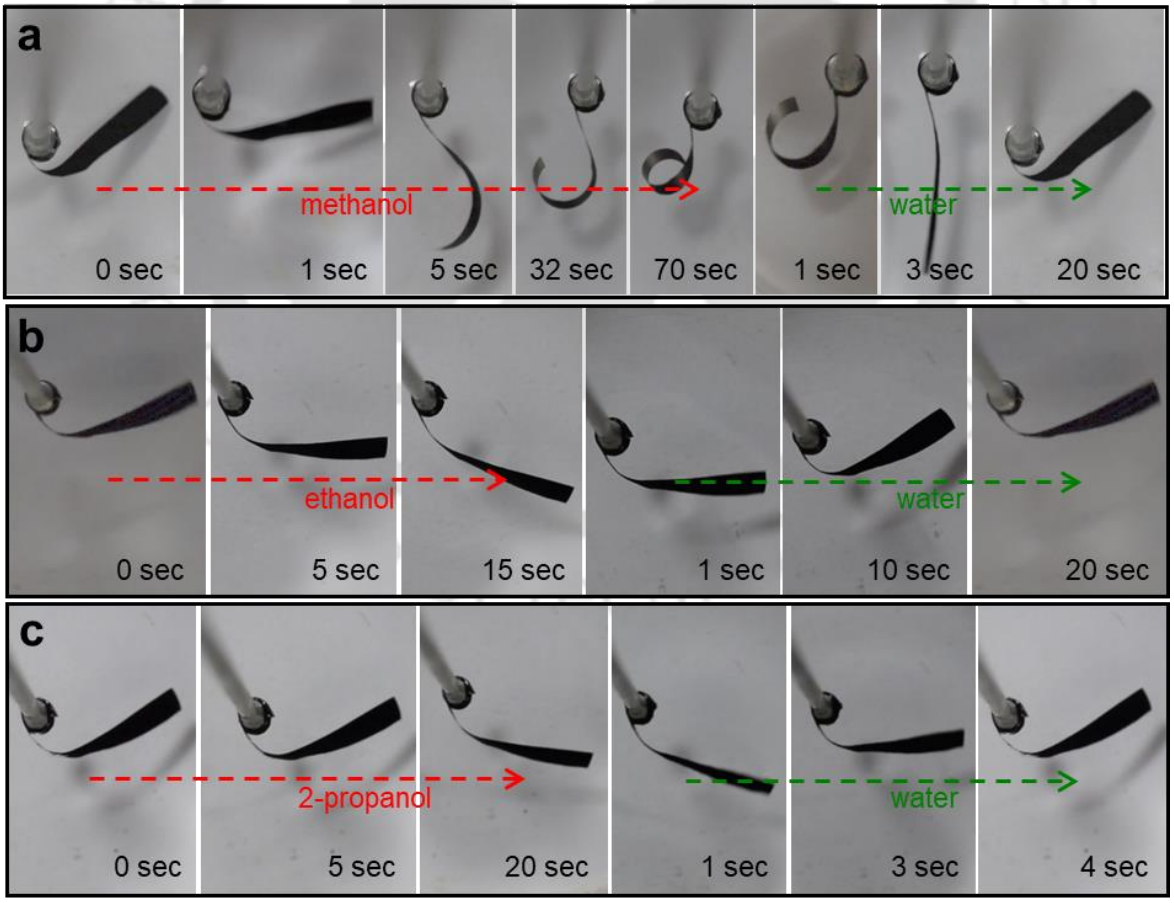

Figure 3.12: *Snapshots showing the bending of a bilayer strip of r-GO/agar bilayer membrane in (a) methanol, (b) ethanol and (c) 2-propanol solvents and its corresponding recovery in water*

and removing from the liquid medium were found to be specific to the chemical nature of the solvent molecules. For example, in the case of methanol, ethanol and 2-propanol the bending speed were calculated to be $50^{o}\ s^{-1}$, $8.5^{o}\ s^{-1}$ and $2.7^{o}\ s^{-1}$, respectively. Similarly, recovery speeds were calculated to be $120.5^{o}\ s^{-1}$, $16^{o}\ s^{-1}$ and $12.5^{o}\ s^{-1}$, for methanol, ethanol and 2-propanol medium respectively. The specific bending and recovering speed of the strip with different solvent molecules could lead to a new kind of electronics-free dart-cheap sensors of solvent molecules. Comparison of the bending and recovery speeds of the bilayer strip inside different solvent systems are shown in the bar diagrams of Figure 3.11b and 3.11c, respectively. The bending and recovery experiments inside liquid systems were repeated with a single bilayer strip for 20 cycles and variations in the bending speed between the 1^{st}, 10^{th} and 20^{th} cycles are presented as error bars in Figure 3.11b.

In order to understand the mechanism of bending inside liquid medium, the effect of solvent molecules in the microstructure of the membranes were studied with the help of X-ray diffraction (XRD). As can be seen from the XRD patterns of Figure 3.13a, the air-dried r-GO strip displayed a broad peak at 2θ value of ~ 24°, corresponding to an interlayer space of

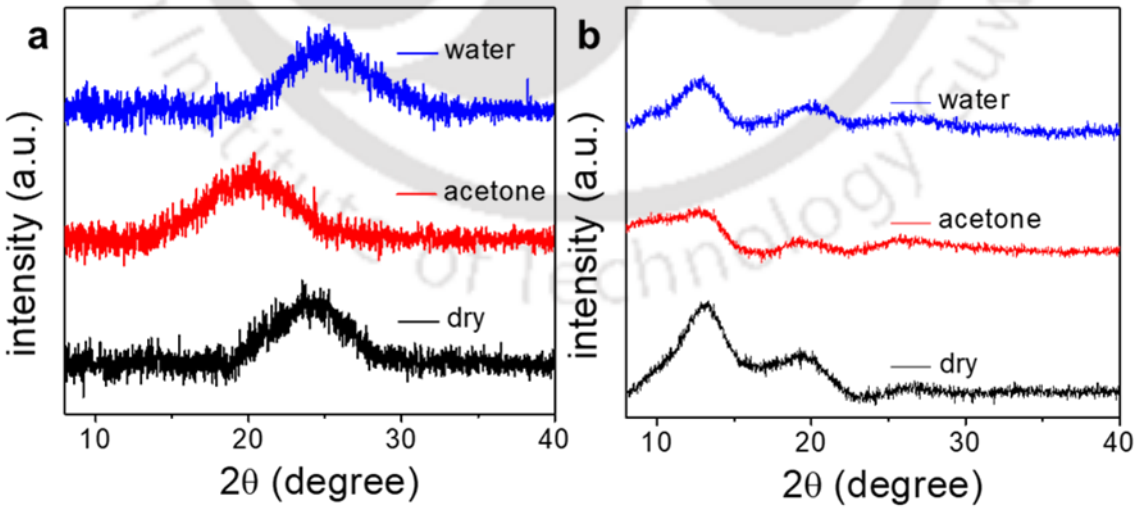

Figure 3.13: *Solvent induced variations in interlayer spacing's of individual membranes: (a) r-GO membrane and (b) agar membrane. Significant variation in d-spacing's was seen in the case of the r-GO membrane but no such definite changes were observed for the agar membrane.*

3.7 Å, (002 reflection). The XRD examination of r-GO strip was repeated after dipping the same in acetone for 15 minutes. The position of the (002) reflection was found to be shifting from 2θ value of 24° to 20° (d = 3.7 Å to 4.4 Å). This increase (0.7 Å) in the interlayer spacing indicate intercalation of acetone molecules into the interlayer galleries of the r-GO membrane. After taking out from acetone, the r-GO strip was again dipped in water for 15 minutes and re-examined the microstructures by recording XRD pattern. As can be seen from Figure 3.13a, the position of the (002) reflection of the r-GO strip shifted back to its original position. Similarly, XRD patterns were also recorded for the agar part of the bilayer strip (Figure 3.13b). The characteristic reflection of agar at 2θ = 13.1° did not show any definite shift due to subsequent dipping in acetone and water. As can be seen from the XRD patterns, inside liquid medium, solvent molecules intercalate in to the interlayer spaces of r-GO strip and alter its d-spacing, which would have a definite impact on its mechanical property. This unequal change in the microstructure of both side of the bilayer membrane is attributed to the asymmetric bending strain along the membrane, which in turn leads to shape changing characteristic of the bilayer membrane.

The mechanical properties of the bilayer actuators were studied by recording stress-strain curves before and after periodic soaking and drying of the strips in liquid acetone. The stress-strain curves shown in Figure 3.14a confirms that the tensile strength (66 MPa) and Young's modulus (358 MPa) of the pristine bilayer strip did not display significant degradation even after 5 (tensile strength 52 MPa and Young's modulus 352 MPa) and 10 (tensile strength 48 MPa and Young's modulus 347 MPa) dips in acetone. In order to further confirm the strength of bilayer membrane under liquid medium, its strips were made to lift weights heavier than own weight. As can be seen from Figure 3.14b and 3.14c, a strip weighing 2 mg (of dimensions $20 \times 3 \times 0.023$ mm^3) could lift 3 mg of weight up to 1.9 cm. Likewise, a strip could lift 5 times

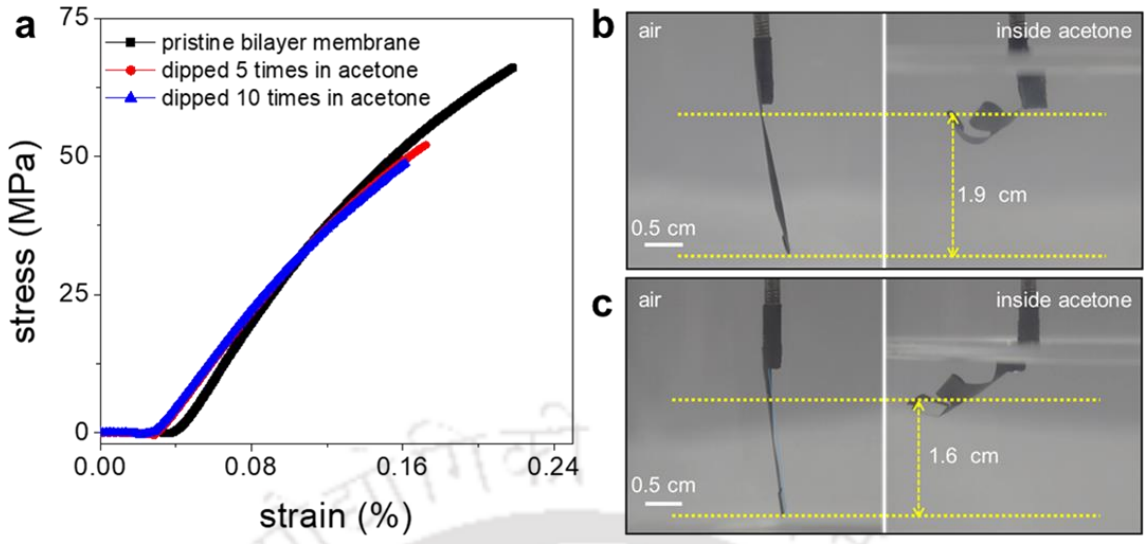

Figure 3.14: *(a) Stress-strain curve of a strip of pristine bilayer membrane is compared with the ones dipped and taken out of acetone for 5 and 10 times respectively. Snapshots showing lifting of weights by the bilayer strip upon dipping in liquid acetone. A strip weighing 2 mg (of dimensions 20 × 3 × 0.023 mm3) could lift a weight of (a) 3 mg up to 1.9 cm and (b) 10 mg up to 1.6 cm inside acetone*

it weights up to 1.6 cm. The chemical robustness of the bilayer membrane was also studied after exposing the strips into harsh chemical environments. As can be seen form from Figure 3.15, the strips exposed to vapours of concentrated HCl and NH_3 for 6 hours from a distance of 5 cm retained their responsiveness.

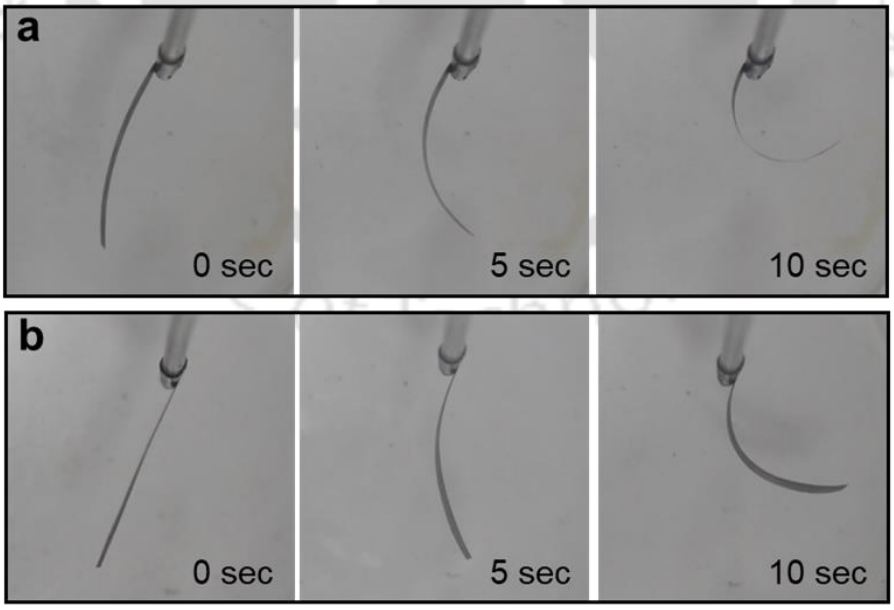

Figure 3.15: *Strips of the bilayer membrane were found to show responsive even after subjecting to extreme conditions. Photos showing acetone vapour induced bending movements of a bilayer strip after exposing to (a) concentrated HCl vapours and (b) NH_3 vapours for 6 hours.*

3.5.4 Detection of liquid contaminants inside a solvent system

The unique bending behaviour of the bilayer membrane can also be utilized to detect trace amounts of liquid contaminants present in a given solvent system. As a proof of concept, detection of a trace amount of water molecules mixed with acetone is demonstrated here. Briefly, a rectangular strip (dimensions 0.6 × 2 × 0.023 mm^3) of r-GO/agar was fixed on to a rod and dipped inside a glass beaker containing 2.5 mL of liquid acetone. Once completely submerged into the liquid solvent, the strip bent itself into a coiled shape. When trace amount of liquid water was added to the acetone medium, the coiled-shaped strip started opening up.

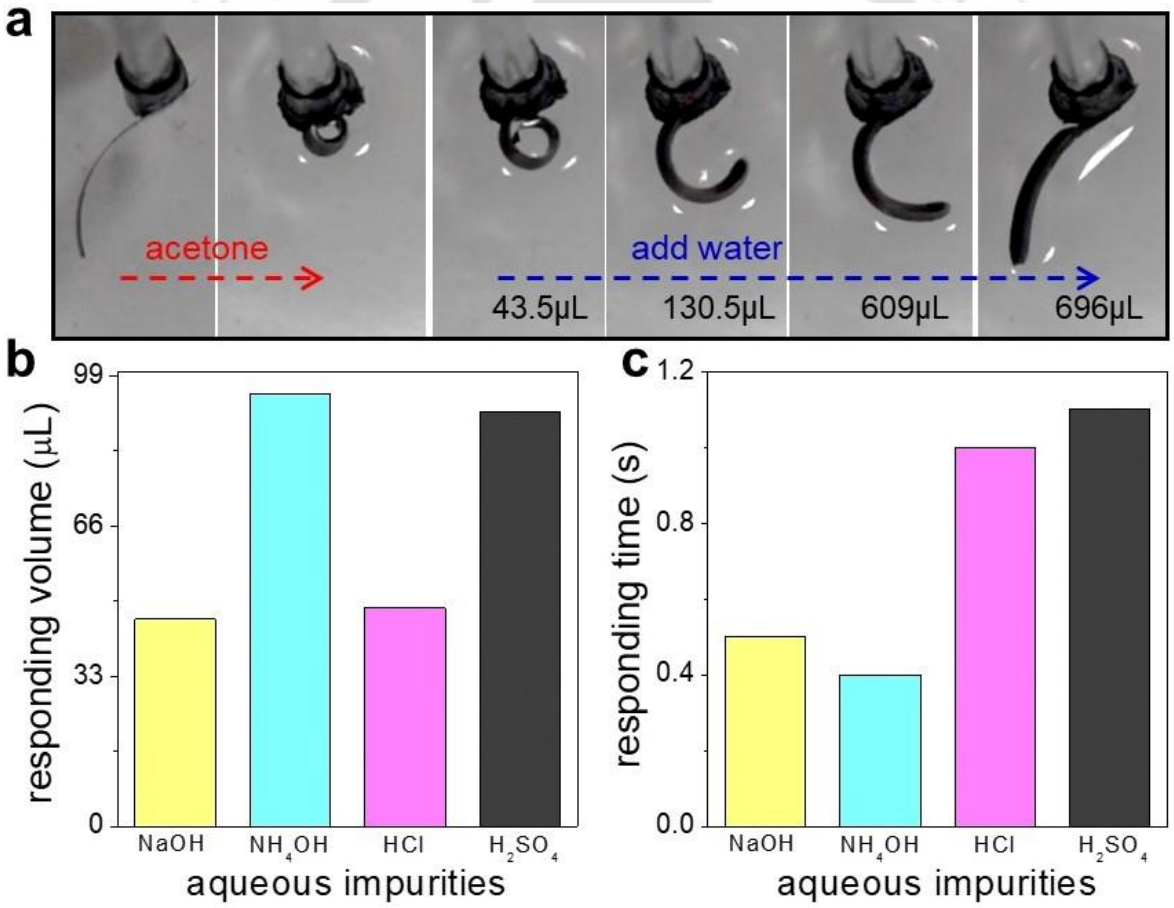

Figure 3.16: *(a) Snapshots showing detection of trace amounts of water in acetone by the r-GO/agar bilayer strip. Bar diagrams showing (b) minimum responding volume and (c) minimum responding time of the r-GO/agar bilayer strip with respect to the trace amounts of aqueous impurities mixed in acetone.*

As more water molecules were added in a dropwise manner, the coiled-shaped strip started opening up to a greater extent. The entire process was recorded from the top with the help of a digital camera. As can be seen from the snapshots in Figure 3.16a, the strip could detect the presence of as little as 43.5 µL of water molecules in 2.5 mL of acetone (1.74% of water in acetone), and responded by starting the opening-up process. After addition of additional liquid water (696 µL), the strip completely opened-up, and regained its original position. The mechanism of the real-time sensing of water molecules in the acetone medium is attributed to the different affinities of the r-GO side and agar side of the bilayer membrane towards water molecules present inside the acetone medium. The interlayer spacing of the r-GO side of the bilayer membrane was found to expand in the acetone medium whereas it was found to shrink in the presence of water. No such changes were observed in the agar side of the bilayer membrane. These unequal changes prompt asymmetric bending strain along the membrane which results in changes in the shape of the stripe. This observation opened-up a new platform to detect presence of water molecules in different solvent systems in a very cost- and time-effective manner. The response time of r-GO/agar strip in the presence of 43.5 µL water in acetone was found to be just 1.5 seconds (120° of bending movement). The response-time was also found to be varying with the varying amount of water molecules present in the acetone medium, and hence could provide an alternative ways to quantify aqueous contaminants present in the organic medium. Upon addition of 218 µL and 435 µL of water, the response-time was found to be decreasing from 1.5 seconds to 1.25 and 1 second, respectively. The responsiveness of r-GO/agar strip can also be exploited to detect the nature of the aqueous impurities present in the organic medium. As a proof of the concept, the response-times and minimum-responding-volumes of r-GO/agar strip in acetone medium were calculated with four aqueous solutions (H_2SO_4, HCl, NaOH and NH_4OH, 1M each). Even though, upon addition of all the four electrolyte solutions, the strip responded by bending in the same direction, the

minimum-responding-volumes and response-time were found to be different in each case (bar diagram in Figure 3.16b and 3.16c), which could provide valuable information about the type of impurities present in the organic medium. For example, in the case of HCl and NaOH having

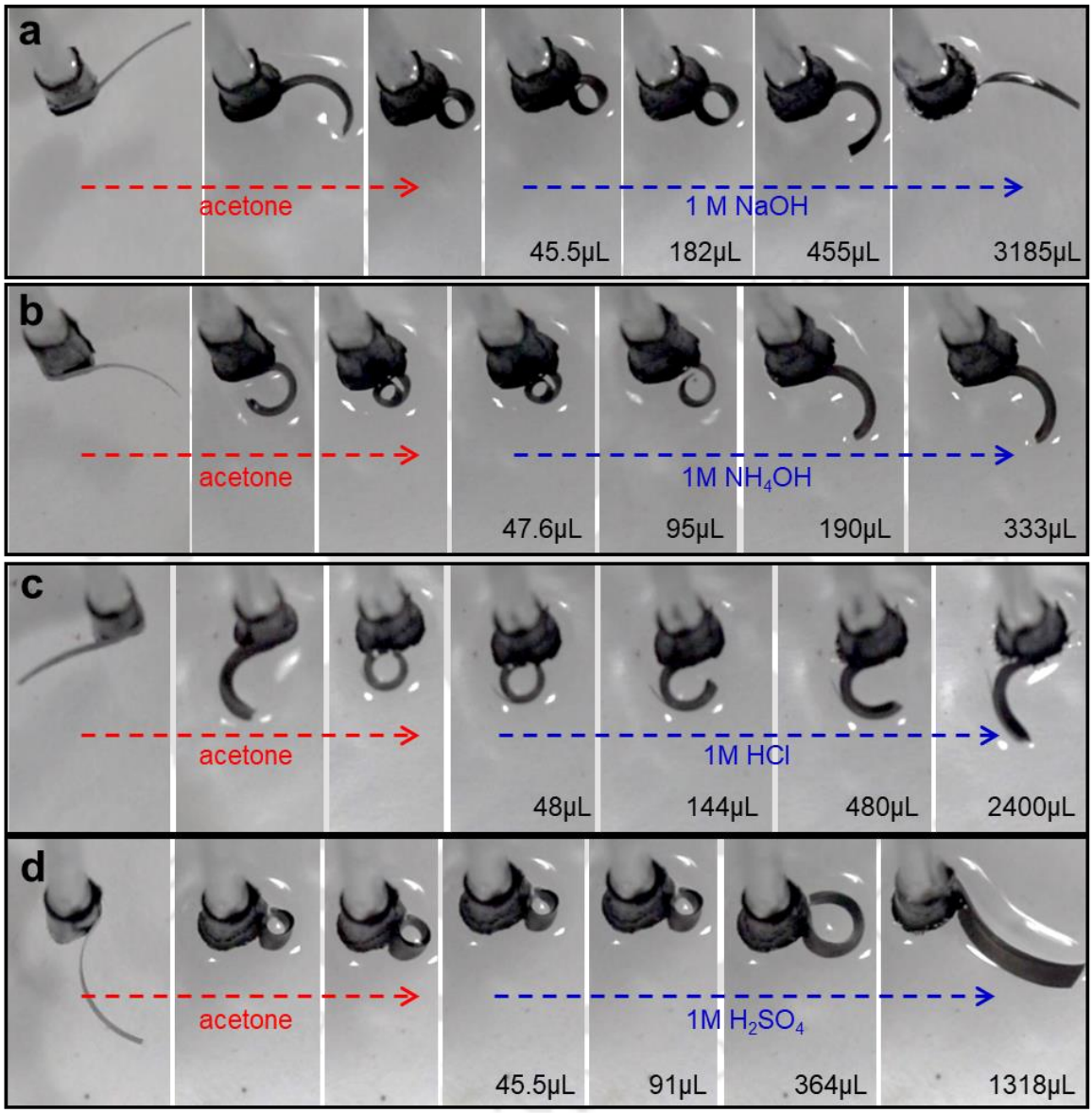

Figure 3.17: *Snapshots showing the detection of trace amounts of aqueous impurities inside acetone by the r-GO/agar bilayer strips: (a) 1M NaOH, (b) 1M NH_4OH, (c) 1M HCl and (d) 1M H_2SO_4.*

concentration of 1 M each, the minimum-responding-volumes were found to be 48 µL and 45.5 µL, respectively. Whereas the response-time were found to be 1 s (24° of bending movement) and 0.5 s (18° of bending movement), for HCl and NaOH, respectively. Similarly, in the case

of H_2SO_4 and NH_4OH, the minimum-responding-volumes were found to be 91 µL and 95 µL, respectively. With the minimum-responding-volumes of H_2SO_4 and NH_4OH, the response-time were calculated to be 1.1s (165° of bending movement) and 0.4s (161° of bending movement), respectively. The difference in the response time and minimum-response-volume

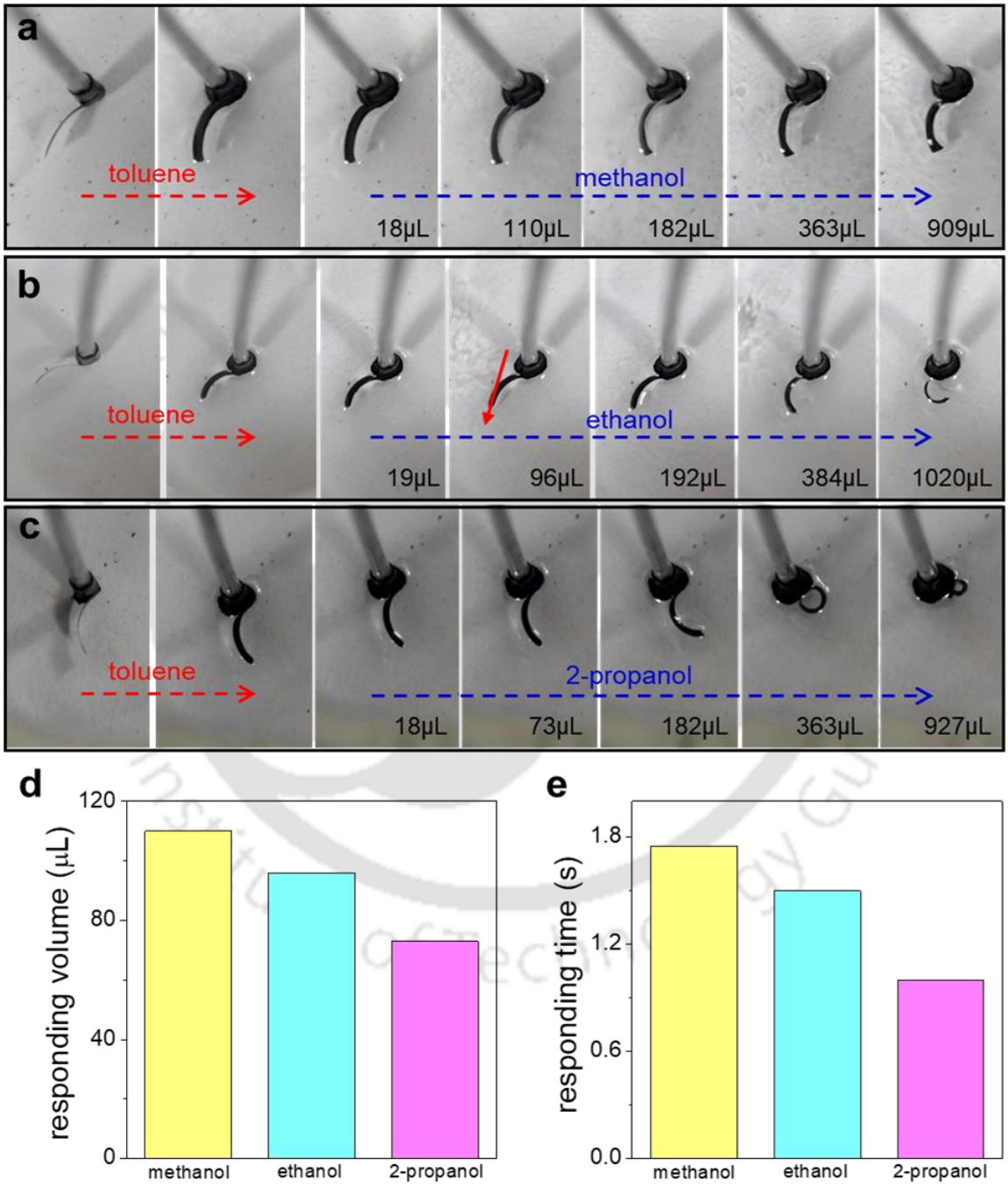

***Figure 3.18**: Snapshots showing the detection of trace amounts of alcohol impurities inside toluene by the r-GO/agar bilayer strips: (a) methanol, (b) ethanol and (c) 2-propanol. Bar diagrams showing (d) minimum responding volume and (e) minimum responding time of the r-GO/agar bilayer strips in the presence of trace amounts of alcohol impurities inside toluene.*

with different electrolyte solutions is attributed to different miscibility of the electrolytes in acetone. (Snapshots are shown in Figure 3.17)

Apart from the above mentioned solvent system, the r-GO/agar strip can also detect foreign molecules in non-aqueous medium. As a proof of concept, the response-times and minimum-responding-volumes of r-GO/agar strip submersed in toluene solvent were calculated for three different alcohols, namely methanol, ethanol and 2-propanol (Figure 3.18). All the three alcohols responded by bending the strip in similar direction but displayed different minimum-responding-volumes and response-times. 2-propanol displayed the minimum-responding-volume of 73 µL followed by ethanol and methanol with minimum-responding-volumes of 96 µL and 110 µL respectively. With the minimum-responding-volumes, the response-times were calculated to be 1 (12° of bending movement), 1.5 (7° of bending movement) and 1.75 (8° of bending movement) seconds for 2-propanol, ethanol and methanol respectively. The difference in miscibility of the three alcohols with toluene is attributed for the difference in minimum-responding-volumes and responding-times.

3.6 Conclusions

In conclusion, we have demonstrated the possibility of applying reconstructed layered materials-based responsive membranes for detecting contaminants dissolved in liquid mediums. The shape of the bilayer strip prepared by re-stacking exfoliated layered materials is determined by the balance between the mechanical properties of the individual components. When soaked-in, liquid molecules interact with the two-dimensional building blocks of the lamellar membranes and influence the attractive and repulsive forces between the layers, and hence alter their mechanical properties. As a result, the shape of the materials becomes dependent on the surrounding atmosphere. The presence of foreign molecules/impurities interferes with the interactions between the liquid molecules and nano-building blocks as well as the attractive/repulsive forces among the 2D nanomaterials, and hence it influences their

shape-morphing properties. The bilayer membrane of r-GO/agar taken here as an example exhibits remarkable under-liquid robustness. Numerous times of soaking/bending into solvents of diverse chemical nature did not seem to alter its mechanical robustness as well as shape morphing properties. Responsive materials with such robustness and specific bending and recovering speed with different solvent molecules could provide a new kind of platform to develop electronics-free dart-cheap sensors of solvent molecules and solvent compositions. Moreover, the fabrication process of this kind of bilayer membranes can be easily scaled up to prepare large area free-standing smart membranes in a very cost-effective manner. It is worth mentioning that the bending performance of bilayer based actuator is dependent on multiple parameters like the size of the vessels, distance of the actuator to the surface of the vessels, the shape and thickness of the actuators and so on. However, inconsistencies arising from these parameters can be minimized through appropriate control experiments and optimization of the device structure.

3.7 References

1 B. Jakoby and M. J. Vellekoop, *Sens. Actuators A Phys.*, 2004, **110**, 28–32.

2 N. S. Foster, J. E. Amonette, T. Autrey and J. T. Ho, *Sens. Actuators B Chem.*, 2001, **77**, 620–624.

3 Y. Ooyama, M. Sumomogi, T. Nagano, K. Kushimoto, K. Komaguchi, I. Imae and Y. Harima, *Org. Biomol. Chem.*, 2011, **9**, 1314–1316.

4 W. Chen, Z. Zhang, X. Li, H. Ågren and J. Su, *RSC Adv.*, 2015, **5**, 12191–12201.

5 J. G. Yu, X. H. Zhao, H. Yang, X. H. Chen, Q. Yang, L. Y. Yu, J. H. Jiang and X. Q. Chen, *Sci. Total Environ.*, 2014, **482–483**, 241–251.

6 V. Pichon, *J. Chromatogr. A*, 2000, **885**, 195–215.

7 D. Kou, S. Zhang, J. L. Lutkenhaus, L. Wang, B. Tang and W. Ma, *J. Mater. Chem. C*, 2018, **6**, 2704–2711.

8 Z. Wang, J. Zhang, J. Li, J. Xie, Y. Li, S. Liang, Z. Tian, C. Li, Z. Wang, T. Wang, H. Zhang and B. Yang, *J. Mater. Chem.*, 2011, **21**, 1264–1270.

9 M. Qing, H. Liang, J. Zhang and H. Zhan, *J. Pet. Sci. Eng.*, 2020, **188**, 106863.

10 K. Allsopp, I. Wright, D. Lastockin, K. Mirotchnik and A. Kantzas, *J. Can. Pet. Technol.*, 2001, **40**, 58–61.

11 C. Ye, Y. Qin, P. Huang, A. Chen and F. Y. Wu, *Anal. Chim. Acta.*, 2018, **1034**, 144–152.

12 Y. Zhou, D. Zhang, W. Xing, J. Cuan, Y. Hu, Y. Cao and N. Gan, *Anal. Chem.*, 2019, **91**, 4845–4851.

13 T. Il Kim and Y. Kim, *Anal. Chem.*, 2017, **89**, 3768–3772.

14 F. Cheng, R. Fu, Y. Wen, Y. Y. Yang, C. Zeng, Y. Zhang, S. Hu and X. Wu, *J. Mater. Chem. C*, 2018, **6**, 12341–12346.

15 J. Zhang, J. Wu, G. Tang, J. Feng, F. Luo, B. Xu and C. Zhang, *Sens. Actuators B Chem.*, 2018, **272**, 166–174.

16 Z. Chen, D. Zhang, E. Peng and J. Ding, *Chem. Eng. J.*, 2019, **373**, 1223–1232.

17 H. Sun, B. Wang and S. G. Dimagno, *Org. Lett.*, 2008, **10**, 4413–4416.

18 T. Wang and H. Li, *Chem. – Eur. J.*, 2016, **22**, 12400–12405.

19 R. K. Gogoi, A. B. Neog, N. Sarmah and K. Raidongia, *J. Mater. Chem. A*, 2019, **7**, 21157–21167.

20 H. J. Kim, S. H. Song and S. H. Ahn, *Smart Mater. Struct.*, 2012, **22**, 014007.

21 M. Sponchioni, U. Capasso Palmiero and D. Moscatelli, *Mater. Sci. Eng. C*, 2019, **102**, 589–605.

22 S. Y. Yang, K. H. Cho, Y. Kim, M. G. Song, H. S. Jung, J. W. Yoo, H. Moon, J. C. Koo, J. Do Nam and H. R. Choi, *Smart Mater. Struct.*, 2017, **26**, 105025.

23 A. A. Basheer, *Air. Eng.*, 2020, **92**, 1027–1035.

24 P. J. Roth and A. B. Lowe, *Polym. Chem.*, 2016, **8**, 10–11.

25 J. W. Sohn, G. W. Kim and S. B. Choi, *Appl. Sci.*, 2018, **8**, 1928.

26 A. Lai, Z. Du, C. L. Gan and C. A. Schuh, *Science*, 2013, **341**, 1505–1508.

27 X. Yu, H. Cheng, M. Zhang, Y. Zhao, L. Qu and G. Shi, *Nat. Rev. Mater.*, 2017, **2**, 1–13.

28 R. K. Gogoi and K. Raidongia, *Adv. Mater.*, 2017, **29**, 1701164.

29 R. K. Gogoi, K. Saha, J. Deka, D. Brahma and K. Raidongia, *J. Mater. Chem. A*, 2017, **5**, 3523–3533.

30 R. K. Gogoi and K. Raidongia, *J. Mater. Chem. A*, 2018, **6**, 21990–21998.

31 C. Wang, Y. Wang, Y. Yao, W. Luo, J. Wan, J. Dai, E. Hitz, K. K. Fu and L. Hu, *Adv. Mater.*, 2016, **28**, 8618–8624.

32 D. D. Han, Y. L. Zhang, Y. Liu, Y. Q. Liu, H. B. Jiang, B. Han, X. Y. Fu, H. Ding, H. L. Xu and H. B. Sun, *Adv. Funct. Mater.*, 2015, **25**, 4548–4557.

33 H. Bi, K. Yin, X. Xie, Y. Zhou, S. Wan, F. Banhart and L. Sun, *Nanoscale*, 2013, **5**, 9123–9128.

34 S. Park, J. An, J. Won Suk, R. S. Ruoff, S. Park, J. An, J. W. Suk and R. S. Ruoff, *Small*, 2010, **6**, 210–212.

35 J. Xue, Z. Gao and L. Xiao, *Front. Chem.*, 2019, **7**, 496057.

36 X. Xie, L. Qu, C. Zhou, Y. Li, J. Zhu, H. Bai, G. Shi and L. Dai, *ACS Nano*, 2010, **4**, 6050–6054.

37 J. Liu, Z. Wang, X. Xie, H. Cheng, Y. Zhao and L. Qu, *J. Mater. Chem.*, 2012, **22**, 4015–4020.

38 E. Palleau, D. Morales, M. D. Dickey and O. D. Velev, *Nat. Commun.*, 2013, **4**, 1–7.

39 Q. Zhao, J. Heyda, J. Dzubiella, K. Täuber, J. W. C. Dunlop and J. Yuan, *Adv. Mater.*, 2016, **27**, 2913–2917.

40 Y. Haldorai and J. J. Shim, *New J. Chem.*, 2014, **38**, 2653–2659.

41 A. Toncheva, B. Willocq, F. Khelifa, O. Douheret, P. Lambert, P. Dubois and J. M. Raquez, *J. Mater. Chem. B*, 2017, **5**, 5556–5563.

42 A. B. Neog, R. K. Gogoi, T. Dutta and K. Raidongia, *ACS Appl. Nano. Mater.*, 2020, **3**, 6629–6635.

43 R. Zeng, Z. Luo, L. Zhang and D. Tang, *Anal. Chem.*, 2018, **90**, 12299–12306.

44 J. Shu, Z. Qiu and D. Tang, *Anal. Chem.*, 2018, **90**, 9691–9694.

45 G. Cai, Z. Yu, R. Ren and D. Tang, *ACS Sens.*, 2018, **3**, 632–639.

46 Q. Zhou, Y. Lin, K. Zhang, M. Li and D. Tang, *Biosens. Bioelectron.*, 2018, **101**, 146–152.

47 Q. Zhou, Y. Lin, J. Shu, K. Zhang, Z. Yu and D. Tang, *Biosens. Bioelectron.*, 2017, **98**, 15–21.

48 F. Kim, J. Luo, R. Cruz-Silva, L. J. Cote, K. Sohn and J. Huang, *Adv. Funct. Mater.*, 2010, **20**, 2867–2873.

49 K. Ai, Y. Liu, L. Lu, X. Cheng and L. Huo, *J. Mater. Chem.*, 2011, **21**, 3365–3370.

50 G. T. S. How, A. Pandikumar, H. N. Ming and L. H. Ngee, *Sci. Rep.*, 2014, **4**, 1–8.

51 S. Fang, D. Huang, R. Lv, Y. Bai, Z. H. Huang, J. Gu and F. Kang, *RSC Adv.*, 2017, **7**, 25773–25779.

52 T. N. Lin, M. R. Inciong, S. R. M. S. Santiago, T. W. Yeh, W. Y. Yang, C. T. Yuan, J. L. Shen, H. C. Kuo and C. H. Chiu, *Sci. Rep.*, 2016, **6**, 1–9.

Chapter 4

Biomimetic remote handling and sensing devices of multiwalled carbon nanotubes and vanadium pentoxide

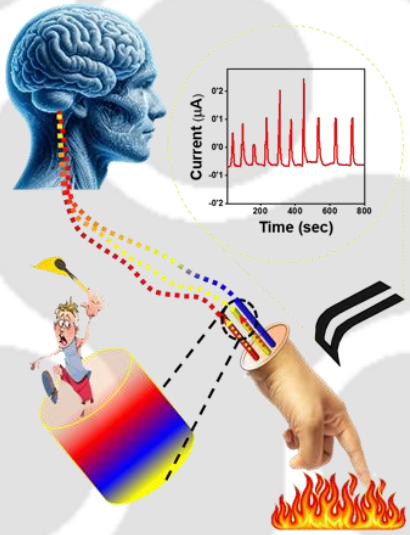

Chem. Eng. J., 2024, **480**, 148181.

Summary

Systems capable of managing toxic, reactive, and explosive substances through remote control mechanisms such as light and electricity hold significant technological promise. In this chapter, the development of bilayer actuators composed of multiwalled carbon nanotubes (CNT) and oxidized multiwalled carbon nanotubes (o-CNT), combined with exfoliated two-dimensional (2D) flakes of vanadium pentoxide (VO), were designed to precisely handle reactive substances. The differential photothermal activity of the carbon nanotubes and reconstructed VO was leveraged to fabricate bilayer membranes (CNT-VO) that exhibit light-controlled shape morphing characteristics, achieving bending speeds of up to 45° s^{-1} under a light intensity of 15k lux. Similarly, the exceptional Joule heating effect of the o-CNT and VO membranes (o-CNT-VO) was harnessed to create electrically driven actuation, with the bilayer membrane bending at speeds of up to 64.5° s^{-1} under an applied voltage of 12V. The light-responsive behaviour of the CNT-VO bilayer membrane was utilized to pick up and release reactive chemicals such as potassium permanganate ($KMnO_4$) and sodium (Na) metal, supporting loads up to ten times their own weight. In parallel, the voltage responsiveness and rose petal like effect of the o-CNT-VO membrane were employed to transport microdroplets (25 µL) of toxic chemicals, including sulfuric acid (H_2SO_4) and sodium hydroxide (NaOH). These CNT-VO-based actuators also possess the capability to sense the nature of the materials they handle, mimicking the sensory functions of human fingers. The robustness of the components ensures that the shape-morphing characteristics of the CNT-VO strips remain intact even after immersion in acidic, basic, and organic liquids.

4.1 Introduction

Given the ever-increasing demand for chemical and biochemical products, the industrial-scale use of toxic and explosive substances continues to rise. Despite their known toxic effects, numerous industrial processes and scientific studies necessitate the use of specific hazardous materials, thereby placing certain technicians and workers at a persistent risk of health hazards. Amidst these concerns, there is a growing demand for systems capable of handling hazardous materials remotely.[1–3] Remote handling systems have the potential to mitigate the risks of direct exposure to toxic substances for operators, enabling them to manipulate and interact with hazardous materials safely within a controlled environment.[4–6] Furthermore, these systems are invaluable in settings where direct human access is restricted due to physical, biological, or radiological hazards.[7,8]

In this context, extensive research efforts are being directed towards developing novel strategies for the precise manipulation of substances using remote controls such as light, solvent vapor, heat, or electricity.[9–13] Stimuli-responsive materials emerge as ideal candidates for fabricating remote handling devices. In recent years, literature on stimuli-responsive materials has expanded dramatically. For instance, moisture-triggered actuators developed from graphene oxide (GO) fibers function like hooks and can navigate through narrow slits.[14] Intelligent robots composed of GO and biaxially oriented polypropylene (BOPP),[15] as well as poly(N-isopropylacrylamide) (PNIPAm) and GO hydrogels,[16] demonstrate the capability to lift and transport masses several times their own weight. Numerous other actuating systems capable of repeatedly grabbing, releasing, and transporting objects have also been developed recently.[17–20] To facilitate the remote handling of substances, researchers are exploring innovative strategies and utilizing various forms of energy, such as light, heat, and electricity.[11–13,19,21–25] These systems enable precise control and manipulation of hazardous

materials without the need for direct physical contact, significantly enhancing safety and efficiency in handling hazardous substances.

The durability of materials in toxic and corrosive environments is essential for the long-term functionality, reliability, and efficiency of actuators. Appropriate material selection, effective monitoring systems, and extensive testing are critical in enhancing the longevity and effectiveness of these devices. Consequently, developing responsive materials with superior robustness and durability is a top priority. For instance, bilayer actuators made from graphene oxide have been developed to remain stable in both aqueous and organic solvents, with the capability to detect chemical impurities with high accuracy.[26–28] Similarly, clay-based bilayer actuators have been fabricated to withstand extreme temperatures, ranging from high (up to 500 °C) to low (−195 °C).[29] Incorporating self-healing capabilities, as seen in iron-catechol coordination crosslinked polymers[30] and natural vermiculite clay,[31] could further extend the lifespan of actuators. In recent years, actuators demonstrating exceptional endurance have been fabricated from materials such as GO, MXene, and polypyrrole.[14,25,32,33]

4.2 Scope of the present investigation

Two-dimensional (2D) materials are extensively utilized to create responsive materials with diverse qualities due to their unique properties. Actuators based on 2D layered materials offer distinct advantages, such as high flexibility, low weight, a high surface-to-volume ratio, and precise and rapid responses.[23,34–38] Advances in the synthesis of 2D nanomaterials and device fabrication are paving the way to realizing the full potential of actuators based on layered materials. In this chapter, the construction of highly adaptable bilayer actuators that can be remotely operated using light and electrical voltage is demonstrated. Bilayer actuators, prepared by assembling CNT and VO, exhibit the ability to lift and sense both liquid and solid objects. The high sensitivity and prolonged durability of these actuators arise from the contrasting responses of the two sides of the actuating materials to stimuli. Due to their

differing chemical natures and morphologies, CNT and VO display markedly different responses to stimuli such as light, heat, electricity, and solvent vapor, while both materials maintain superior chemical, thermal, and mechanical stability. Specifically, CNTs are renowned for their intriguing photochemical activities, reliable electronic conductivity, and high robustness. The precise responsiveness of CNTs to their surroundings has been explored for sensing a wide range of analytes.[39–42] Various synergistic combinations of CNTs and other carbonaceous materials with metal oxide-based nanomaterials are well documented in the literature.[43–45] For example, research has shown that CNTs act as highly feasible hosts for VO, with their hybrid nanostructures exhibiting properties (such as electrothermal and electromagnetic) not displayed by the individual components. VO was chosen for this study due to its distinctive photothermal activities and superior thermal and chemical stability.[46] VO membranes are among the few materials that demonstrate mixed conductivity, exhibiting both electrical and ionic conductivity. Materials with mixed conductivities are ideal for sensing and related applications, making VO an excellent choice for the development of advanced actuators.

Due to the exceptional durability of CNT and VO, CNT-VO-based actuating systems have demonstrated the ability to withstand immersion in acidic, basic, and organic solvents. These actuating systems are capable of transferring various chemically reactive solid and liquid substances, such as potassium permanganate, sodium metal, sulfuric acid, and sodium hydroxide, while also sensing the objects they handle. This type of bilayer actuator can be seamlessly integrated with existing technologies to enable the remote handling of toxic and explosive materials from a safe distance.

CNTs (SWCNT/MWCT/o-CNT/ and CNT membranes)

Sp^2 hybridized rolled graphene is what makes up CNTs. Their low weight, small size with a high aspect ratio, outstanding tensile strength, and good conducting characteristics are among

their key qualities. CNTs are a valuable filler in a variety of materials, including polymers, metallic surfaces, and ceramics. Additionally, CNTs have great potential uses in membranes, capacitors, transistors, actuators, sensors, nanotechnology, and nanomedicine. The synthesis of CNTs can be done using a variety of methods. These consist of the sol-gel technique, chemical vapour deposition (CVD), laser ablation, and arc-discharge methods. The distinct mechanical, electrical, thermal, and optical qualities of CNTs have all been well-researched. CNTs can be classified into three groups based on the number of tubes they contain. They are of three types: single-walled, double-walled, and multi-walled. Single-walled CNTs consist of a solitary layer of graphene that is rolled into a cylindrical shape with a diameter ranging from 1 to 2 nanometers. The length may vary based on the techniques used for preparation. Double-walled CNTs consist of two carbon nanotubes arranged concentrically, with the outer tube enclosing the inner tube. Multi-walled CNTs are composed of several layers of graphene that are rolled up, with diameters varying from 2 to 50 nm depending on the number of graphene tubes. The tubes possess an estimated inter-layer distance of 0.34 nm.

The chemical inertness of the graphitic network poses a significant obstacle in the manufacturing of composite materials. The oxidation of CNTs (o-CNT) using wet chemical processes such as photo-oxidation, oxygen plasma, or gas phase treatment has received significant interest as a means to both purify and improve the chemical reactivity of the graphitic network. Usually, by using the aforementioned rigorous methods, the pure CNTs may be successfully cleansed and oxygen-containing groups, primarily carboxyl and hydroxyl, have been seen to adorn the graphitic surface.[47,48] The presence of oxygen-containing groups improves the exfoliation of CNT bundles, and boosts the solubility in polar fluids. This, in turn, impacts the processing of CNTs and raises the possibility of additional modification/functionalization depending on its application.[49–51]

CNT membranes constitute a significant advancement in nanotechnology, delivering outstanding features for different applications.[52] These membranes are particularly famous for their outstanding filtration properties. In water purification, CNT membranes efficiently remove pollutants, including heavy metals and microorganisms, while retaining high flux rates.[53,54] Their excellent permeability and selectivity additionally enhance gas separation processes, permitting effective carbon dioxide collection and hydrogen synthesis.[55] Additionally, CNT membranes show promise in biological applications, such as drug delivery systems and biosensors,[56,57] due to their biocompatibility and functionalization potential. The unique features of CNT membranes position them as key components in environmental protection,[58] energy production,[58] and healthcare breakthroughs.[59]

V_2O_5 and its reconstructed membranes

Vanadium is one of the most plentiful elements in the Earth's crust, renowned for its multivalent nature, displaying +2, +3, +4, and +5 oxidation states. It produces a range of stable and metastable structures in the form of vanadium oxides, such as VO, VO_2, V_2O_3, V_2O_5, V_3O_5, and VO_3. These oxides have unique crystal structures, including cubic for VO, tetragonal for VO_2, trigonal for V_2O_3, orthorhombic for V_2O_5, and monoclinic for V_3O_5.[60] Vanadium oxides show tremendous promise for use in chemical sensors, catalysts, supercapacitors, electrodes in sodium/lithium-ion batteries, and energy storage devices.[61] Many vanadium oxides have fascinating features, such as insulator-to-metal transitions reported at different temperatures in VO_2, V_2O_3, and V_2O_5.[62,63] Additionally, vanadium oxides have switchable optical properties; for instance, VO_2 and V_2O_5 demonstrate remarkable electrochromism, changing their optical properties in a persistent and reversible manner in response to voltage changes.[64,65] V_2O_5 also exhibits photochromism, shifting color from yellow to bluish-black upon visible light irradiation.[66,67] Thin films of VO_2, V_2O_3, and V_2O_5 have been reported to demonstrate thermochromism in the infrared region.[68–70] The strong electron-lattice and electron-electron

correlations in vanadium oxides explain many of their features, giving prospective applications in smart windows, variable reflectance/emittance surfaces, and electrical/optical switching devices.[71,72]

The fabrication of freestanding V_2O_5 membranes (VO-M) involves restacking exfoliated 2D sheets generated from the interaction of bulk V_2O_5 powder with H_2O_2 in an aqueous solution.[73] The fabrication of VO-M is easily scalable since V_2O_5 flakes may be easily separated and dispersed in water.[74] The high natural abundance and remarkable chemical and thermal stability of V_2O_5 make these membranes very suitable for a wide range of applications.[10] Due to their elevated surface charge density and sensitivity to moisture, VO-M show great potential for the advancement of intelligent systems.[10] Moreover, these membranes demonstrate a notable ability to selectively allow ions to pass through, owing to the interconnected network of extremely small channels created by the interlayer gaps in the reconstructed structure.[73] VO-M provide excellent stability and proton conductivity,[73] rendering them well-suited for constructing power delivery systems that are chemically durable, thermally stable, and environmentally sustainable.[75] Furthermore, VO-M have been investigated for their capacity to be used in nanofluidic devices, enabling the precise and regulated transport of ions with nanomole accuracy.[76] Additionally, they are being examined for their potential use in ionic thermoelectricity[77] and forward osmosis processes.[78] The bilayer shape of VO-M enables them to respond to diverse environmental stimuli[9] and be exploited in the sensible design of systems for translocating items.[10] The abundant raw ingredients and uncomplicated construction processes ensure that VO-M have no substantial practical restrictions for real-world applications.[10]

4.3 Experimental section

Materials: Multi-walled carbon nanotube (>99.9%), sodium dodecyl sulphate (SDS) (≥97%), nitric acid (HNO_3) (68-72%), potassium permanganate (99.5%), Sulphuric acid (98%), Sodium

hydroxide (≥97%), sodium (99%) was purchased from Sigma Aldrich-India. Vanadium pentoxide (99.5%), was purchased from SRL Pvt., Ltd. Hydrogen Peroxide (33% w/v extra pure) was purchased from Finar Ltd. The copper electrodes were purchased from the local market. Silver paste was purchased from Alfa-Aesar Pvt. Ltd.

Preparation of VO nanosheets:

VO nanosheets were prepared by exfoliating bulk V_2O_5 powder with H_2O_2 in an ice-cold condition.[9,73] Typically, to a 25 ml 0.5 M aqueous solution of bulk V_2O_5 powder (at 0-5 °C), 50 % H_2O_2 was added progressively. Upon H_2O_2 addition, vigorous bubbling took place yielding a dark brown gel. The gel was diluted to 400 ml with deionized (DI) water before sonicating in a bath sonicator for 30 minutes to obtain VO nanosheets.

Preparation of free-standing VO membrane:

Freestanding VO membranes were prepared by vacuum filtrating 30 ml (3 mg/ml) aqueous dispersion of VO nanosheets through polytetrafluoroethylene (PTFE) membranes of pore size 100 nm. The membrane was peeled off from the PTFE membrane after drying it in a hot air oven at 60 °C for 1 hour.

Preparation of CNT aqueous dispersion:

Stable homogenous dispersion of CNTs in aqueous medium was obtained by probe-sonicating (1s on and 1s off pulse) 50 mg of pristine CNTs in 50 ml of DI water containing 75 mg SDS for 30 minutes.

Preparation of CNT free-standing membrane:

Upon vacuum filtration of 20 ml aqueous dispersion of CNT (1 mg/ml) through a PTFE membrane (100 nm pore size), yielded freestanding and flexible membrane of CNT. The membrane was peeled off from the PTFE membrane after drying it in a hot air oven at 60 °C for 1 hour.

Preparation of CNT-V_2O_5 bilayer membranes (CNT-VO):

CNT-VO bilayer membrane was prepared by assembling a layer of VO flakes on top of the freestanding CNT film prepared from their respective aqueous dispersions. At first, 10 mL of CNT dispersion (1 mg/mL) was vacuum filtered through a PTFE membrane (100 nm pore size). On top of this CNT membrane, 5 mL of the VO dispersion (3 mg/mL) was filtered. The CNT-VO membrane was peeled off from the PTFE membrane after drying it in a hot air oven at 60 °C for 1 hour.

4.4 Characterizations

Atomic force microscope (AFM) (Make: Oxford; Model: Cypher), and Field Emission Transmission Electron Microscope (FETEM) (JEOL; Model: 2100F) was used to characterize CNT and VO samples. Field Emission Scanning Electron Microscope (FESEM) (Make: Zeiss, Model: Sigma) was used to analyze the membranes' morphology and cross-sections. Raman spectroscopy (Make: Horiba Jobin Vyon, Model: LabRam HR) was also used to characterize

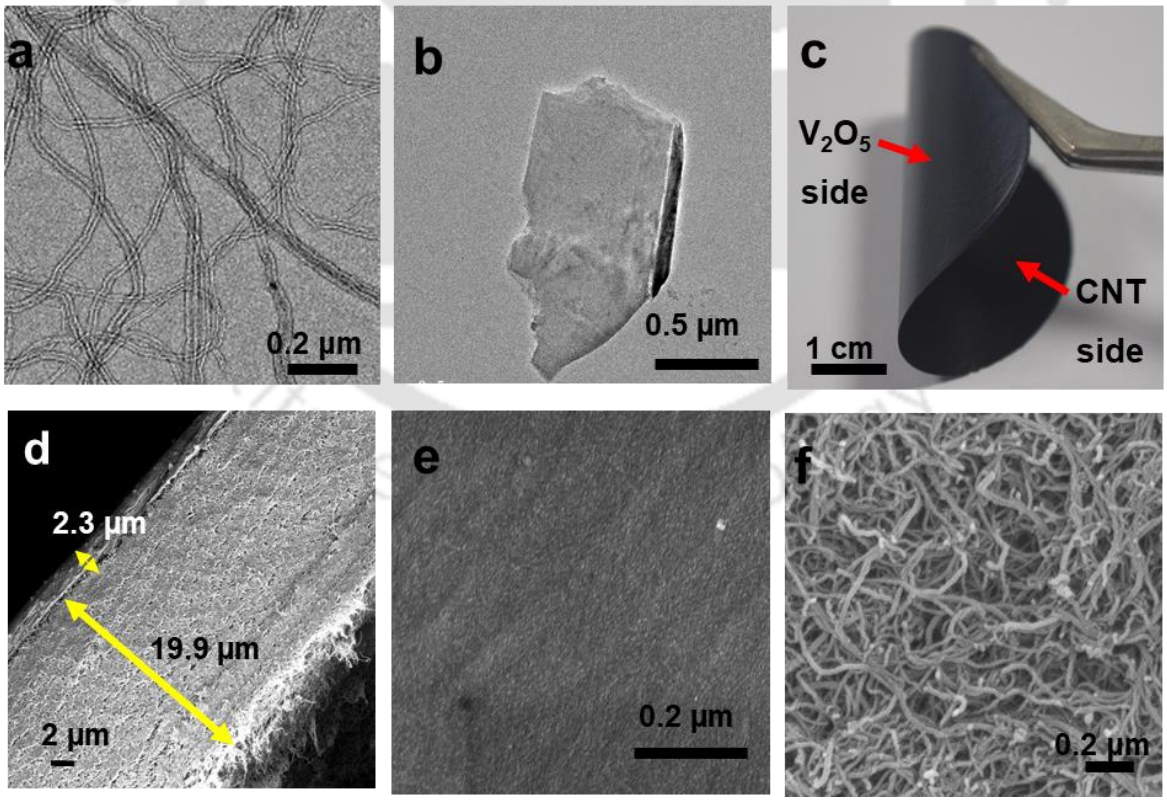

Figure 4.1: *FETEM images of (a) CNT and (b) V_2O_5 nanosheets. (c) Digital photo of CNT-VO bilayer membrane (d) cross-sectional FESEM image of the CNT-VO bilayer membrane. FESEM images of surfaces of (e) V_2O_5 and (f) CNT membranes.*

CNT, VO, and CNT-VO membranes. Studies on X-ray diffraction were conducted using a Bruker D-205505 Cu-Kα radiation (λ = 1.54 Å) (Rigaku, model: Micromax-007HF). IR spectroscopic analysis was carried out in Perkin Elmer (Spectrum Two). The compositional analysis was performed by using X-Ray Photoelectron Spectroscopy (XPS) (Thermo Fisher Scientific Pvt. Ltd., UK, model: ESCALAB Xi+). A digital camera, the Nikon D5200, was used to record the bilayer actuator's shape transformations, object lifting, and droplet transfer operations in the presence of infrared light, white light, and voltage. A High-resolution Thermal Camera, Testo 872, was used to take photo-thermal images of the membranes. A source meter device (Keithley 2450) was used for all electrical investigations. On a Holmarc Goniometer apparatus, contact angle measurements were made.

4.5 Results and discussion

4.5.1 Fabrication and characterizations of responsive bilayer membranes

The CNTs used in this work have an average length of ~ 10 μm with 5-20 nm diameters, a representative FETEM and spectroscopic characterizations of the CNT sample is shown in Figure 4.1a, and Figure 4.2a,4.2b respectively. Hydrophobic CNTs possess poor dispersibility in the aqueous medium. Therefore, it was probe sonicated with SDS to prepare a stable homogenous dispersion (as shown in Figure 4.2c) in aqueous medium. Upon vacuum filtration through a PTFE membrane, the CNTs are readily assembled into a freestanding and flexible membrane. Thus-prepared CNT membrane displayed a water contact angle of 150° (Figure 4.2d). Freestanding and flexible membranes of VO were prepared by vacuum-assisted assembly of VO 2D flakes. Nanosheets of VO were obtained by exfoliating bulk VO powder with ice-cold H_2O_2 solutions (0-5 °C), following a procedure reported in the literature.[9,73,75,77,79] Stable dispersion of the VO nanosheets in water is shown in Figure 4.3a. AFM investigation revealed the lateral sizes of the as-obtained VO nanosheets to be in the range of 100 to 230 nm having a thickness of ~ 7 nm. Representative TEM and AFM (along with height profile) images

are shown in Figure 4.1b and Figure 4.3b, respectively. CNT-VO bilayer membranes were prepared by assembling a layer of VO flakes on top of the freestanding CNT film prepared from their aqueous dispersions.

The individual sides of the bilayer membrane could be easily distinguished from their respective colours. As can be seen in Figure 4.1c, the shiny dark side represents the VO layer and the black side for the CNT. The cross-sectional FESEM investigation of the bilayer membrane revealed the uniform stacking of the VO layer on top of the CNT layer, shown in

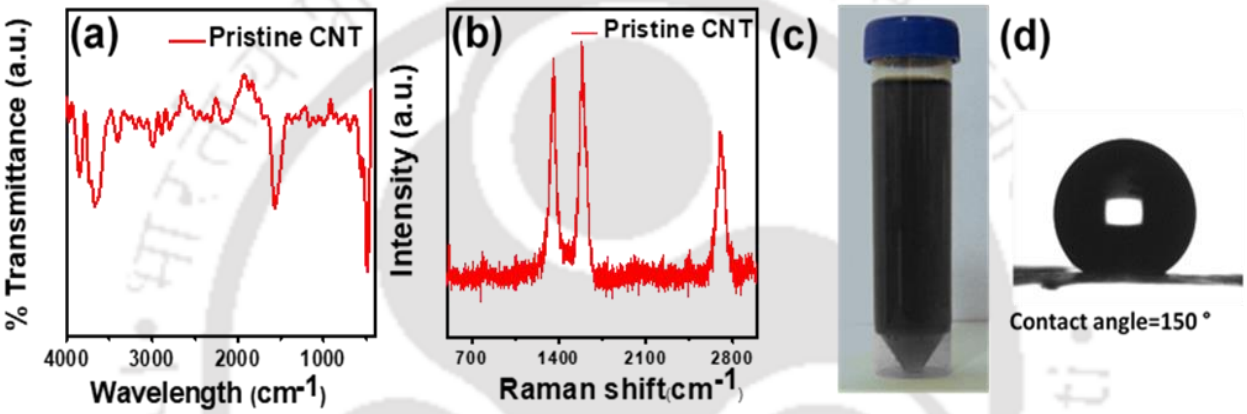

Figure 4.2: *Plot showing (a) IR spectra of CNT, (b) Raman Spectra (c) CNT dispersion (d) Contact angle measurement of CNT membrane.*

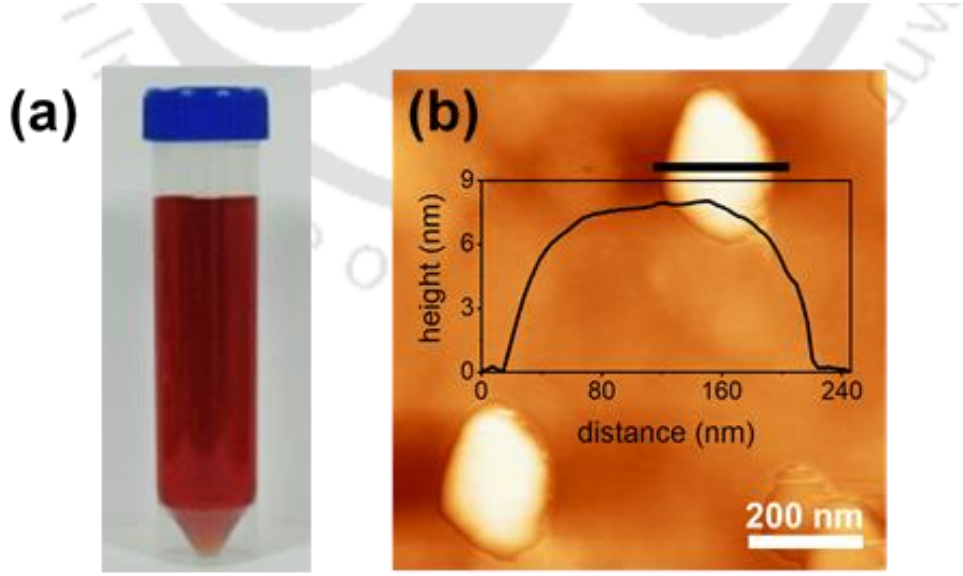

Figure 4.3: *(a) V_2O_5 nanosheet dispersion in water and (b) AFM image (corresponding height profile of the nanosheets in the insets) of V_2O_5 nanosheets.*

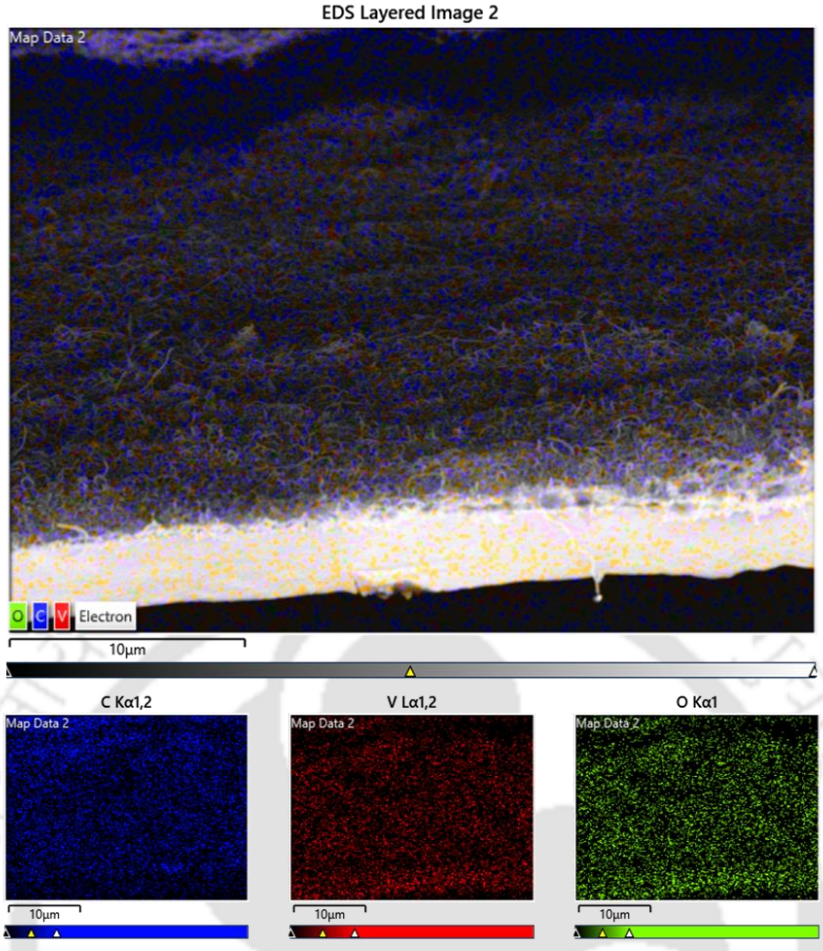

Figure 4.4: *EDX mapping image of CNT-VO cross section.*

Figure 4.1d. An EDX Mapping image of the CNT-VO cross section is shown in Figure 4.4. Preliminary investigation revealed that the VO side of the bilayer membrane is more uniform than that of the CNT side. The surface FESEM examination confirmed the uniformity of the VO sides of the membrane, in contrast to the hierarchical and porous structure of the CNT side, Figure 4.1e and 4.1f, respectively. Typically, CNTs acquire defects in the post synthesis processes, that consists of reactive dangling bonds associated with one or more vacancies. To saturate these reactive sites, species from the surrounding (like adsorbed gases, moisture, etc.) interact and create surface groups due to which CNT surfaces contain hydroxyl, carboxyl, and carbonyl groups which can act as centers for condensation reactions with vanadium pentoxide.[46,80] This leads to the strong attachment of VO flakes onto the CNT surface and ensures a stable connection between VO and CNT layers. To demonstrate strong interfacial

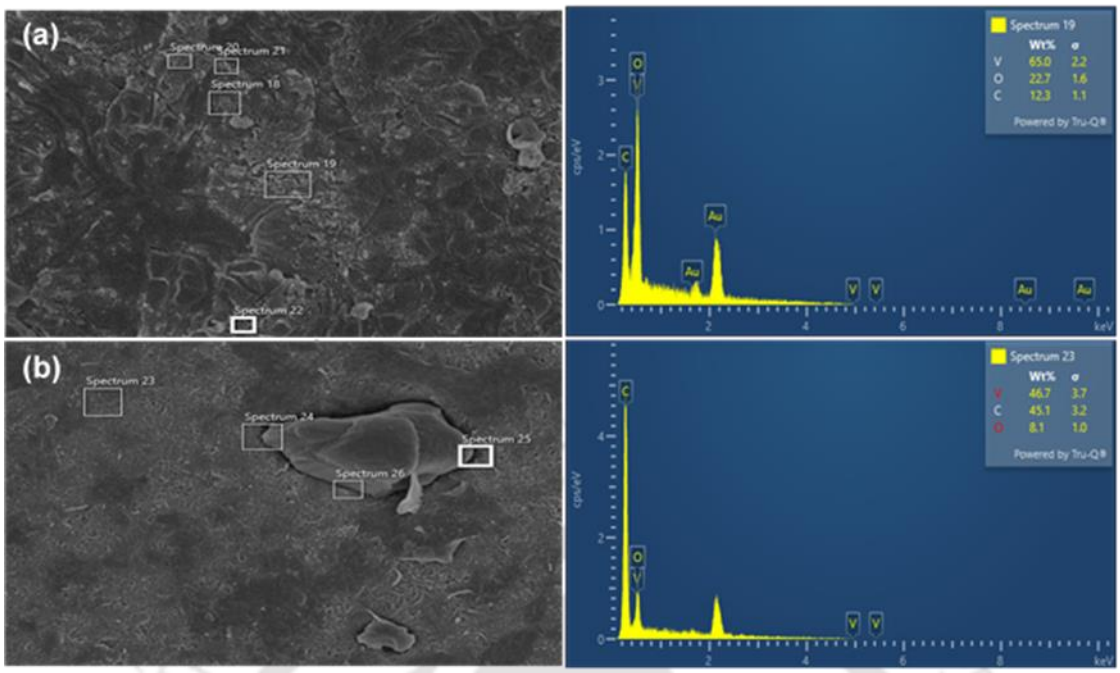

Figure 4.5: *EDX examination showing (a) CNT deposition on the peeled-off surface of VO and, (b) VO deposition on the peeled-off surface of CNT.*

attraction between the two components, they were pressed to each other placing a water droplet in between. After evaporation of the water droplet, two layers were peeled off. EDX examination shows CNT deposition on the peeled-off surface of VO, and VO flakes were seen on the peeled-off surface of CNT, indicating strong interactions between the two as can be seen in Figure 4.5.

4.5.2 Responsiveness towards light

The shape of the CNT-VO bilayer membrane was found to be responsive toward infrared (IR) light. To demonstrate the same, strips of dimension 20 × 3 × 0.015 mm^3 were cut from the bilayer membrane and fixed to a steel rod, as shown in Figure 4.6. The strip was then exposed to the IR light, and the responsive movements of the strips were recorded in a digital camera. It was found that the strip responded quickly to the presence of IR light and achieved its maximum bending angle within 5 seconds. Further exposures to IR light showed no observable

changes in the bending angle of the strips. The IR-induced bending of the CNT-VO strip was found to be highly reversible, and the strip quickly regained its original position upon switching off the IR source. Exposure of the CNT-VO strip to IR light more than 500 times did not affect its bending performance. The snapshots of the IR-induced bending of the bilayer strip are shown in Figure 4.7a. The CNT-VO strip was also exposed to white light. Like IR light, white light also induced the bending of the CNT-VO strip. The snapshots of the bending and recovery movements are shown in Figure 4.7b.

Figure 4.6: *Digital image of the CNT-VO bilayer strip employed for bending angle measurement in response to light source.*

The bending and recovery process of the CNT-VO strip was also studied as a function of the intensity of exposed light. The plot of bending speeds as a function of the intensity of IR and white light is shown in Figure 4.7c and 4.7d respectively. From the plots, it can be inferred that for similar light intensities, IR light induced higher bending speeds in comparison to white light. For example, with white light intensity of 15k lux, the bending speed of the CNT-VO strip was only 8.5° s^{-1}. For the IR light of intensity 15k lux, the same strip displayed a bending speed of 45° s^{-1}. As the intensity of the light source decreases, the bending speed decreases and becomes almost negligible at 1.1k lux for IR light and 4k lux for white light. As we increase the intensity of light, the overall temperature and the difference in temperature between the two layers of the bilayer membrane also increase. Hence, the bending speed increases as shown in Figure 4.8a. In order to study the mechanism of the light-induced responsiveness, the photo-thermal images of the individual membranes were captured before and after irradiation with

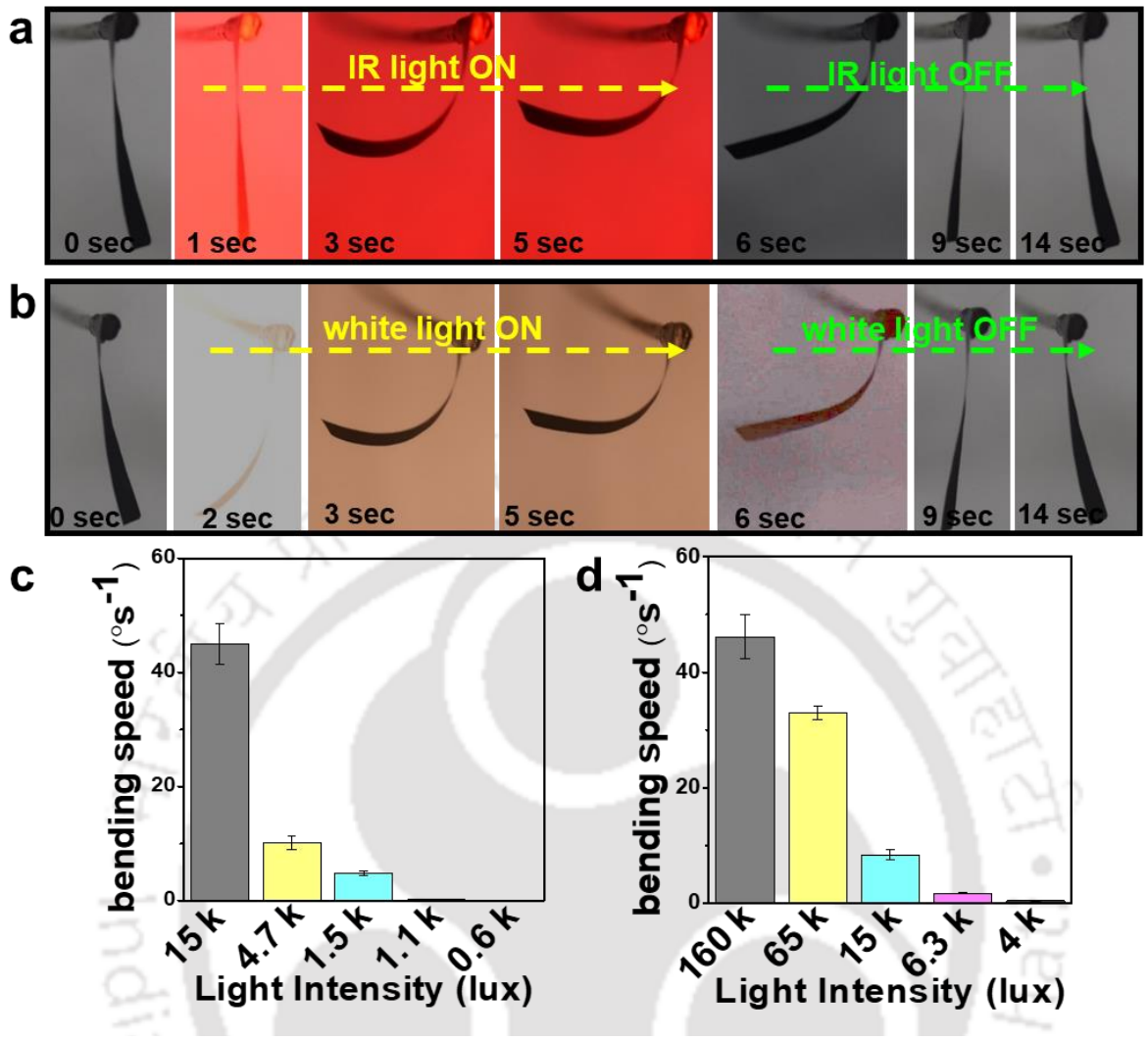

Figure 4.7: *Photos showing bending (for 5 s) and recovery movements of a bilayer strip upon exposure to (a) IR light of intensity 15k lux (b) White light of intensity 160k lux. Bar diagram showing the bending speed of the bilayer strip as a function of the intensity of (c) IR light and (d) white light.*

the respective light source (of intensity 15k lux each). The photo-thermal images of the individual CNT and VO membranes shown in Figure 4.8c reveal that upon irradiation of the IR light for 5 seconds, the temperature of the VO membrane increased by 21.5 °C (22 to 43.5 °C) while of the CNT membrane increased by 41.7 °C (22 to 63.7 °C). A bar diagram comparing the change in temperature is shown in Figure 4.8b.

The light-induced shape transformation of the bilayer strip is attributed to this imbalance in temperature due to unequal heating on the opposite sides. Materials with suitable electronic

and vibrational energy states undergo photoexcitation upon interaction with electromagnetic radiations. The energy of the photoexcited materials is transferred to the lattice through electron-phonon coupling, producing heat.[81] The black-coloured samples of both VO and CNT absorb a wide spectrum of electromagnetic radiation. However, IR light is known to possess higher efficiency of light-to-heat conversion. Owing to their drastically different chemical and morphological nature, light illumination causes unequal heating of VO and CNT. It has also been observed experimentally. For example, upon irradiation of the white light for 5 seconds, the temperature of the VO membrane increased by 4.6 °C (22 to 26.6 °C), while that of the CNT membrane increased by 10.2 °C (22 to 32.2 °C). The CNT side heated up to a higher temperature than the VO side, this unequal light-induced heating of the components is

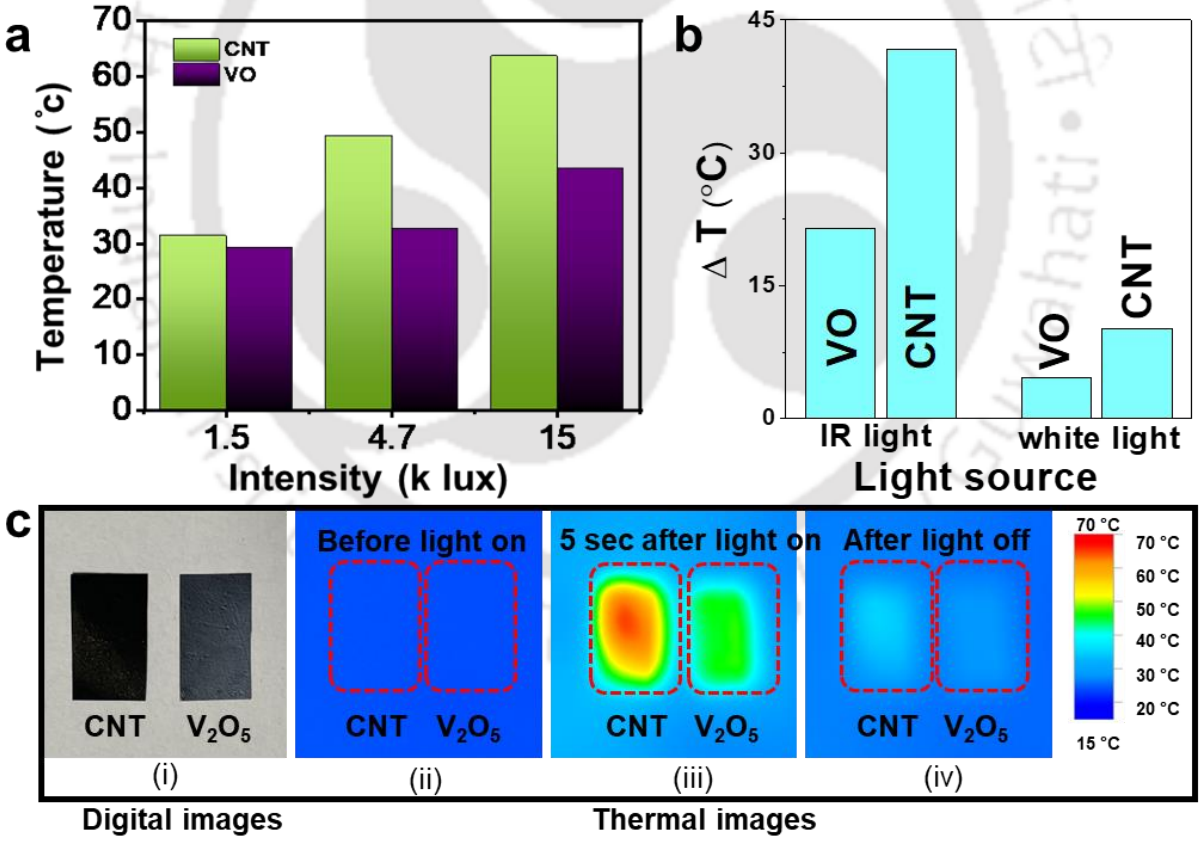

Figure 4.8: *(a) Effect of change in temperature with intensity. (b) Bar diagram comparing the change in temperature (Δ T) of VO and CNT membranes upon exposure to light sources. (c) (i) Digital images and (ii), (iii) and (iv) Photothermal images showing the temperature change of the individual CNT and VO strips before, 5 Sec after application of IR light and after switching off IR light respectively.*

attributed to the shape transformation. CNTs exhibit broadband absorption and excellent thermal conductivity and are explored for a wide range of photothermal applications.[81] Upon exposure to both IR and white lights, the CNT side heats up to a higher temperature, thereby, the bilayer strip bends towards the V_2O_5 side upon light irradiation. Lorentzen and Wetter's 2-point technique[26,27,29] is used to determine the bending stiffness values of the individual membranes in the light-on and light-off scenarios, as illustrated in Figure 4.9a. The individual strip's other end was kept fastened to a glass rod while a force was applied at one end using known loads. The V_2O_5 strip used in the experiment had dimensions of 20 × 2 × 0.016 mm^3 and was applied a load of 3.2 mg and. Similar to that, a 3.2 mg load was applied to a CNT strip with dimensions of 20 × 2 × 0.025 mm^3. The following equation was used to get the bending stiffness (Sb).

$$S_b = \frac{60 \times F \times l^2}{\pi \times \theta \times b}$$

Where, bending force (F) = weight × gravitational constant, l = distance between the fixed end and the load, θ = deflection, b = width of the strip. Under IR light, the bending stiffness of the

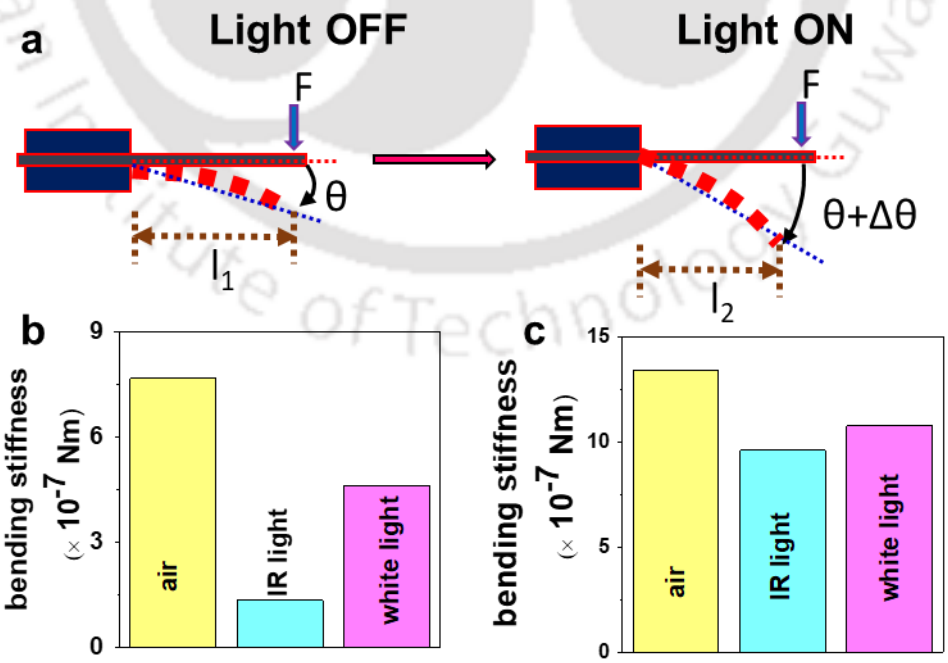

Figure 4.9: *(a) Schematic illustration of bending stiffness measurement using Lorentzen & Wettre's two-point method. Bar diagrams comparing the bending stiffness of (b) VO and (c) CNT membranes upon exposure to light sources.*

V_2O_5 membrane was reduced by 83%, while the CNT membrane decreased by just 28%. This disproportionate change in the mechanical properties of the constituents of the bilayer membrane is attributed to its shape-morphing characteristics. Furthermore, with white light the bending stiffness of the VO membrane reduced by 40%, while it decreased by 20% for the CNT membrane. The plot is illustrated in Figure 4.9b and 4.9c.

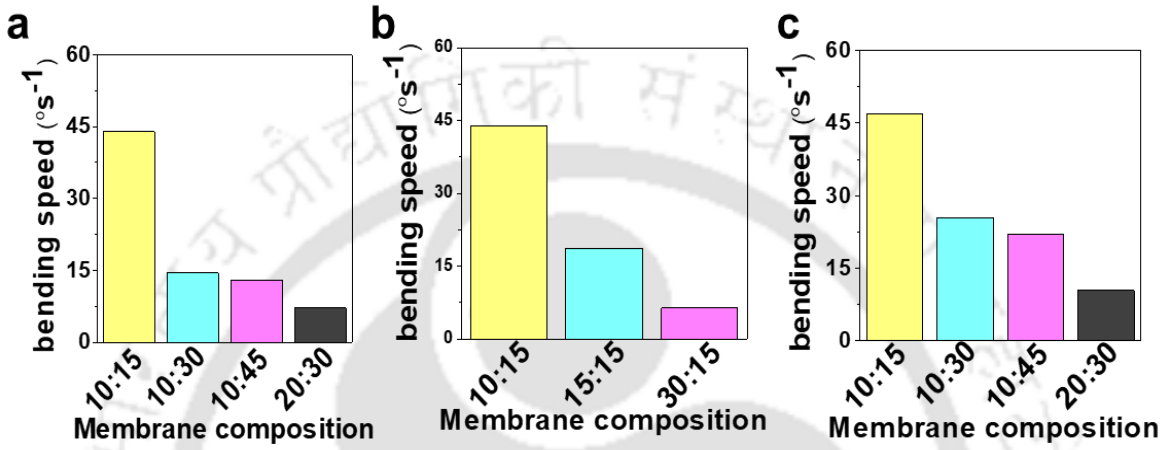

Figure 4.10: *Plot showing the dependence of the composition of the bilayer membrane on the bending speed upon exposure to (a) IR light of intensity 15k lux and (c) white light of intensity 160k lux. (b) Effect of bending speed with increasing the ratio of CNT: VO by increasing CNT amount upon exposure to IR light of intensity 15k lux.*

This light-induced bending speed of the bilayer membrane was also dependent on the composition of the components. Four CNT-VO bilayer membranes with different CNT to VO ratios (10:15, 10:30, 10:45, and 20:30) were prepared, and strips ($20 \times 3 \times (0.015\text{-}0.030)$ mm^3) cut from these bilayer membranes were exposed to IR light (15k lux). As the quantity of VO in the bilayer membrane increases from 15 mg to 45 mg, the bending speeds decrease gradually from 45° s^{-1} to 13° s^{-1}. Similarly, when the amount of CNT in the bilayer membrane was increased, the bending speed started decreasing, as can be seen from the plot in Figure 4.10a and 4.10b. This is because as the amounts of the components were increased, the flexibility of the bilayer membrane was compromised. The CNT to VO in the ratios 10:15 of all the combinations gave the best bending speeds. Similarly, this experiment was also performed in

the case of the white light of intensity 160k lux, and the bending speeds are plotted as a function of composition, as can be seen in Figure 4.10c. As in the case of IR light, an increase in either of the components of the bilayer resulted in a decrease in the bending speed values.

4.5.3 Responsiveness towards electrical potentials

The responsiveness of the CNT-VO strips was also explored against electrical potential. Because the electrical potentials can be applied precisely and accurately, they can be easily interfaced with the existing technologies. Due to the high electrical conductivity of CNT, pristine CNT-VO strips did not respond to electrical potential. A modified version of CNT-VO (o-CNT-VO) was prepared by oxidizing the CNT sample with HNO_3 before assembling it into the membranes.[48] Appropriate characterization of o-CNT is shown in Figure 4.11.

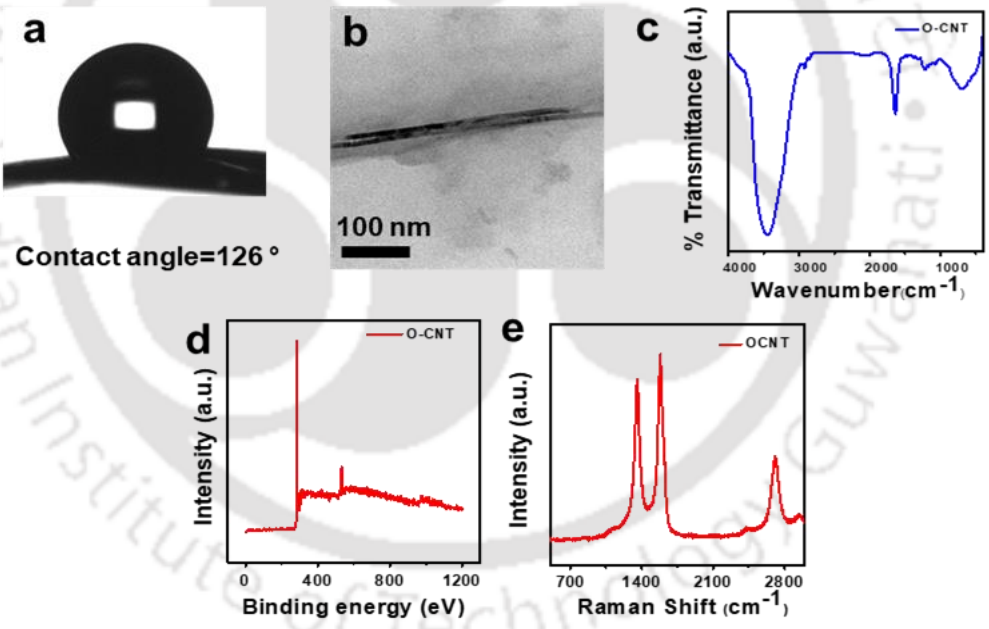

Figure 4.11: *Characterization of o-CNT membrane (a) Contact angle measurement, (b) TEM image, (c)IR spectra, (d) XPS pattern, and (e) Raman spectra of CNT membrane.*

The electrical responsiveness of o-CNT-VO was studied with a U-shaped strip cut from the bilayer membrane. A digital photo of the as-prepared U-shaped device and its dimensions are shown in Figure 4.12. Copper wires were connected to both ends of the strip using Ag-paste and conducting carbon tape. A Sourcemeter (Keithley 2450) instrument was used for applying

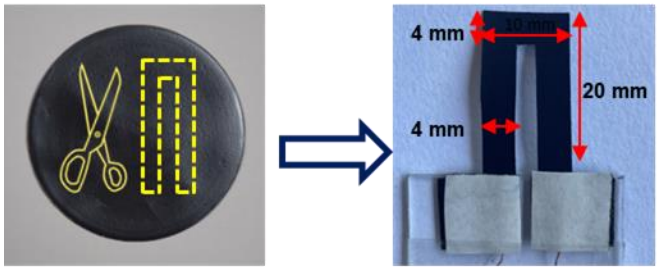

Figure 4.12: *Digital Photo showing the cutting of a U-shaped strip from a o-CNT-VO bilayer membrane (thickness, 16 µm) and fabrication of the corresponding U-shaped actuator device.*

electrical voltages between the two terminals of the device. As can be seen from the snapshots in Figure 4.13a, upon application of an electrical potential difference of 12 V across the two arms, the U-shaped strip started to curl towards the V_2O_5 side with a bending speed of 64.5° s^{-1}. As soon as the potential difference was cut off, the strip returned to its original shape. The V to 378° at 12 V). As shown in the plot in Figure 4.13c, at a specific applied voltage, the extent of bending increases with increasing time and reaches a saturation point.

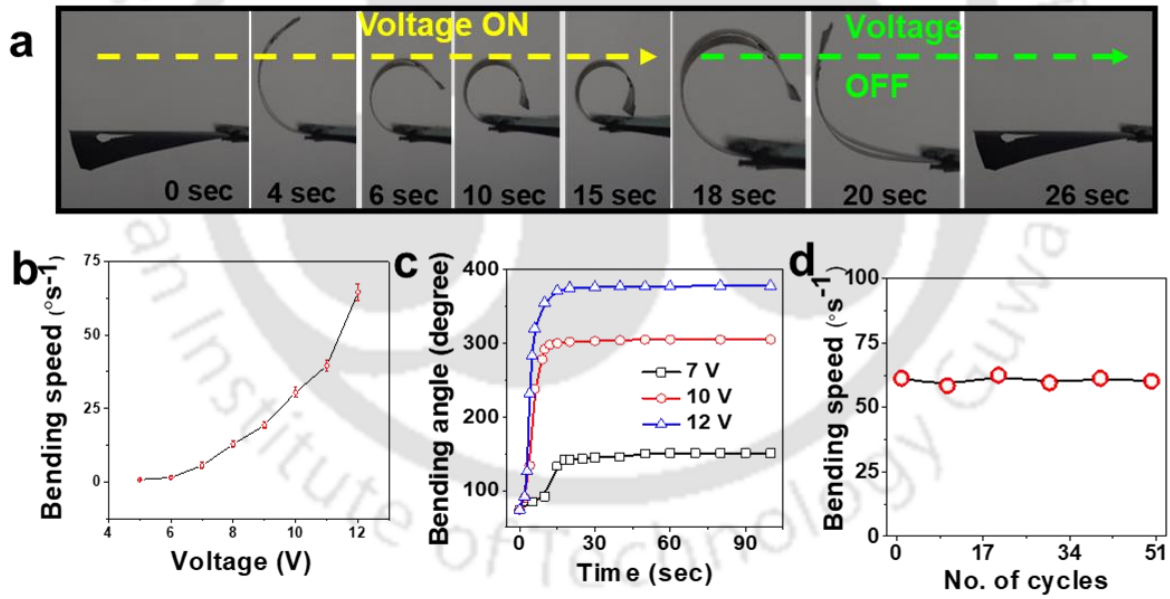

Figure 4.13: *Voltage-induced shape transformation of o-CNT-VO bilayer membrane: (a) snapshots showing bending and recovery of the U-shaped strip upon application of a potential of 12 V for 15 s. (b) Plot comparing the bending speeds of a U-shaped o-CNT-VO bilayer device upon application of different voltages (c) Plot showing total bending achieved upon application of potentials of 7, 10, and 12 V for 100 s. (d) Deviations in the voltage-induced bending speeds (12 V) in the 1st, 10th, 20th, 30th, 40th and 50th cycle of a U-shaped strip of the o-CNT-VO bilayer membrane.*

This voltage-induced bending of the o-CNT-VO bilayer device is highly reversible, and the deviations (±1.18°) in the voltage-induced bending speeds (for 12V) in the 1st, 10th, 20th, 30th, 40th, and 50th cycles are shown in Figure 4.13d. The table comparing bending performance of CNT-VO and o-CNT-VO with that of recently reported actuators is presented in the Table 4.1.

Materials	**Fabrication**	**Mechanism**	**Stimuli**	**Performance**	**Actuation or applications**	**References (year)**
CNT/PDMS	Bilayer	Electrothermal Photothermal	10V Visible light (100mW/cm^2)	235° in 4.84 sec 215° in 0.83 sec	Bending Bending, jumping, wobbling	2017[82]
CNT/PVDF	Bilayer	Photothermal	Light (not specified)	28.9 MPa in1.06 s	Bending, Twisting	2016[83]
CNT/BOPP	Bilayer	Electrothermal	5V	389° in 10 sec	Bending, walking	2015[84]
CNT/graphite/paper/ PP	Bilayer	Electrothermal Photothermal	30V Visible light (160 mW/cm^2)	13.9 mm in 30 sec 7 mm in15 sec	Bending Bending	2018[85]
CNT/PC	Bilayer	Photothermal	Visible light (100 mW/cm^2)	90° in 0.7 sec	Bending, Rolling	2014[86]
Graphene/PDA	Bilayer	Photothermal	NIR light	60° in 2 sec	Bending, Handshaped Walking	2015[87]
Graphene/BOPP	Bilayer	Photothermal Moisture	IR light RH 80%	2.8 cm^{-1} / degree 3.1 cm^{-1} / degree	Gripper Bending, Twisting	2017[15]

CNT/PI/paraffin wax	Layered	Photothermal	Visible light	85° in 1.86 & 60° in 1.1s	Bending Gripper	2016[88]
Graphene/PE	Laser patterning	Electrothermal	30 V	5 s/cm (curvature)	Bending	2019[89]
CNT/VO	Bilayer	Photothermal Electrothermal	Visible light 12V	44°/ s 61.3 °/ s	Bending Bending	This Work

Table 4.1: *Comparison of performance with previous works.*

The non-uniform joule heating of the two constituents is attributed to the voltage-induced bending of the o-CNT-VO device. To validate our hypothesis, a potential of 5V was applied to U-shaped devices of individual membranes (CNT and VO) for 15 seconds, and temperatures of both devices were recorded using a thermal camera. As can be seen from the Figure 4.14a, the application of the electrical potential increased the temperature of o-CNT from 22 to 35.3 °C (a rise of 13.3 °C), but the temperature of the VO device increased to only 27.2 °C (a rise of 5.2 °C). A bar diagram comparing the change in temperature is shown in Figure 4.14b.

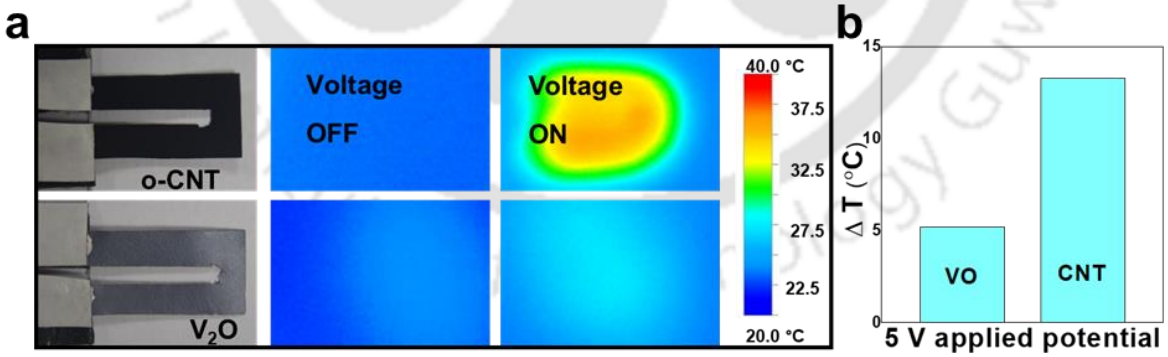

Figure 4.14*: (a) Comparison of the photothermal images of the U-shaped device of pure o-CNT and VO during OFF and ON (5 V for 15 s) states of the voltage. (b) Bar diagram comparing the change in temperature (Δ T) of VO and CNT membranes upon application of 5V for 15 seconds.*

The correlation between the mechanical characteristics of the two constituting layers and the shape of a bilayer membrane is well-established in the relevant literature.[28,90,91] The thermal

imbalance of the bilayer membrane caused by the voltage between its two layers is attributed to the change in the shape of the strip by shifting the mechanical equilibrium between its components.

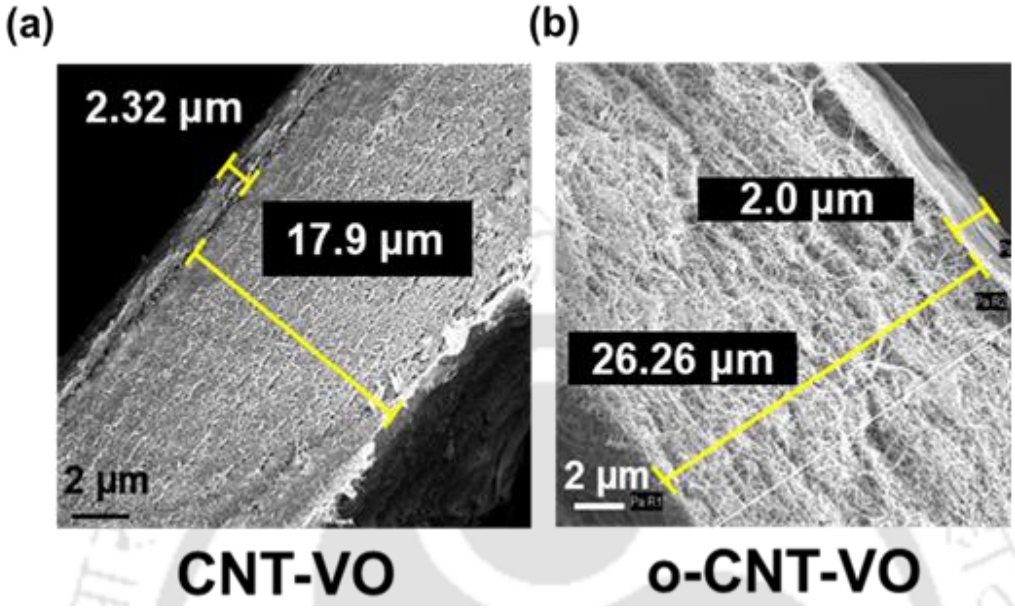

Figure 4.15: *Cross-sectional FESEM images of (a) CNT-VO and (b) o-CNT-VO after multiple bending experiments..*

As demonstrated earlier, in CNT-VO and o-CNT-VO, carbon nanotubes and vanadium pentoxide flakes possess strong interfacial attractions. The cross-sectional FESEM examination of CNT-VO and o-CNT-VO showed no sign of defacement even after repeated bending maneuvers as can be seen in Figure 4.15.

4.5.4 Transfer of objects

The precise and reliable light-induced bending moment of CNT-VO and o-CNT-VO can also be used to transfer objects from one location to another. As a proof of concept, a soft gripper was fabricated out of six bilayer strips (20 × 3 × 0.015 mm^3 in size) by mounting them to a glass rod in such a way that the V_2O_5 side of the bilayer membrane faces each other, as can be seen from the digital image in Figure 4.16. When exposed to IR light, the arms bowed inward and recovered their original shape once the light source was turned off. This gripper can be remotely operated by exposing it to IR light to move substances from one location to another.

Figure 4.16: *Digital photo of the soft gripper used to transfer objects from one location to another*

Figure 4.17a shows the snapshots of an object's displacement (for 30 cm) (weighing 6 mg) using the bilayer actuator. It was experimentally found that an actuator with a weight of 15 mg can lift objects of a maximum weight of 146 mg (~ ten times its body weight).

The CNT-VO gripper was also employed to lift and release highly reactive chemicals like $KMnO_4$ and Na metal to demonstrate the practical applicability of the CNT-VO gripper. As depicted in the snapshots in Figure 4.17b, the CNT-VO gripper can conveniently lift and deliver $KMnO_4$ per the user's requirements. The quantity of $KMnO_4$ picked up by the gripper in each cycle was plotted, as can be seen in Figure 4.17c. After repeating this maneuver for 15 cycles, strips were characterized with IR, XPS, and Raman spectroscopy, and no significant changes in the composition was observed, as can be seen in Figure 4.18. Similarly, lifting and delivering of Na metal did not show any visible change in physical appearance or bending speed of the CNT-VO gripper (Figure 4.17d). However, translocating sodium metal (4 mg) for 5 cycles shows the presence of Na atoms on the surface of the CNT-VO gripper (XPS in Figure 4.18b). Similarly, the characteristics of the Raman spectrum of the CNT-VO gripper changed

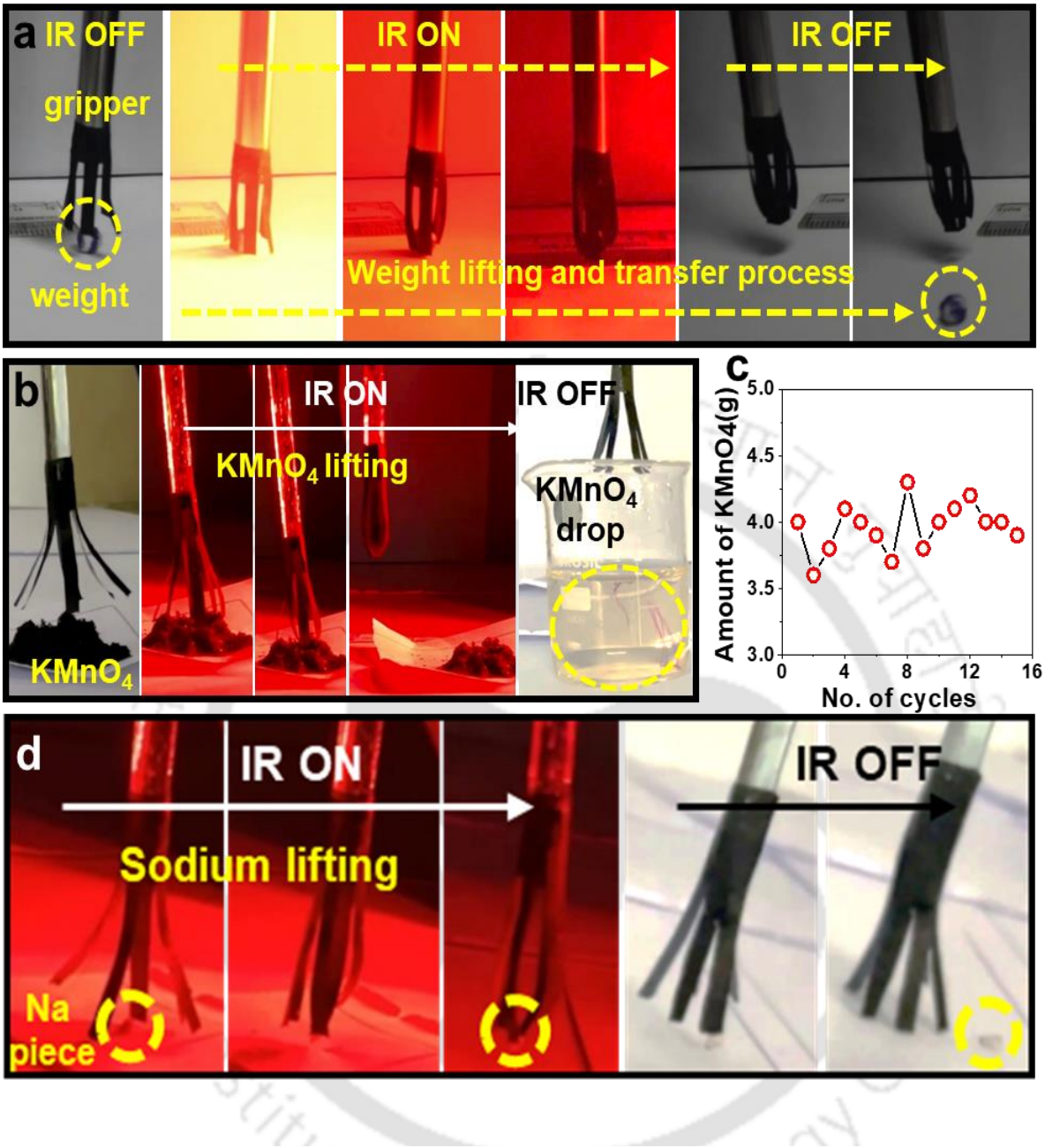

Figure 4.17: *(a) Snapshots showing the lifting and dropping of weight (6 mg) by a gripper for a distance of 30 cm. (b) Remote handling of $KMnO_4$ by the gripper. (c) Plot showing the weight of $KMnO_4$ picked up by the gripper each time for 15 cycles. (d) Snapshots showing the transfer of a piece of Na by the soft gripper on application of IR light ON and OFF cycles.*

after lifting Na metal pieces five times (Figure 4.18c), which is attributed to the explosive/exothermic reaction of Na metal towards atmospheric water molecules.

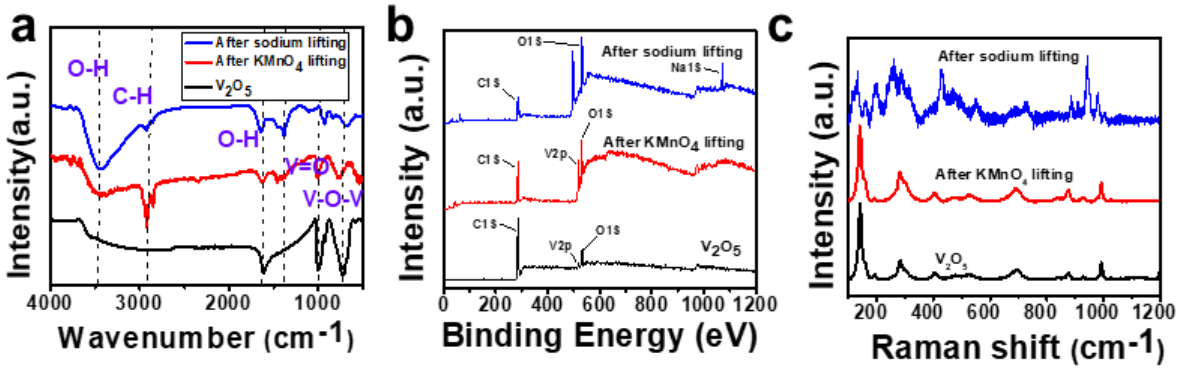

Figure 4.18: *Characterization of the VO side of the bilayer strip before and after lifting sodium and $KMnO_4$. (a) IR, (b) XPS, and (c) Raman spectra.*

To demonstrate the ability of the bilayer strip to move like a worm, a trapezoidal strip (22 mm in length, 7 mm at the base, and 4 mm at the tip) was cut, as shown in the Figure 4.19a. The strip started to move like a worm when exposed to light at regular intervals. Snapshots of this worm-like walking is shown in Figure 4.19b. This worm-like movement is attributed to the fact that it bends in the presence of light and returns to its original shape when the light source is cut off. During the OFF cycles, the larger end of the trapezoidal strip offers higher resistance to move in the backward direction (original shape) than that of the smaller end. This unequal movement of the opposite end of the trapezoidal strip assimilated to generate the worm-like movement propelled by light exposure's ON and OFF cycles.

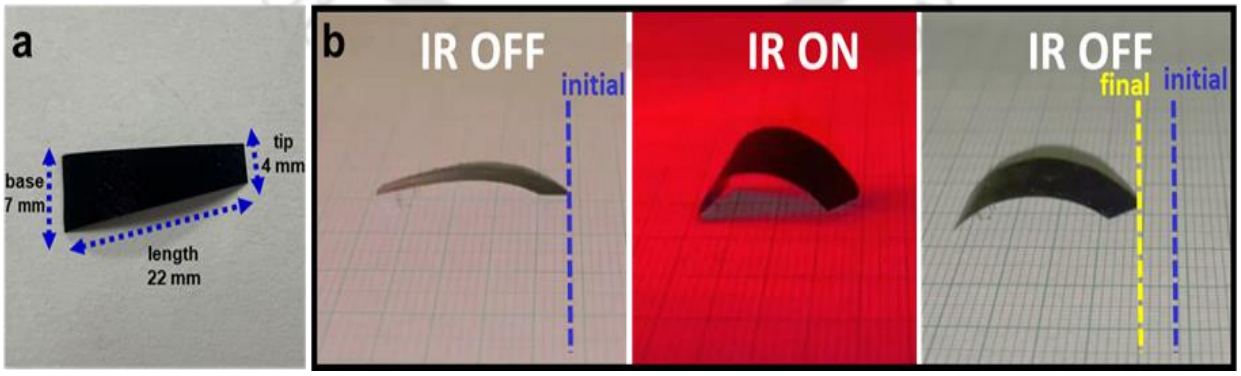

Figure 4.19: *(a) Digital photo of the strip used to demonstrate worm-like walking. (b) worm-like walking of the CNT-VO bilayer actuator.*

Remote handling systems that transfer microliter-sized liquid droplets are significant for technological applications and fundamental studies. Remarkably, the bilayer strip of o-CNT-VO can transfer microdroplets of liquids. The hydrophobic o-CNT side (contact angle = 126°) possesses amazing adhesiveness toward water droplets. Like Rose petals, on the hydrophobic surface of o-CNT, water droplets were found to be pinned on even after turning it upside down as can be seen in Figure 4.20. These unique properties of the o-CNT-VO strip were explored to prepare a microdroplet transferring system remote-handled with light and electricity. Typically, the bilayer membrane was cut into a rectangular strip of 20 × 3 × 0.016 mm^3 dimensions and affixed to a steel rod to touch the water droplet. A 10 µL water droplet is placed

Figure 4.20: *Hydrophobic surface of o-CNT of holding water droplet at upside down position.*

on a taro leaf surface (contact angle 150°) just underneath the bilayer strip. As soon as the IR light was turned on, the strip bowed upwards, returned to its previous shape, and touched the droplet from the CNT side as soon as the light was switched off. When the IR source was put back on, a portion of the droplet (4 µL) clung up with the CNT surface and travelled along with the bilayer strip. A hydrophilic pH paper was placed just beneath the lifted water droplet, and the IR source was switched off. The transfer was finished as soon as the droplet made contact with the pH paper and broke free from the bilayer strip (snapshots of the entire process are shown in Figure 4.21a). Similarly, an electrical potential of 7 V applied to a U-shaped o-CNT-VO device was shown to transfer a small water droplet (6 µL) from a bulk water droplet as can

be seen in Figure 4.21b. The light-induced liquid transfer capability of the bilayer membrane was expanded to showcase its wide range of applicability. The membrane successfully facilitated the transfer of dilute acid (0.1 M H_2SO_4) and base (0.1 M NaOH), as evidenced by the snapshots provided in the Figure 4.22. Repetition of microdroplet lifting experiment with both acidic and basic solutions for more than 10 times each did not show any visible change in the spectroscopic characterizations of o-CNT-VO strip (Figure 4.23).

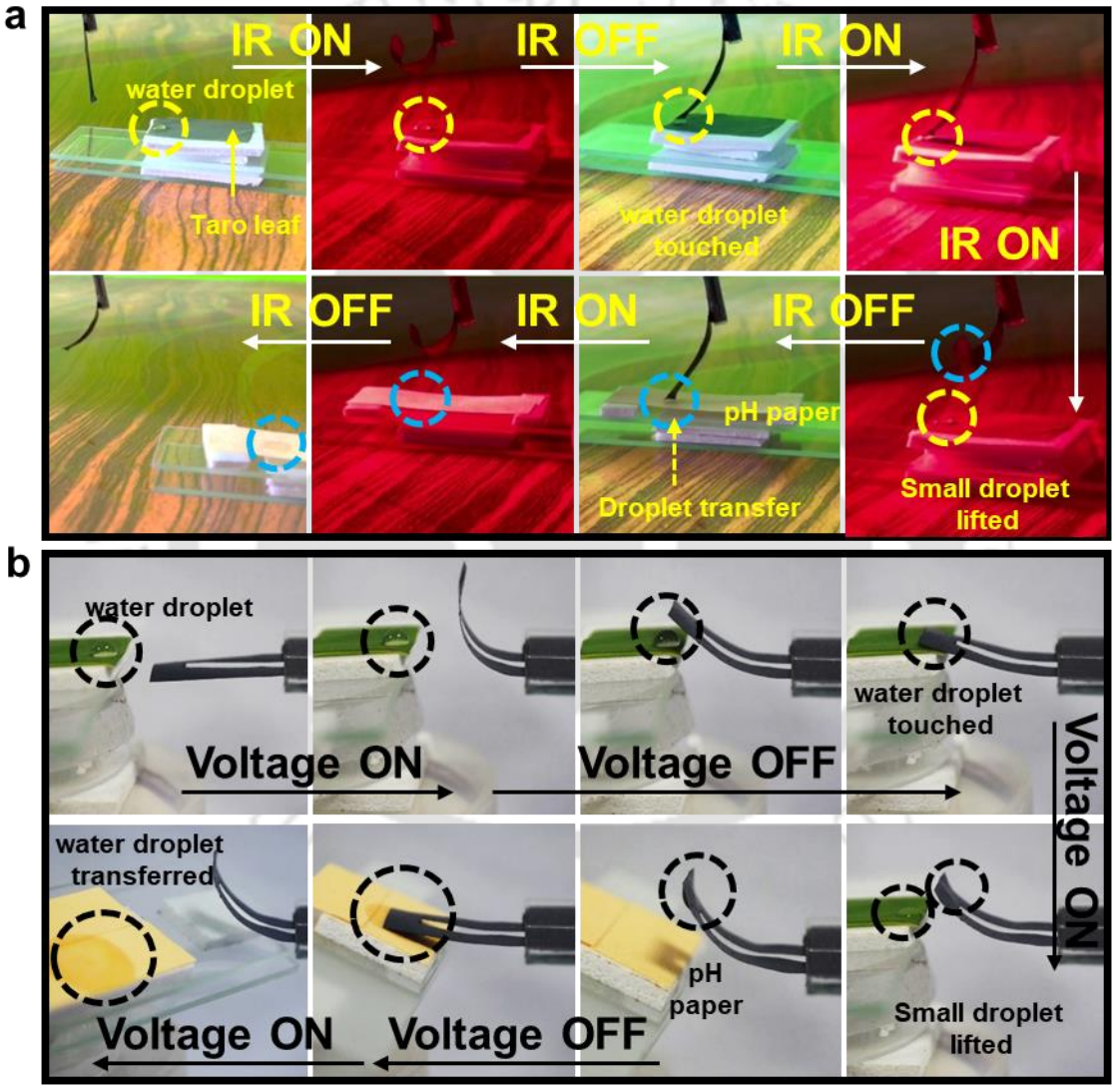

Figure 4.21: *(a) Snapshots showing a rectangular-shaped strip of o-CNT-VO bilayer membrane picking up a 4 μL water droplet from a taro leaf surface and its corresponding transfer to a pH indicator paper using IR light. ON and OFF cycles are shown. (b) Snapshots of a U-shaped o-CNT-VO device picking up a tiny droplet of water from a bulk droplet and its subsequent transfer to a pH indicator paper using an applied potential of 7V.*

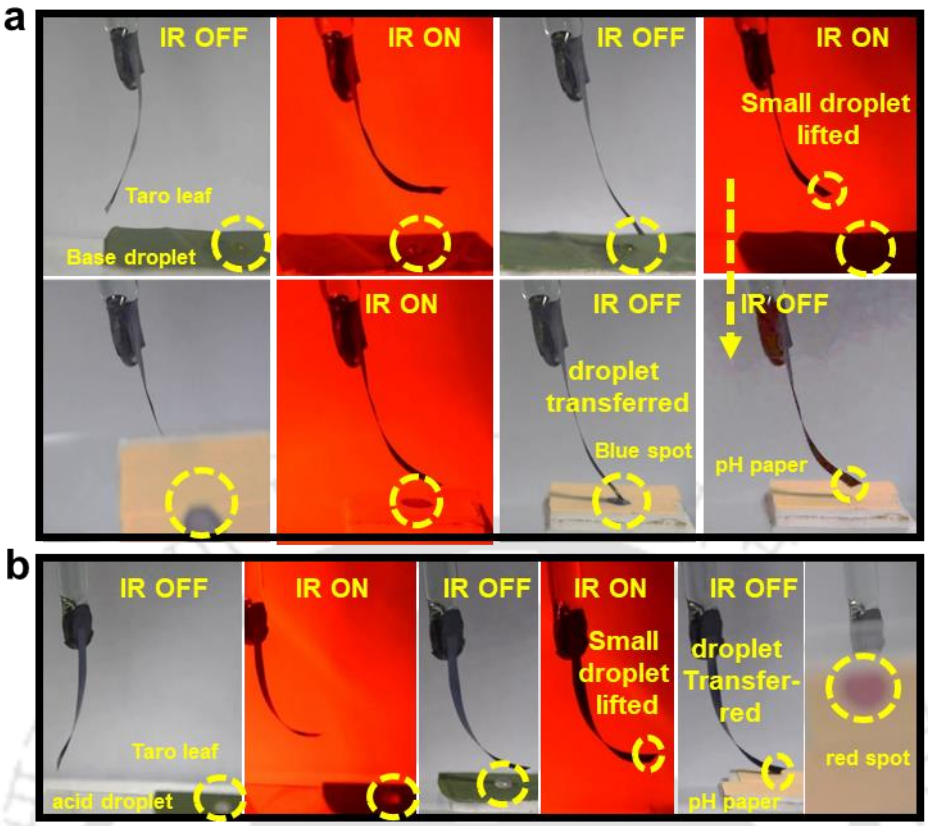

***Figure 4.22**: Snapshots showing a rectangular-shaped strip of o-CNT-VO bilayer membrane picking up (a) base (0.1 M NaOH) and (b) acid (0.1 M H_2SO_4) droplet from a taro leaf surface and its corresponding transfer to a hydrophilic pH indicator paper using IR light. ON and OFF cycles are shown.*

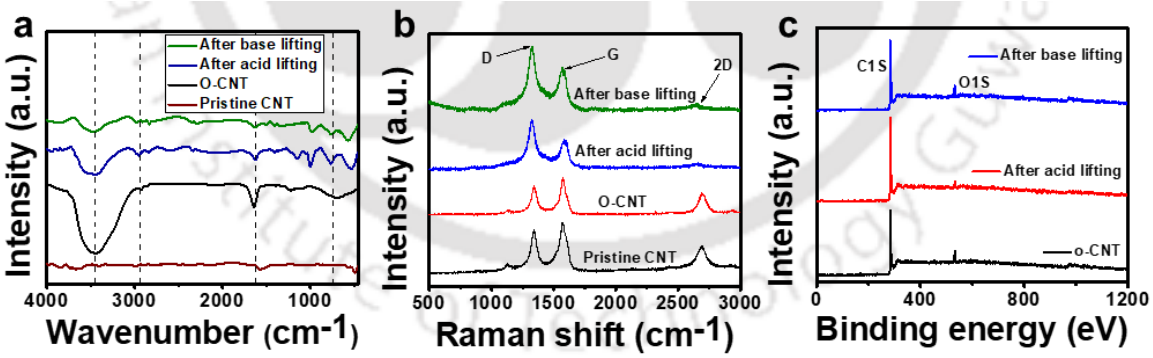

***Figure 4.23:** Characterization of the o-CNT side of the bilayer strip before and after lifting acid and base. (a) IR, (b) Raman, and (c) XPS spectra.*

4.5.5 Simultaneous transferring and sensing of microdroplets

Most interestingly, the o-CNT-VO-based remote handling system transfers micro-objects and can sense the substances it is transferring. A U-shaped strip was cut from the bilayer membrane

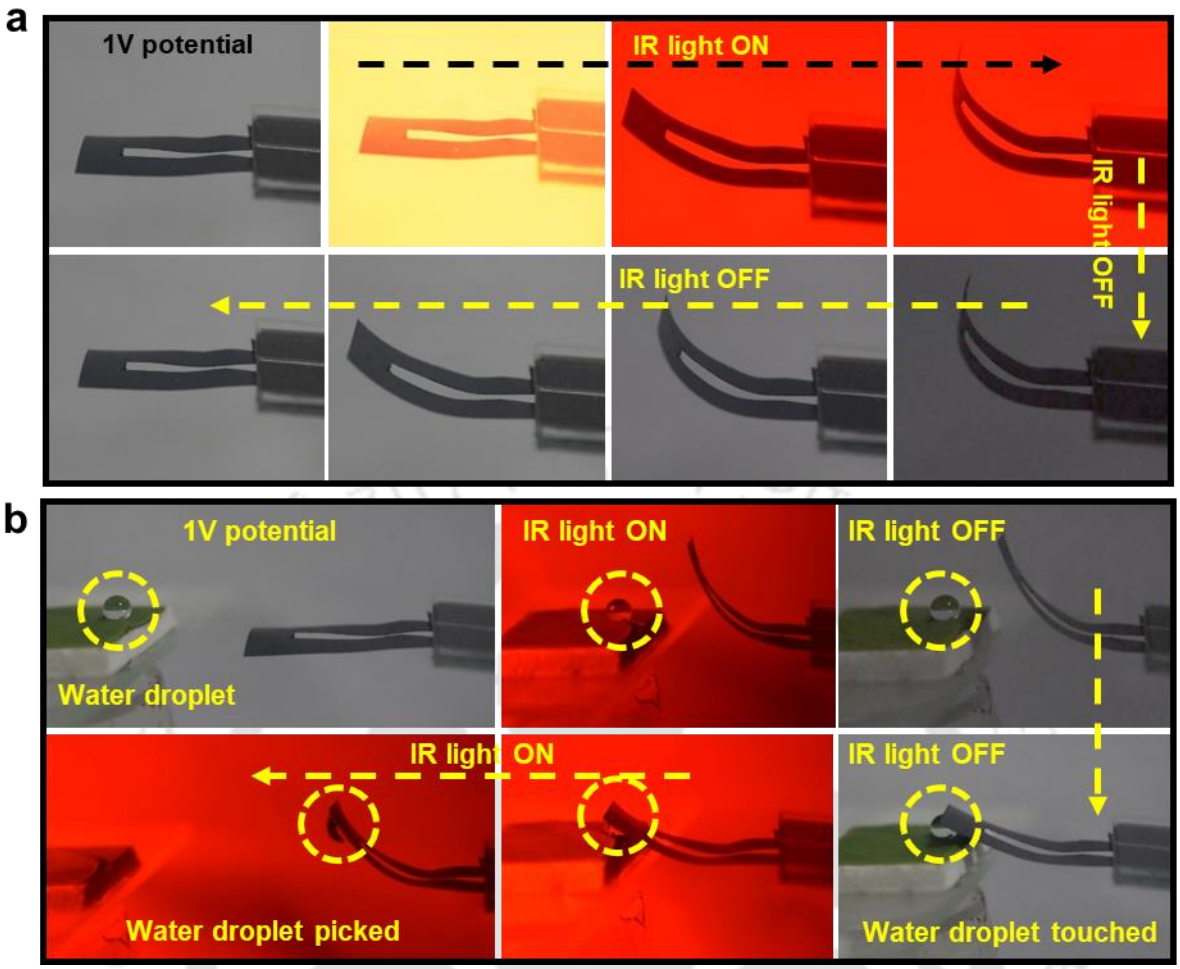

Figure 4.24: *(a) Snapshots of a U-shaped device of o-CNT-VO on application of an electrical potential of 1 V and bending on response to IR light. (b) Snapshots of sensing a water droplet on touching by the o-CNT side under conditions of 1 V applied potential and IR ON and OFF cycles.*

to demonstrate the lifting and sensing capability of o-CNT-VO (Figure 4.24). A potential of 1V was applied between the two arms of the U-shaped strip, and the current was recorded as a function of time. As shown in the snapshots of Figure 4.24a and 4.24b, the U-shaped strip can also be remotely controlled with light to lift and deliver microdroplets of different liquids. As soon as the U-shaped strip touched the water droplet, a definite change in the current values was observed, as can be seen in Figure 4.25a. Such change in electrical signals will have enormous importance during the technical application of this remote handling system as it can directly provide feedback about the successful completion of the operation. The decrease in

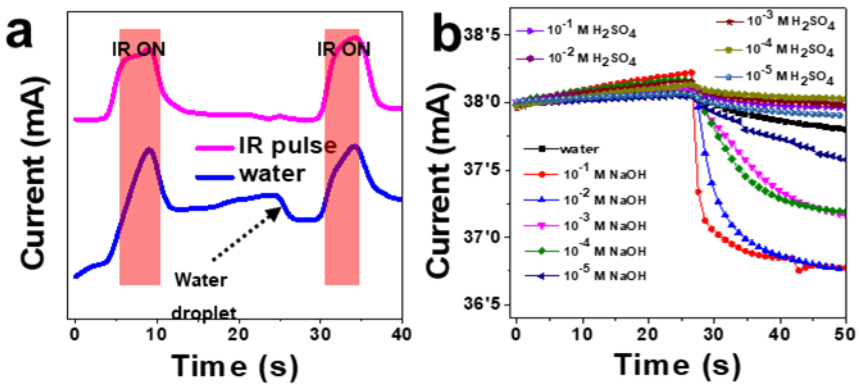

Figure 4.25: *(a) Plot of current vs time recorded when the U-shaped device of o-CNT-VO touches a droplet of water under conditions of 1 V applied potential and IR ON and OFF cycles. (b) A rectangular strip of o-CNT-VO device sensing droplets of water, 10-1 - 10-5 M H_2SO_4 and 10^{-1} - 10^{-5} M NaOH.*

current values upon exposure to liquid droplets is attributed to the increasing electric resistance due to the presence of liquids on the surface of the CNT strip. A similar experiment was also repeated with H_2SO_4 and NaOH solutions. In order to further investigate the sensing behavior, two copper wires were connected to both ends of an o-CNT-VO strip as shown in Figure 4.26, using Ag-paste. A potential of 1 V was applied with the help of a Sourcemeter (Keithley 2450) instrument, and the current was recorded as a function of time. As soon as the droplet of water (25 µL) was placed on the o-CNT surface, a change in the current value was observed as can be seen in Figure 4.25b.

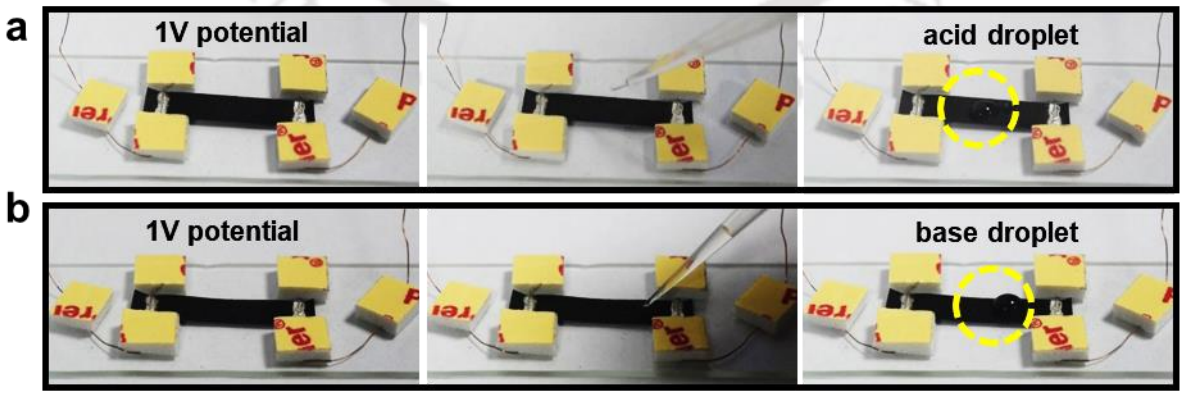

Figure 4.26: *A rectangular strip of o-CNT-VO sensing droplets of (a) 10^{-1} M H_2SO_4 and (b) 10^{-1} M NaOH respectively.*

The experiment was repeated with 10^{-1} to 10^{-5} M H_2SO_4 and 10^{-1} to 10^{-5} M NaOH solutions, and a similar response was detected. As can be seen from Figure 4.25b, for the same volume of liquid (25 µL), the NaOH droplets induced a more significant decrease in current values than that of DI water and acids. The sensitivity of the o-CNT-VO for acid and base was defined by using the following equation $\frac{\Delta I}{\Delta c \times A}$, where ΔI is the change in current, Δc is the change in concentration and A is the total area of the device. The sensitivity for acid and bases were calculated to be 0.108 mA $M^{-1}cm^{-2}$ and 0.28 $mAM^{-1}cm^{-2}$, with an error limit of 0.004 mA M^{-1} and 0.001 mA M^{-1}, respectively.

This change in the electrical current between the ends of the o-CNT-VO strip in the presence of liquid droplets could provide accurate feedback on the kind of samples the bilayer-based remote handling system is dealing with. When the CNT membrane was exposed to liquid samples (water, acid and base), the resistance between the nanotubes increased due to the penetration of liquid molecules in the junction between the tubes. However, pristine CNT and

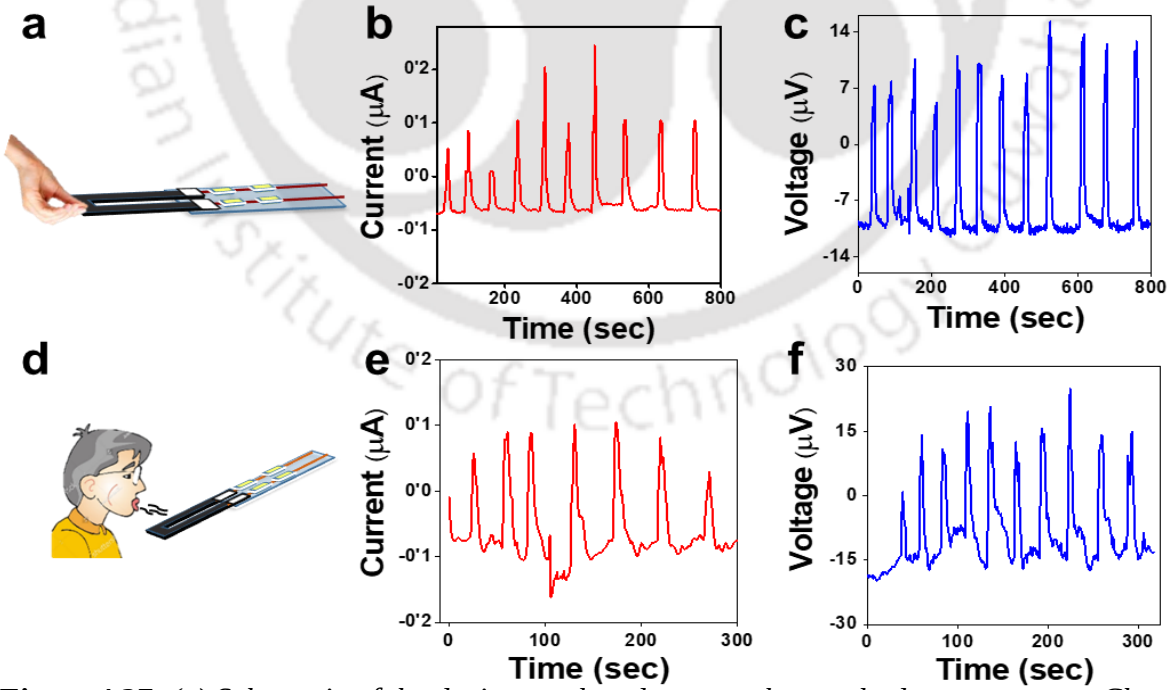

Figure 4.27: *(a) Schematic of the device employed to sense human body temperature. Change in (b) current and (c) voltage on response to human touch. (d) Schematic showing application of the device to sense warm air from mouth. Change in (e) current and (f) voltage on response to warm air exhalation.*

o-CNT are p-type materials, with most charge carriers being holes. In the case of acid, the H^+ ion binds to the surface of CNT and accepts e^- from the p-orbital of the nanotube. This increases the concentration of holes in the CNT and minimizes the decrease in conductance due to increasing inter-tube resistance. On the other hand, the hydroxide (OH^-) ions cause the opposite effect, further decreasing the conductance of CNT by decreasing the hole concentration.[92–94]

The bilayer actuator can also detect the temperature of objects it touches and provide definite signals of changing current and voltage values. Electrical signals obtained with every touch of fingers on a U-shaped device are shown in Figure 4.27a-c. Furthermore, the U-shaped device of o-CNT-VO also senses the warmth of mouth air and responds by generating electrical signals (Figure 4.27d-f). To verify whether current and voltage signals are due to the heat release from the mouth or the vapours, same experiments was repeated with vapours of water, ethanol, methanol and acetone (Figure 4.28), but no detectable response was observed, indicating that the signals of mouth air is due to the heat only. To further investigate the effect

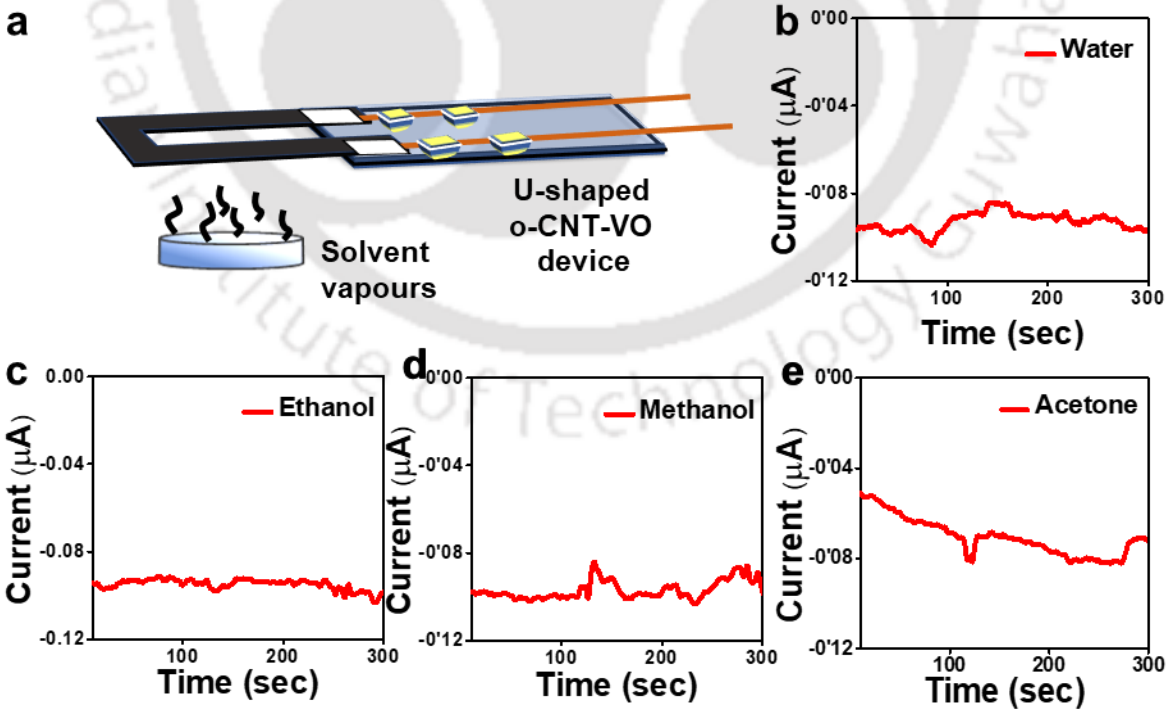

Figure 4.28: *(a) Schematic of the device used to detect probable signals due to different solvent vapours. Plot of current signals vs time with vapours of different solvents (b) water, (c) ethanol, (d) methanol and (e) acetone.*

of temperature on the electrical signal, the U-shaped o-CNT-VO device was exposed to different temperatures with the help of a nichrome belt (Figure 4.29a). As shown in Figure 4.29b, with the gradual increment of the heat on the device, the intensity of the electrical signal gradually increased.

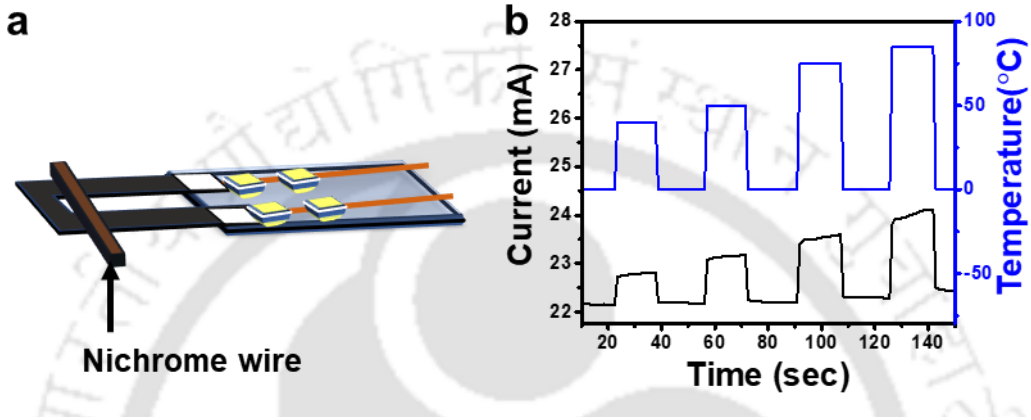

Figure 4.29: *(a) Schematic of the device used to investigate the effect of temperature on the electrical signal of the U-shaped device. (b) The plot of increase of current with an increment of temperature.*

4.5.6 Robustness of CNT-VO membrane

The responsive membranes discussed here possess an enormous potential for practical application. However, for any practical device, robustness is a prerequisite. To examine the robustness of the CNT-VO membrane, three strips (of dimension 20 × 3 × 0.015 mm^3) were

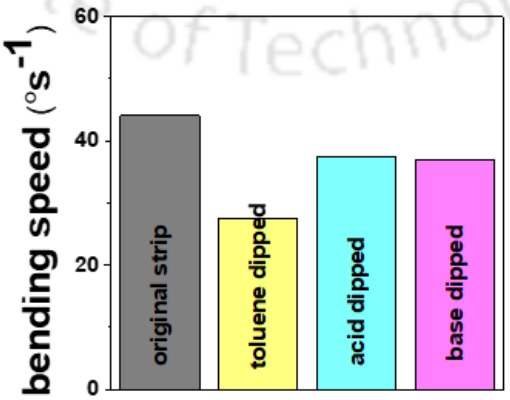

Figure 4.30: *Plot of comparison of bending speeds of the CNT-VO strip after dipping in toluene, acid, and base solution with the original speed.*

cut from the bilayer membrane, dipped in three different solvents (toluene, 0.1 M H_2SO_4, and 0.1M NaOH) for 2 minutes, and allowed to dry. Once dried, strips were exposed to IR light of intensity 15k lux, and bending speeds were calculated. It was found that in all the cases, the bilayer strips recovered its shape-morphing characteristics with a negligible decrease in bending speed, as can be seen in the bar diagram of Figure 4.30.

4.6 Conclusions

In summary, this chapter demonstrates the potential of responsive materials for the development of remote handling systems capable of operating with toxic and explosive substances. We have established this concept by preparing bilayer membranes of CNT and VO, as well as oxidized CNT and VO, using a sequential vacuum filtration method. The light responsiveness of the CNT-VO membrane is attributed to the distinct photothermal activities of CNT and VO, while the unequal Joule heating in the CNT-VO membrane accounts for the electrically induced actuation behaviour observed in the oxidized CNT-VO strip. These CNT-VO and o-CNT-VO based remote handling systems exhibit the capability to grasp, release, and sense the materials being transported, akin to the functions of human fingers. The robustness of the CNT and VO based responsive materials was confirmed by their ability to withstand immersion in corrosive and toxic liquids, underscoring the practical utility of the developed remote handling system. Given the wide array of mechanically robust and chemically inert responsive systems, further research on light and voltage-responsive actuators is anticipated to lead to the development of commercial remote handling systems. This advancement will significantly benefit individuals working with hazardous chemicals, biochemical agents, and radioactive materials.

4.7 References

1 M. Abolhasani and E. Kumacheva, *Nat. Synth.*, 2023, **2**, 483–492.

2 P. Segura, O. Lobato-Calleros, A. Ramírez-Serrano and I. Soria, *Adv. Ind. Manuf. Eng.*, 2021, **3**, 100060.

3 M. D. Cole, J. R. Owen and S. R. Adams, 2006.

4 D. K. Dennison, R. D. Merrill and R. K. Reed, 1995.

5 R. Bogue, *Industrial Robot*, 2012, **39**, 113–119.

6 G. R. D. Prabhu and P. L. Urban, *TrAC Trends Anal. Chem.*, 2017, **88**, 41–52.

7 D. A. Vargas Medina, E. V. S. Maciel and F. M. Lanças, *TrAC Trend Anal. Chem.*, 2023, **166**, 117171.

8 E. J. Jaselskis and M. R. Anderson, *J. Environ. Eng.*, 1994, **120**, 359–378.

9 R. K. Gogoi, A. B. Neog, N. Sarmah and K. Raidongia, *J. Mater. Chem. A*, 2019, **7**, 21157–21167.

10 P. P. Saikia, P. Garg, K. Mayawad, T. Paul, A. B. Neog, B. J. Sarmah, K. Raidongia and R. K. Gogoi, *Mater. Adv.*, 2023, **4**, 3619–3627.

11 D. Chen and Q. Pei, *Chem. Rev.*, 2017, **117**, 11239–11268.

12 F. D. Jochum and P. Theato, *Chem. Soc. Rev.*, 2013, **42**, 7468–7483.

13 P. Martins, D. M. Correia, V. Correia and S. Lanceros-Mendez, *Phys. Chem. Chem. Phys.*, 2020, **22**, 15163–15182.

14 H. Cheng, J. Liu, Y. Zhao, C. Hu, Z. Zhang, N. Chen, L. Jiang, L. Qu, H. Cheng, J. Liu, Y. Zhao, C. Hu, Z. Zhang, N. Chen and L. Qu, *Angew. Chem. Int. Ed.*, 2013, **52**, 10482–10486.

15 L. Chen, M. Weng, P. Zhou, L. Zhang, Z. Huang and W. Zhang, *Nanoscale*, 2017, **9**, 9825–9833.

16 Y. Yang, Y. Tan, X. Wang, W. An, S. Xu, W. Liao and Y. Wang, *ACS Appl. Mater. Interfaces*, 2018, **10**, 7688–7692.

17 Y. Zhang and L. Ionov, *ACS Appl. Mater. Interfaces*, 2014, **6**, 10072–10077.

18 K. Yang, W. Cai, M. Lan, Y. Ye, Z. Tang, Q. Guo and M. Weng, *Soft Matter*, 2022, **18**, 9057–9068.

19 G. Wu, X. Wu, Y. Xu, H. Cheng, J. Meng, Q. Yu, X. Shi, K. Zhang, W. Chen, S. Chen, G. Wu, X. Wu, H. Cheng, J. Meng, S. Chen, Y. Xu, Q. Yu, X. Shi, K. Zhang and W. Chen, *Adv. Mater.*, 2019, **31**, 1806492.

20 S. Xiao, Y. Yang, M. Zhong, H. Chen, Y. Zhang, J. Yang and J. Zheng, *ACS Appl. Mater. Interfaces*, 2017, **9**, 20843–20851.

21 J. Lv, L. Zhu, M. Zhang, Z. Zhao, S. W. Chen and J. Wang, *Polymer*, 2022, **245**, 124669.

22 X. Wang, B. Yang, D. Tan, Q. Li, B. Song, Z. S. Wu, A. del Campo, M. Kappl, Z. Wang, S. N. Gorb, S. Liu and L. Xue, *Mater. Today*, 2020, **35**, 42–49.

23 L. Li, G. Jia, W. Huang, J. Zhou, C. Li, J. Han, Y. Zhang and X. Zhou, *Sens. Actuators A Phys.*, 2023, **351**, 114149.

24 M. Kong, H. Li, Y. Liang, K. Cheng, X. Zhou, X. Song, Z. Yang, J. Xu and L. Zhao, *Sens. Actuators B Chem.*, 2023, **380**, 133390.

25 Y. Hu, L. Yang, Q. Yan, Q. Ji, L. Chang, C. Zhang, J. Yan, R. Wang, L. Zhang, G. Wu, J. Sun, B. Zi, W. Chen and Y. Wu, *ACS Nano*, 2021, **15**, 5294–5306.

26 A. B. Neog, R. K. Gogoi, P. Deka, T. J. Konch, B. R. Bora and K. Raidongia, *New J. Chem.*, 2021, **45**, 16883–16891.

27 R. K. Gogoi, K. Saha, J. Deka, D. Brahma and K. Raidongia, *J. Mater. Chem. A*, 2017, **5**, 3523–3533.

28 A. B. Neog, R. K. Gogoi, T. Dutta and K. Raidongia, *ACS Appl. Nano Mater.*, 2020, **3**, 6629–6635.

29 R. Kumar Gogoi, K. Raidongia, R. K. Gogoi and K. Raidongia, *Adv. Mater.*, 2017, **29**, 1701164.

30 K.-X. Hou, P.-C. Zhao, C.-H. Li, K.-X. Hou, P.-C. Zhao and C.-H. Li, *Adv. Opt. Mater.*, 2023, **11**, 2202949.

31 R. K. Gogoi and K. Raidongia, *J. Mater. Chem. A*, 2018, **6**, 21990–21998.

32 J. E. Yim, S. H. Lee, S. Jeong, K. A. I. Zhang and J. Byun, *J. Mater. Chem. A*, 2021, **9**, 5007–5015.

33 J. Cao, Z. Zhou, Q. Song, K. Chen, G. Su, T. Zhou, Z. Zheng, C. Lu and X. Zhang, *ACS Nano*, 2020, **14**, 7055–7065.

34 X. Yu, H. Cheng, M. Zhang, Y. Zhao, L. Qu and G. Shi, *Nat. Rev. Mater.*, 2017, **2**, 1 –13.

35 X. Zhu, Y. Hu, G. Wu, W. Chen and N. Bao, *ACS Nano*, 2021, **15**, 9273–9298.

36 Paras, K. Yadav, P. Kumar, D. R. Teja, S. Chakraborty, M. Chakraborty, S. S. Mohapatra, A. Sahoo, M. M. C. Chou, C. Te Liang and D. R. Hang, *Nanomater.*, 2022, **13**, 160.

37 Y. Wang, N. Xu, D. Li and J. Zhu, *Adv. Funct. Mater.*, 2017, **27**, 1604134.

38 S. Fleischmann, M. A. Spencer and V. Augustyn, *Chem. Mater.*, 2020, **32**, 3325–3334.

39 M. Guo, J. Han, Q. Ran, M. Zhao, Y. Liu, G. Zhu, Z. Wang and H. Zhao, *Ceram. Int.*, 2023, **49**, 37549–37560.

40 M. Guo, F. Li, Q. Ran, G. Zhu, Y. Liu, J. Han, G. Wang and H. Zhao, *Microchem. J.*, 2023, **190**, 108709.

41 H. Zhao, Y. Liu, F. Li, G. Zhu, M. Guo, J. Han, M. Zhao, Z. Wang, F. Nie and Q. Ran, *Ceram. Int.*, 2023, **49**, 26289–26301.

42 Y. Liu, Q. Wang, G. Zhu, Q. Ran, F. Li, M. Guo, G. Wang and H. Zhao, *Ceram. Int.*, 2023, **49**, 21234–21245.

43 H. Zhao, G. Zhu, F. Li, Y. Liu, M. Guo, L. Zhou, R. Liu and S. Komarneni, *Sens. Actuators B Chem.*, 2023, **380**, 133309.

44 H. Zhao, M. Guo, F. Li, Y. Zhou, G. Zhu, Y. Liu, Q. Ran, F. Nie and V. Dubovyk, *J. Mater. Res. Technol.*, 2023, **24**, 2100–2112.

45 Y. Liu, T. Wu, H. Zhao, G. Zhu, F. Li, M. Guo, Q. Ran and S. Komarneni, *Ceram. Int.*, 2023, **49**, 23775–23787.

46 M. Sathiya, A. S. Prakash, K. Ramesha, J. M. Tarascon and A. K. Shukla, *J. Am. Chem. Soc.*, 2011, **133**, 16291–16299.

47 V. Datsyuk, M. Kalyva, K. Papagelis, J. Parthenios, D. Tasis, A. Siokou, I. Kallitsis and C. Galiotis, *Carbon*, 2008, **46**, 833–840.

48 I. D. Rosca, F. Watari, M. Uo and T. Akasaka, *Carbon*, 2005, **43**, 3124–3131.

49 F. Avilés, J. V. Cauich-Rodríguez, L. Moo-Tah, A. May-Pat and R. Vargas-Coronado, *Carbon*, 2009, **47**, 2970–2975.

50 J. Zhang, H. Zou, Q. Qing, Y. Yang, Q. Li, Z. Liu, X. Guo and Z. Du, *J. Phys. Chem. B*, 2003, **107**, 3712–3718.

51 T. A. Saleh, *Appl. Surf. Sci.*, 2011, **257**, 7746–7751.

52 N. Jain, E. Gupta and N. J. Kanu, *Smart Sci.*, 2022, **10**, 1–24.

53 R. Das, M. E. Ali, S. B. A. Hamid, S. Ramakrishna and Z. Z. Chowdhury, *Desalination*, 2014, **336**, 97–109.

54 C. Rizzuto, G. Pugliese, M. A. Bahattab, S. A. Aljlil, E. Drioli and E. Tocci, *Sep. Purif. Technol.*, 2018, **193**, 378–385.

55 K. Sears, L. Dumée, J. Schütz, M. She, C. Huynh, S. Hawkins, M. Duke and S. Gray, *Materials*, 2010, **3**, 127–149.

56 Z. Liu, S. Tabakman, K. Welsher and H. Dai, *Nano Res.*, 2010, **2**, 85–120.

57 B. S. Harrison and A. Atala, *Biomater.*, 2007, **28**, 344–353.

58 G. Centi and S. Perathoner, *ChemSusChem*, 2011, **4**, 913–925.

59 S. Kumar, R. Rani, N. Dilbaghi, K. Tankeshwar and K. H. Kim, *Chem. Soc. Rev.*, 2017, **46**, 158–196.

60 N. Bahlawane and D. Lenoble, *Chem. Vap. Depos.*, 2014, **20**, 299–311.

61 R. B. Darling and S. Iwanaga, *Sadhana – Acad. Proc. Eng. Sci.*, 2009, **34**, 531–542.

62 G. S. Nadkarni and V. S. Shirodkar, *Thin Solid Films*, 1983, **105**, 115–129.

63 F. J. Morin, *Phys. Rev. Lett.*, 1959, **3**, 34.

64 M. Mousavi, A. Kompany, N. Shahtahmasebi and M. M. Bagheri-Mohagheghi, *Mod. Phys. Lett. B*, 2013, **27**, 1350152.

65 M. R. J. Scherer, L. Li, P. M. S. Cunha, O. A. Scherman and U. Steiner, *Adv. Mater.*, 2012, **24**, 1217–1221.

66 C. Lamsal and N. M. Ravindra, *J. Mater. Sci.*, 2013, **48**, 6341–6351.

67 S. Nishio and M. Kakihana, *Chem. Mater.*, 2002, **14**, 3730–3733.

68 M. Nazemiyan and Y. S. Jalili, *AIP Adv.*, 2013, **3**, 112103.

69 M. S. Thomas, J. F. DeNatale and P. J. Hood, *Mater. Res. Soc. Symp. Proc.*, 1997, **479**, 161–166.

70 J. B. K. Kana, J. M. Ndjaka, P. O. Ateba, B. D. Ngom, N. Manyala, O. Nemraoui, A. C. Beye and M. Maaza, *Appl. Surf. Sci.*, 2008, **254**, 3959–3963.

71 V. Simic-Milosevic, N. Nilius, H. P. Rust and H. J. Freund, *Phys. Rev. B*, 2008, **77**, 125112.

72 C. Wu, H. Wei, B. Ning and Y. Xie, *Adv. Mater.*, 2010, **22**, 1972–1976.

73 R. K. Gogoi, A. B. Neog, T. J. Konch, N. Sarmah and K. Raidongia, *J. Mater. Chem. A Mater*, 2019, **7**, 10552–10560.

74 R. K. Gogoi, A. B. Neog, N. Sarmah and K. Raidongia, *J. Mater. Chem. A*, 2019, **7**, 21157–21167.

75 J. Deka, K. Saha, R. Gogoi, G. K. Dutta and K. Raidongia, *ACS. Appl. Electron. Mater.*, 2021, **3**, 277–284.

76 K. Mayawad, R. Gogoi and K. Raidongia, *Nano Lett.*, 2024, **24**, 15.

77 R. Gogoi, H. Madeshwaran, A. Ghosh, Y. Green, K. Raidongia, R. Gogoi, H. Madeshwaran, A. Ghosh, K. Raidongia and Y. Green, *Adv. Funct. Mater.*, 2023, **33**, 2301178.

78 P. Deka, S. Roy, T. Jyoti Konch, B. Rani Bora, R. Gogoi, A. Bikash Neog, K. Sundararajan, S. Subbiah and K. Raidongia, *Chem. Eng. J.*, 2023, **469**, 143964.

79 K. Saha, J. Deka and K. Raidongia, *ACS Appl. Energy Mater.*, 2021, **4**, 8410–8420.

80 T. H. Kim, D. H. Nam, D. H. Kim, G. Leem and S. Lee, *Polymers*, 2022, **14**, 2942.

81 B. Han, Y.-L. Zhang, Q.-D. Chen, H.-B. Sun, A. B. Han, Y.-L. Q. Zhang, -D Chen and -B H Sun, *Adv. Funct. Mater.*, 2018, **28**, 1802235.

82 Y. Hu, J. Liu, L. Chang, L. Yang, A. Xu, K. Qi, P. Lu, G. Wu, W. Chen and Y. Wu, *Adv. Funct. Mater.*, 2017, **27**, 1704388.

83 Y. Tai, G. Lubineau, Z. Yang, Y. Tai, Z. Yang and G. Lubineau, *Adv. Mater.*, 2016, **28**, 4665–4670.

84 L. Chen, M. Weng, Z. Zhou, Y. Zhou, L. Zhang, J. Li, Z. Huang, W. Zhang, C. Liu and S. Fan, *ACS Nano*, 2015, **9**, 12189–12196.

85 M. Amjadi, M. Sitti, M. Amjadi and M. Sitti, *Adv. Sci.*, 2018, **5**, 1800239.

86 X. Zhang, Z. Yu, C. Wang, D. Zarrouk, J. W. T. Seo, J. C. Cheng, A. D. Buchan, K. Takei, Y. Zhao, J. W. Ager, J. Zhang, M. Hettick, M. C. Hersam, A. P. Pisano, R. S. Fearing and A. Javey, *Nat. Commun.*, 2014, **5**, 1–8.

87 J. Mu, C. Hou, H. Wang, Y. Li, Q. Zhang and M. Zhu, *Sci. Adv.*, 2015, **1**, 1500533.

88 J. Deng, J. Li, P. Chen, X. Fang, X. Sun, Y. Jiang, W. Weng, B. Wang and H. Peng, *J. Am. Chem. Soc.*, 2016, **138**, 225–230.

89 B. Han, H.-B. Sun, L. Zhu, Y.-Y. Gao and Y.-L. Zhang, *Opt. Lett.*, 2019, **44**, 1363–1366.

90 H. Bi, K. Yin, X. Xie, Y. Zhou, S. Wan, F. Banhart and L. Sun, *Nanoscale*, 2013, **5**, 9123–9128.

91 C. Wang, Y. Wang, Y. Yao, W. Luo, J. Wan, J. Dai, E. Hitz, K. Fu, L. Hu, C. Wang, Y. Wang, Y. Yao, W. Luo, J. Wan, J. Dai, E. Hitz, K. Fu and L. Hu, *Adv. Mater.*, 2016, **28**, 8618–8624.

92 W. Xue, Y. Liu and T. Cui, *Appl. Phys. Lett.*, 2006, **89**, 163512.

93 S. Takeda, M. Nakamura, A. Ishii, A. Subagyo, H. Hosoi, K. Sueoka and K. Mukasa, *Nanoscale Res. Lett.*, 2007, **2**, 207–212.

94 D. Lee and T. Cui, *J. Vac. Sci. Technol. B*, 2009, **27**, 842–848.

Chapter 5

Boosting of Concentration Gradient-Driven Energy Output by Employing Electrodes Possessing Contrasting Interfacial Activity

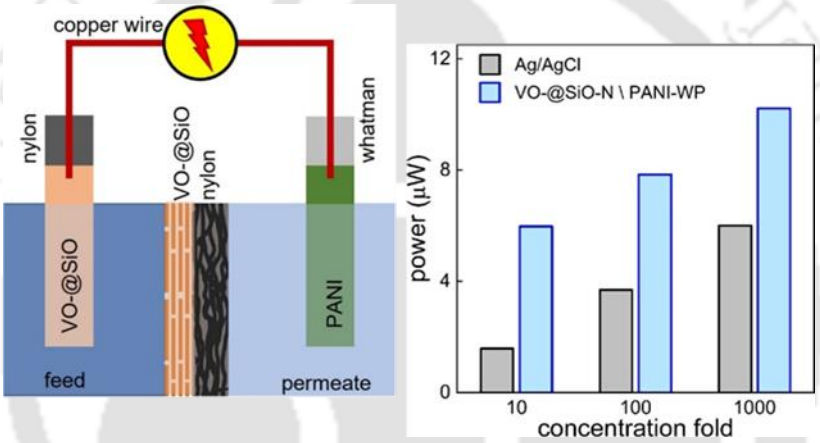

Summary

Motivated by its substantial theoretical potential, the concentration gradient is currently a focal point in pursuing sustainable energy resources. Widespread research efforts are directed towards advancing critical components for concentration gradient-driven energy harvesting devices, such as perm-selective membranes and electrode systems. This chapter presents the development of a novel permselective nanofluidic membrane. This was achieved through the coating of a commercial nylon membrane with two-dimensional (2D) nanosheets of vanadium pentoxide (V_2O_5) functionalised with –SiO– (VO-@SiO). The membrane potential (E_m) values obtained, after accounting for the redox contributions of the Ag/AgCl electrode, indicate that the coating is approximately ~14 µg.mm^{-2} VO-@SiO enhances the transport number of non-ion-selective nylon membranes from ~0.5 to ~0.8 (for K+ ion). The output potential of concentration gradient-driven energy harvesting devices can be significantly augmented by using electrodes prepared from materials with contrasting interfacial activities. The electrodes prepared from functionalised V_2O_5 and polyaniline (PANI) can generate electrical potential up to 150 mV through complementary charge transfer activities from quiescent water, without necessitating a concentration gradient. By employing a combination of V_2O_5 and PANI, the overall power output of the concentration gradient-driven energy generator was found to increase by 300% (in the presence of a 10-fold concentration gradient) compared to that of Ag/AgCl electrodes.

5.1 Introduction

Over the past few decades, there has been a noticeable increase in research endeavours aimed at developing innovative approaches for generating electricity from sustainable sources such as wind, waves, solar radiation, humidity, and concentration gradients.[1–3] Salinity gradient, among the contemporary sustainable energy sources, has garnered considerable attention due to its substantial theoretical potential and associated advantages, including accessibility, operational simplicity, predictability, and stable power output.[4] The prospective global capacity for utilizing the untapped estuarine salinity gradient power, achieved through the convergence of river and ocean water, is estimated at 2.6 TW, with 0.98 TW readily accessible for immediate extraction. Efficient harnessing of the world's salinity gradient power (SGP) has the potential to yield an annual production of 38 million tons of hydrogen.[5] In contrast to intermittent solar and wind energy sources, SGP is consistently available for utilization round the clock throughout the year. Pilot plants have already established the technological potential of membrane-based SGE systems.[6] The first pilot scale was officially launched in 2014 in the Netherlands Afsluitdijk.[7] An escalation in research endeavours is evident in the pursuit of optimizing various facets of reverse electrodialysis, thereby yielding a plethora of innovations across domains such as ion-selective membranes, electrode systems, and feed solutions.[8–11] For instance, Cao and his research team achieved an outstanding power density of 10.6 Wm^{-2} by utilizing vertically transported graphene oxide membranes and combining simulated river water with seawater.[12] Likewise, Alshareef et al., demonstrated a lamellar membrane by assembling nanoporous $Ti_3C_2T_x$ MXene sheets to overcome the trade-off between permeability and ion selectivity to attain power density as high as 17.5 Wm^{-2} under a 100-fold KCl gradient.[13] Concentration gradient-driven energy harvesting processes traditionally prioritize seawater and river water; however, researchers have also investigated other sustainable feed solutions.[14–19] Li et al. showed that using enzymatic biowaste as a feed solution and graphene-

based composite membranes resulted in electrical energy generation in a few milliwatts per square meter.[19] Wen et al. found a significant increase in the output power density (87.23 Wm^{-2}) by combining light and acid-base reactions using composite membranes of MXene and cellulose nanofiber.[20]

The electrode system is a vital component in converting concentration gradient to electricity, which converts ionic events into electric current. Several innovative approaches are being published in the literature to enhance the efficiency of electrode systems.[21] Park et al. developed a porous carbon-coated graphite electrode for the reverse electrodialysis (RED) application that exhibited approximately 10% higher power density compared to the metal mesh electrodes under similar conditions.[22] Kjelstrup et al. showed that inexpensive graphite and environmentally friendly salts ($FeCl_2$ and $FeCl_3$) in moderate concentrations could reduce the overpotential of RED electrodes.[23] Likewise, the $MoS_2/TiO_2/Ti$ heterostructure of Jeong et al. has shown great potential as a high-performance cathode for RED. Interfacial engineering between MoS_2 and TiO_2 has dramatically improved the catalytic activity and charge transfer efficiency.[21,24]

5.2 Scope of the present investigation

Recently, it has been demonstrated that immersing nanomaterials with contrasting interfacial activities into quiescent deionized water can generate electrical potentials of up to hundreds of millivolts. For instance, when yarns of pristine and oxygen-modulated carbon nanotubes were dipped in such a manner, He et al. achieved electrical power generation of up to 700 mWm^{-2}.[25] Deka et al. effectively utilized the discrepant interfacial properties of boron- and nitrogen-doped reduced graphene oxide to induce an electrical potential reaching 570 mV.[26] The current chapter presents a novel electrode system employing functionalised V_2O_5 and polyaniline. This system has demonstrated the ability to generate electrical potential from quiescent water, devoid of concentration gradients, through complementary charge transfer activities. Through

the utilization of this potential-generating electrode, the overall power of the concentration gradient-driven energy generator was observed to improve by up to 300% when matched to the performance of Ag/AgCl electrodes. As a consequence of the negatively charged functionalized V_2O_5 and the positively charged PANI, charge separation occurs, disrupting electrical neutrality and thus generating electrical energy. Collectively, these scientific advancements highlight the potential of the novel electrode system and underscore the promising prospects of blue energy harvesting through salinity gradients, offering valuable insights into sustainable energy generation from aquatic resources.

Material structure and properties: Polyaniline is a conducting polymer renowned for its distinctive structural and electrical properties emanating from its conjugated backbone comprising alternating single and double bonds. The polymer manifests several oxidation states, predominantly appearing in three discernible forms: leucoemeraldine (insulating), emeraldine (conducting), and pernigraniline (fully oxidised). Emeraldine, the most stable and widely employed form, exhibits favourable conductivity when doped.[27–29] The material's electrical conductivity is substantially augmented by adding dopants, such as acids, allowing it to modify its properties. This feature renders it suitable for application in electronic devices, batteries, and sensors. Notably, PANI demonstrates exceptional resistance to fluctuations in temperature and humidity and is adept at forming composites with other substances, such as metals and carbon nanotubes, thereby fortifying its mechanical and thermal properties.[30–33] Owing to its adaptable morphology, PANI can adopt various forms, including films, fibres, and nanostructures, thereby endowing it with pivotal significance in contemporary technologies, particularly energy storage and corrosion prevention.[34–36] The electrochemical attributes and outstanding environmental stability of PANI make it a judicious choice for diverse energy and electrical applications.[37–39]

5.3 Experimental section

Materials: Vanadium pentoxide (V_2O_5) (99.5 %) was purchased from SRL Pvt., Ltd. Hydrogen Peroxide (H_2O_2) (33 % w/v extrapure) was procured from Finar Ltd. The silver and copper electrodes were purchased from the local market. Silver paste was purchased from Alfa-Aesar Pvt. Ltd. Potassium chloride, bis[3-(triethoxysilyl) propyl] tetrasulfide (MW: 538.95 g/mol)., aniline, ammonium persulphate, acetone and hydrochloric acid were purchased from Merck and used as received. Nylon membrane (0.22 µm pore size) was purchased from Sterlitech Corporation, USA (Lot No. 7125851). The Whatman filter paper was purchased from Merck (Cat No. 105125R).

Preparation of vanadium pentoxide (V_2O_5) nanosheets: The V_2O_5 nanosheets were prepared by reaction of the bulk powder with H_2O_2 in water under ice-cold condition.[40,41] 2.4 g of V_2O_5 powder was poured into 25 mL of deionized (DI) water under ice-cold conditions and was continuously steered. 25 mL H_2O_2 (50%) was added slowly, which formed effervescence, turning the light brown-coloured solution into a dark brown gel. This gel was then diluted with DI water and sonicated in a bath sonicator for 30 minutes. The as-prepared V_2O_5 nanosheets from stable dispersion in water.

Functionalisation of V_2O_5 nanosheets with bis[3-(triethoxysilyl) propyl]tetrasulfide (VO-@SiO): To synthesise the VO-@SiO dispersion, 40 µl of bis[3-(triethoxysilyl) propyl] tetrasulfide (SiO) was agitated with 25 ml of ethanol for 1 hour.[42] Subsequently, 13 ml of V_2O_5 dispersion (15 mg/ml) was combined with the SiO solution and subjected to reflux conditions at 80°C for 3 hours. Following the reaction with SiO, the initial dark brownish-coloured V_2O_5 dispersion transitioned to a dark greenish-coloured VO-@SiO dispersion. The resultant solution was filtered through a PTFE membrane with a pore size of 0.1 µm, followed by drying under ambient conditions to yield the VO-@SiO membrane, which was then dispersed in deionised water. VO-@SiO nanosheets formed a stable dispersion in water.

Preparation of VO-@SiO nanosheets coated nylon membrane (VO-@SiO-N) membrane: Nylon membranes were coated by vacuum filtration of the nanosheets dispersion (1 mg/mL). Once the filtration was completed, the coated membranes were dried in a desiccator for 24 hours, followed by heating at 150 °C for 2 hours in a vacuum oven. The concentration (1 mg/mL) and volume of the dispersion used during the filtration process determines the magnitude of the coating.

Synthesis of polyaniline: Polyaniline was synthesised by the polymerisation of aniline using ammonium persulfate (APS).[43] Aniline (0.2 M) was oxidised with APS (0.25M) at 20 °C in 100 mL of 0.2 M HCl. The precipitated polymers were collected via filtration, washed successively with 0.2 M HCl and acetone, and dried.

PANI coated Whatman filter paper (PANI-WP): Like the VO-@SiO-N, the PANI-WPs were coated by vacuum filtration of the PANI dispersion (1 mg/mL) through Whatman filter paper, followed by drying in a desiccator for 24 hours.

VO-@SiO-N and PANI-WP electrodes preparation: The VO-@SiO-N and PANI-WP electrodes were prepared by cutting rectangular strips for the respective membranes. Strips of 4 cm × 2.5 cm were used for experiments related to electricity generation from calm water. The dipping area was fixed as ~6.25 cm^2 (2.5 cm × 2.5 cm). Likewise, for the energy generation from the reverse electrodialysis (RED), the dimensions of the strips are 2 cm × 0.5 cm, and the dipping area was ~0.5 cm^2 (1 cm × 0.5 cm).

5.4 Characterizations

Characterisation of V_2O_5 and VO-@SiO samples was conducted using an Atomic Force Microscope (AFM) (Oxford Cypher) and a Field Emission Transmission Electron Microscope (FETEM) (JEOL 2100F). PANI sample, morphology and cross-sections of the membranes were analysed using a Field Emission Scanning Electron Microscope (FESEM) (Zeiss Sigma). X-ray diffraction studies were performed using a Bruker D-205505 instrument with Cu-Kα

radiation (λ = 1.54 Å) (Rigaku Micromax-007HF model). Infrared spectroscopic analysis was performed using a Perkin Elmer instrument (Spectrum Two). The zeta potentials of the samples were analysed using a zetasizer instrument. Electrical investigations were conducted using a source meter device (Keithley 2450).

5.5 Result and discussion

A novel energy conversion system based on ion-selective membranes and charge-selective electrodes was developed to convert the potential energy stored in liquids into electricity. The ion-selective membrane was prepared by coating a commercial nylon membrane (purchased from Sterlitech Corporation) with –SiO– functionalised vanadium pentoxide (V_2O_5) nanosheets (VO-@SiO). The V_2O_5 nanosheets were prepared by the reaction of bulk V_2O_5 powder with H_2O_2 in aqueous medium under ice cold condition.[40,41] Figure 5.1a shows a digital photo of a 1 mg/mL aqueous dispersion. AFM (Figure 5.1b) revealed the height of the nanosheets ~ 5 nm with a lateral dimension of 300 to 800 nm. The formation of nanosheets

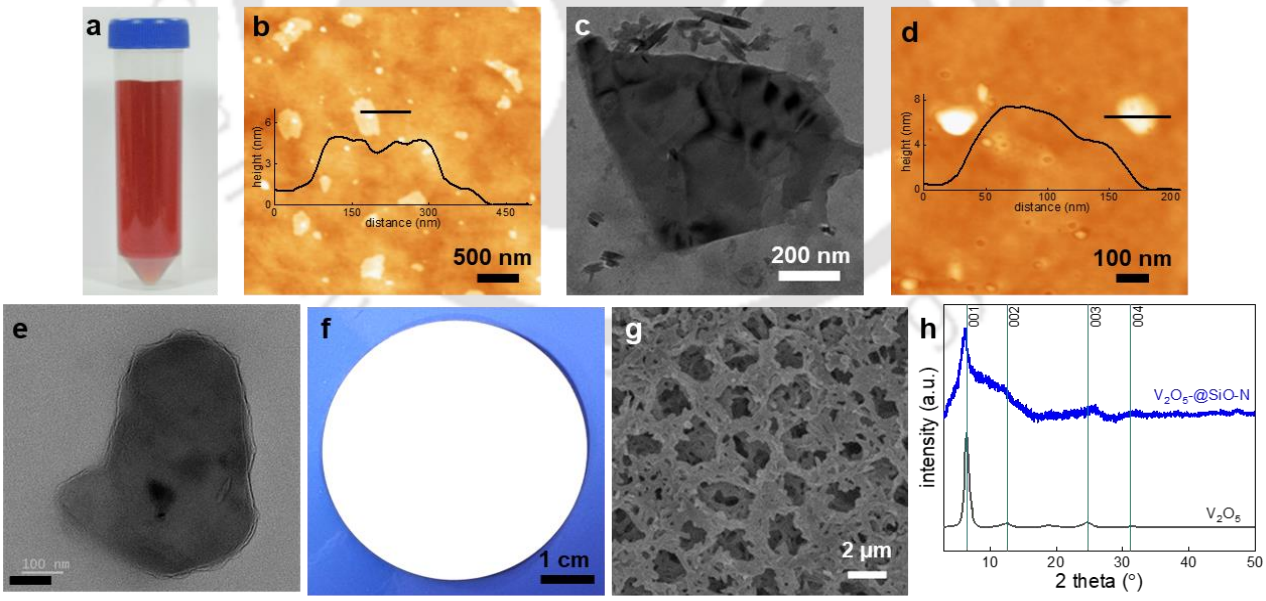

Figure 5.1: *(a) Photo of an aqueous dispersion of the V_2O_5 nanosheets (1 mg/mL). (b) AFM image with its corresponding height profile and (c) TEM image of V_2O_5 nanosheets. (d) AFM image with its corresponding height profile and (e) TEM image of VO-@SiO nanosheets. (f) Digital photo and (g) surface FESEM of the nylon membrane (as received). (h) Comparison of the XRD spectra of V_2O_5 nanosheets (black curve) membrane and VO-@SiO-N membranes (blue curve).*

was also supported by TEM analysis (Figure 5.1c). The functionalisation of the V_2O_5 nanosheets was performed by treating bis[3-(triethoxysilyl) propyl]tetrasulfide with V_2O_5 nanosheets in aqueous medium at 80 °C for 3 hours.[42] Functionalization of the V_2O_5 nanosheets with –SiO– is confirmed by IR spectroscopy (Figure 5.2a). Two newly emerged peaks centered at 1100 and 1250 cm^{-1} in the IR spectra of VO-@SiO nanosheets signifies the presence of the Si-O linkage, providing evidence for the effective attachment of SiO groups onto the surface of VO nanosheets through chemical bonding. AFM investigation (Figure 5.1d) revealed the lateral sizes of the as-obtained VO-@SiO nanosheets to be in the range of 150 to 600 nm, having a thickness of ~7 nm. The formation of nanosheets was also supported by TEM analysis (Figure 5.1e). Like V_2O_5 nanosheets, the functionalised nanosheets also form a stable dispersion in water, as seen in Figure 5.2b. Nylon membranes were coated with the VO-@SiO

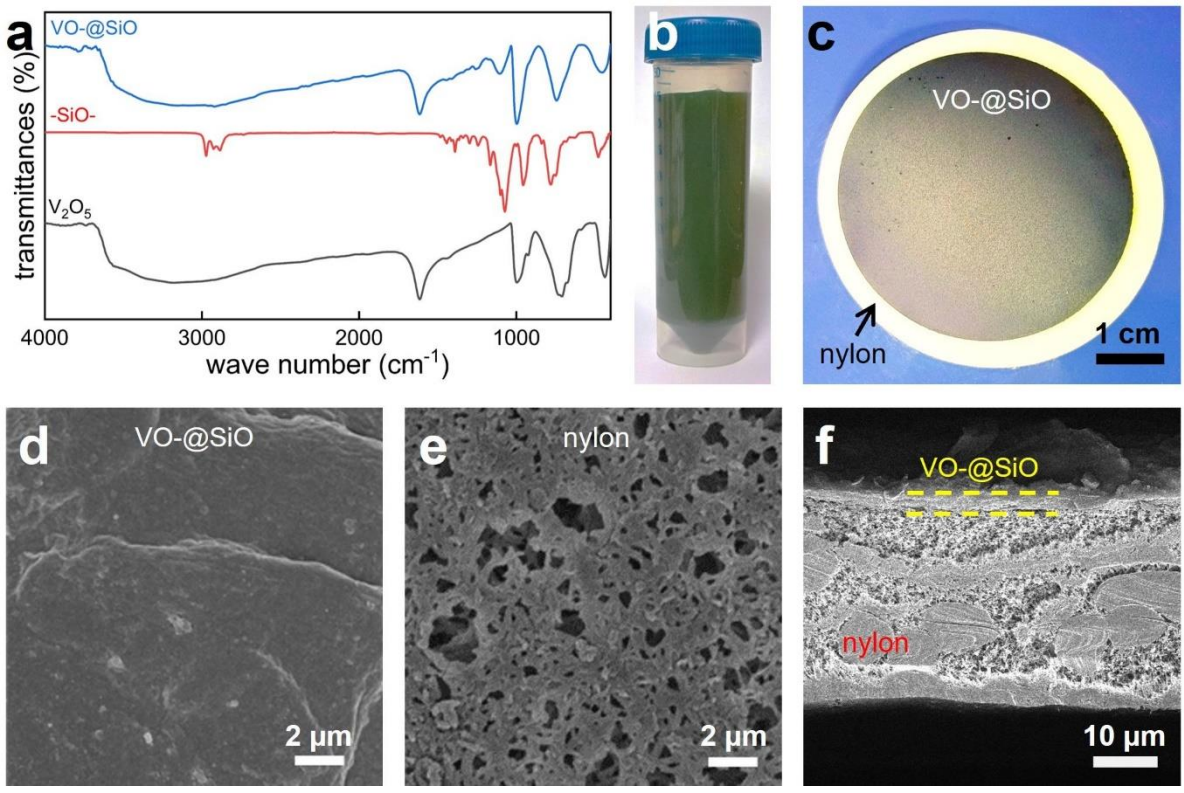

Figure 5.2: *Functionalized VO-@SiO nanosheets coated nylon (VO-@SiO-N) membrane. (a) Comparison of IR spectra of V_2O_5 (black curve), bis[3-(triethoxysilyl) propyl]tetrasulfide (-SiO-, red curve) and VO-@SiO nanosheets (blue curve). Photo of (b) aqueous dispersion (1mg/mL) of VO-@SiO nanosheets and (c) VO-@SiO-N membrane. FESEM images showing the (d) VO-@SiO side, (e) nylon side and (f) cross-section of VO-@SiO-N membrane.*

nanosheets by vacuum-assisted filtration of the aqueous nanosheets dispersion through the membrane, the concentration and volume of the dispersion determine the thickness of the coating. The membranes were then dried for 24 hours in a desiccator, followed by heating at 150 °C for 2 hours under vacuum conditions. A digital photo of the VO-@SiO nanosheets coated nylon membrane (VO-@SiO-N) is shown in Figure 5.2c. X-ray diffraction investigation (Figure 5.1h) of the V_2O_5 nanosheets (black curve) membrane revealed a sharp peak at 2θ value of 6.5 Å, which decreased to 6.2 Å for the VO-@SiO-N membranes (blue curve).

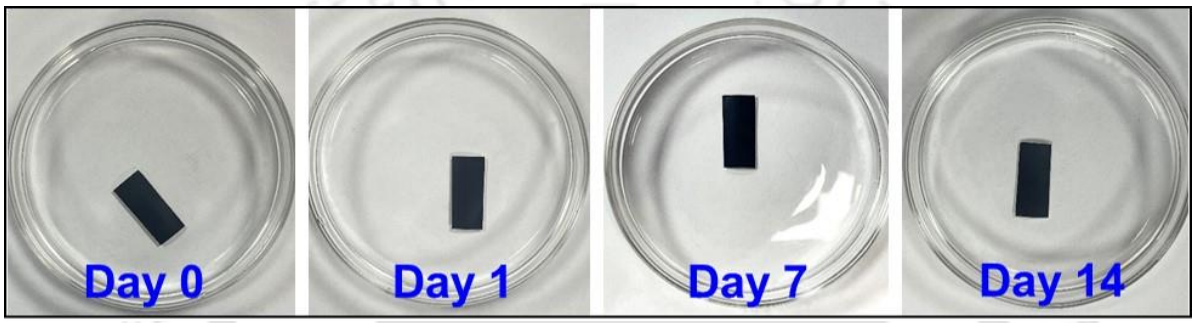

Figure 5.3: *Photos showing the stability of VO-@SiO-N membrane immersed in water.*

This suggests the increase in the interlayer spacings because of the incorporation of the cross-linker (SiO). Reflections in the 2θ values of 6.2 Å suggest the existence of molecularly thin 2D nanofluidic channels in the VO-@SiO-N membrane. FESEM image of the VO-@SiO nanosheets side (Figure 5.2d) and the nylon side (Figure 5.2e) of the coated membrane shows that the nanosheets are coated on the top side of the nylon membrane, leaving the bottom side unchanged (for comparison, FESEM of pure nylon membrane is shown in Figure 5.1g). The cross-sectional FESEM image of the VO-@SiO-N membrane clearly shows the VO-@SiO nanosheets and the nylon have a distinct but intact interface, Figure 5.2f. The membrane displayed good stability in aqueous environments. Soaking in water for two weeks did not deteriorate its chemical integrity, as seen from the snapshots in Figure 5.3.

The out-of-plane ion-transport properties of the VO-@SiO-N membranes were studied by placing the membrane between two electrolyte reservoirs, and two Ag/AgCl electrodes

immersed in the reservoirs (schematically shown in Figure 5.4a) were connected to the terminals of a Keithley 2450 sourcemeter for the electrical measurements. The thickness and the diameter of the VO-@SiO-N membrane are 85 µm and 2 mm, respectively. The voltage-dependent-current (*IV*) curves were recorded through the VO-@SiO-N membrane having a coating of 14 µg.mm^{-2} (thickness of 85µm = 80 µm nylon + 5 µm VO-@SiO) with KCl as electrolytes (equal volume and concentration (*C*) in both reservoirs). The *IV* curves are linear, and conductance (*G*) is found to be dependent on the *C* of the electrolyte, Figure 5.4b. For *C* > 1 mM, G linearly increases with *C*, but deviates from the linear dependency forming a plateau from *C* < 1mM, Figure 5.4c. This type of curves was well known for charged nanofluidic

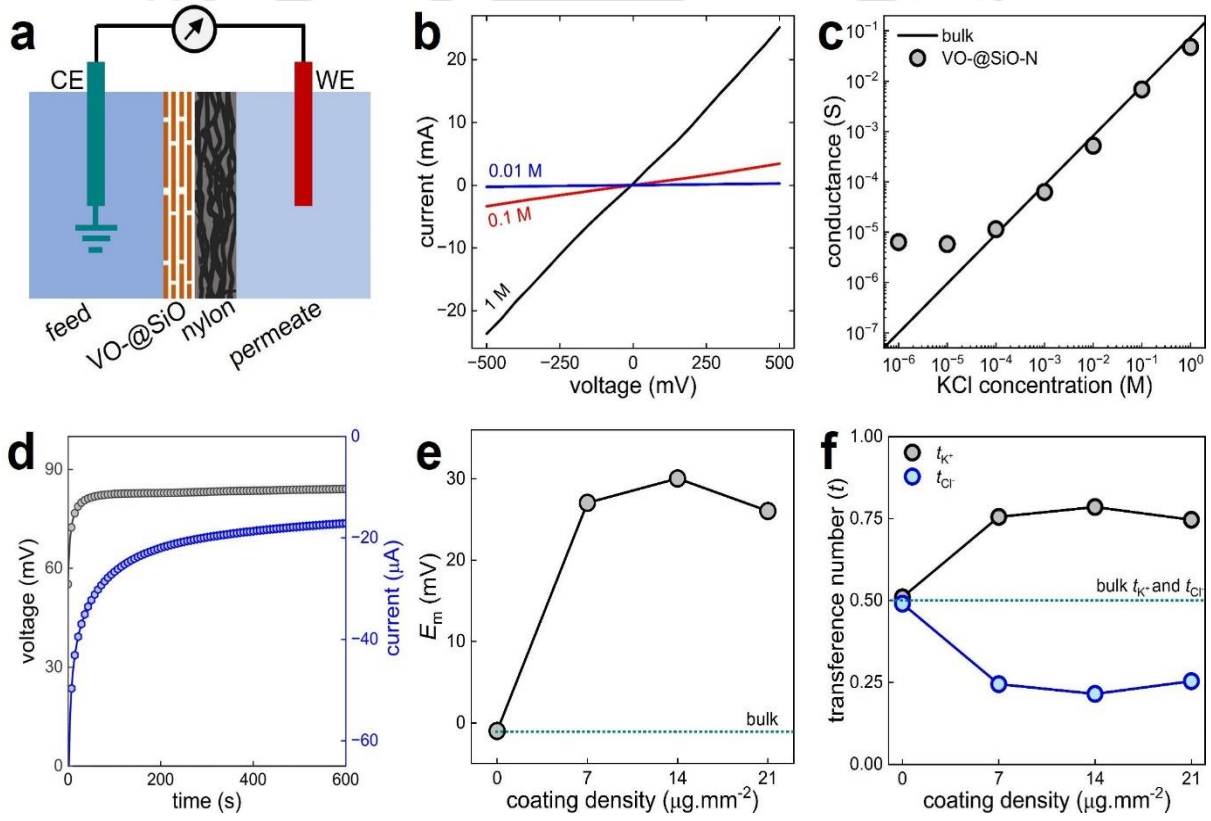

Figure 5.4: *Ion transport through VO-@SiO-N membrane. (a) Schematic representation of the experimental set-up used to investigate the ion-transport characteristics. (b) Current versus voltage (IV) curves were measured through the VO-@SiO-N with 1, 0.1 and 0.01 M KCl as electrolyte. (c) KCl concentration dependence conductance. (d) Open circuit voltage and short circuit current generated across VO-@SiO-N membrane under a gradient of 10 fold (C_{feed} = 1 M and $C_{permeate}$ = 0.1M KCl) using Ag/AgCl electrodes pair. Comparison of the (e) membrane potential and (f) transference number of nylon and VO-@SiO-N membrane membranes under a gradient of 10 fold (C_{feed} = 1 M and $C_{permeate}$ = 0.1M KCl).*

channels, where the G at the low C is determined by the surface density of the fluidic channels.[44–46] The pristine V_2O_5 membrane could not survive dipping in water and readily disintegrated, so its ion conductivity could not be measured. One of the essential criteria for generating osmotic energy is the preferential transport of one ion over the other through the fluidic channels. To investigate this, the feed and permeate reservoirs are filled with 1 M and 0.1 M KCl solutions (2 mL in each reservoir). The open-circuit-voltage and the short-circuit-current recorded using Ag/AgCl electrodes were found to be around ~83 mV and -17 µA, respectively (Figure 5.4d). The E_{redox} of the electrodes immersed in different salt solutions is given by:[47] $E_{redox} = \frac{RT}{nF} ln\left(\frac{\gamma_{feed} C_{feed}}{\gamma_{permeate} C_{permeate}}\right)$, where F is the Faraday constant; R is the universal gas constant; T is the temperature; n is the number of electrons involved in the reaction; $\gamma_{feed/permeate}$ and $C_{feed/permeate}$ are the mean activity coefficient electrolytes and corresponding concentration in the feed/permeate reservoirs respectively. For C_{feed} = 1 M and $C_{permeate}$ = 0.1M KCl, the E_{redox} is estimated to be 53 mV using $\gamma_{1M\ KCl}$ = 0.604 and $\gamma_{0.1\ M\ KCl}$ = 0.768. Thus, the E_m can be estimated from the total potential (E_{total}, i.e., the voltage measure by the Ag/AgCl in the RED experiments) as $E_m = E_{total} - E_{redox}$. Subtracting the redox contribution of the Ag/AgCl electrode (E_{redox} = 53 mV) gives the true E_m of 30 mV. The E_m for the pristine nylon membrane and VO-@SiO-N membranes with different coating densities were measured with C_{feed} = 1 M and $C_{permeate}$ = 0.1M of KCl solutions and are compared with the bulk values, Figure 5.4e. While nylon exhibits zero E_m, coating it with VO-@SiO nanosheets generates E_m dependent on the coating density. Coating with 7, 14 and 21 µg.mm^{-2}, the E_m are obtained as 27, 30 and 26 mV, respectively. E_m increased slightly with higher coating density because once the membrane becomes cation-selective, it has a minor effect on the additional coating of the 2D materials. However, as the coating thickness exceeds an optimal point, it can obstruct or constrict the membrane pores, reduce effective porosity, and increase ionic resistance, thereby hindering cation transport. Excessive coating is also known to cause non-uniform charge distribution,

structural defects, and altered hydration properties.[48] From the E_m the ion selectivity can be estimated in terms of transference number (t) as:[49] $E_m = (t_{K^+} - t_{Cl^-})\frac{RT}{nF} ln\left(\frac{\gamma_{feed}C_{feed}}{\gamma_{permeate}C_{permeate}}\right)$, where t_{K^+} and t_{Cl^-} are the transference numbers of the K^+ and Cl^-, respectively and $t_{K^+} + t_{Cl^-} = 1$; F is the Faraday constant; R is the universal gas constant; T is the temperature; n is the number of electrons involved in the reaction; $\gamma_{feed/permeate}$ and $C_{feed/permeate}$ are the mean activity coefficient electrolytes and corresponding concentration in the feed/permeate reservoirs respectively. The t_{K^+} and t_{Cl^-} for the different membranes are compared in Figure 5.4f, which shows that the VO-@SiO nanosheets coating makes the non-selective nylon membrane K^+ selective and the highest t_{K^+} ~ 0.8 is obtained for coating with 14 µg.mm^{-2}. As can be seen in Figure 5.4f, the cation transfer number initially increases and then decreases with increasing coating density of VO-@SiO. A thin layer of VO-@SiO on the nylon membrane enhances potassium ion selectivity by increasing the membrane's negative charge density. However, as the coating thickness surpasses an optimal point, it causes non-uniform coating and structural defects, which decreases the cation transfer number.[50]

While we have achieved a cation-selective membrane, our next goal was to create an electrode system capable of generating electricity from calm water and enhancing the osmotic energy of the VO-@SiO-N membrane. We have chosen the VO-@SiO-N membrane as one electrode. The other electrode is fabricated by coating PANI on Whatman filter paper (PANI-WP). PANI was synthesised by polymerization of aniline in acidic conditions using ammonium persulphate as the catalyst.[43] PANI forms a stable dispersion in water, as shown in the digital photo of a 1 mg/mL dispersion in Figure 5.5a. A digital photo and FESEM images of PANI are shown in Figures 5.5b and 5.5c, respectively. FESEM images revealed that the PANI is coated on the top side of the PANI-WP (Figure 5.5e, 5.5g and 5.5h). To investigate the possibility of electric energy generation from calm water, the VO-@SiO-N membrane and PANI-WP were paired against the Ag/AgCl electrode. Rectangular strips (dimensions, 4 cm × 2.5 cm) were cut from

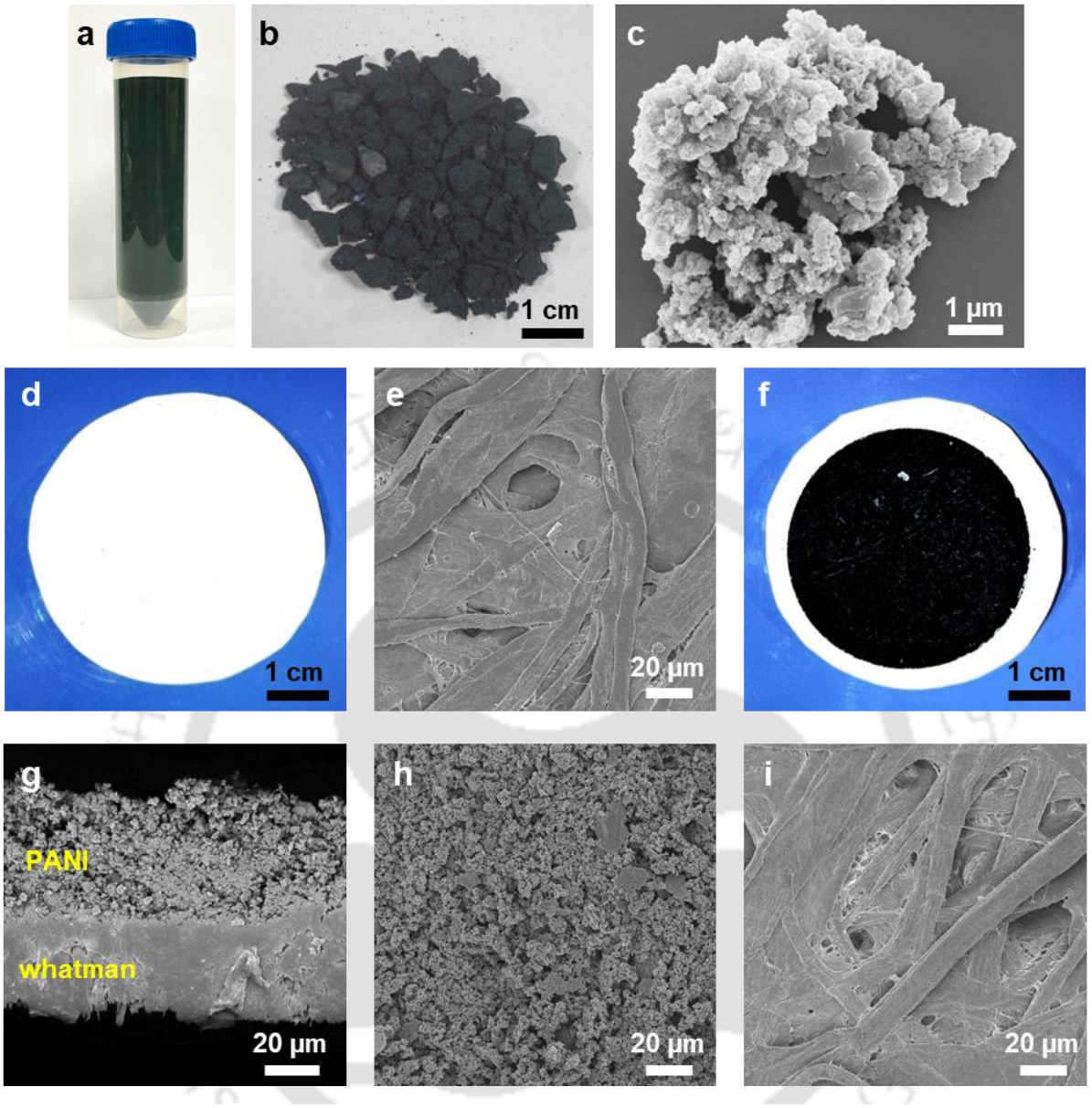

Figure 5.5: *Digital photos of (a) aqueous dispersion (1mg/mL) and (b) air dried samples of PANI. (c) FESEM image of the as prepared PANI. Digital photos of (d) pure Whatman paper and (f) PANI-WP. (e) Surface FESEM images of the pure Whatman paper. FESEM images showing the (g) cross-section, (h) PANI side and the (i) Whatman side of the PANI-WP.*

the VO-@SiO-N and PANI-WP, and a copper wire was glued to one end of each strip using conducting silver paste, as depicted in Figure 5.6. The Ag/AgCl electrode served as the working electrode (WE), while the strips were utilised as the counter electrodes (CE). The voltage and current generated by such electrode pairs were recorded by dipping them in calm water using a Sourcemeter unit. When strips were dipped in deionised (DI) water, taking care to avoid the

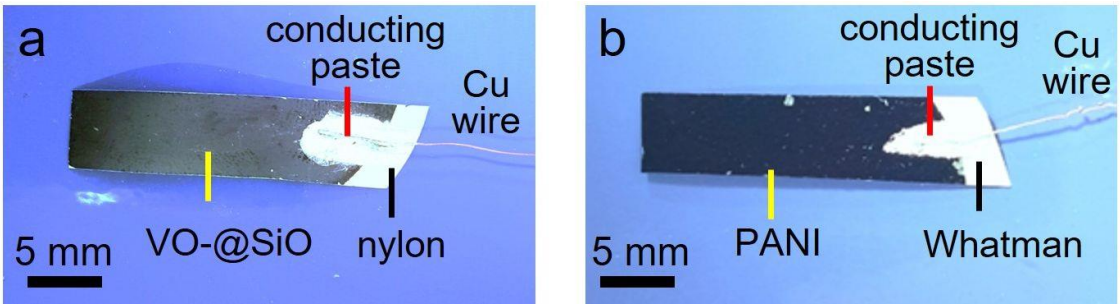

Figure 5.6: *Photo of the (a) VO-@SiO-N and (b) PANI-WP electrodes.*

conduction paste contacting the water, the dipping area was ~ 6.25 cm^2 (2.5 cm × 2.5 cm). The schematic diagram of the experimental setup is shown in Figure 5.7a. The voltages generated by VO-@SiO-N with coating densities of 7, 14, and 21 $\mu g.mm^{-2}$ against Ag/AgCl in DI water were around - 58 mV, -80 mV, and -110 mV, respectively, with corresponding currents of 0.18 µA, 0.5 µA, and 0.4 µA (Figure 5.7b and 5.7c). For similar experiments taking PANI (the schematic diagram of the experimental setup is shown in Figure 5.7d) with coating densities of 26, 35, and 52 $\mu g.mm^{-2}$, the voltages were -92 mV, -225 mV, and -122 mV, respectively, with corresponding currents of 0.45 µA, 0.19 µA, and 0.14 µA (Figure 5.7e and 5.7f). The decline in voltage and current with lower weight loading can be attributed to reduced active material available for polarising water molecules at the electrode-water interface. Conversely, excessive weight loading leads to active materials' saturation, reducing the effective surface area.[26] The redox potential of the VO-@SiO-N and PANI-WP electrodes was calculated by taking Ag/AgCl electrode as the reference electrode. The standard electrode potential for the Ag/AgCl electrode is +222 mV at 25ºC.[51] An output potential of ~227 mV (25ºC) was measured by connecting Ag/AgCl against PANI electrode. The redox potential of PANI (~5 mV) was calculated by subtracting the standard electrode potential for the Ag/AgCl electrode (+222 mV) from the output potential (227 mV). Similarly, the output potential of VO-@SiO-N electrode against Ag/AgCl was measured to be ~107 mV (25ºC). The redox potential of VO-@SiO-N

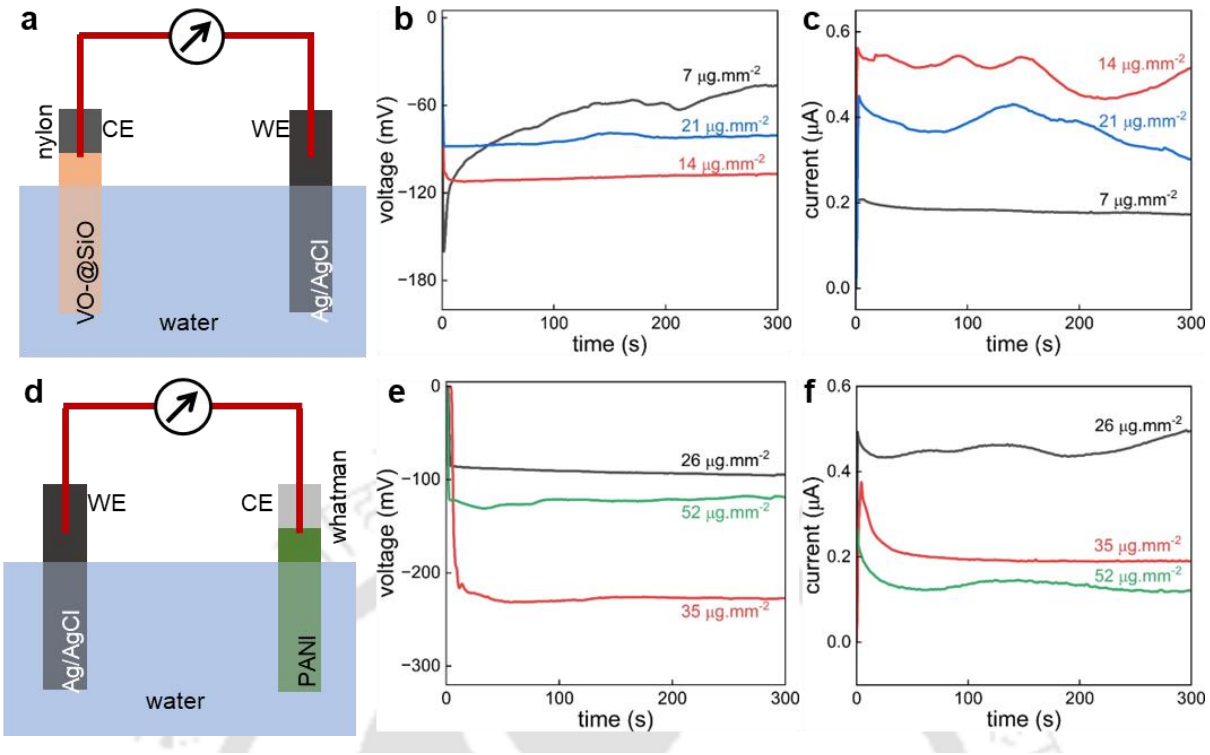

Figure 5.7: *(a) Schematic diagram of the experimental setup, (b) voltage and (c) current generated by the VO-@SiO-N vs Ag/AgCl electrodes in water. (d) Schematic diagram of the experimental setup, (e) voltage and (f) current generated by the PANI vs Ag/AgCl electrodes in water.*

was calculated to be 115 mV by subtracting the output potential (107 mV) from the standard electrode potential for the Ag/AgCl electrode. The graph of the generated voltage of VO-@SiO-N and PANI-WP electrodes against Ag/AgCl is shown in Figure 5.7.

As the VO-@SiO-N with a coating density of 14 µg.mm^{-2} and PANI-WP with a coating density of 35 µg.mm^{-2} deliver the highest potential against the Ag/AgCl electrode in their respective experiments, they are selected as the electrode system for the energy generation process. Upon immersion in DI water (schematic in Figure 5.8a), electrical energy is generated by the VO-@SiO-N and PANI-WP strips, resulting in a voltage of approximately 150 mV and a current of approximately -3 µA (Figure 5.8b) when the strips are placed around 5 mm apart. However, significantly low electricity is generated when pairs of VO-@SiO-N and PANI-WP electrodes are immersed in water (Figure 5.9a and 5.9b, respectively). Pair of VO-@SiO-N generated around 6 mV and -130 nA of voltage and current, respectively. These values are around 37 mV

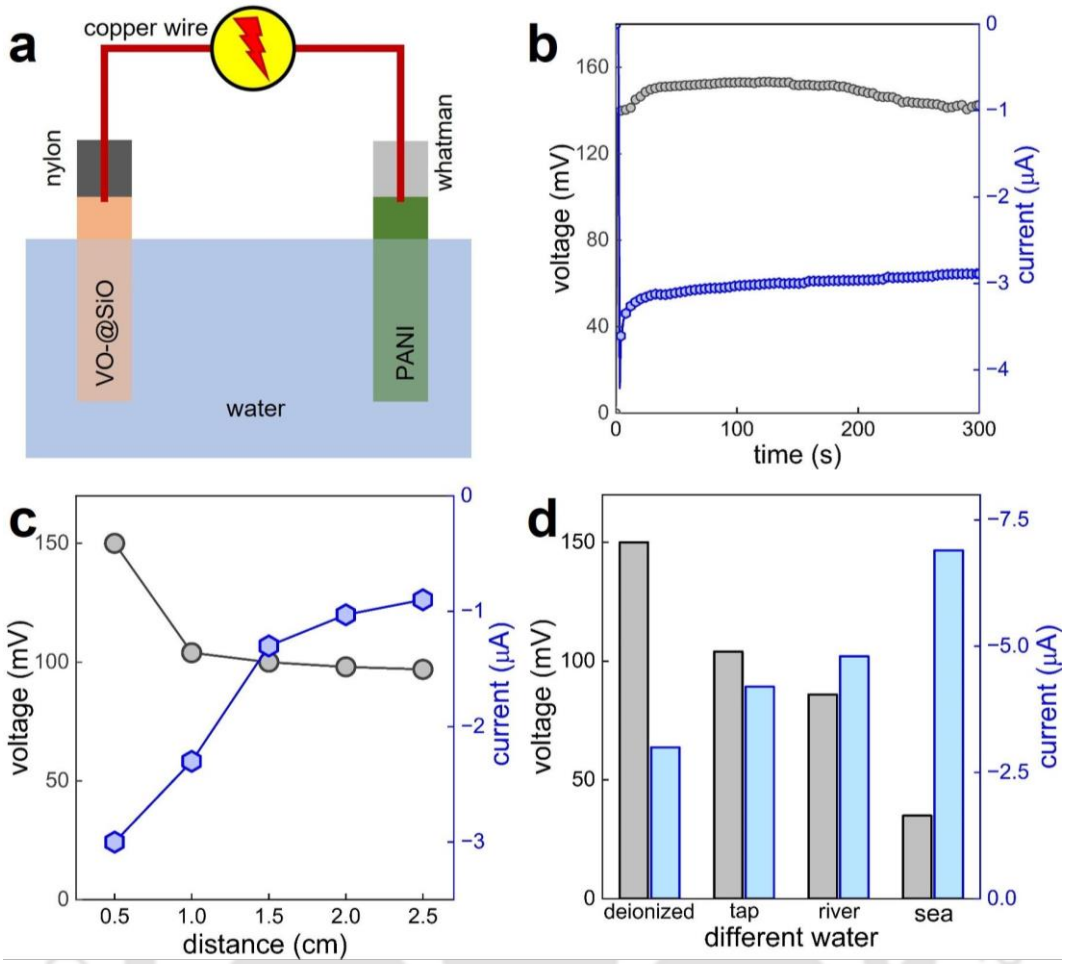

Figure 5.8: *Energy generation from calm water. (a) Schematic diagram showing the energy generation from calm water. (b) Comparison of voltage and current generated by VO-@SiO-N and PANI-WP electrodes upon dipping in water. (c) Dependency of the electrode distance in voltage and current generation. (d) The voltage and current generated by the VO-@SiO-N and PANI-WP electrodes upon dipping in deionized, tap, river, and sea water. In this figure, the length, l and width, w of the strips are 4 cm and 2.5 cm, respectively, and the portion of the electrodes immerged in water were of dimension 2.5 cm × 2.5 cm.*

and -30 to -40 nA for the PANI-WP electrode pair. Furthermore, we investigate the effect of the electrode distance on electricity generation by increasing the electrode distance from 0.5 cm to 2.5 cm, which resulted in a decrease in both the magnitude of the voltage and current, as shown in Figure 5.8c. In addition, the compatibility of this electrode system was explored with water samples collected from tap, river, and sea sources. The voltage and current values in these water sources are compared in Figure 5.8d, revealing that deionised water produces higher voltage with lower current, while seawater produces higher current with lower voltages.

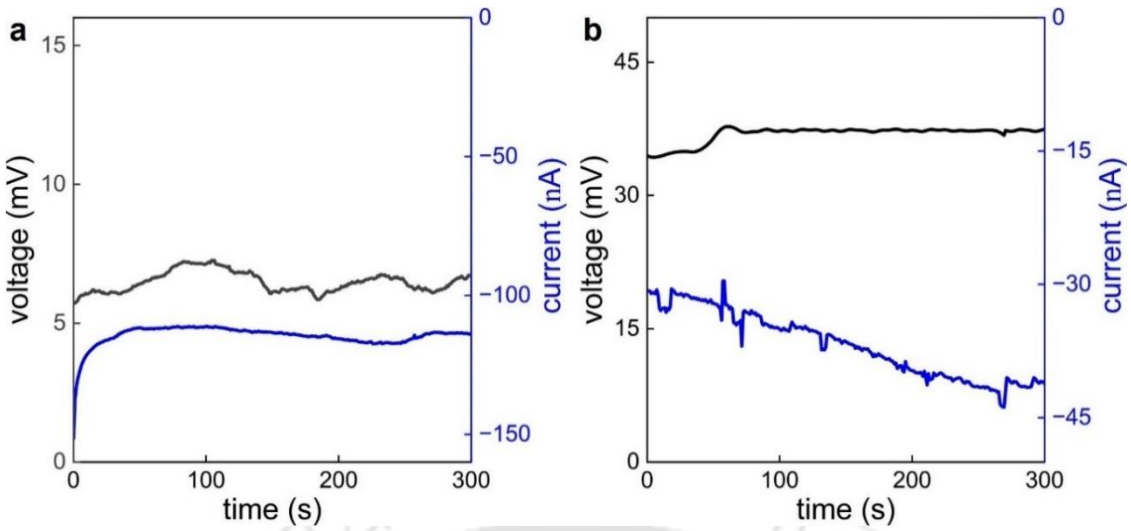

Figure 5.9: *Comparison of voltage (black curves) and current (blue curves) generated by electrode pairs of (a) VO-@SiO and (b) PANI. The amount of area immersed in water is ~6.25 cm^2 (2.5 cm × 2.5 cm).*

It is widely acknowledged that a single water molecule possesses a dipole moment, but in the liquid state, this dipole moment is typically neutralised owing to the random alignment of molecules. However, if the water dipole can be aligned at charged surfaces, the positive and negative charges can be separated, leading to a charge transfer that can be harnessed to generate electricity. The zeta potential of materials arises from their surface charge density, which is also proportional to the polarisation inside the material. To further understand the mechanism of electricity generation, the zeta potentials of VO-@SiO and PANI were measured in aqueous

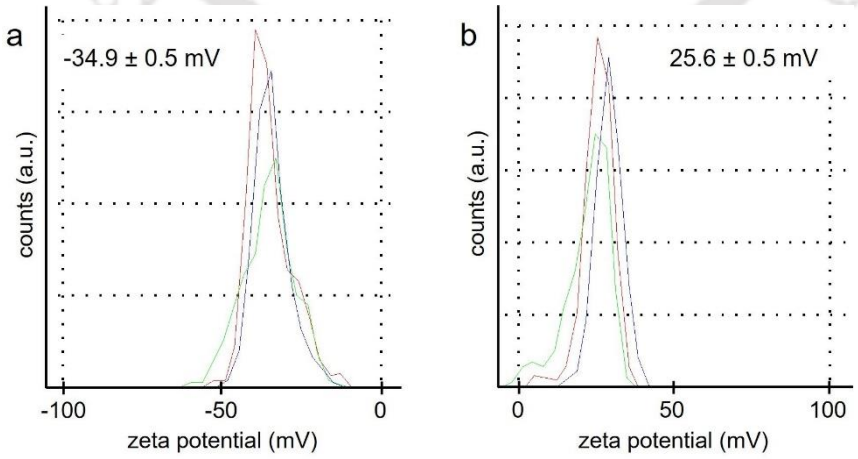

Figure 5.10: *Comparison of the zeta potentials of (a) VO-@SiO and (b) PANI dispersions in water.*

mediums, yielding values of -34.9 ± 05 mV and 25.6 ± 0.5 mV, respectively (Figure 5.10a and 5.10b, respectively). These zeta potential values indicate the opposite surface polarisation where PANI acts as a p-type (electron-deficient) and the VO-aSiO acts as an n-type (electron rich) material.[26,52] The two half-reactions taking place on the cathode (VO-aSiO) and anode (PANI) during the process can be written as:[25]

Cathode: $VO\text{-}@SiO + H_2O + e^- \rightarrow VO\text{-}@SiO\text{-}H + OH^-$

Anode: $PANI + OH^- \rightarrow PANI\text{-}OH + e^-$

Hence, an electrical potential is generated when VO-@SiO-N and PANI-WP electrodes are dipped in water.

To study the effect of the VO-@SiO-N and PANI-WP electrodes on the osmotic energy generation of the VO-@SiO-N membrane, we placed the VO-@SiO-N electrode in the feed reservoir (C_{feed} = 1 M KCl) and the PANI-WP electrode in the permeate reservoir ($C_{permeate}$ = 0.1 M KCl) and measured the open-circuit voltage and short-circuit current. The schematic diagram of the experimental set-up is shown in Figure 5.11a. The voltage and current generated by the VO-@SiO-N and PANI-WP electrodes pair with those of Ag/AgCl electrode pairs across the VO-@SiO-N membrane under a concentration gradient of 10 fold (C_{feed} = 1 M; $C_{permeate}$ = 0.1 M KCl) are compared in Figure 5.11b and 5.11c, respectively. The voltage was enhanced by ~116 mV (~ 140%) and the current is enhanced by 11 µA (~25 %) upon using VO-@SiO-N and PANI-WP as electrodes, even though the Ag/AgCl have redox contributions. We measured the synergic voltage and current generation under different concentration gradients by varying the $C_{permeate}$ as 100 mM, 10 mM and 1 mM KCl, fixing the C_{feed} = 1 M KCl. The voltage and current values are enhanced in all three concentration gradients of 10, 100 and 1000 folds, compared in Figure 5.11d (voltage comparison) and Figure 5.11e (current comparison). The power of this synergic energy generation system is estimated as: power = voltage × current and is compared with the Ag/AgCl electrodes in Figure 5.11f. The power is

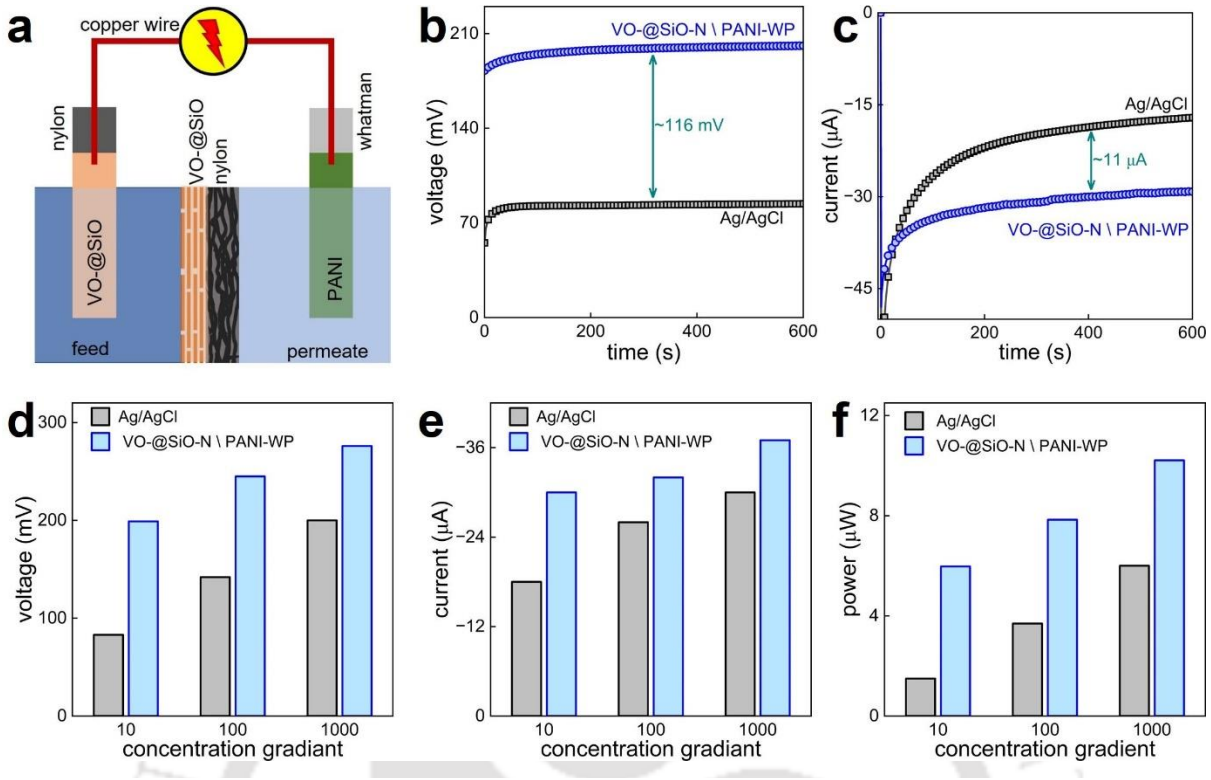

Figure 5.11: *Hybrid energy generation system. (a) Schematic diagram showing the energy generation setup to generate electricity. Comparison of (b) voltage and (c) current generated by VO-@SiO-N membranes (as ion selective membrane) under a gradient of 10 fold (C_{feed} = 1 M and $C_{permeate}$ = 0.1M KCl) using Ag/AgCl electrodes pair and VO-@SiO-N\PANI-WP electrodes pairs. Comparison of the (d) voltage, (e) current and (f) power generated by VO-@SiO-N membrane under 10-, 100- and 1000-fold concentration gradients using Ag/AgCl electrodes pair and VO-@SiO-N\PANI-WP electrodes pairs. In (d), (e) and (f), C_{feed} is fixed at 1 M KCl and $C_{permeate}$ is varied to 100 mM, 10 mM and 1mM KCl. In this figure, the length, l and width, w of the strips are 2 cm and 0.5 cm, respectively, and portion of the electrodes immerged in water are l = 1 cm and width, w = 0.5 cm.*

enhanced by ~300 %, 112 % and 70 % under the concentration gradients of 10, 100 and 1000 folds, respectively.

5.6 Conclusion

In conclusion, an ion-selective membrane by coating a commercial nylon membrane with functionalized V_2O_5 is demonstrated. These coated membranes generate a membrane potential of ~30 mV with a transference number ~0.8 for K^+ with a coating density ~14 µg.mm^{-2} on one side of the nylon membrane. Moreover, the generation of electrical energy from calm water by using charged nanomaterials, *i.e.* VO-@SiO and PANI is also demonstrated. Strips of VO-

@SiO-N and PANI-WP generate a voltage of 150 mV and a current of -3 µA upon dipping in water. It is believed that the charge separation of the water molecules on the surfaced of the charged nanomaterials results in electricity generation. The ion-selective VO-@SiO-N membrane and the VO-@SiO-N and PANI-WP electrodes can generate electric energy in a synergic way from the still water and the osmotic flow of ions. This improves the power generated by the VO-@SiO-N membrane up to ~300 %, 112 % and 70 % under the concentration gradients of 10, 100 and 1000 folds, respectively, in comparison to that of Ag/AgCl electrodes. This new finding will pave the way for exploring new energy-generating systems, which can generate energy in a synergic manner.

5.7 References

1 K. Hansen, C. Breyer and H. Lund, *Energy*, 2019, **175**, 471–480.

2 D. Bogdanov, J. Farfan, K. Sadovskaia, A. Aghahosseini, M. Child, A. Gulagi, A. S. Oyewo, L. de Souza Noel Simas Barbosa and C. Breyer, *Nat. Commun.*, 2019, **10**, 1–16.

3 M. Z. Jacobson, M. A. Delucchi, M. A. Cameron and B. V. Mathiesen, *Renew. Energy*, 2018, **123**, 236–248.

4 R. E. Pattle, *Nature*, 1954, **174**, 660–660.

5 R. A. Tufa, S. Pawlowski, J. Veerman, K. Bouzek, E. Fontananova, G. di Profio, S. Velizarov, J. Goulão Crespo, K. Nijmeijer and E. Curcio, *Appl. Energy*, 2018, **225**, 290–331.

6 G. Laucirica, M. E. Toimil-Molares, C. Trautmann, W. Marmisollé and O. Azzaroni, *Chem. Sci.*, 2021, **12**, 12874–12910.

7 M. Tedesco, C. Scalici, D. Vaccari, A. Cipollina, A. Tamburini and G. Micale, *J. Membr. Sci.*, 2016, **500**, 33–45.

8 A. Siria, P. Poncharal, A. L. Biance, R. Fulcrand, X. Blase, S. T. Purcell and L. Bocquet, *Nature*, 2013, **494**, 455–458.

9 L. Yang, T. Sun, J. Tang, Y. Shao, N. Li, A. Shen, J. Chen, Y. Zhang, H. Liu and G. Xue, *Nano Energy*, 2021, **87**, 106163.

10 S. Kim, M. Lee, S. Choi, J. Won, T. Kim, T. Kim, J. Bae and W. Shim, *J. Phys. Energy*, 2022, **5**, 014010.

11 J. Ji, Q. Kang, Y. Zhou, Y. Feng, X. Chen, J. Yuan, W. Guo, Y. Wei and L. Jiang, *Adv. Funct. Mater.*, 2017, **27**, 1603623.

12 Z. Zhang, W. Shen, L. Lin, M. Wang, N. Li, Z. Zheng, F. Liu and L. Cao, *Adv. Sci.*, 2020, **7**, 2000286.

13 S. Hong, J. K. El-Demellawi, Y. Lei, Z. Liu, F. Al Marzooqi, H. A. Arafat and H. N. Alshareef, *ACS Nano*, 2022, **16**, 792–800.

14 S. Mehdizadeh, M. Yasukawa, M. Kuno, Y. Kawabata and M. Higa, *Desalination*, 2019, **467**, 95–102.

15 A. H. Avci, R. A. Tufa, E. Fontananova, G. Di Profio and E. Curcio, *Energy*, 2018, **165**, 512–521.

16 J. Wang, Y. Zhou and L. Jiang, *Acc. Mater. Res.*, 2023, **4**, 86–100.

17 M. Tedesco, A. Cipollina, A. Tamburini and G. Micale, *J. Membr. Sci.*, 2017, **522**, 226–236.

18 K. Kwon, J. Han, B. H. Park, Y. Shin and D. Kim, *Desalination*, 2015, **362**, 1–10.

19 L. Lin, L. Zhang, L. Wang and J. Li, *Chem. Sci.*, 2016, **7**, 3645–3648.

20 P. Liu, T. Zhou, L. Yang, C. Zhu, Y. Teng, X. Y. Kong and L. Wen, *Energy Environ. Sci.*, 2021, **14**, 4400–4409.

21 H. I. Jeong, H. J. Kim and D. K. Kim, *Energy*, 2014, **68**, 229–237.

22 S. Y. Lee, Y. J. Jeong, S. R. Chae, K. H. Yeon, Y. Lee, C. S. Kim, N. J. Jeong and J. S. Park, *J. Phys. Chem. Solids*, 2016, **91**, 34–40.

23 O. S. Burheim, F. Seland, J. G. Pharoah and S. Kjelstrup, *Desalination*, 2012, **285**, 147–152.

24 N. Jeong, H. ki Kim, W. sik Kim, J. Yeon Choi, S. C. Yang, K. sik Hwang, J. youn Nam, J. hyung Han, E. J. Jwa and S. C. Park, *Appl. Surf. Sci.*, 2020, **504**, 144323.

25 S. He, Y. Zhang, L. Qiu, L. Zhang, Y. Xie, J. Pan, P. Chen, B. Wang, X. Xu, Y. Hu, C. Thang Dinh, P. De Luna, M. Norouzi Banis, Z. Wang, T.-K. Sham, X. Gong, B. Zhang, H. Peng, E. H. Sargent, S. He, L. Qiu, L. Zhang, J. Pan, P. Chen, B. Wang, X. Xu, Y. Hu, B. Zhang, H. Peng, Y. Zhang, Y. Xie, X. Gong, C. T. Dinh, E. H. Sargent, P. De Luna, M. N. Banis, Z. Wang and T. Sham, *Adv. Mater.*, 2018, **30**, 1707635.

26 J. Deka, K. Saha, S. Kumar, H. K. Srivastava and K. Raidongia, *ACS Appl. Nano Mater.*, 2019, **2**, 7997–8004.

27 P. Kolhar, B. Sannakki, M. Verma, P. S.V, M. Alshehri and N. A. Shah, *Nanomater.* 2023, **13**, 2223.

28 V. S. Dutka and Y. P. Kovalskyi, *Mol. Cryst. Liq. Cryst.*, 2023, **750**, 42–49.

29 Y. Luo, R. Guo, T. Li, F. Li, Z. Liu, M. Zheng, B. Wang, Z. Yang, H. Luo and Y. Wan, *ChemSusChem*, 2019, **12**, 1591–1611.

30 S. Sinha, S. Bhadra and D. Khastgir, *J. Appl. Polym. Sci.*, 2009, **112**, 3135–3140.

31 W. S. Huang and A. G. MacDiarmid, *Polymer*, 1993, **34**, 1833–1845.

32 M. Beygisangchin, S. A. Rashid, S. Shafie, A. R. Sadrolhosseini and H. N. Lim, *Polymers*, 2021, **13**, 2003.

33 M. K. Ram, M. Salerno, M. Adami, P. Faraci and C. Nicolini, *Langmuir*, 1999, **15**, 1252–1259.

34 F. R. Rangel-Olivares, E. M. Arce-Estrada and R. Cabrera-Sierra, *Coatings*, 2021, **11**, 653.

35 X. Hong, Y. Liu, Y. Li, X. Wang, J. Fu and X. Wang, *Polymers*, 2020, **12**, 331.

36 S. Yang, S. Zhu and R. Hong, *Coatings*, *2020*, 2020, **10**, 1215.

37 A. G. Macdiarmid, S.-L. Mu, N. L. D. Somasiri and W. Wu, *Mol. Cryst. Liq. Cryst.*, 1985, **121**, 187–190.

38 K. Okabayashi, F. Goto, K. Abe and T. Yoshida, *Synth. Met.*, 1987, **18**, 365–370.

39 K. M. Molapo, P. M. Ndangili, R. F. Ajayi, G. Mbambisa, S. M. Mailu, N. Njomo, M. Masikini, P. Baker and E. I. Iwuoha, *Int. J. Electrochem. Sci.*, 2012, **7**, 11859–11875.

40 R. K. Gogoi, A. B. Neog, N. Sarmah and K. Raidongia, *J. Mater. Chem. A*, 2019, **7**, 21157–21167.

41 R. K. Gogoi, A. B. Neog, T. J. Konch, N. Sarmah and K. Raidongia, *J. Mater. Chem. A*, 2019, **7**, 10552–10560.

42 P. Deka, S. Roy, T. Jyoti Konch, B. Rani Bora, R. Gogoi, A. Bikash Neog, K. Sundararajan, S. Subbiah and K. Raidongia, *Chem. Eng. J.*, 2023, **469**, 143964.

43 N. V. Blinova, J. Stejskal, M. Trchová, J. Prokeš and M. Omastová, *Eur. Polym. J.*, 2007, **43**, 2331–2341.

44 K. Raidongia and J. Huang, *J. Am. Chem. Soc.*, 2012, **134**, 16528–16531.

45 J. J. Shao, K. Raidongia, A. R. Koltonow and J. Huang, *Nat. Commun.*, 2015, **6**, 1–7.

46 A. Esfandiar, B. Radha, F. C. Wang, Q. Yang, S. Hu, S. Garaj, R. R. Nair, A. K. Geim and K. Gopinadhan, *Science*, 2017, **358**, 511–513.

47 S. W. Lee, H. J. Kim and D. K. Kim, *Energies*, 2016, **9**, 49.

48 D. Akinwande, C. J. Brennan, J. S. Bunch, P. Egberts, J. R. Felts, H. Gao, R. Huang, J. S. Kim, T. Li, Y. Li, K. M. Liechti, N. Lu, H. S. Park, E. J. Reed, P. Wang, B. I.

Yakobson, T. Zhang, Y. W. Zhang, Y. Zhou and Y. Zhu, *Extreme Mech. Lett.*, 2017, **13**, 42–77.

49 S. W. Lee, H. J. Kim and D. K. Kim, *Energies*, 2016, **9**, 49.

50 B. Kang, H. J. Kim and D. K. Kim, *J. Membr. Sci.*, 2018, **550**, 286–295.

51 A. A. G. F. Beati, R. M. Reis, R. S. Rocha and M. R. V. Lanza, *Ind. Eng. Chem. Res.*, 2012, **51**, 5367–5371.

52 S. Sinha, S. Bhadra and D. Khastgir, *J. Appl. Polym. Sci.*, 2009, **112**, 3135–3140.

Chapter 6

Conclusions and future perspectives

6.1 Overview

This thesis explored the use of responsive lamellar membranes composed of layered materials in various applications, such as energy harvesting, microdroplet handling, and sensing. The development of r-GO/agar-based bilayer actuators with accurate microdroplet manipulation holds potential applications in analytical systems and small chemical reactors. Furthermore, the potential of these reassembled membranes as sensors was explored, showing that the interactions between the liquid and the lamellar structure can shape-morph the membranes to detect pollutants in liquid media. Remote handling systems that detect and grip dangerous chemicals with light and electrical responsiveness were developed by creating CNT and VO-based membranes. Additionally, an ion-selective membrane for osmotic energy harvesting was created. Combined with newly designed electrode systems, this allowed for the synergistic harvesting of energy from calm water and concentration gradients, aiding in creating innovative, long-lasting energy solutions. These studies emphasize the adaptability and potential of responsive lamellar membranes for advanced scientific and technological applications.

In chapter 2, a novel method for remotely manipulating microdroplets using electrical potential and IR light was demonstrated. The r-GO/agar-based bilayer actuators were able to accurately pick up and drop microdroplets with high precision. This work has the potential to benefit the development of autonomous tiny chemical reactors and analytical systems. These bilayer membranes could be used with suitable spectrophotometers and microscopes to further miniaturize the technology and handle nano or picogram-sized analytes. This chapter paves the way for new developments in chemistry at smaller scales by establishing the groundwork for the future production of responsive materials with customizable wettability surfaces.

Chapter 3 explores the use of responsive membranes made of reconstructed layered materials to detect contaminants in liquid environments. The study found that the mechanical properties

of the bilayer strip's components determine its shape. Additionally, the interaction between two-dimensional lamellar membrane building blocks and liquid molecules can alter their mechanical characteristics and their ability to change shape. Specifically, the r-GO/agar bilayer membrane showed significant shape-morphing properties in different solvents and maintained its mechanical integrity through multiple cycles. This research highlights the potential for these materials to be used more widely for large-scale applications and as inexpensive, electronics-free sensors for solvent molecules.

In chapter 4, it was demonstrated that remote handling systems for explosive and dangerous items could be constructed using responsive materials. By employing a gradual vacuum filtration procedure, bilayer membranes of CNT and VO, and o-CNT and VO were produced. The o-CNT-VO membranes exhibited actuation behaviour under electrical potential due to unequal Joule heating, while the CNT-VO membranes demonstrated light responsiveness because of the differing photothermal activities of CNT and VO. These membranes displayed a sensing ability similar to human fingers, as well as the capability to grab and release items. Moreover, these materials are resistant to the touch of dangerous and corrosive liquids, highlighting their utility for remote handling applications. This initiative could possibly lead to the creation of commercial remote-handling devices, substantially easing the burden of controlling dangerous substances by humans.

In chapter 5, the construction of an ion-selective membrane by coating functionalised V_2O_5 on a commercial nylon membrane was demonstrated. This membrane yielded a high transference number for K^+ ions and a membrane potential of 30 mV. It was also shown how charged nanomaterials like VO-@SiO and PANI may generate electrical energy from still water. When submerged in water, the combination of these materials produced a certain voltage and current. The ion-selective membrane and charged nanomaterials operated in concert to dramatically boost power generation, offering new possibilities for osmotic flow and still-water energy

harvesting. This chapter examines revolutionary energy-harvesting technology that may find many uses in sustainable energy solutions.

Summary of our contribution and its distinction from existing literature:

In the second chapter of this thesis, we present the fabrication of electrically controllable smart arms designed for the manipulation of liquids at the microliter scale. These smart arms are constructed using bilayer membranes composed of reduced graphene oxide and agar. Although similar electrical actuation behaviours have been documented in bilayer membranes that incorporate reduced graphene oxide with various polymers and nanomaterials, this work represents a novel application of such actuators specifically for the precise handling of microdroplets. In the third chapter, we delineate the exceptional responsiveness of r-GO/agar bilayer strips in liquid media, underscoring their capability to detect trace contaminants within liquid samples. To the best of our knowledge, this represents the inaugural report of bilayer membranes being utilized for such applications, signifying a noteworthy advancement in the field. The fourth chapter explores the development of bilayer actuators comprising multi-walled carbon nanotubes and oxidized multi-walled carbon nanotubes in combination with exfoliated two-dimensional vanadium pentoxide flakes. These actuators demonstrate exceptional durability, withstanding exposure to acidic, basic, and organic solvents. This bilayer system exhibits the ability to handle chemically reactive substances while simultaneously sensing the properties of the materials being manipulated. This unique capability allows for seamless integration with existing technologies to enable the remote handling of toxic and explosive materials, offering enhanced safety and precision. Finally, the fifth chapter introduces a novel electrode system employing functionalized vanadium pentoxide and polyaniline. This system exhibits the unprecedented ability to generate electrical potential from quiescent water without relying on concentration gradients, utilizing complementary charge transfer activities. By incorporating this innovative electrode into a

concentration gradient-driven energy generation system, we observed an improvement in power output of up to 300% compared to systems using conventional Ag/AgCl electrodes. Although energy generation from still water has been previously reported, to the best of our knowledge, this work is the first to synergistically combine the effects of electrodes and concentration gradients to achieve such enhanced performance.

6.2. Future perspectives

The work presented in this thesis provides a number of directions for future investigation and development. The technique for microdroplet manipulation described in chapter 2 could be further refined by examining a broader range of 2D nanomaterials. This could lead to the fabrication of highly specialised, sensitive materials customised for certain chemical reactions and analytical processes at the microscale. In chapter 3, the potential for electronics-free sensors using responsive membranes could be explored by examining different material combinations and solvent interactions. Scaling up production and incorporating these sensors into current monitoring systems could provide cost-effective solutions for environmental and industrial applications. The remote handling technologies discussed in chapter 4 have promise for applications beyond hazardous material handling. Future studies could focus on strengthening the sensitivity and responsiveness of these systems, as well as examining their integration into automated processes and robotics for greater industrial use. Finally, the energy generation processes detailed in chapter 5 reveal the prospect of developing new, sustainable power sources. Future work could explore the optimisation of these systems for improved efficiency and their incorporation into larger-scale energy harvesting and storage solutions. Integrating ion-selective membranes with other nanomaterials could lead to creative energy generation methods under varied environmental circumstances.

Lamellar membranes show promise in revolutionizing various industries such as water treatment, gas separation, energy storage, and biomedicine. This potential is especially

significant when utilizing 2D materials. The aim is to create advanced membranes by combining the unique properties of multiple 2D materials to achieve exceptional strength, permeability, and selectivity. This involves creating hybrid membranes that blend favourable characteristics to deliver superior performance customized for specific applications. For instance, these membranes could be engineered to eliminate a broad spectrum of contaminants while upholding high flow rates in desalination and water purification processes. Furthermore, they could afford precise selectivity in gas separation, benefiting critical procedures like natural gas purification and carbon capture, thereby contributing to environmental sustainability. Refinements in fabrication techniques, including 3D printing and scalable synthesis processes, will enable meticulous control of pore size, distribution, and structural integrity. This elevates membrane performance and facilitates large-scale production, rendering them economically viable for widespread utilisation. Additionally, integrating intelligent components such as sensors and adaptive nanostructures will endow these membranes with the capacity to respond promptly to dynamic environmental conditions, augmenting their efficacy in real-time applications. Furthermore, these membranes harbour substantial promise for use in energy-related applications, augmenting the efficiency and capacity of supercapacitors and batteries. By amalgamating 2D materials in these devices, researchers may attain novel performance standards, paving the way for more efficient and sustainable energy storage systems. The distinctive properties of 2D materials in biomedicine offer potential for innovative approaches in medication administration, tissue engineering, and health monitoring, thereby amplifying the significance of these membranes across diverse domains. In conclusion, lamellar membranes fashioned from 2D materials possess the potential to substantially propel global resource management, environmental sustainability, and technological innovation. Owing to their multifunctionality and scalable production processes, these membranes are poised to emerge as a fundamental element of future technologies, conferring noteworthy advantages

across a wide spectrum of applications. Overall, the field of responsive materials is set for considerable improvements. Continued research and collaboration across disciplines will be critical in unlocking the full potential of these materials, leading to innovative solutions that solve pressing global concerns in energy, environment, and safety.

List of works performed during the PhD tenure

From the thesis:

1. A. B. Neog, R. K. Gogoi, T. Dutta and K. Raidongia, *ACS Appl. Nano Mater.*, 2020, **3**, 6629-6635.
2. A. B. Neog, R. K. Gogoi, P. Deka, T. J. Konch, B. R. Bora and K. Raidongia, *New J. Chem.*, 2021, **45**, 16883-16891.
3. P. Garg, A. B. Neog, K. Mayawad, A. K. Rajak, P. Deka, R. K. Gogoi and K. Raidongia, *Chem. Eng. J.*, 2024, **480**, 148181.
4. A. B. Neog, A. K. Rajak, B. Saikia, N. Nath, D. Das, P. Deka, R. K. Gogoi, & K. Raidongia, (*manuscript under communication*).

Not from the thesis:

(i) R. K. Gogoi, A. B. Neog, T. J. Konch, N. Sarmah and K. Raidongia, *J. Mater. Chem. A*, 2019, **7**, 10552-10560.

(ii) R. K. Gogoi, A. B. Neog, N. Sarmah and K. Raidongia, *J. Mater. Chem. A*, 2019, **7**, 21157-21167.

(iii) P. Deka, V. K. Verma, B. Yurembam, A. B. Neog, K. Raidongia and S. Subbiah, *Sustain. Energy Technol. Assessments*, 2021, **44**, 101093.

(iv) T. J. Konch, T. Dutta, A. B. Neog, R. Gogoi and K. Raidongia, *J. Phys. Chem. C*, 2021, **125**, 17939-17949.

(v) P. Deka, V. K. Verma, A. Chandrasekaran, A. B. Neog, A. Bardhan, K. Raidongia and S. Subbiah, *J. Memb. Sci.*, 2022, **660**, 120884.

(vi) P. P. Saikia, P. Garg, K. Mayawad, T. Paul, A. B. Neog, B. J. Sarmah, K. Raidongia and R. K. Gogoi, *Mater. Adv.*, 2023, **4**, 3619-3627.

(vii) P. Deka, S. Roy, T. Jyoti Konch, B. Rani Bora, R. Gogoi, A. Bikash Neog, K. Sundararajan, S. Subbiah and K. Raidongia, *Chem. Eng. J.*, 2023, **469**, 143964.

List of Conferences/Seminars attended during the PhD tenure

1. Oral presentation in the International Conference on "Materials Chemistry And Catalysis'' (Virtual Mode) organized by Department of Chemical Sciences, Tezpur University, Assam, India during 4th & 5th of March **2021**.

   Title of Presentation: *Electrical Actuation of Hydrophobic Bilayer Membranes of Reduced Graphene Oxide and Agar for Inducing Chemical Reactions in Microdroplets*
2. Poster presentation entitled "*Hydrophobic reduced graphene oxide and agar based bilayer membrane*" in the International e-Poster Conference on Current Outlook in Material Science and Engineering (COMSE-2k20) from 15-16th of May **2020** Organized by Bodoland University in Association with Tripura University, ADP College, Nagaon & MIT Aurangabad on Facebook.
3. Poster Presentation entitled "*Multi responsive actuator based on reduced graphene oxide and agar*" in Emerging Trends in Chemical Sciences (ETCS-**2020**) conference from 13-15th of February 2020 organised by Department of Chemistry, Gauhati University.
4. Poster presentation entitled "*Stimuli responsive bilayer membrane of reduced graphene oxide and agar*" in the National Conference on 'Recent Advances in Chemistry 2019' (RAC-**2019**) organised by Department of Chemistry, NIT Meghalaya.
5. Poster presentation entitled "*Tailor-cut Nanofluidic Characteristics of Vanadium Pentoxide Ion-Channels*" in the International conference on Frontiers in Chemical Sciences (FICS-**2018**) organised by Indian Institute of Technology, Guwahati.
6. Poster presentation entitled *"Hydrophobic Reduced Graphene Oxide and Agar based Electrical Arms to Perform Chemical Reactions in Microdroplets"* in the International

Conference on “Recent Advances in Materials Chemistry and Catalysis” during 1-3 March, **2023** organised by Department of Chemistry, Dibrugarh University.

7. Poster presentation entitled “*Biomimetic remote handling and sensing devices of multiwalled carbon nanotubes and vanadium pentoxide”* in the International Conference on “Current Trends of Research in Chemistry Towards Sustainability, Health Care and Forensic Analysis (SusChemHeca-2024)” during 14-15 March, **2024** organised by Department of Chemical Sciences, Tezpur University.